MICROSTRUCTURE AND MECHANICAL PROPERTIES EVALUATION OF Al-Cu-Mg ALLOYS PRODUCED BY POWDER METALLURGY (P/M) AND HOT EXTRUSION

A Dissertation
Submitted in Partial Fulfilment of the Requirements
for the Award of the Degree of

DOCTOR OF PHILOSOPHY

in

METALLURGICAL AND MATERIALS ENGINEERING

by

KATTI BHARATH
(Roll No. 716037)

Under the guidance of

Dr. Asit Kumar Khanra

&

Dr. M.J. Davidson

DEPARTMENT OF METALLURGICAL AND MATERIALS ENGINEERING
NATIONAL INSTITUTE OF TECHNOLOGY
WARANGAL - 506 004, TELANGANA STATE

June-2021

DEPARTMENT OF METALLURGICAL AND MATERIALS ENGINEERING

NATIONAL INSTITUTE OF TECHNOLOGY

WARANGAL - 506 004 (T.S.) INDIA

CERTIFICATE

This is to certify that the dissertation work entitled **"MICROSTRUCTURE AND MECHANICAL PROPERTIES EVALUATION OF Al-Cu-Mg ALLOYS PRODUCED BY POWDER METALLURGY (P/M) AND HOT EXTRUSION"** which is being submitted by **Mr. Katti Bharath (Roll No: 716037),** is a bonafide work submitted to National Institute of Technology, Warangal in partial fulfilment of the requirements for the award of the degree of **Doctor of Philosophy** in **Metallurgical and Materials Engineering Department.**

To the best of our knowledge, the work incorporated in the thesis has not been submitted elsewhere for the award of any degree.

Dr. Asit Kumar Khanra
Supervisor
Department of Metallurgical and Materials Engineering
National Institute of Technology
Warangal

Dr. M.J. Davidson
Co-Supervisor
Department of Mechanical Engineering
National Institute of Technology
Warangal

Dr. Asit Kumar Khanra
Head, Department of Metallurgical and Materials Engineering
National Institute of Technology
Warangal-506004

THESIS APPROVAL FOR PH.D.

This Thesis entitled "**MICROSTRUCTURE AND MECHANICAL PROPERTIES EVALUATION OF Al-Cu-Mg ALLOYS PRODUCED BY POWDER METALLURGY (P/M) AND HOT EXTRUSION"**, by **Katti Bharath,** Roll No: 716037, is approved for the degree of Doctor of Philosophy.

Examiners

Supervisors

Dr. Asit Kumar Khanra

&

Dr. M.J. Davidson

Chairman

Dr. Asit Kumar Khanra

Associate Professor, MMED, NIT Warangal

DECLARATION

This is to certify that the research work presented in the thesis entitled **"MICROSTRUCTURE AND MECHANICAL PROPERTIES EVALUATION OF Al-Cu-Mg ALLOYS PRODUCED BY POWDER METALLURGY (P/M) AND HOT EXTRUSION"** is a bonafide work done by me under the supervision of **Dr. Asit Kumar Khanra** and **Dr. M.J. Davidson**, was not submitted elsewhere for the award of any degree. I declare that this written submission represents my ideas in my own words and where others' ideas or words have been included, I have adequately cited and referenced the original sources. I also declare that I have adhered to all principles of academic honesty and integrity and have not misrepresented or fabricated or falsified any idea / data / fact / source in my submission. I understand that any violation of the above will be a cause for disciplinary action by the Institute and can also evoke penal action from the sources which have thus not been properly cited or from whom proper permission has not been taken when needed.

_____

(Signature)

Katti Bharath

Roll No. 716037

Date:…….

ACKNOWLEDGEMENT

First and foremost, I am truly indebted and I express my earnest gratitude for my Research Supervisor **Dr. Asit Kumar Khanra**, Associate Professor, Department of MMED, National Institute of Technology, Warangal for his inestimable expertise and astute guidance. I also thank my joint supervisor, **Dr. M.J. Davidson**, Mechanical Engineering Department, National Institute of Technology, Warangal, for his continuous guidance, support and motivation during my research work. Their unabated enthusiasm, which stems from their absolute command over the subject, has been a constant source of inspiration for me to work hard and the outcome is expressed in the form of this thesis.

Besides my supervisors, I express my gratitude to the Doctoral Scrutiny Committee members: **Dr.Ajoy Kumar Pandey**, Department of Metallurgical and Materials Engineering, **Dr. G. Brahma Raju Golla,** Department of Metallurgical and Materials Engineering and **Dr. Abdul Azeem,** Department of Physics, NIT Warangal for their detailed review, constructive suggestions and excellent advice during the progress of this research work.

My sincere thanks to **The Director**, National Institute of Technology, Warangal, for giving me the opportunity to carry out the work and allowing me to submit in the form of a thesis. I greatly acknowledge **Ministry of Human Resource Development, Govt. of India** for the financial support in the form of fellowship.

I take this opportunity to thank **Prof. D. Chakrabarti**, Indian Institute of Technology-Kharagpur, India, **Dr. Sambasiva Rao**, DMRL-Hyderabad, **Dr. Seetharam**, IIIT-Jabalpur, **Dr. Anish Karmakar**, IIT-Roorkee, and **Mr. Arka Mandal**, IIT-Kharagpur for their support in experimentation.

I also wish to thank all my colleagues in the Department of MME, along with the kind help from non-teaching staff. I would like to thank my friends and seniors who were always with me, encouraged me, and gave support all through the way in my life at NITW.

My heart goes to my beloved parents, and family members who are with all their patience, prayers and faith in the almighty, waited all these long years to see me reaching this stage. Their blessings and care always give me new gusto to do something with more perfection.

Katti Bharath

ABSTRACT

The present study pertains to investigate the deformation behavior of powder metallurgy (P/M) processed Al-Cu-Mg preforms during hot extrusion. A series of hot extrusion studies were carried out on P/M Al-Cu-Mg preforms under various processing conditions to evaluate microstructures and mechanical properties. The present study made an attempt to design the aluminium (Al) alloys by P/M and hot extrusion routes. Hot extruded Al P/M products are extensively used in automotive, aerospace, transportation, building and construction sectors particularly in cam shaft bearing caps productions, trucks suspension parts and aircraft wheels, screw fittings and rivets.

Initially, sinterability studies were performed to optimize the sintering conditions of Al alloy performs. Mechanical and metallurgical properties of aluminum P/M alloys can be enhanced by macro (1-20 wt. %) or micro (<1 wt. %) additions of different alloying elements. Micro addition of magnesium (Mg) was alloyed into Al-4%Cu matrix in the range of 0-1wt.% (0, 0.25, 0.5, 0.75 and 1 wt. %). Optimization of the amount of Mg in the Al-4%Cu was performed by analyzing the microstructure and densification behavior of all compositions at different sintering temperature ranges from 400 °C-600 °C. The liquid phase fraction increased with Mg content in the alloys. This liquid phase was distributed in the gaps between the particles with capillary force and this increased the formation of secondary phase particles such as Al_2Cu (θ) and Al_7Cu_2Fe (ω). The maximum sintered density of 95.38% of theoretical density was observed at sintering temperature of 550 °C in Al-4%Cu-0.5%Mg alloy with comparable sintered densities of all other compositions sintered at 400 °C, 450 °C, 500 °C and 600 °C. A similar trend was also observed in the case of apparent hardness that reflected as in the sintered density. The liquid phase remained at grain boundaries in the compositions above 0.5% Mg which led to the formation of brittle grain boundary networks and thicker grain boundaries. Appreciable shrinkage was observed in the samples sintered at 600 °C but these were observed to be over sintered and formed coarse grains. Thus, the 550 °C temperature and Al-4%Cu-0.5%Mg were optimized as sintering temperature and the desired composition for all future studies.

Semi-solid extrusion was carried out on optimized Al-4%Cu-0.5%Mg P/M preforms for deformation behavior analysis. The extrusions were performed in the temperature range between solidus (542.7 $^{\circ}$C) and liquidus (662.8 $^{\circ}$C) temperatures so that the minimum to maximum solid fraction range could be achieved. The curve obtained by TG/DTA was used to calculate the solid-liquid fractions between solidus and liquidus temperature range. Extrusion tests of the preforms were conducted with extrusion ratios of 1.44, 2.55, and 4 and approach angles of 30°, 45°, and 60° for three different working temperatures such as 550 °C, 575 °C, and 600 °C, respectively. The existence of precipitates and dispersoids such as θ and ω phases was observed in SEM, XRD and EDS analyses of extruded samples, which improved the hardness. The average grain size of semi-solid extrudates decreased with increasing extrusion ratio and increased with increasing die approach angle and deformation temperature. All the extruded samples were demarcated into three regions (front end, middle part and rear end) to study the structure-property correlation and to understand the temperature and metal flow profiles during deformation process. The deformation temperature of 550 °C, extrusion ratio of 4 and approach angle of 30° gave the best results in semi-solid extrusion process without extrusion defects such as surface cracks and hot shortness.

To reduce extrusion defects and increase the properties of extruded rods, the deformation temperature was reduced to below 550 °C and used an optimized die with extrusion ratio of 4 and an approach angle of 30° for further studies of hot extrusion. Hot extrusion tests were performed at temperatures of 450 °C, 500 °C and 550 °C, strain rates of 0.1s^{-1}, 0.2 s^{-1} and 0.3 s^{-1}, and initial preform relative densities (IPRD) of 70%, 80% and 90%, respectively. The constitutive base analysis was conducted to develop mathematical equations to predict hot deformation and densification behavior of P/M Al preforms. The aim of the study was to analyze the effect of IPRD on hot deformation behavior and to model and predict the flow stress of extruded samples using constitutive equations. Furthermore, the effect of other process parameters such as temperature and strain rate on plastic flow properties was evaluated. This was carried out by constructing and analyzing true tress-true strain curves at different IPRDs of 70%, 80% and 90% for a temperature ranging from 450 °C-550 °C and strain rate range of 0.1-0.3 s^{-1}. The true stress-strain curves exhibited three stages of deformation which represent work hardening (WH), dynamic recovery (DRV) and dynamic recrystallization (DRX) during deformation at different temperatures, strain rates and IPRDs. The results showed that flow stress

values were influenced by IPRD, deformation temperature and strain rate. The results showed that the flow stress exhibited peak flow stress (PFS) at certain strain value, and then held constant or decreased gradually till it reached high strain value, showing dynamic softening. Arrhenius-type constitutive equations were developed to predict the flow stress of hot extruded products. Zener-Hollomon (Z-H) parameter was used to explain the relationship between peak flow stress (PFS), temperature and strain rate in an exponential equation containing deformation activation energy and material constants. Subsequently, the statistical indicators correlation coefficient (R) and the average absolute relative error (AARE) were assessed to confirm the validity of constitutive equations. The results indicate the experimental and predicted PFS values were in good agreement which indicate the accuracy and reliability of the developed model for P/M processed Al-4%Cu-0.5%Mg preforms. Microstructure evaluation was carried out and the grain size of extruded samples was measured by line intercept method. A mathematical model was developed between Z-H parameter and DRX grain size which helps in calculating the DRX grain size for various deformation temperatures, strain rates and IPRDs. The measured DRX grain size (d_m) was compared with mathematically calculated DRX grain size (d_c) to validate the accuracy of the developed mathematical model. It was observed that the measured DRX grain size agreed well with calculated DRX grain size thereby proving the precision and reliability of the developed mathematical model for various deformation conditions. Finite element method (FEM) simulations were performed to analyze metal flow, stress behavior and the corresponding strain induced in Al-Cu-Mg alloys at different deformation conditions during extrusion. The commercial finite element analysis software i.e., DEFORM 2D used as the simulation tool. The flow behaviour and microstructure of hot extruded samples were modelled by formulating Arrhenius type constitutive relation.

Later, a systematic study was carried out to establish a structure-property correlation of Al-Cu-Mg P/M alloys as a function of extrusion temperature and strain rate. Superior mechanical properties were attained by the formation of precipitates and dispersoids under deformation in extrusion, as witnessed in scanning electron microscopy (SEM), electron backscatter diffraction (EBSD), electron probe micro analyzer (EPMA) and X-ray diffractometry (XRD) analyses. DRX was facilitated with the increase in deformation temperature and a decrease in strain rate. Brass {110}<112>, Copper {112}<111> and S {123}<634> texture components were developed due to extrusion while Cube {100}<001> and Goss {110}<001> orientations were found to be

strengthened due to deformation temperature. The final microstructure of extrudates indicated the presence of α-Al matrix, Al_2Cu eutectic structure and Al_7Cu_2Fe compounds. Primary Al_2Cu precipitates dissolved in the matrix with increase in deformation temperature and decrease in strain rate of extrusion. Both dislocation density and residual stress reduced with an increase in extrusion temperature as estimated from nanoindentation experiments following established models. Both yield strength and young's modulus increased after extrusion due to dislocation propagation; however, both decreased with increasing extrusion temperature and decreasing strain rate.

Taguchi Experimental design, analysis of variance (ANOVA) and response surface methodology (RSM) were applied and successfully modeled to predict the influence of input process parameters, namely, deformation temperature, strain rate and IPRD on the densification behavior and mechanical properties of hot extruded Al-Cu-Mg P/M alloys. The models were then tested for adequacy and prediction capability.

CONTENTS

List of Figures

List of Tables

List of Symbols and Abbreviations

Symbols

A_c	True contact area
A_{dyn}	Material constants
A_g	Geometrical area
d_c	Calculated DRX grains
d_{dyn}	Dynamically recrystallized grain size
d_m	Measured DRX grains
k	Partition coefficient
n_{dyn}	Material constants
n	Material stress index
P	Normal stress
Q	Activation energy
R	Universal gas constant
R^2	Correlation coefficient
T	Absolute temperature
T_s	Solidus temperature
T_l	Liquidus temperature
Z	Zener-Hollomon parameter
α	Poisson’s ratio
έ	Strain rate
ε_{eff}	Effective strain
a	Material constant
A	Material constant
β	Material constant
δ	Absolute error
δ_m	Mean absolute error
σ	Flow stress
σ_{Ex}	Experimental flow stress
σ_P	Predicted flow stress

Abbreviations

ANOVA	Analysis of variance
BBD	Box-Behnken experimental design
CDRX	Continuous dynamic recrystallization
DDRX	Discontinuous dynamic recrystallization
DEFORM	Design environment for forming
EBSD	electron backscatter diffraction
EDS	Energy-Dispersive Spectroscopy
EPMA	Electron probe micro-analyzer
WH	Work hardening
DRV	Dynamic recovery
DRX	Dynamic recrystallization (DRX)
FEM	Finite element method
GDRX	geometric dynamic recrystallization
HSFE	High stacking fault energy
HAB	Higher angle grain boundaries
IPF	Inverse pole figures
IPRD	Initial preform relative density
LAB	Lower angle grain boundaries
LAM	Local Average Misorientation
ODF	orientation distribution function
OM	Optical microscope
PFS	Peak flow stress
P/M	Powder metallurgy
RSM	Response surface methodology
SEM	Scanning electron microscope (SEM)
Std. Dev.	Standard deviation
WH	Work hardening
XRD	X-ray diffractometry

List of Appendices

CHAPTER 1

INTRODUCTION

1.1 Foreword of the present work

Professionals and researchers in the field of manufacturing industries have been continuously researching light-weight materials to understand the nature of processing and the factors affecting their behavior. The prime motive for conducting intensive investigation is to enhance the efficiency of light-weight materials in the fields of aerospace, automotive, defense, transportation, building and architecture. Aluminium alloys have been extensively used in numerous structural and industrial applications because of their innumerable advantages such as high strength-to-weight ratio, low density, high hardness, good corrosion resistance, etc.[1–3]. Conventional pressing-and-sintering powder metallurgy (P/M) process is the most promising technology compared to other conventional manufacturing processes such as forging, casting, and machining, to develop different engineering components to satisfy the requirements of above mentioned industries with high rates of production at low cost. In general, P/M process is a very rapid and highly economic technique for producing high volume components with better surface finish, more accuracy, superior near net shape, and strength. P/M is the optimum choice over other conventional manufacturing processes to produce products with intricate and near net shape, involving marginal utilization of materials and having low energy requirements [4].

P/M industries have been rapidly growing over the decades due to the continuous increase in demand for high performance parts. However, the presence of inherent porosity in the sintered parts degrades the mechanical properties. Thus, the P/M industries usually undergo secondary forming processes such as forging, rolling, extrusion and hot deformation to eliminate maximum porosity. Therefore, investigation of secondary forming of P/M components is the most stimulating new field in metal forming industries due to superior metallurgical and mechanical properties and also because of its flexibility over other conventional production processes. Hot extrusion of light-weight materials is a very competitive technology for producing new products with a wide range of mechanical properties in less time. The widespread use of hot

extruded light-weight material is due to the adoptability of applications from the combination of the extruded product form and the characteristics of light-weight materials. Hot extruded P/M products are extensively used in automotive, aerospace, transportation, electrical, medical, building and construction, household, and sports applications.

1.2 Introduction to Al/Al alloys

Aluminium and its alloys have an unusual combination of properties that make Al one of the most versatile, attractive, and economical metallic material for a wide range of applications. Al alloys are the second most processed materials after steels in use as structural metals. The report from Organization for Economic Cooperation and Development (OECD) and International Energy Association (IEA) claims that the natural gas and fossil fuels supplies will be exhausted in the near future [5]. It is possible to reduce weight by up to 300 kg in a medium size vehicle (~1400 kg) and save 0.3 to 0.6 liters per 100 km by reducing the car weight by 100 kg [6]. These works proved that Al alloys are the most promising materials in order to reduce the vehicle's weight for next generation vehicles [7]. Al alloys possess a strong affinity for oxidization that causes steel to rust away. Al and its alloys have been replacing ferrous materials in many industrial and engineering applications because of their optimal physical and mechanical properties.

Mechanical and metallurgical properties of Al can be improved by either macro (1-20 wt.%) and/or microscale (<1 wt.%) addition of some alloying elements such as Copper, Magnesium, Silicon, Manganese, Zinc, and Nickel. The 2xxx series (Al-Cu alloys), the 3xxx series (Al-Mn alloys), the 5xxx series (Al-Mg alloys), the 6xxx series (Al-Mg-Si alloys), and the 7xxx series (Al-Zn-Mg alloys) are the primary alloys classes of Al [8]. Specifically, 2xxx series alloys have higher strength and hardness among all others at elevated temperatures. [9, 10]. Pure Al and its alloys can be used to make products ranging from structural materials to thin packaging foils due to various combinations of their advantageous properties: high strength to weight ratio, lower density, relatively high corrosion resistance, high thermal and electrical conductivity, high ductility, recyclability and formability, resultant low working cost, etc.

1.3 Effects of alloying additions to Al

The physical, metallurgical, chemical and mechanical properties of pure Al are greatly enhanced by the addition of selected elements. The major alloying elements for Al are Cu, Mg, Si, Mn and Zinc. The maximum addition of Cu in Al (2000 series) is in between 4 to 6% which is highly susceptible to heat treatment and subsequent aging. The strength and hardness of Al increase with increasing Cu content up to a maximum of 6% due to its solubility effect. The foremost advantages of adding Mg to Al-Cu alloys are to accelerate age hardening at room temperature and also to disrupt the oxide layer formed around the Al particles. As little as about 0.5% Mg addition to Al-Cu alloys is effective in improving aging characteristics and contributes to an increase in strength [11]. Mg is the primary alloying element in 5xxx alloys. The addition of Mg in Al alloys increases the strength without compromising the ductility. Al-Mg alloys are especially used in sea-water and marine applications due to higher corrosion resistance and weldability [12].

Silicon is the highest impurity in the 6xxx series heat-treatable alloys and is added in Al with Mg at levels up to 1.5% to form Mg_2Si. Al-Si alloys have good machinability, formability, weldability, and corrosion resistance but lower strength as compared to most of the 2xxx and 7xxx series alloys. Si also has the tendency to reduce the cracking in Al-Cu-Mg alloys. The existence of Zinc in 7xxx series alloys increases solution potential, hence it has been used in protective cladding and in anodes. But the application of these alloys is curtailed due to hot-cracking and stress-corrosion cracking. Thus, 2xxx series Al-alloys have been adopted in the present study.

1.4 Phase diagram of Al-Cu alloy

The Al-Cu phase diagram has been carefully studied by several researchers and their overviews have been published [13–16]. The phase diagram of Al-Cu alloy system is shown in Fig. 1.1 (developed in Thermo-Calc software-2016b) in which it shows only up to 60% Cu by weight. According to the Al-Cu phase diagram, the solid solubility of Cu in Al is 5.65 wt.% at the eutectic temperature of 548.2 °C [13]. The solid solubility decreases as the temperature decreases. The liquid phase appears or starts at the eutectic temperature on Al boundaries. Due to

the Cu partials solubility in the Al matrix and less Cu content, the liquid phase could be partially or completely absorbed into Al particles. Thus, this leads to effective sintering of Al-alloys. Al-4%Cu is the best optimized alloy composition in which the age hardening and precipitate hardening phenomena are more [17]. The supersaturated Cu precipitates out as Al_2Cu (θ) phase and improves the mechanical properties at this eutectic temperature [18]. The solubility limit of Cu in Al could be reduced if other alloying elements such as Mg, Si, Mn, Zn etc. are added.

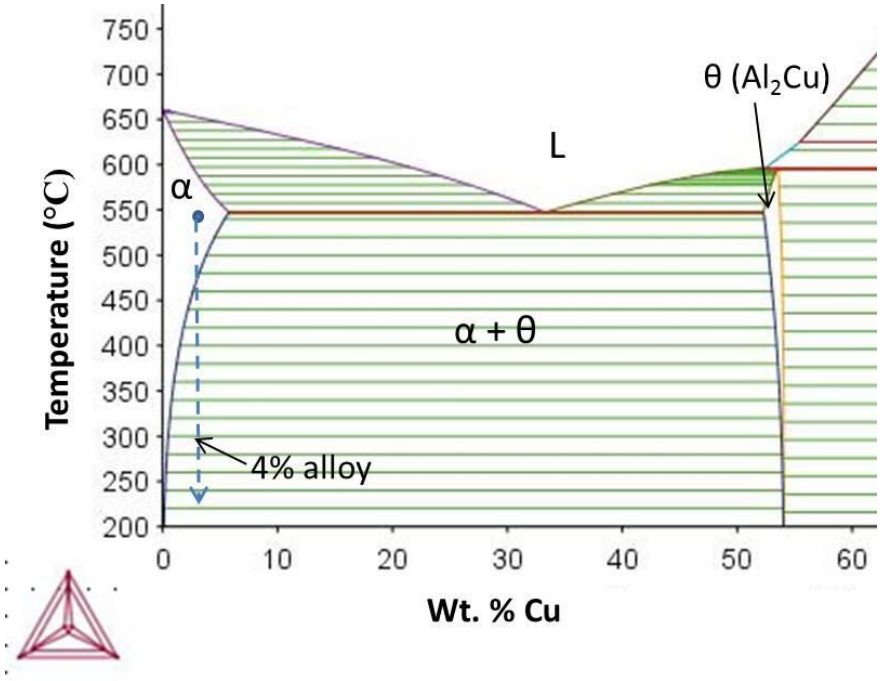

Fig. 1.1 Al-Cu phase diagram

1.5 Powder metallurgy (P/M) of Al-alloys

Aluminium P/M is a metal forming process that is employed to produce vehicle components which can offer the combination of materials savings due to near net shape processing and weight savings due to low density of Al attributes. The properties of sintered Al alloys also depend on powder morphology, alloy composition, compaction pressure, sintering temperature and time [17, 19, 20]. The market share of the Aluminium P/M automotive parts has been increasing year by year due to their advantages: fine grain structure, homogeneous microstructure, higher strength, high corrosion resistance, high production efficiency and unlimited alloy design [21–23].

Mechanical properties of Aluminium P/M alloys can be improved by macro and micro additions of alloying elements. Especially, 2xxx (Al-Cu-Mg) and 6xxx (Al-Mg-Si) series P/M alloys have been studied [24, 25] for different applications due to their eutectic structure [26] at elevated temperatures. Aluminium P/M is now well known as a robust, cost effective and reliable technology that is employed in various engine platforms, for example, production of Cam shaft bearing caps in combustion engines. Automotive sectors are replacing cast ones with P/M Al alloys due to higher change in properties. Al alloys produced through P/M are also used in potential automotive applications such as connecting rods and oil pump G rotors in automotive transmissions [17].

1.6 Advantages of P/M over casting

There are many advantages of powder metallurgy over traditional casting.

1) One greater advantage of Al-Cu-Mg parts out of P/M over casting is their consistency. The amount and weight of powder used in P/M is uniform throughout the process and compacted to the same density after sintering.
2) Near-net shape products can be produced by P/M process. Sintering of powder compacted parts fuses the powder mix into a fully hardened piece.
3) Porosity and blowholes form during the casting process. The localized cracking is most likely possible due to the blowholes and porosity.
4) The shear stresses fracture the oxide layers (formed during the atomization process) covering the particle surfaces of powders during deformation of P/M alloys, resulting in a well-bonded microstructure and improved mechanical properties.
5) Another advantage of Al-Cu-Mg alloy processed by P/M is its control over microstructure. P/M can provide greater control and consistency in forming finer microstructures. Products with fine microstructure provide much higher mechanical properties than cast materials.
6) Intermetallic phases and precipitates form during sintering and after sintering which improve the mechanical properties of P/M Al alloys.
7) Al-Cu-Mg alloys produced by P/M have shown superior mechanical properties such as high temperature strength, stiffness and wear resistance.

8) Overall operating cost makes P/M better than casting. The scrap rates of P/M are significantly lower than casting. No secondary processing is required for P/M parts as casting parts. The total energy consumption of P/M is lower than casting.

1.7 Development of porous P/M preforms

Though the plastic deformation of P/M materials is similar to the conventional fully dense materials, the presence of a substantial amount of pores in P/M components complicates the mechanical properties of materials. Initial preform relative density (IPRD) plays a vital role in altering final density and mechanical properties of P/M materials. The material density and porosity mainly depend on the mass of the powder mixture and compacting pressure. Powder to compaction pressure ratio produces different IPRD compacts. The density of compacts increases either by increase or decrease in compaction pressure and mass of the powder during compaction. Several researchers have investigated the effect of IPRD on the formability of P/M compacts [27, 28]. Thus, the density and porosity of P/M materials can be controlled by proper use of compaction pressure and mass of the powder. However, the accurate prediction of compaction pressure is not possible to produce different IPRD samples. So, the trial and error method has been adopted in many conditions.

1.8 Densification behaviour of P/M preforms

The porous components usually undergo secondary processes such as forging, rolling and extrusion to eliminate the porosity and increase the density of components. During deformation process, the metal flows into the pores and hence the volume of component decreases and increases the density persistently. Several scientists have reported the densification behavior of P/M compacts during forging and extrusion [29–32]. The density after deformation determines the performance and service life of the components. Very few works have been published on densification behavior after extrusion of P/M alloys. Thus, the secondary process which is carried-out in the present investigation is hot extrusion. This work is aimed at minimizing uncertainties in mechanical properties and non-uniformities in metallurgical properties by eliminating the pores and making P/M parts available for advanced applications.

1.9 Semi-solid extrusion/Hot extrusion of P/M preforms

Semi-solid forming is a new technology in forming near net shape products and offers several potential benefits compared to conventional casting and forging. The major advantages of semi-solid forming are flow stress reduction during shearing, reduced porosity, reduced operating temperature, low solidification shrinkage, and a minimal risk of hot tearing [33–36]. The other advantages of semi-solid extrusion include lower friction and extrusion force, high productivity, longer tool life, much more material fluidity, uniform microstructure, etc. [37]. The final product of the semi-solid extrusion coexists between solidus and liquidus temperatures. This semi-solid behavior of the materials was first studied by Flemings et al. [38]. Since then, scientists and engineers have started working on different alloys [39]. However, the application of this process is limited to large volume production and thin plate fabrication. This is due to a drop in quality of components attributed to cracks propagation and crease caused by material shrinkage [40]. The other disadvantages of semi-solid forming are the preparation of the feedstock material and cost.

The hot extrusion process offers lower energy consumption and extrusion pressure, high productivity, longer die life, fine and uniform microstructure without propagation of cracks on the surface of the samples [41]. The application of hot extrusion to Al alloys is very attractive because of their versatility and low density coupled with higher mechanical properties [42]. Automobile industries have been working hard to reduce the weight of automobile parts by using light-metal parts because of environmental concern and oil crisis. As a consequence, hot forming of Al alloys have been concentrated predominantly and used for automobile applications such as cam shaft bearings, brake cylinders, chassis components, rims and so on. [43]. Aluminium P/M alloys produce globular and homogeneous microstructure even after deformation. This method needs careful control of the sample and tool temperature, strain rate, and rate of deformation in order to improve the thermal exchange between tool and sample [41, 44].

1.10 Constitutive modeling of hot deformed materials

It is essential to understand the hot deformation behavior of porous materials to develop the best processing route and overcome crack propagation in the final deformed products. Optimum processing parameters can improve the properties of materials in hot deformation process [45].

During hot deformation, the material flow, mechanical and metallurgical properties are significantly affected by many factors such as deformation temperature, strain rate, strain, friction etc. In order to describe the material deformation behavior and to establish optimum processing variables, it is essential to investigate constitutive modeling. Constitutive equations are expressed in terms of linear and non-linear relationships between process parameters mainly stress, strain, strain rate, temperature and IPRD of the materials. Several researchers [46–48] developed constitutive equations to describe the plastic flow of metals during deformation at elevated temperatures. However, the literature on constitutive equations proposed for porous materials is very limited. Therefore, it is also fascinating to investigate the hot deformation behavior and develop a constitutive equation to predict the flow stress by considering the influence of porosity and other process parameters such as temperature and strain rate on deformation and densification behavior.

1.11 Finite Element Method aspects of deformation

Finite element method (FEM) is one of the most successful numerical methods reported in the literature. It provides detailed and accurate results in the study of plastic deformation behavior of materials regarding metal flow, distribution of stress, strain, strain rate, density, temperature and friction behavior, and hence it reduces the process development cost and effort. Over the past few years, FEM analysis codes have been successfully applied in predicting and improving metal flow in various metal forming operations. Oh et al [49] revealed that FEM code based on rigid viscoplastic formulation which had been developed at Battelle labs in 1980s was one of the first successful 2D implementations of the forming process to use in the forging industry. Further, they released an improved and commercially supported form of FEM code which is Deform 2D. Deform 2D is well equipped with improved preprocessor and postprocessor capability and automatic mesh generation module. Since then, Deform 2D has been successfully applied to simulate and predict the metal flow and defects for different metal forming operations under cold and hot working conditions [50, 51]. The information generated by FEM simulations regarding work piece and tool is very useful for designers to improve the die and process design, and thus save efforts and cost in making products. FEM can also be used for the simulation of extrusion process. However, the application of FEM simulation in the extrusion industries is limited due to

the difficulties involved, such as strong temperature gradients, large deformations, large strain rate gradients, and transient behavior. So, the present work has concentrated on simulation of hot extrusion process as it is a challenging area of research and intellectually stimulating too.

1.12 Taguchi's robust design method of optimization

Robust design is a powerful tool and an engineering methodology for the design of a high quality system at low cost. Design of Experiments (DOE) was introduced by Sir R.A. Fisher which was first used in ancient agricultural science to optimize trial conditions and treatments in order to procure the best crop [52]. DOE is considered as the most comprehensive approach to product or process development which provides prophetic knowledge of a multi-variable and complex process with few trials. DOE method has been divided into two designs, such as full factorial design and fractional factorial design [53]. Although these designs are well known, the full factorial design results in performing a large number of experiments and the use of fractional factorial design is concluded as too complex and no proper guidelines for its application [54] Considering all these difficulties, Dr. Genich Taguchi has developed a standardized and modified designs i.e., Taguchi designs [55, 56]. Taguchi designs are easy to adopt and provide a efficient, simple and systematic approach for optimization [57]. The application of Taguchi method has been widely expanded to engineering and scientific communities such as Biotechnology [54], mechanical component design [58], and manufacturing systems [59].

The success of Taguchi method is due to achieving desired results and designing high quality systems by discretizing the process parameters into control and noise factors. Taguchi method utilizes some major techniques such as Orthogonal Array (OA), Signal-to-noise (S/N) ratios, and Analysis of Variance (ANOVA) to identify the proper process control factors, and to obtain the desired results. These techniques are used to simplify the experimental design, analyze the data, and predict the optimum results and quality of components. Hence, the interest in Taguchi method continues to grow as it provides much reduced variance of experiments [60]. OAs provides a best set of minimized experiments. Table 1.1 shows different orthogonal arrays along with number of rows and columns.

Table 1.1 Standard orthogonal arrays [60]

Orthogonal Array	Number of Rows	Maximum number of factors	Maximum number of columns at these levels			
			2	3	4	5
L4	4	3	3	-	-	-
L8	8	7	7	-	-	-
L9	9	4	-	4	-	-
L12	12	11	11	-	-	-
L16	16	15	15	-	-	-
L16	16	5	-	-	5	-
L18	18	8	1	7	-	-
L25	25	6	-	-	-	6
L27	27	13	-	13	-	-
L32	32	31	31	-	-	-
L32	32	10	1	-	9	-
L36	36	23	11	12	-	-
L36	36	16	3	13	-	-
L50	50	12	1	-	-	11
L54	54	26	1	25	-	-
L64	64	63	63	-	-	-
L64	64	21	-	-	21	-
L81	81	40	-	40	-	-

1.13 RSM aspects of deformation

P/M components usually undergo secondary forming process such as forging, rolling and hot deformation to reduce the porosity [61]. As a result, the final density and mechanical properties of components increase persistently. Understanding the final density of the P/M preforms after bulk forming process is important as it determines the service performance of components. Nowadays, the more number of manufactures are interested in predicting the final density of the P/M components and optimizing the process parameters. Currently, several modeling techniques

have been used to predict and optimize process variables in different manufacturing areas [62–64]. Response surface methodology (RSM) is found to be a widely used optimization technique for predicting and validating the final density after deformation. RSM technique was first developed by Box and Wilson in 1951. RSM is an effective statistical technique for experimental design, model building and searching optimum conditions [65–68].

This technique develops a statistically validated predictive model which integrates all the independent variables (input parameters) and uses this input data to generate a set of equations that can give optimum process configurations and theoretical values of an output (dependent variable). The well-designed regression analysis produces output based on the controlled values of input parameters (independent parameters). Thereafter, the dependent variable (output) can be anticipated based on the controlled value of independent variables. RSM creates the relationship between input process parameters and output and finds the location of optimum conditions in precise estimations. This technique can also be used to evaluate the relationship and interactions between multiple parameters using quantitative data by establishing a model equation. RSM methodology can be done in two designs such as Box-Behnken design (BBD) and face-centered central composite design (CCD). BBD design has been used in large scale manufacturing industries as it has advantages of avoiding treatment combinations that are at extremes [69].

1.14 Applications of Al and P/M Al-alloys

Al and its alloys are being used as substitutes for ferrous materials in many applications. In most of the engineering applications, P/M aluminium and its alloys are preferred due to low density, high strength to weight ratio, better wear resistance, high surface finish and dimensional control. The vast applications of P/M aluminum and its alloys are in automobile and aerospace industries to reduce the weight of the product and, thereby increase the fuel efficiency and reduce exhaust emission. Some of the common applications of aluminium alloys are listed below:

- Automotive parts: Engine cylinder block, chassis, bodies, radiators, hubcaps, drive shafts etc.
- Aerospace components: Fan and compressor cases, light structures, extrudates, forgings, sheets, plates, fuel tanks, brackets, fixtures, chassis, covers, and casings for many tools and devices.

- Rail materials: aluminium alloy sheets and extrudates.
- Buildings: Sheet-rolled or moulded form for window frames and other glass supports, for siding, partitions, roofing, doors, and canopies.
- Marine equipment: Hulls, masts, and superstructures on pleasure boats and the bridges and superstructures of passenger ships and merchant ships.
- Mechanical industry and engineering sectors: robots, heat exchange parts in electronics, seawater desalination devices, HVAC exchangers and the plastic industry.
- Packaging: foils, beverage containers, aerosols, bottle caps, lids, etc.
- Energy distribution: high tension wires, telephone cable shields, and protectors against electrical and magnetic fields.
- Sports and leisure: Household appliances, refrigerators, radiators, CD coatings, hang gliders, scooters, etc.

P/M aluminium and its alloys are mainly used for better material characteristics or ease of making complex shapes at low production cost. They have high Young‘s modulus, low density, better high-temperature strength and better wear resistance. Their improved material characteristics make them potentially suitable for several applications in automobile and aerospace industries as follows:

- Aerospace components: Airframe primary-load-carrying structural members, engine components, oil fins, winglets, helicopter rotors, etc.
- Automobile industries: shock absorbers, brake rotor disk, rod guides, transmission gears, drive shaft, connecting rods, sensor housing suspension vanes, etc.
- Business machines: Hubs, drive-belt pulleys, end caps, connecting collars.
- Electrical and electronic applications: Substrate/housing for microelectronics package, heat-sinks, and spacers on structural electric transmission towers.

Al-Cu-Mg P/M alloys are heat treatable and artificial age hardening materials which can be used in many automobile and aerospace applications. The mechanical properties of these alloys are almost and sometimes exceed low carbon steel. Further deformation and aging improve the mechanical properties such as yield strength without affecting tensile strength of P/M Al-alloys. Deformed Al P/M alloys can be used in parts and structures requiring high strength-to-weight ratios, cam shaft bearing caps productions, trucks suspension parts and aircraft wheels, screw fittings and rivets to aircraft structures, cylinder liners, vanes and rotors

for automotive air conditioners and oil pump rotors [70, 71]. Thus, to find the applicability of these alloys in industrial applications as stated above and for other similar applications, formability and, in depth microstructural and mechanical property studies need to be conducted on Al-Cu-Mg alloys. Fig. 1.2 shows some of the components that are and to be made from Al P/M alloys.

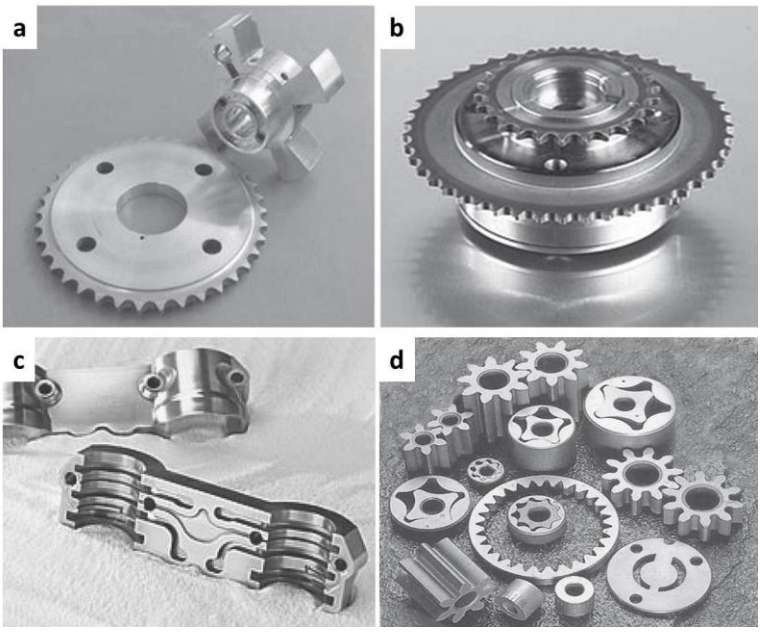

Fig. 1.2 Engineering components that are produced from P/M Al-alloys, a) Sprocket and rotors (credit: EPMA) [1], b) Variable valve timing (credit: MPIF) [1], c) Cam shaft bearing caps (credit: MPIF) [72], and d) Oil pump rotors and gears [72]

Al-Cu-Mg alloys processed through P/M and hot extrusion are being used in many applications as mentioned above. So, the present work is organized as shown below to develop components with higher microstructural and mechanical properties.

1.15 Organization of the thesis

The thesis is presented in seven chapters including the present part **Chapter 1** which presents the effects of elemental additions to Al, deformation and densification behavior of P/M Al preforms. It also explains the constitutive modeling and FEM aspects of hot deformed materials. The relevance of P/M aluminium its alloys in industrial applications has been discussed.

Chapter 2 provides a detailed survey of literature relevant to current investigations. The main objective of critical review of literature was to carefully examine any research work done previously which is related to the present work and identify the gaps existing in the current knowledge of sintering behavior, deformation, densification, microstructural and mechanical properties evolution of P/M Al preforms.

Chapter 3 reports the objectives and the scope of the present research work. The objectives are adopted based on the gaps identified in the available literature related to the current work.

Chapter 4 projects pictorial representation of the methodology adopted in the current research work, experimental plan on the preparation of sintered and extruded materials and characterization and mechanical properties evolution techniques used in the current work.

Chapter 5 illustrates experimental and material characterization machinery details, such as the selection of materials, specimen preparation, extrusion test, macrostructure and mechanical analysis, and Taguchi and RSM modeling techniques for final relative density and mechanical properties prediction.

Chapter 6 provides results and discussion of the investigation in which the experimental results are analyzed using photographs, graphs and charts. The sintering behavior of different Al-Cu-Mg P/M alloys and their microstructural analysis are presented. Then the deformation, densification, microstructural analysis and mechanical properties of P/M Al-Cu-Mg preforms during semi-solid extrusion and hot extrusion are discussed. Constitutive modeling was developed in terms of IPRD to predict the flow stress during deformation with various process parameters. In addition, the effect of various parameters on the hot extrusion using FEM simulation and prediction of final density and mechanical properties using statistical modeling techniques during hot extrusion are explained in detail.

Chapter 7 contains conclusions drawn from the current research work and the scope of future research work.

CHAPTER 2

Literature Review

Several researchers have done commendable work in various aspects of sintering behavior, semi-solid forming, and hot deformation on Aluminium P/M alloys. Most of the studies have been grouped into developmental studies, microstructural and mechanical properties evolution studies, and simulation and modeling studies. The present chapter summarizes the works performed by several researchers on various aspects of semi-solid forming and hot forming technologies.

2.1 Introduction to powder metallurgy process

The typical press and sinter P/M process is one of the metal forming processes in which finished or semi-finished products are made from mixed metallic powders. The art of preparing components by pressing and sintering of powdered materials is an old age prehistoric process. Many metallic products of the bygone ages could be made by P/M technique [73]. As a notable witness, the natives of Matakam tribe of central Africa and certain Egyptian implements are believed to be made by primitive P/M technology [74, 75]. The modern P/M technology emerged in 1920s, and then it has been drastically taken to advanced levels. Over the last few decades, the modern P/M technique has been established as competitive and the most flexible method over other manufacturing processes such as machining, forging, casting and stamping for making most of the engineering parts in automobile, aerospace, electric and defence industries. P/M is the best choice when there is need for a rapid, high volume production and for products with better strength, near net shape, corrosion resistance, and wear resistance.

The major steps involved in P/M technique include powder mixing, compaction and sintering. Compaction of powders improves the density of loose powders due to the mechanical interaction of metal particles with neighboring particles. Universal die compaction is the most precise method of powder consolidation because it is a rapid and highly suitable technique for large production. Friction at the die-powder during compaction has influence on the behavior of particle interactions and densification. Thus, several researchers [76–78] have reported

experimental investigations on controlling friction between die wall and powder, and the effects of lubrication on density distribution during compaction under various processing conditions. In addition to die compaction, the other advanced compation techniques such as frictionless isostatic pressing [79], high speed compaction [80], equal channel angular pressing [81], and rotary die pressing [82] have been used for achieving productive powder consolidated products.

Sintering is an essential stage of P/M process which has emerged to increase the strength, density and dimensional control of powder cold compacts. The density and mechanical properties of sintered products mainly depend on parameters such as sintering temperature, time and atmosphere [83]. Protective gas atmosphere is necessary to prevent oxidation of compacts during sintering; hence proper control of sintering parameters is very important for successful sintering. The final sintered products can only be applicable to all applications when the sintering process creates strong bonding between particles with minimum oxides and good dimensional control [83].

2.2 Sintering behaviour of Al-alloys

High performance and near net shaped components can be produced by Al P/M process which combines the superior properties of Al with the ability of P/M. Thus the operating or capital costs associated with intricate machining operations can be reduced or eliminated [84]. In order to produce components with good sinterability and higher mechanical properties, it is essential to control the sintering process parameters such as die compaction pressure, addition of elemental powders, sintering temperature, atmosphere, peak temperature holding time and heating rate. Besides, the mechanical properties, microstructure and phase transformation of materials are also controlled by the above mentioned parameters. Liquid phase sintering (LPS) [85, 86] is a widely accepted technique that is capable of producing components with improved mechanical properties. Density of any Al alloy is improved by typical LPS mechanism involving rearrangement of particles, breaking up of oxide layers, filling of pores and solid state sintering [87]. However, a high degree of liquid phase in materials leads to distortion of compacts and a reduction in mechanical properties [88]. Padmavathi et al. [89] investigated the effect of sintering temperature and compaction pressure on 2712 alloy (Al-3.8Cu-1Mg-0.8Si-0.3Sn). The results obtained illustrated that the densification and mechanical properties of 2712 alloy

increased with increasing sintering temperature and compaction pressure. However, higher sintering temperature resulted in microstructural coarsening which led to reduction in mechanical properties [89]. An optimum sintering temperature of 580 °C was observed in sinterability of Alimix 431D which showed higher tensile strength and hardness of 329 MPa and 40 HRB, respectively [23, 90]. Under the compaction pressure of 400 MPa and 600 °C sintering temperature, P/M 2324 alloys exhibited excellent sintering response [22]. Besides sintering temperature and compaction pressure, sintering time also affects the densification of P/M Al-alloys. Du et al. [11] studied the effect of sintering time on microstructural and mechanical properties evolution during the sintering of Al-Cu-Mg alloy. The results showed that the densification and mechanical properties improved continuously from 30-120 min sintering time. Then reduction in densification was observed at 180 min sintering time due to new pores created by material migration [11].

Along with these sintering parameters, the addition of trace elements can also affect the densification of Al-alloys during sintering. For example, Mg in Al-Cu alloys is considered to be the best agent to react with oxide layer of Al powder. The Mg content removes the oxide layer and promotes atomic diffusion of Cu in Al [91–93]. Bishop et al. [94] observed the effect of addition of Ag and Sn on wear behavior of P/M 2014 alloys which resulted in improved wear resistance with Sn additions. The introduction of Sn to 2xxx Al P/M alloys also improved the sintering density of 98.4% (theoretical density) and out-standing hardness and tensile properties [89, 95]. Schaffer et al. [96–98] researched on the addition of several trace elements which can help LPS of Al-Cu alloys by diffusing into the Al-matrix.

The choice of sintering atmosphere and powder morphology also influences the sinterability of Al-alloys. Nitrogen, argon, and hydrogen gases and their mixture, as well as vacuum have been using as sintering atmospheres. Hydrogen sintering atmosphere was observed to be detrimental to the sinterability of Al [99] and its alloys [100, 101]. Several researchers [102–105] had concluded that N_2 is an active sintering atmosphere for Al-alloys as it promotes dimensional shrinkage and sintered mechanical properties but the formation of AlN is thereby a key consequence of sintering. Elsewhere, some scholars [103, 106, 107] have reported Ar and vacuum are more effective sintering atmospheres for 2xxx series Al-alloys.

2.3 Literature on Semi-solid forming

Semi-solid forming is a new metal shaping process in which the material is being deformed in its partially solid and partially liquid state, rather than in fully solid or liquid state [108]. Semi-solid forming process has many advantages over conventional forming processes such as casting and forging. Less energy consumption and forming load are the major advantages of semi-solid forming. Porosity problems are easily eliminated due to the forming temperature and loads [109]]. The key feature of the semi-solid forming is that it produces globular microstructure even after deformation so that it can be handled like a solid but is ready to flow when it gets sheared. This offers several advantages over the conventional forming processes which include improved flow properties, near net shape forming and improved mechanical properties [110]. As stated in chapter 1, Flemings and his coworkers [34] worked on the behavior of metallic alloys in semi-solid state resulted globular microstructure (Fig. 2.1b) where a dendritic microstructure was seen under normal conditions (Fig. 2.1a).

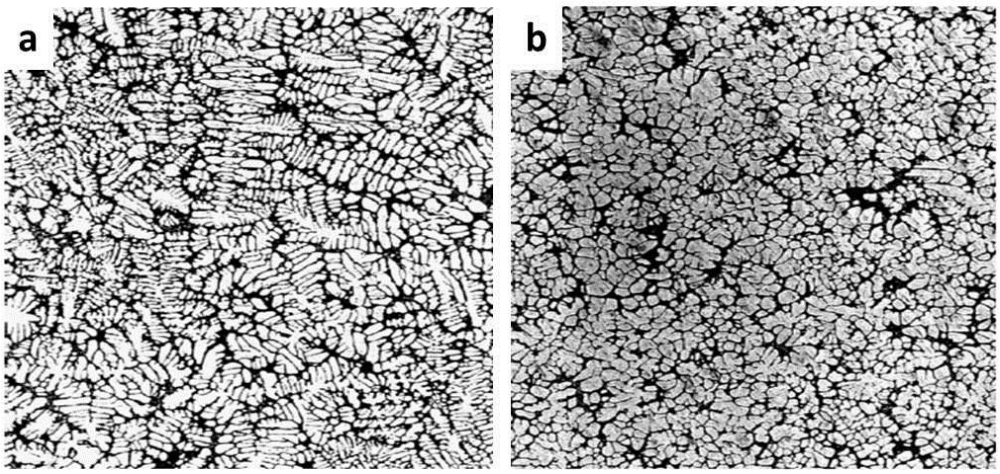

Fig. **2.1** a) Dendritic structure under normal condition and b) Globular microstructure after semi-solid forming [34]

The semi-solid forming process requires 60-80% of solid fraction to produce the best quality products [111, 112]. Semi-solid forming requires a meticulous control of the sample and tool temperature, and deformation rate in order to improve the thermal exchange between the sample and tool [113]. Thixoforming and rheocasting are well-known technologies in semi-solid forming and these are mostly used for Al and some other alloys [36].

The solid fraction of a material plays an important role that affects the viscosity of the semi-solid slurry. The percentage of solid fraction at any given temperature within the solidification limit is determined by Scheil equation [114].

$$f_s = 1 - \left(\frac{T_s - T}{T_s - T_l}\right)^{\left(\frac{1}{1-k}\right)} \quad (2.1)$$

Where f_s = Solid fraction of material, k = Partition coefficient, T_s = Solidus temperature and T_l = Liquidus temperature

The semi-solid forming process has more advantages such as forming high melting point materials, lower deformation resistance, extended die life, good material mobility, less forming defects, fine grain structure, etc. [38, 115]. The semi-solid forming techniques were established to study the behavior of low melting point alloys such as Al and Mg which have been used in many components in automobiles, aircraft and electronic goods. The first commercial thixoformed alloys were A356 and A357. These alloys were produced with strength between 220-260 MPa and 8-13% elongation [116]. Later, several researchers started developing semi-solid forming for higher performance Al-alloys such as 2xxx series, 6xxx series and 7xxx series. Dong et al. [117] worked on thixoforming of wrought 7075 Al-alloys and observed fine, uniform and globular grains in microstructure with higher UTS of 357.9 MPa before heat treatment and 468 MPa after T6 treatment, respectively. Chayong et al. [118] also worked on thixoformability of 7075 Al-alloys. The results showed fine spheroidal solid grains surrounded by liquid in microstructure with yield strength and elongation of 478 MPa and 6.9%, respectively when the material thixoformed into a graphite die and heat treated to T6 condition. Atkinson et al. [119] worked on recrystallization behavior of 7075 Al-alloys in semi-solid state. The recrystallized grains formation was closely associated with the area of the first liquid to above the solidus. Recrystallization and liquid formation occurred during preheating, and the liquid penetrated into recrystallized boundaries to form spheroids in microstructure. They also stated that the fraction and size of the spheroidal grains increased with increase in temperature. Partially remelted materials show fine and equiaxed recrystallized microstructures at sufficiently high temperature and sufficient holding time in the semi-solid range.

With the application of semi-solid forming, formation of fine spherical grains which leads to higher mechanical properties without sacrificing ductility was observed in wrought 2024 Al-alloy [120]. So, it was concluded that the fine spheroidal solid grain structure plays a vital

role in obtaining materials with a reasonable combination of strength and ductility. Ozdemir et al. [121], focused on the distribution of reinforcement, porosity content, intermetallic phase formation, the interfacial state and mechanical properties of thixoformed AA2017 Al-alloy composites. The results showed that the particle size and semi-solid forming temperature had a strong influence on the distribution of reinforcement, quality of the sample and mechanical properties. Elsewhere, Onat et al. [122] worked on semi-solid forming of Al-Cu-Mg/SiC_p composite which resulted in refinement of microstructure, reduction in porosity and casting defect such as shrinkage cavities. Then, Rachmat et al. [123] reported that during deformation, the semi-solid materials completely spread into the die cavity at above 624 °C temperature for 2024 and 617 °C for 7075 without liquid segregation. The tensile properties of these Al-alloys showed an improvement over conventional casting and forging samples of same composition. Cho and Kang [124] investigated microstructure and mechanical properties evolution of thixoforged 2024 Al- alloy at different pressures and die temperatures. The results showed that the UTS, yield strength and elongation were high at higher applied pressure. Semi-solid forming of Al alloys 2618, 7075 and 6000 series was investigated by Tausing and Xia [125]. The strength and ductility of semi-solid alloy 2618 in T6 condition was better than the conventional forged 2618 alloy. New rheocasting was introduced by Kaufmann et al. [126] and they reported that this technology can be applied to wrought Al-alloys to produce materials with higher mechanical properties than the standard casting and forging alloys.

Zhang et al. [127] studied the microstructural and mechanical characterization of 6061 Al-based composites reinforced with SiC particles. The results revealed that the microstructure of powder thixoformed 6061 composite consisted of near-spheroidal primary grains and intergranular secondary solidified structures whereas coarse and equiaxed α dendrite microstructure was observed in permanent mold cast 6061 composite. Therefore, the UTS and yield strength were better than the permanent mould cast alloys. The above observed improvements in microstructure and mechanical properties are mainly attributed to the pore-free structure, reinforcement of the matrix and increase in bonding between matrix and reinforcement. The microstructure and mechanical properties of thixoformed materials are strongly affected by the processing route. Tekmen [128] worked on semi-solid extrusion and concluded that extrusion is the only effective process to reduce porosity content and size to low level compared to other semi-solid forming processes. Hot tearing and hot shortness is the main

defect in deformed Al alloys, especially in alloys like Al-Cu alloys with large solidification range. Hot tearing in wrought Al-alloys is caused by the level of strains and stresses created by thermal gradients, hindered liquid phase, shrinkage-related brittleness, etc. [129]. These defects can be controlled by optimum temperature, strain rate, die lubrication, die approach angle and extrusion ratios in semi-solid extrusion.

A new approach was developed to produce a non-dendritic semi-solid microstructure i.e., semi-solid powder processing. In general, four steps are involved in semi-solid powder processing such as powder preparation, compaction of powder mixture, preheating, and semi-solid forming. Small and spheroidal alloy sintered powders can be used as feedstock in semi-solid forming. The combined advantages of P/M and thixoforming technologies provide fine and more uniform structures which provide much higher mechanical properties than casted feedstock semi-solid forming. Unfortunately, very few investigations have been carried out on the powder thixoforming technology. One of the studies was done by Li et al. [120], in which they investigated the phase transformation and microstructure evolution of the 2024 Al-alloys prepared by P/M to clarify how the consolidated powder with already spheroidal grains behaves during thixoforming. The results indicated that the powder metallurgy components do not need to experience spheroidal stage (remelting) if the primary particles are small and spheroidal. This was regarded as one of the overwhelming advantages of semi-solid forming. However, the potential semi-solid powder forming cannot be developed until the processing temperature is properly controlled. Wu et al. [130] also worked on semi-solid powder processing. They used Al6061-SiC composite and investigated the effect of Sic volume fraction, SiC particle size, forming pressure, and matrix particle size on the microstructure and mechanical properties evolution. They concluded that semi-solid compaction pressure was increased with reducing SiC particle size which decreased SiC loading limit (volume) for a given pressure. Non-uniformity in microstructure was observed when SiC particles were smaller than the Al6061 particles. This resulted in much variation in fracture surfaces and hardness. In addition, dense components were produced with smaller SiC particles which resulted in uniform microstructure without micro-cracks and higher hardness. Thus, the present work concentrated on semi-solid powder processing which offers the combined advantages of P/M and semi-solid forming to fabricate near-net shape products.

2.4 Literature on semi-solid extrusion

Densification and mechanical properties of materials can be improved by secondary processes such as casting, forging and hot deformation. Among all the semi-solid forming processes, semi-solid extrusion has more advantages and is of great interest for high productivity. Materials produced through casting route have low mechanical strength due to defects such as cracks and porosity. Forging techniques provide high mechanical strength but require high forming loads to yield good products and machining is required later which affects the productivity and economic efficiency [131]. The combined advantages of casting and forging can be utilized to form better products of Al alloys if semi-solid extrusion process is used. Semi-solid extrusion process has many advantages over conventional forming processes such as casting and forging. Conventional extruded materials generally suffer from high pressure and low extrusion speeds. Hence, it is more effective to extrude materials in semi-solid state for technical and economic reasons. Extrusion in semi-solid state offers lower energy consumption and extrusion pressure, reduction in extrusion force and frictional force between the material and tool, longer die life, and formation of fine and uniform grain structure than conventional extrusion process [132]. Semi-solid extrusion was first investigated by Kiuchi et al. [133], in which they studied the influence of extrusion temperature and force on Pb and Al alloys of 40 mm diameter and height ranging from 25 to 40 mm billets. A preliminary level investigation revealed that the extrusion force increased with decreasing liquid fraction in the material. The researchers also revealed that the optimum liquid fraction to be 5-10% and extrusion force of one-quarter to one-fifth of the conventional extrusion process. Kuichi et al. much later in the year 1994 [134] performed semi-solid extrusion studies on Al-alloys with die diameter of 2 to 10 mm in steps of 2 mm and 20-30% liquid fraction. Moller T [135] worked on semi-solid extrusion of A356+20 vol.% Sic Al composites with 76 mm diameter and 100 mm height billet. Shell formation in the extruded samples was observed and they were unable to solve the issue either by increasing or decreasing tool temperature/pressure in the extrusion channel. Miwa K and Kumara S [136] studied the semi-solid extrusion of stainless steel alloy UNS:S3040 (AISI 304) of 30 mm diameter and 20 mm height billets. These experiments helped many researchers to investigate the effect of press velocity on the segregation problem. The researchers observed phase separation (solid and liquid fractions) at 100-1800 mm/s press velocity and a homogeneous phase distribution at a low press velocity of 10 mm/s. Abdelfatah S et al. [137] investigated the influence of process parameters

during semi-solid extrusion and reported that the extrusion pressure and load was increased with increasing extrusion ratio.

The effect of experimental conditions on 7075 Al-alloy during thixoextrusion was examined [138]. The extrusion temperatures such as 602 °C, 609 °C and 617 °C and the corresponding solid fractions 0.82, 0.77 and 0.69 were used. The forming load increased as slug temperature decreased and solid fraction increased. With increasing temperature, sliding between solid and liquid phase and rearrangement of grains with each other without any plastic deformation was observed. Neag et al. [115] emphasized the importance of solid fraction in simulation results of semi-solid extruded aluminium. Simulation and modeling results showed the evolution of the degree of agglomeration as a function of temperature and strain rate field during semi-solid extrusion. The work on semi-solid processing at high solid fraction ($0.5<fs<1$) in 7075 Al-alloys was studied by Vaneetveld and his co-workers [139]. They also worked on the influence of four parameters such as material temperature, flow speed, tool lubricant casting, and tool temperature. The optimum temperature to reach laminar flow without liquid ejection was 600 °C, and ceraspray and MoS_2 as lubricants produced better surface finish without causing material waves and creating compression-traction efforts.

Dazhi et al. [140] analysed the microstructure and mechanical properties of semi-solid extruded bars of ZL116 (ZAlSi8MgBe) cast Al-alloy. The results showed that the Beryllium content in the alloy significantly improved the mechanical properties and corrosion resistance by promoting the precipitation hardening phases during aging. They also found that the extruded samples were smooth and microstructurally fine and homogeneous. Birol [141] results revealed that the peak hardness value was observed to be same for extruded and thixoformed 2014 Al-alloy after heat treatment. He also observed the formation of ternary Al-Cu-Si eutectic at low melting point which was attributed to the segregation of Si and Cu at the grain boundaries during partial remelting. Effect of cooling rate also plays an important role in mechanical properties of semi-solid extruded products. Ketabchi et al. [142] worked on the effect of cooling rate during semi-solid extrusion and simultaneous microstructural and mechanical properties evolution with change in temperature and holding time of 7075 Al-alloys. The investigation revealed that the optimum temperature and holding time for producing suitable microstructure were 580 °C and 10 minutes, respectively. It also showed improvement in mechanical properties of alloys with

increasing cooling rate severity, due to decrease in shrinkage porosity and final grain size. The authors concluded that the optimum process parameters of semi-solid extrusion result in higher mechanical properties similar to or higher than conventionally extruded products.

The extrusion ratio and final extrudate diameter have a great influence on the final components which increase the mechanical properties with increasing extrusion ratio [40]. Amir et al. [143] worked on thixoforming of two different extrusion billets of A356 Al-alloy. The initial billets were processed by conventional extrusion (COE) and curved-die extrusion (CDE). The results showed that some elongated grains were observed in COE billet after semi-solid reheating whereas no elongated grains (only globular) were observed in CDE billets. The tensile properties of semi-solid formed COE material were lower than CDE billet which could be attributed to different levels of defects such as the presence of elongated grains, liquid segregation, and varying strain distribution. They concluded that the thixoformed CDE materials showed higher tensile properties due to more uniform globular microstructure and constant strain distribution. Two other feedstock preparation methods such as near-solidus casting and roll-casting were investigated by Kapranos and his co-workers [37]. The results obtained in the semi-solid extrusion of roll-casted component showed uniformly distributed grains and near-spheroidal microstructures than near-solidus casting components. Semi-solid extrusion of AlSi7MgBe alloy was studied by Dazhi et al. [144], in which the results showed the tensile strength of 325 MPa with 14.6% elongation after semi-solid extrusion and heat-treatment process. Semi-solid extrusion was also used in manufacturing double-layer composite tubes which have been used in aerospace and electronics industries [145].

Although it is 30 years since the first work of semi-solid forming, there is very limited research on semi-solid extrusion of P/M processed components. Thus, the present work has concentrated on semi-solid extrusion of P/M feedstocks to fabricate components with superior mechanical properties.

2.5 Hot extrusion of Al-alloys

Forward extrusion and backward extrusion are widely used extrusion processes for deforming Al and its alloys. Forward extrusion is the most preferred process over backward extrusion which

has some drawbacks [146]. One of the major drawbacks is to take out the material through hallow ram stem. Another disadvantage is that the material in the outer layer of the billet tends to flow out through the die to a large extent. Homogeneous and uniform distribution of grain formation was observed in direct extrusion compared to indirect extrusion when the billets were extruded into quasi-static stage. The formation of primary and secondary deformation zones, shear zone and dead zone have been observed in unlubricated extrusion billets; see Fig. 2.2. The secondary deformation zone and dead zone in lubricated extrudates may not be well developed or may be absent. Because of this difference in metal flow, more homogeneous deformations can be observed in lubricated extrusions than in unlubricated extrusions [146].

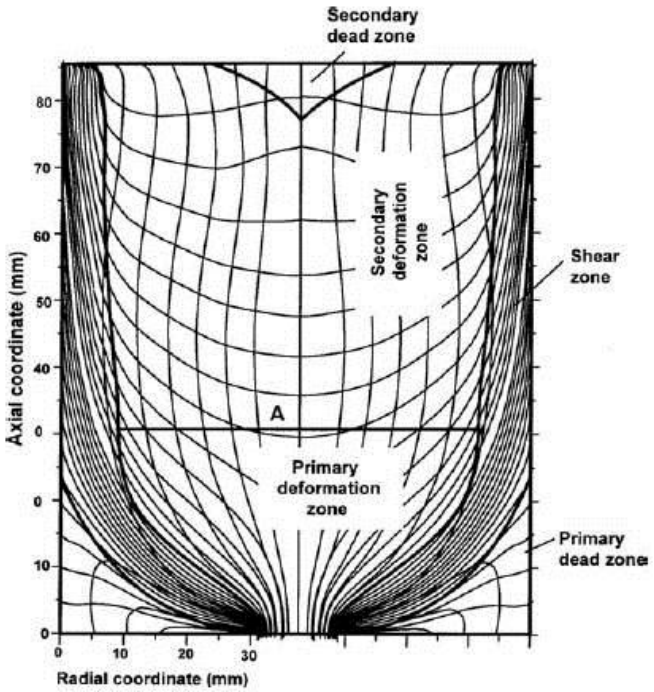

Fig. 2.2 Partial extruded billet with partitioned zones of different deformation characteristics (unlubricated extrusion) [146]

2.5.1 Classification of metal flow in extrusion

The metal flow of material during extrusion is varied due to continuous change in friction over the boundary interface among the die, billet, and container. Further, on the basis of types of metal flow patterns, flow related extrusion defects can be explained. The most commonly utilized classification system was proposed by Schikorra [147], and Pearson and Parkins [148]. The metal flow in axisymmetric extrusion was divided into four different classes of flow patterns

S, A, B, and C. This classification system was modified and proposed with particular adoption to Al-extrusion [149] see in Fig. 2.3.

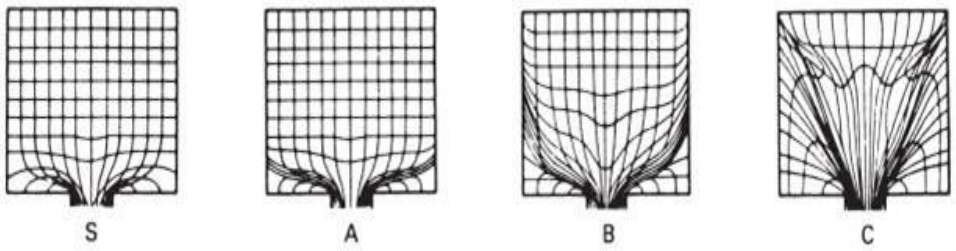

Fig. 2.3 Different Flow patterns during extrusion [149]

Flow pattern S: This flow pattern occurs when the billet is extruded with uniform flow stress over the cross-section with sufficiently low friction between the billet, container, and the die. Completely sliding nature of the material could be seen due to the low friction at these interfaces during extrusion. Then the materials peripheral layers start flowing along the die faces and through the die opening but slightly behind the core of the billet. This can be observed in flow type S in Fig. 2.3.

Flow pattern A: This pattern develops when the billet shows uniform flow stress over the cross section if there is complete sliding nature along the container-billet interface but sticking friction at the die-billet interface. Under these circumstances, a dead zone appears in which the material remaines unextruded in the corner between the die and container.

Flow pattern B: This flow pattern occurs if there is a sticking friction along the billet-die interface and also if the friction at the billet-container interfaces is much enough to reduce metal sliding adjacent to the wall of the container. The core of the billet flows faster with such conditions and peripheral layer of the billet retains along the container wall and in the dead zone corner. Then, the size of the dead zone is increased because of reduced sliding along the container wall.

Flow pattern C: This type of flow pattern occurs as a combined effect of high friction at the billet-container interface and the flow stress gradients across the billet section. This flow characteristically occurs when the container is considerably having lower temperature than the billet. Because of the temperature difference, the outer peripheral layer of the billet will have higher flow stress than the billet core. A large dead zone develops due to this which extends from the die faces to the rear end of the billet.

Flow stress is an important material parameter which determines the difficulty of extrusion. The alloys with low flow stress are commonly easy to extrude and in contrast alloys with high flow stress are difficult to extrude. Non-uniform densification could be observed along the length of the materials due to the friction present during cold extrusion. This phenomenon is called “thinning” [150]. Cracks propagate in the greater thinning preforms under extrusion because of the impaired ductility and lack of densification. Tool stresses due to friction are other major source of failure during cold extrusion. The friction between the preform, die and container interfaces is the source of differential velocities that can cause chevron failure. The variation in degree of compression in outer region and interior of the material during cold extrusion varies the mode of the stresses and arise tensile stresses which can cause surface cracks on the extrudates. P/M extrusion components easily fail under these secondary tensile stresses due to inherent brittleness. These moderate tensile stresses are more responsible for the circumferential and longitudinal cracks propagation in cold extruded P/M alloys. So, the hot extrusion is the preferred technique for preparing best finishing P/M components.

Hot extrusion is the most advanced technology in terms of making Al-alloy products, tooling, press design, etc. The 6xxx series and 2xxx series alloys are widely used materials for hot extrusion based on their best economical and technical characteristics such as ease of extrudability into any shape, susceptible to heat treatment, higher mechanical properties and corrosion resistance, good electrical conductivity, high surface finish quality, and good weldability for different applications. Due to inherent porosity, the P/M preforms suffer from low ductility, low tensile strength, and poor impact and fatigue properties. All these properties are found to be density dependent. Hot extrusion is the best approach to produce higher density P/M components at low cost. Extrudability of an alloy can be improved through the control of deformation geometry, and optimum temperature and speed parameters [151].

2.5.2 Influence of extrusion die geometry

The successful hot extrusion of P/M alloys depends mainly on the appropriate combination of extrusion ratio and the die included angle. Longitudinal and circumferential cracks are the major defects encountered in extrudates if the extrusion geometry is inappropriate. Venugopal et al. [150], worked on failure studies in extrusion of P/M Iron preforms. They concluded that the

friction between preform, die, and container increased the stresses in extrusion process and led to differential velocities which can cause failure in samples. The die approach angle of 40° showed smooth surface without any cracking and a further increase in die angle to 60° and 90° increased the tendency of cracking. The cracks in P/M preforms during extrusion can be reduced by reducing the friction between tools and preforms and avoiding generation of tensile stresses and ensuring generation of only compression stresses. The amount of plastic strain is reduced with reduction in extrusion ratio. The amount of work done during extrusion is less at lower extrusion ratio. The pressure required for extrusion with higher ratio is higher due to high plastic strains. The samples extruded with lower extrusion ratio may not meet the required mechanical and physical properties and higher extrusion ratios affect the shape, and surface finish of the materials which lead to detrimental effect on mechanical properties. So, optimized extrusion ratios should be employed for extrusion process.

Experimental investigations were carried out by Onuh et al. [152] on the effect of die angle, reduction in area and extrusion speed on the quality of the cold extruded aluminium and lead alloys. The results depicted that the average hardness of extrudates increased with increasing extrusion speed and reduction in area. Ajiboye and Adeyeni [153] worked on the effect of die land on flow pattern, extrusion pressure and variation in hardness along the length of the extrudate of lead alloys. The extrusion pressure increased with an increase in die land length for any extrusion ratio. Tiernan and Draganescu [154] studied the effect of reduction in area, die angle and lubrication on surface roughness and hardness of the cold extruded Al-alloys. Statistical modeling results showed that the surface roughness of the extrudates was mostly influenced by the die angle than reduction ratio and lubrication. Shahzad and Wagner [155] carried out studies on microstructural development variation in crystallographic texture and mechanical properties of AZ80 Mg-alloy during extrusion at different extrusion ratios. It was observed that the finer grain size was provided higher yield and ultimate tensile strengths. Das et al. [156] worked on die land length, extrusion ratio, and lubrication on the surface roughness and hardness during extrusion of Al-alloys. The results depicted that the average hardness of the extruded products came out from 15 mm die land length was 5% higher as compared to die with 10 mm die land length. The plastic strain and strain hardening were low at low extrusion ratio. Huang et al. [157] worked on effect of extrusion die angle on the microstructure and properties of Ti-composite. They depicted that both tensile strength and elongation were reduced with

increasing die angle from 45° to 75°. This was due the lower contact length between the die and billet at higher die angle. Therefore, the optimal extrusion die angle should be controlled less than 60°. The surface roughness increased with increasing extrusion ratio but reduced after applying lubricants.

The microstructural and mechanical properties of hot extruded materials are also improved by altering other important parameters such as deformation temperature, IPRD, stress, strain rate and the frictional environment.

2.5.3 Influence of temperature during extrusion

Temperature is the most influencing and important parameter in extrusion. The flow stress of materials is reduced with increasing temperature and hence the deformation becomes easier. The maximum extrusion speed is also reduced with increasing temperature. Heat transfer between the container, die, and preform and also heat generation due to friction and deformation could be observed during extrusion. Dimensional stability, product quality, die wear and its performance may depend on the exit temperature. The temperature distribution in the sample during extrusion process depends on many factors namely, extrusion ratio, ram speed, material properties, type of die and friction conditions at billet, die and container interfaces. The temperature distribution within the material leads to varying physical and mechanical properties at different locations of the sample. So the isothermal extrusion has gained practical interest to produce uniform product quality with superior mechanical properties and productivity [158]. Laue and Stranger [159] compiled a review on isothermal extrusion. They concluded that the optimum extrusion speed can control the exit temperature of sample except at the very beginning of the process. Then the same authors [160] developed a system for isothermal extrusion in which the product temperature is maintained constant by varying the ram speed. Later Kialka [161] developed a system of isothermal extrusion in which he employed a force-speed feedstock system to control the extrusion temperature. A signal processing system was also developed for isothermal extrusion [162]. Control signal processing algorithms and the pyrometer were developed and installed in an industrial extruder. An extruder with satisfactory isothermal temperature was obtained by simulations and experiments. Venas et al. [163] also developed a simulation process for the isothermal extrusion by means of FEM. The model included the billet, die, container and

ram variables. The effect of varying process conditions has been studied using this model. But the most practical method for isothermal extrusion is to make use of a preheated preform. The optimum temperature gradient could be determined between the front and back of the billet before it is inserted into the container. The billets of isothermal extrusion should have uniform surface quality, greater dimensional stability, and consistent mechanical properties with uniform microstructure.

2.5.4 Influence of strain rate during extrusion

Large strains and significant friction could be applied to produce extruded Al-alloy products. These parameters generate heat and subsequent irregular recrystallization within the extruded components, leading to nonuniformity and decline in mechanical properties. The unsteady state of extrusion and nonuniformity in mechanical properties can be shortened by controlling strain rate or ram speed during extrusion. The deformation time is increased with decreasing strain rate. High prolongation in time for reaching the steady state temperature increases the annihilation in dislocation and results in irregularity in microstructure of the extruded products. Thus, the strain rate or ram speed should be optimized to acquire uniformity in microstructure and mechanical properties throughout the extruded products. Peres et al. [164] worked on hot extrusion of nanostructured Al alloy powders produced by gas atomization. The results showed that both compressive strength and elongation of the extruded samples increased with increasing strain rate. They also depicted that the high strain rate during extrusion may cause cracks on the surface of the samples due to high friction and temperature difference inside the sample. Zhang et al. [165] worked on the effect of stem speed on metal flow behavior, surface quality and temperature distribution during extrusion. They observed uniformity in metal flow and temperature distribution at an optimum stem speed of about 0.3 mm/s. Non-uniformity in metal flow during extrusion occurs at higher strain rates which lead to cracks and surface burning, and twist deformation in extrudates [166]. The required extrusion force increases with increasing strain rate or ram speed. Welding quality and mechanical properties of extrudates rise with optimum strain rate. The flow stress of any material increases with increasing strain rate for a specific temperature [167].

2.5.5 Strengthening mechanisms during extrusion

a. Grain refinement

As stated in chapter 1, fine grained materials impede the dislocation motion due to large number of grain boundaries in it and become harder and stronger than coarse-grained materials. The mechanical properties of materials increase with fineness of grains. The general relation between grain size (d) and the yield stress (σ) was proposed by Hall [168] and Petch [169] is;

$$\sigma_y = \sigma_0 + \frac{k}{\sqrt{d}} \tag{2.2}$$

Where σ_y is the yield stress; σ_0 is the frictional stress; k is the locking (constant) parameter and d is the grain diameter.

The grain boundary acts as a strong barrier to dislocation motion. This leads to increase in the applying load or stress to deform the material and enhances the strength and hardness of material. So the strength of material is increased with increasing grain boundary area by reducing the grain size of a material [170]. Iqbal et al. [171] aimed to investigate the effect of extrusion temperature, number of passes on the twist extrusion and equal channel angular extrusion behavior of hot extruded AA7075-T6 Al-alloy. More grain refinement was observed in twist extruded samples compared to equal channel angular extrusion at higher deformation temperature. They also found that severe orientation of the grains during extrusion enhanced the strength of extrudates. Grain coarsening increased with increase in deformation temperature, which was found to be the reason for tensile strength reduction. The effect of the extrusion ratio on the microstructure and mechanical properties of AZ80 wrought Mg alloys was studied by Shahzad and Wagner [155]. They observed that the reduction in grain size increased the yield and ultimate tensile strength. Schikorra et al. [147] worked on grain size distribution in AA7075, AA6060 and AA6082 alloys during extrusion. Grain size of extruded Al-alloys were influenced by process parameters such as temperature, punch speed, strain rate and die design parameters. Grain size distribution also depends on the heat treatment process before or after extrusion [172]. Influence of extrusion parameters on grain size and texture was also studied by Zhang et al. [173]. They concluded that the initial coarse equiaxed grains in the billet evolved gradually into fine equiaxed grains due to DRV and DRX during extrusion. But the surface of the extruded profile observed with coarse grain layers under specific extrusion conditions. The refinement of grains increased the UTS of materials. The average grain size of the extruded product was

influenced by CDRX and increased with increasing deformation temperature. The grain size of the extrudates increased with decreasing strain rate as the time required for deformation is larger under lower strain rate deformation conditions [174].

b. Precipitation hardening

Precipitation hardening is the primary strengthening mechanism in the P/M alloys and heat treatable materials. The strength and hardness of these materials enhance by the propagation of uniformly dispersed and extremely small secondary particles in the matrix. The shape, size, volume fraction and distribution of secondary phase particles are the major factors in enhancing the precipitate hardening phenomenon in alloys. Precipitation strengthening mechanism has been observed in many 2xxx series Al-Cu-Mg alloys (e.g. 2014, 2124, 2618 and 2219), which are being used in automobile and aerospace applications due to good heat resistance up to 150 °C [175–178]. In Al-Cu-Mg alloys, the main hardening and equilibrium precipitate phase (θ-Al_2Cu) forms uniformly within the matrix, thereby increase the strength of the alloy [179, 180]. This θ-phase is sensible and coarsens at a temperature above 100 °C [181], resulting in a gradual deterioration of the mechanical properties. To overcome this effect, the dispersoid strengthening mechanism can be invoked by adding alloying elements that are susceptible to thermal decay. Dispersoid strengthening phases usually form during the solidification of the ingot. Commonly adopted elements for dispersoid strengthening include Mn, Ni, and/or Fe [182]. Dispersoids are comparatively less distributed than the phases formed by precipitation hardening and form as coarser (typically >5 μm). These particular dispersoid strengthening phases have been observed in many Al-alloys, for example, $Al_{12}Mn_3Si$ and $Al_{12}(Mn, Fe)_3Si$ dispersoids in the microstructure of wrought alloys such as 6013 [183] and 2014 [184]. Al_7Cu_4Ni, Al_7Cu_2Fe, and Al_9FeNi dispersoids in 2618, 2218, and 8001 with deliberate inclusions of Fe and/or Ni in the order of 1 wt.%, etc. Many wrought/cast Al-alloys have been prepared to utilize dispersoid strengthening as well as precipitation strengthening simultaneously to achieve the high mechanical properties. However, in aluminium P/M alloys, there exists precipitation hardening as the strengthening mechanism. Dispersoid strengthening elements merely exist as trace impurities in P/M materials and are not added deliberately as is done with wrought and/or cast Al-alloys. A small amount of Fe which comes from the based Al and Cu powders in Al-Cu-Mg P/M alloys forms a dispersoid phase (Al_7Cu_2Fe). Such dispersoids improve the hardness and strength of Al P/M alloys [185].

The intermetallic phases usually distribute uniformly in the matrix instead of merely distributing along the grain boundaries during extrusion [172].

c. Work hardening

Work hardening of any material can be easily observed when the material is deformed at room temperature. Higher shear stress is required for dislocation movement and to increase the dislocation density which enhances the yield strength of materials. Jabbari et al. [84] worked on processing of 7075 Al-alloys consolidated by cold compaction and hot extrusion and studied their microstructural and mechanical properties. They concluded that there was no porosity present in the extrudates, which therefore effectively enhanced the hardness of extruded samples. The increased hardness through extrusion process was attributed to the work hardening effect associated with extrusion process. Many researchers have worked on true stress-true strain curves during deformation process [186–188]. Those curves showed peak stress values at the early stages of deformation. This flow stress increased rapidly with increasing strain, which resulted from the work hardening caused by the dislocation generation, accumulation and multiplication. Work hardening is the dominant phenomenon observed at low temperature deformation [189]. With increasing severity of deformation, dislocation density and dislocation accumulation lead to interactions between dislocations in grains [190]. Meanwhile, the stress concentration increases on the grain boundaries which increase the deformation resistance and impede dislocation motion. This phenomenon increases the strength and hardness of extruded products.

d. Solid solution strengthening

There are two types of solid solution strengthening mechanisms: one is substitutional solid strengthening mechanism in which the solvent and solute atoms are similar in size and causes the solute atoms to occupy lattice sites; the second one is the interstitial solid solution strengthening in which solute atoms are smaller in size than solvent atoms and causes the solute atoms to inhibit interstitial sites in the solvent lattice [191].

2.5.6 Microstructure and mechanical properties evolution of hot extruded P/M Al-alloys

It is essential to understand the hot workability of materials to determine the best processing route and to overcome cracks propagation in the resulting deformed products. Optimum processing parameters can improve the properties of materials in hot deformation process [45]. During deformation process, the material flow is influenced by many factors such as deformation temperature, strain, strain rate, friction, etc which vary the properties of the deformed samples [192]. Thus, the processing parameters applied during hot deformation process have to be optimized to acquire not only the desired shape but also the required properties and microstructure in the deformed material [193]. Several researchers have investigated the effect of processing parameters on the mechanical properties and microstructural evolution during hot deformation of Al-alloys such as AA-2030 [194], 7050 [195] and 7050-HI12 [196] alloys.

During hot deformation, flow behavior, microstructure and mechanical properties are controlled by three metallurgical phenomena such as work hardening (WH), dynamic recovery (DRV), and dynamic recrystallization (DRX) [197] and [198, 199]. Fig. 2.4 shows the microstructural developments during DRV and DRX [197]. The WH rates are counterbalanced by DRV and DRX during hot deformation. Fig. 2.4a illustrates that the original grains in the sample are increasingly strained, but the sub-boundaries remain more or less equiaxed during dynamic recovery. This indicates that the substructure is "dynamic" and adapted again continuously to the increase in strain. At a critical strain and with a corresponding variation in driving force, DRXed grains appear along the original grain boundaries and form as "necklace structure". With increasing strain and deformation, more potential nuclei are activated and form as new recrystallized grains. Saturation/equilibrium sets in after a certain amount of strain as seen in Fig. 2.4b. This equilibrium is reached between hardening and softening due to dislocation accumulation and DRX, respectively. At this stage, the microstructure consists of grains with different dislocation densities and the flow curve shows up as a plateau. So it is important to study the structure-property correlation accompanying DRV and DRX respectively [200]. In hot deformation process, DRX in an alloy begins when strain hardening and recovery can stop storing more immobile dislocations. Crystal defects such as dislocations obtained by the work hardening would be eliminated by DRX, which will refine microstructure, increase hot plasticity and reduce deformation resistance. The evolution of dislocations mostly depends on the

deformation temperature and strain rate during DRV and DRX [201]. DRX can occur in FCC alloys (e.g. Al-alloys and Fe-alloys) and is promoted by increase in deformation temperature and a decrease in strain rate. Higher deformation temperature provides more energy to nucleation and growth of the recrystallized grains. During the deformation process, misorientation angle of lower angle grain boundaries (LABs) increases due to subgrain rotation and a large fraction of LABs merge and transform into higher angle grain boundaries (HABs) which can also be featured as continuous dynamic recrystallization (CDRX) [174]. High stacking fault energy (HSFE) metals, such as Al-alloys, ferritic steels, beta-titanium alloys, etc. undergo CDRX rather than discontinuous dynamic recrystallization (DDRX) during hot deformation process [202, 203]. The existence of CDRX was confirmed by Driver et al. [204] and suggested that the temperature of $0.5T_m<T<0.7T_m$ favors the CDRX for Al alloys. Different characteristics within the recrystallized microstructure were observed in the as-extruded AA7075 alloys at a deformation temperature above $0.6T_m$ [174].

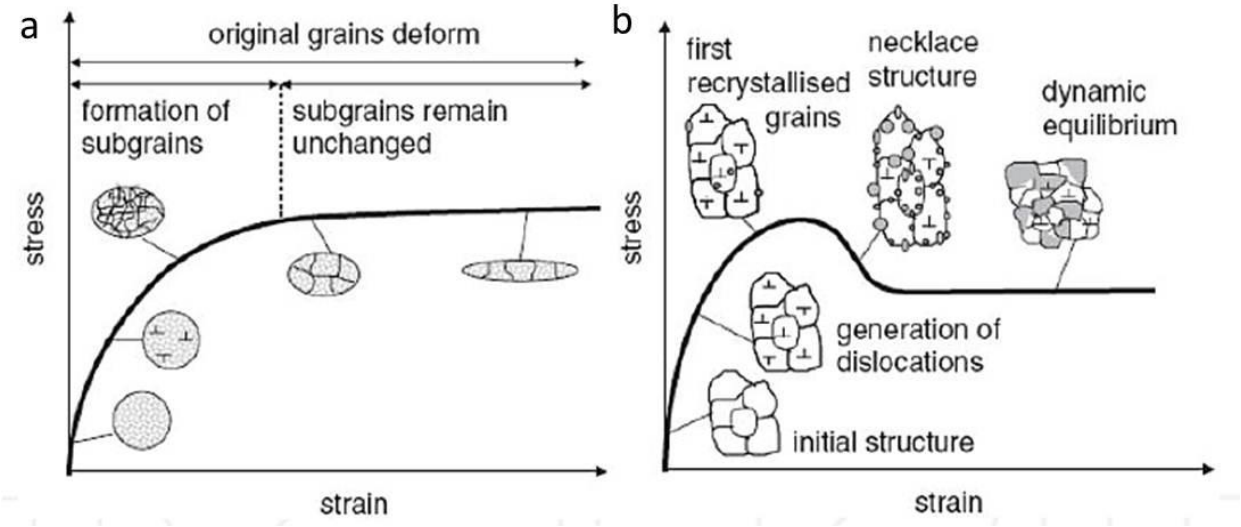

Fig. 2.4 Microstructure evolution during a) hot deformation of a material showing dynamic recovery and b) continuous dynamic recrystallization [197]

In general, due to the high efficiency of DRV in HSFE metals, new grains are formed by recrystallized microstructure instead of classical nucleation mechanism by the progressive transformation of subgrains into nuclei of new grains within the deformed original grains. The dislocations produced by the work hardening accumulate steadily in subgrains (LABs), leading to grow mis-orientation angle and undergo the formation of HABs after reaching a critical value of mis-orientation [197]. Thus, the microstructure is intermediate between subgrains and a grain

structure and bonded partly by LABs and partly by HABs. These observations have been reported in Al-alloys [1, 205] and ferritic steels [2] by optical microscopy and transmission electron microscopy (TEM). Later these have been confirmed with the help of local mis-orientation measurements by electron backscattered diffraction (EBSD) and Kikuchi line analysis of particular area diffraction patterns in TEM. According to Wang and Zhao [205] study, mobility of grain boundaries is less and the pinning effect of secondary particles on the grain boundaries is strong at low extrusion temperature. DRV is the main phenomenon observed during extrusion at low temperature which results in dislocation annihilation and subsequent sub-structure formation. The fraction of LABs is high at low extrusion temperature due to the formation of sub-structures. As the extrusion temperature increases, LABs gradually transform into HABs. Meanwhile, the secondary phase particles in the matrix are significantly reduced with increasing temperature which results in a reduction in pinning effect. The reduction in pinning effect results in acceleration of transformation of LABs to HABs which further promote grain fragmentation and growth. DRX during hot extrusion also changes the texture components in the extruded billets. The DRX grains in deformed Al-alloys usually nucleate and grow with specific orientation, resulting in formation of different recrystallization texture compared to deformation ones [207, 208]. The texture is another contributor to strengthen the extruded components. Commonly developed textures during DRX in Al-alloys are Cube {100}<001>, Brass {110}<112>, Copper {112}<111>, S {123}<634>, and Goss {110}<001> [208]. Hales et al. [207] studied the recrystallized texture evolution in deformed 2195 Al-alloy and observed that the texture components of R-Cube {013}<100> and Cube {100}<001>.

During high temperature deformation, HSFE metals such as Al alloys undergo continuous dynamic recrystallization (CDRX) instead of discontinuous dynamic recrystallization (DDRX). Many investigated CDRX phenomenon in various Al-alloys [197, 202, 203, 210]. Recent studies have shown the main characteristics of CDRX in stress-strain curves in which the general flow stress trend is decreased with increase in deformation temperature and decrease in strain rate [211–214]. Lyttle and Wert [215, 216] explained the CDRX in Al-alloys and concluded that HAB fraction increased during hot deformation. The deformation texture of Al-alloys during hot deformation may be affected by the grain boundary migration [216]. Small crystallites associated with CDRX generate during deformation at lower strain rates which favor grain boundary sliding and show the superplastic behavior. So the path of microstructure and

texture evolution may change and lead to randomization of texture. These effects have been observed in the temperature and strain rate ranges considered in the present work.

Pre-alloyed powders are generally harder compared to premixed Al-powders. Pre-alloyed powders exhibit high flow stresses as a result of which the compressibility and hot deformability of these alloys are lower than that of premixed powders. In fact these powders are more difficult to process than those of the premixes. Zubizarreta et al. [217] worked on hot extrusion of Alumix13 premix powder without sintering. The components produced by Al powder extrusion had shown inhomogeneous and banded microstructures, resulting in lower hardness in extrudates. Considering these factors, many researchers have started working on hot extrusion of cold compacts and then sintered preforms produced by Al premixed powders resulting in homogeneous microstructure and superior mechanical properties. Recent work on microstructure and mechanical properties evolution of 7075 Al-alloy consolidated from P/M and hot extrusion was explored by Taleghani et al. [84]. They concluded that a higher degree of alloy was developed by presintering than those of the green compacts and delubricated compacts. These high degrees of extruded alloys development was attributed to the formation of recrystallized grain structures and homogeneous distribution of second phase particles after extrusion, which had improved the mechanical properties of extruded components.

Rashad et al. [218] reported the mechanical properties of Al-Gr (0.3 wt.%) synthesized by P/M and hot extrusion. The extruded composites showed an increment of 14.7% in yield strength, 11.1% in UTS, and 11.8% in hardness when compared to pure Al sample processed under 170 MPa compaction pressure and 600 °C sintering temperature for 6 hours. Keshavamurthy and Praveennath [219] also worked on the same material with increasing Gr content (1 wt.%) and that resulted in 46% improvement in UTS due to dislocation density and grain refinement. Hardness of the extruded samples also increased due to reduction in material defects such as porosity, which were obtained during powder compaction. Some researchers showed that the increase in dislocation density and pile-up of dislocations at grain boundaries during extrusion resulted in high strain hardening and reduction in elongation [221, 222]. Yi et al. [222] carried out work on mechanical properties evolution of hot extruded Aluminium-Graphite composites with Al-Si alloy additions and resulted higher compressive strength for Aluminium-Graphite composite containing some vol.% of Al-Si compared to conventional

squeeze-cast composites. Hisashi et al. [223] worked on hot extrusion of AA7075 Al-alloys processed by rapid solidification (P/M water atomization) route. Rapidly solidified powders were sintered and extruded at 623 K, 673 K, and 723 K. They concluded that the secondary phases such as Al_2Cu and Mg_2Si reduced with increasing extrusion temperature due to the release of induced strains and supersaturated solution formation between Al atoms. The maximum hardness and tensile strength of extruded P/M sample were obtained at 623 K extrusion temperature due to the precipitate formation and severe plastic deformation. These properties were reduced with increasing extrusion temperature due to grain coarsening and reduction in intermetallic volume in matrix. But uniform distribution of Al_2Cu phase inside the grains was observed which showed a good balance of high strength and ductility. These secondary phases are much harder than Al matrix and they do not experience as much deformation as the matrix phase during extrusion. These secondary phases usually impose extra deformation on the matrix. These high deformations due to secondary phases in Al alloys are susceptible to the nucleation of new grains formation, which encourage recrystallization and give rise to the grain refinement [225–228]. As a result, the strength and ductility of the extruded components were improved. The enhancement in mechanical properties such as ductility, toughness, and strength during hot extrusion of Al-alloys was also observed by Abdellah [228] & Peres [164]. These enhancements were attributed to the formation of smaller equiaxed recrystallized grains by breaking down and refining the coarse columnar grains in initial billet, reducing porosity, and increasing the bonding between particles. The elemental additions (ex: Cu in Al) and hot deformation also improve adhesive and abrasive resistance [230–232]. Significant metallurgical improvements were observed in the recent work on hot extrusion of Aluminium P/M 2000 series metal matrix composite. These included improvements in UTS, yield strength, and ductility by 20%, 10% and 400%, respectively compared to initial T6 counterpart sample [42]. Although isothermal compression, forging, and/or hot extrusion behavior of many Al powder metallurgy alloys with various grain sizes have been studied [42, 233–236], a detailed discussion of the influence of temperature and strain rate on DRX mechanism, precipitate strengthening, texture control and subsequent mechanical performances of hot extruded Al P/M alloys are have not been reported. In light of the above, the present work aims to study the influence of temperature and strain rate on grain refinement, work hardening DRX behavior, precipitate strengthening, texture control and subsequent mechanical performances of P/M Al-Cu-Mg alloys during extrusion. It also aims to

elucidate the piling-up and sinking-in behavior of deformed materials under nano-indentation deformation, and their mechanical properties by refinement of the microstructure.

2.6 Constitutive modeling of Al-alloys during hot deformation

It is essential to understand the workability of materials to determine the best processing route and overcome cracks propagation in the resulting deformed products. Optimum processing parameters can improve the properties of materials in hot deformation process [45]. During the deformation process, the material flow is influenced by many factors such as deformation temperature, strain, strain rate, friction etc which vary the properties of the deformed samples [192]. Thus, the processing parameters applied during hot deformation process have to be optimized to acquire not only the desired shape but also the required properties and microstructure in the deformed material [193]. Hot deformation can affect the flow behavior, microstructure and energy required for deformation through various metallurgical phenomena, namely, WH, DRV and DRX [198, 199]. Thus, several researchers [237–240] worked on Al-alloys to understand the hot deformation behavior during compression at elevated temperatures. Li et al. [241] reported the microstructure evolution of 7050 Al-alloy during deformation at elevated temperature and revealed that the existence of DRV and DRX contributed to the flow softening of metal. Sun et al. [213] explained and modeled the hot deformation of as-extruded 7075 aluminium alloy. They described that the flow stress increased rapidly with increasing strain and exhibited peak stress at a particular strain value, after which the flow stress decreases gradually showing dynamic flow softening until high strain values. The effect of IPRD on hot deformation behavior to predict the flow stress of 7075 Al-alloy powder compacts was examined by Jabbari et al. [239]. They observed that the true stress-true strain curves exhibited peak flow stress (PFS) at a critical strain value and then decreased with increasing temperature or decrease in strain rate and IPRD.

In order to explain the materials deformation behavior and to establish the optimum processing variables, it is essential to investigate the constitutive modeling under different deformation conditions. Further, it can also be used to evaluate the material attributes, optimize the design, and predict the failure and lifetime which can help in the development of new products or improved products [240]. Investigation of deformation mechanisms, flow stress

behavior and development of constitutive modeling equations at different temperatures, strain rates, strains and IPRD is essential for successful working of materials. In this regard, many researchers have proposed different types of constitutive models and studied constitutive base analysis of Al-alloys during hot deformation [47, 212, 242–245]. Among the phenomenological constitutive models, the Arrhenius type model has been extensively used to explain the correlation between deformation temperature, strain rate, strain and flow stress [246]. Sellers and McTegart [247] developed hyperbolic-sine constitutive equation i.e., an Arrhenius-type equation to describe the hot working of different materials under different deformation conditions. Then the revised Arrhenius-type equation was proposed by Lin et al. [248] which introduced material constants (α, β, n, A and Q) into the constitutive equation. The hot deformation activation energy (Q) is a very important physical parameter in the model which acts as an energy barrier to dislocation motion on a slip plane and determines the critical conditions for DRX initiation [197]. The activation energy values may vary with varying microstructure of Al-Cu-Mg alloys during deformation [249]. The hot deformation activation energy is mostly influenced by the material composition and microstructure during hot deformation process of Aluminium alloys (Al-Cu-Mg alloys) [249, 250]. Zener-Hollomon parameter (Z) is another important physical parameter to depict the relationship between flow stress of different materials and deformation parameters [213, 251, 252].

The modified constitutive equation (Arrhenius-type equation by Z-H parameter) possesses reliable and good ability to predict the metal flow behavior of Al-alloys under different deformation conditions [253]. Li et al. [254] worked on the flow behavior modeling of the 7050 Al-alloys and used exponent-type Zener-Hollomen equation to investigate the influence of temperature and strain rate on the deformation behavior. The investigation revealed that the PFS levels were decreased with increase in deformation temperature or decrease in strain rate which were represented by Z-H parameters with the hyperbolic-sine equation with hot deformation activation energy of 160.3 kJ/mol. Subsequently, the constitutive equation was validated by introducing the correlation coefficient (R) and the average absolute relative error (AARE) with values of 0.9922% and 6.285, respectively. Consequently, the results indicated that the flow stresses calculated from the constitutive equation were in good agreement with measured values. Rokni et al. [211] studied the hot deformation behavior and constitutive base analysis of 7075 Al-alloy bars. The results showed that the PFS values which were obtained from the developed

constitutive model were in good approximation with experimental PFS values. Jin et al. [255] studied the hot deformation behavior of 7150 Al-alloys and their flow stress behavior during compression which can be represented by Z-H parameter in the Arrhenius-type equation with hot deformation activation energy of 229.75 kJ/mol. Later, Saravanan et al. [256] worked on the effect of temperature and strain rate on deformation behavior of Zinc based Al-alloys ascertained by the Z-H parameter. The results indicated good agreement between measured and predicted flow-stress values in relevant temperature and strain rate ranges. The R and AARE of the model were found to be 0.9965 and 4.26% respectively, and confirmed accuracy of developed Arrhenius-type equation. Hot deformation behavior of 2xxx Al-alloys was studied by Haung et al. [45]. They also concluded that the PFS decreased with increase in deformation temperature or decrease in strain rate, which was represented by the Z-H parameter in the hyperbolic-sine equation with the activation energy of 340.98 kJ/mol.

Though the plastic deformation of P/M materials is similar to that of the conventional fully dense materials, the presence of a substantial amount of pores complicates the deformation process. The residual pores in the sintered preforms are reduced and closed during plastic deformation process, leading to a highly densified product [30]. In addition to matrix work hardening, densification hardening or geometric work-hardening also takes place during hot deformation of different IPRD powder preforms and then improves the flow stress of the material [28]. Desalegn et al. [257] worked on the formability of P/M Al-Cu composite. They revealed that the coefficient of friction is extremely high in P/M materials due to the influence of porosity during the deformation process. Further, the uniformity of density distribution in porous material increases with increasing IPRD and decreasing coefficient of friction [258]. Thus, the information on plastic deformation of fully dense products is less essential for plastic deformation of the corresponding P/M processed materials of the same composition. Jabbari et al. [239] worked on powder compacts of 7075 Al-alloys. The other objective of his work was to evaluate the effect of IPRD on the hot deformation behavior and to model and predict the flow stress of sintered and compressed samples using constitutive equations. The results revealed that a decrease in PFS was observed with decrease in IPRD. Z-H parameter in an exponential-type equation which contains IPRD compensated deformation activation energy was used to describe the relation between deformation temperature, strain rate, and PFS of powder compacts. Mann et al. [31] studied hot deformation response of a novel Al-Cu-Mg P/M alloy (P/M 2324) and the

results were compared with its counterpart AA2024. Modeling of these alloys yielded very similar PFS values with both materials adhering to standard Z-H curve fitting approach. The results confirmed that full density was achieved by 2324 P/M alloy. The results obtained from constitutive analysis of sintered preforms benefit industries/researchers by providing information for further modeling of secondary powder processing routes, such as hot extrusion and hot forging of sintered materials [259, 260].

2.7 Microstructural evolution and modeling of hot deformed Al-alloys

Microstructural evolution in an alloy affects the flow stress and mechanical properties, and hence influences the forming process [261–264]. So, it is of great importance for designers to understand the hot deformation behavior of Al-alloys. The constitutive model relation is often used to explain about plastic flow properties of any alloy. Therefore, some constitutive models of materials have been used to describe the sensitivity of the flow stress and microstructure to the forming temperature, strain, strain rate, and IPRD in commercial hot working applications. Productivity and lifetime of the final products are influenced by mechanical properties such as strength and hardness. These mechanical properties can be controlled by the grain size of the deformed materials. So, it is essential for designers of metal forming processes to understand the correlation between process parameters and grain size effect during hot deformation process. DRX phenomenon also affects the mechanical properties of hot deformed materials. Therefore, over the last few years, researchers have been analyzing the effect of process parameters on DRX grains and their sizes of different materials during deformation and establishing the mathematical models to predict the accuracy of experimental values with respect to theoretical calculations.

Several researchers [265–268] have been working on hot deformation behavior of cast/wrought materials (fully dense) and establishing the mathematical model between Z-H parameter and DRX grain size. Shaban et al. [266] worked on Nb-Ti micro-alloyed steel during hot torsion test and revealed that DRX grains are very sensitive to deformation temperature and strain rate. They developed the relation between critical strain, DRX grain size and Z-H parameter. Shuai He and Sheng Li [253] established the relation between the modified Arrhenius equation and Z-H parameter at a given strain to exhibit the effect of temperature and strain rate, and evaluated the extent of DRX. The results revealed that the value of ln Z declined steadily

with increasing deformation temperature and decrease in strain rate. DRX was easily occurred with lowering the ln Z values which means large extent of dynamic softening happened. They further revealed that the increase in deformation temperature benefited nucleation and growth of recrystallized grains. Quan Guo-Zheng [197], studied the evolution of DRX volume fraction of as-extruded 7075 Al-alloy, as-cast AZ80 Mg-alloy and as-extruded 42CrMo high strength steel by conventional hyperbolic-sine equation. Based on the calculation results of this model, the DRX volume fraction increased and reached a constant value with increase in strain. He concluded that the DRX was delayed to a larger time with decreasing deformation temperature at a specific strain rate. He also summarized that as the strain rate increases, the deformation strain needed for the same amount of DRX volume fraction increases. The summary of this work revealed that the microstructure of the extruded and casted materials becomes more and more refined with increasing strain rate due to decreasing grain growth time and increasing migration energy stored in grain boundaries. Huang et al. [269, 270], studied the relation between DRX and the Z-H parameter of Cu-Cr-Zr and Cr-Mo steel alloys. They developed constitutive equations before and after critical strain of Cu-alloy based on the kinetics of DRX and stress-dislocation relationship. They concluded that the experimental stresses were in good agreement with the predicted stresses of the established DRX constitutive model.

Constitutive models for microstructure and mechanical properties relations for Al alloys have been studied and developed for various applications and different processing aspects. Huang and Zhang [45] developed a relation between the hot deformed microstructure and Z-H parameter. The microstructures with a great amount of precipitates within the subgrains were developed and associated with the Z-H values. The distribution of coarse precipitates in the grain interior and the formation of subgrains with HABs were observed at low Z values. At high Z values, high dislocation density and considerable fine dynamic precipitates were observed. Zhang [271] also worked on hot deformation behavior of Al-Mg-Si-Cu alloys and concluded that the deformed material microstructure consists of very small amount of fine precipitates within the subgrains. These precipitates developed serrations in the grain boundaries which resulted DRV and DRX due to dynamic flow softening. Mann et al. [31] confirmed that tensile properties were significantly higher for P/M 2324 alloy compared to its wrought counterpart AA2024 alloys. These properties improvements were attributed to the formation of secondary phases such as θ phase (Al_2Cu) and S phase (Al_2MgCu) in P/M 2324 alloy. There are very few studies

available relating to constitutive models for DRX evolution of powder metals during hot deformation.

The deformation, microstructure, and DRX grains formation of P/M processed materials are different from cast/wrought materials. The presence of residual pores in the P/M compacts lead to plastic volume change and densification during deformation. A substantial amount of pores present in the P/M materials show nonuniformity in density distribution due to friction between tool and powder/compacts [32]. Therefore, it is essential to investigate microstructural evolution and modeling to predict the DRX grain size by considering parameters such as temperature, strain rate and also the influence of porosity.

2.8 FEM aspects in deformation

The optimization of process parameters for extrusion is usually achieved by extended technological experiments. Finite Element Method (FEM) is an appropriate computer simulation technique to predict the optimal temperature-strain rate conditions in extrusion. The first effort to develop FEM data back to work was done in 1941-1942. After decades, it was further improved and provided with a mathematical formulation [272]. FEM is a numerical technique, and first applied in structural mechanics to evaluate the behavior of structures for various real applications [273]. FEM has been successfully used for simulation of forging and die forging [274, 275], hot rolling [276–278], and hot extrusion [279]. The FEM models have been used for investigation of physical and mechanical properties, recrystallization prediction, and grain size development over the last few years by many researchers [280, 281]. Nowadays, FEM technique has been gained the industrial stage in analyzing, predicting and simulating the deformation, frictional and densification behavior of materials in various metal forming processes. It has taken the standard of engineering design one step, and substantially saves efforts, time and cost required to turnout finished engineering products.

2.8.1 FEM based program: DEFORM

DEFORM is a reliable and practical computer code which is suitable to simulate the complex metal forming processes. Three essential parts of DEFORM software are explained as:

i. **Pre-Processor** is an interactive program designed to prepare input data for analysis and assist users step by step in the process of simulation. It contains: a) an input model for interactive data input and verification which includes die surface description, material properties, interface properties and FEM meshes for the dies and workpiece, b) an automatic mesh generating program and c) an interpolation module.

ii. **The simulation engine** performs numerical calculations to solve the problem. Kodayashi et al. [282] addressed that in the simulation engine, the basic constitutive equations and boundary conditions can be converted to non-linear equations through FEM discretization. After solving the problem, which is based on the input data from the data base, the solution data stored back in the data base and displayed or plotted through post processor.

iii. **Post processor** provides a graphic display or alphanumeric form of the FEM results such as contour plots of field variables, velocity, stress, strain, strain rate, density, damage and temperature, and load-stroke curves. Further, the "flow net" module is used to compute and then represent the flow path of a selected element and the "fiber" or grain flow in the work piece.

2.8.2 Applications of FEM in metal forming

FEM technique can predict detailed information about deformation, metal flow, friction, thermal influence, as well as information about metal forming mechanics. Ko et al. [50] adopted FEM technique to predict the material flow and defects in the semi-solid forging of A356 Al alloy. Folding defects and their rewelding were predicted with enough accuracy, and they showed that the result was more realistic and accurate when reliable data was used as input. The complicated interactions between die design, forming parameters and product quality during hot extrusion of Al alloy was successfully explored using FEM by Xinjian Duan et al. [283]. Taylan Altan and Markus Knoerr [284] worked on the application of the 2D FEM to simulate forging processes. The FE simulation provided useful information on extrusion defects, material flow streamline, surface cracks, microstructure, stress distributions during metal forming, design of multi-stage cold forging operations, and design of net-shape cold forging operations therefore the process development effort and cost can be reduced. Several researchers [285–287] were successfully applied FEM to model and simulate the deformation behavior of metals and alloys for various

processing conditions under forging, and they showed that the accuracy of FEM results depends on the accuracy of the input data and friction model used in the analysis.

FEM has been one of the popular numerical methods which is suitable for the analysis of material formation precisely. HE Zhao et al. [288] studied the extrusion process of complicated Al profile with the help of FE simulation. They reported that more uniform velocity distribution was observed with an optimized die land in the simulation of extrusion process. Good agreement between experimental and FE simulation results was observed and also shown that FEM can forecast the distribution trends in the actual extrusion process. Simulation of the flexible thixo-extrusion process of Al356 Al-alloy was investigated by Wang et al. [40]. They developed a mathematical constitutive equation describing the relationship between temperature, strain rate, stress and strain and then imported to the DEFORM-3D simulation software. The results showed that the surface quality of extruded products improved by simulation process prior to experimentation. A case study was conducted on the extrusion of an AZ31 alloy in which the correlations between process variables such as extrusion temperature and peak extrusion pressure and the response (output) from the deformed material were established from FEM simulations and verified by experimental results [289]. Simulation results in this work provided guidelines for the optimum process conditions and minimized the number of trial extrusion experiments needed for the process optimization. Xinjian et al. [283] also studied the influence of process parameters on the occurrence of surface cracks with the use of FEM. The simulation results found that the higher extrusion ratio showed higher influence on the initiation of surface cracks. The surface crack propagation also increased with increasing billet temperature, temperature difference between die and the billet and the ram speed. Marin et al. [290] analyzed the influence of the temperature during extrusion process by means of FEM. The results emphasized that the optimum temperature values of die and billet allowed achieving an increase in the efficiency of the extrusion process and enhancing the quality of the final product. Isothermal extrusion process provides uniform distribution of properties throughout the extrudates [291]. The best way to perform isothermal extrusion is to optimize the process parameters such as die temperature, billet temperature, strain rate and the container temperature. This requires the use of simulation. Xinjian et al. [291] also reported that FEM is a very efficient and effective way to design the extruded profiles and they also depicted that a single temperature value during simulation resulted in uniform microstructure and mechanical properties in the extrusion process. The best

combination of process parameters for isothermal extrusion was found for Al alloys using transient finite element simulation [292]. Prediction of microstructure and control of subgrain size in the hot extrusion of Al-alloys using FEM have been studied by many researchers [293–297]. Several micromechanical mechanisms and thermomechanical aspects such as diffusion, recovery, recrystallization, grain growth, hat transfer between the sample, die and container, heat generation by friction and cooling process after the hot deformation are involved in the hot extrusion process and result in change in microstructure parameters subsequently. Therefore, modeling and simulation which include all the above mentioned aspects are required for an accurate prediction of the evolution of microstructure and mechanical properties [295].

2.9 Taguchi and RSM applications in metal forming

Product quality is the main concern of customers and manufacturers while high production rate and consistency in product quality is the key to the success of industries [298]. There are many factors which affect the quality of products during deformation and metal forming such as deformation temperature, stress, strain, strain rate, die design, etc. Inappropriate combination of these factors can cause numerous production problems (e.g. product defects, high production costs, long lead time, much scrap, etc.). Identifying the root cause of these defects not only eliminates defects but also leads to the product quality improvement during deformation. Taguchi method has been applied to different fields like manufacturing [58, 299] and mechanical component design [59, 300]. The popularity of Taguchi method has been increasing due to designing high quality systems which provide much reduced variance in experimentation with optimized process control parameters. Liu et al. [301] employed Taguchi method for improving the surface roughness of material in injection moulding by optimizing process parameters. The results revealed that the setting of optimized process parameters successfully improved the surface roughness, with melt temperature being the most important process parameter influencing surface roughness.

Li et al. [302] conducted experiments adopting a L9 OA to study the influence of processing parameters on the weld-line of copy machine. The weld-line defect was reduced through the best combination of process parameters optimization. Melt temperature was found to be the most important factor influencing the visibility of weld-line. Krishnakant et al. [303]

applied Taguchi method to optimize turning process parameters. The same method was employed by Srinivas and Venkatesh [304] for optimizing process parameters and to improve the quality of surface in facing operations. Then the velocity in the vehicle's ride comfort with respect to sprung mass of vehicle was reduced by Taguchi method along with DOE methodology and ANOVA [305]. Taguchi design was also used to find the relation between microstructure and process variables in a sand cast A360 Al-alloy [306]. Nenad et al. [307] used Taguchi method to optimize the tribology behavior of Zinc based composite. Taguchi method along with ANOVA was used to execute the analysis of the wear rate. The results depicted that the sliding speed has more impact on wear rate than the SiC content and applied load. Recently, Taguchi methodology was used to optimize the turning parameters over chip thickness ratio in machining P/M aluminium metal matrix composite [308]. L9 OA was adopted for experimental investigation and resulted that the cutting speed was influenced more for formation of chip than the depth of cut. In order to further improve the robustness of the optimization process and efficiency, many researchers have been incorporating other approaches with Taguchi method [309–311]. The statistical techniques and concepts of Taguchi method are much compatible with other approaches such as grey relational analysis (GRA), numerical simulation and principal component analysis.

Response surface methodology (RSM) emerged in the 1950s as an attempt to develop empirical models capable of relating all the variables making the industrial system for chemical engineering. It consists of a group of mathematical and statistical techniques for developing adequate functional relationship between input process parameters and the response (output) [312]. The objective of the RSM is to analyze and optimize the response by careful experimental design of the input process parameters. There are two categories of RSM as mentioned in Chapter 1. BBD has the advantage of avoiding treatment combinations that are at extreme, and thus fewer experimental runs are required compared to CCD [312].

The design procedure of RSM is as follows

i. Identifying the important influencing factors
ii. Developing the experimental design matrix
iii. Performing the experiment as per the design matrix
iv. Measuring and recording the response

v. Developing a mathematical prediction model
vi. Checking the adequacy of model using ANOVA method
vii. Analysing the influence of input process parameters on the response

RSM has recently been employed successfully by several researchers to examine the interaction between numerous process variables and one or more response variables in various industrial applications. Muthuraman et al. [313] adopted RSM to model and analyze the material removal rate of wire electric discharge machining of WC-Co composite and they derived a mathematical equation to predict the material removal rate and identified optimum setting conditions that enhance the response. They revealed that on-time and ignition-current tension has a positive influence on material removal rate whereas the off-time affects the response negatively. The formability, tensile properties and void coalescence parameters of Al sheets were studied using RSM by Velmanirajan et al. [314]. They developed empirical relations to predict the effective formability and void coalescence properties with respect to process parameters, namely, sheet thickness, annealing temperature and specimen geometry. Noordin et al. [315] applied RSM to describe the performance of the multilayer tungsten carbide tool when turning AISI 1045 steel under constant depth of cut and dry cutting conditions. They established a mathematical model which could adequately describe the performance in terms of critical input parameters, namely, cutting speed, feed and side cutting edge angle. Among all the input parameters, the feed was found to be the most substantial factor that influences the surface roughness and the tangential force. Tiernan et al. [316] used RSM to investigate the effects of process parameters such as conical die angle and die exit diameter on the behavior of extrusion force. Using RSM, Srinivasulu et al. [317] investigated the effects of process parameters on the mean diameter of AA6082 tube in flow forming process. The results revealed that the roller's axial feed and radius had a considerable influence on the mean diameter than the speed of the mandrel. Singaram et al. [64] were successful in optimizing parameters of electric discharge machining (EDM) using RSM for EN31 tool steel machining. They found that the parameters such as pulse off and current were most influencing parameters while pulse on and voltage were non-significant to the material removal rate during EDM operation. Wu et al. [318] applied BBD to the optimization of the process parameters in foam cup molding. They showed that this approach is scientific, reasonable and efficient to analyze and optimize the different input process parameters on the response.

The literature review confirmed that research works relating to modeling of deformation and densification behavior of P/M preforms during plastic deformation is scarce. In this part of research, the influence of various process parameters such as deformation temperature, strain rate, and IPRD on the mechanical properties and final relative density of P/M Al-Cu-Mg preforms were presented using Taguchi and RSM when samples are subjected to hot extrusion. RSM model was successfully employed to predict the final relative density of the hot extruded Al-preforms. Optimum condition for enhanced strength and hardness of extruded rods and their densification were identified in this research work.

2.10 Limitations in the literature survey

After thoroughly going through the literature, some of the major limitations in the existing literature on P/M parts processing are given below:

i. There is very limited research on semi-solid extrusion of P/M processed Al-Cu-Mg alloys. Thus, the present work has been focussed on semi-solid extrusion which has the combined advantages of P/M and semi-solid forming to fabricate components with near-net shape and higher mechanical properties.
ii. There is limited research on the effect of Mg content on sintering behaviour of Al-Cu preforms.
iii. An appropriate combination of the extrusion ratio and the die included angle for hot extrusion of P/M alloys has not been studied.
iv. The Hot extrusion of sintered Al-Cu-Mg alloys with various IPRD at different temperature and strain rate conditions has not been explained.
v. The densification behaviour of P/M Al-Cu-Mg preforms during extrusion at elevated temperatures has not been reported.
vi. Limited studies have been reported on developing constitutive relations in considering the effect of IPRD to predict the flow stress of P/M Al-Cu-Mg preforms during hot extrusion
vii. Mathematical relations to predict the DRX grain size of sintered Al-Cu-Mg alloys after plastic deformation considering the effect of temperature, strain rate and IPRD are not yet reported.

viii. Not many studies have been reported on the application of FEM analysis to investigate the hot extrusion and densification behaviour of P/M preforms.

ix. Very limited was reported on the effect of processing parameters on the microstructural evolution and corresponding mechanical properties during hot extrusion of P/M Al-Cu-Mg alloys.

x. Mathematical relations such as Taguchi and RSM have not been presented to predict the density and mechanical properties of P/M Al-Cu-Mg preforms after plastic deformation considering the effect of various process parameters.

CHAPTER 3

Objectives and scope

Based on the limitations identified from the available literature concerning plastic deformation of P/M components during hot working, the current investigations were initiated to study the deformation, densification, and structure-property correlation of P/M Al-Cu-Mg preforms under hot extrusion. The main objectives of the current investigation are as follows:

- To study the sintering and densification behavior of Al-Cu-Mg alloys by varying Mg content.
- To evaluate the effect of extrusion ratio and die approach angle on optimum sintered composition during semi-solid extrusion.
- To explore the densification and deformation studies on extruded Al-Cu-Mg P/M alloys at different temperatures, strain rates and IPRD.
- To establish the constitutive equation that predicts the flow behavior of the extruded material at elevated temperatures, strain rate and IPRD.
- To model the microstructure of dynamically recrystallized grain size of hot extruded P/M Al–Cu-Mg alloy.
- To understand the effect of hot extrusion on the evolution of microstructure and associated mechanical properties in sintered Al-Cu-Mg alloys.
- To optimize the process parameters through FEM analysis and investigate the deformation and densification behavior of hot extruded P/M preforms.
- To optimize the percentage contribution of process parameters on final relative density, hardness and strength of extruded material by using Taguchi and RSM methodology.

Al-Cu-Mg alloys are high performance materials and the use of such alloys has increased in engineering applications, namely, aerospace, automobile and transportation industries. P/M processed products contribute a great deal compared to wrought parts. The role of compaction pressure, powder to weight ratio, the sintering atmosphere, sintering temperature and sintering time on sintering behavior and properties remain unsolved and is one of the fundamental

problems in P/M of Al alloys. Optimum compaction pressure, aspect ratio of billet, sintering temperature can support powder mixture to produce optimum sintering density and higher mechanical properties. Microscale addition of alloying elements has significant influence on the sintering properties of P/M Al-Cu alloys [92, 98, 185, 319–321]. According to existing literature [92, 322], Mg facilitates the sintering by disrupting or eliminating the oxide film by forming secondary phases and promotes atomic diffusion of Cu in Al. Mg also improves the mechanical properties of Al-Cu alloys by forming precipitates. So, the current research is mainly focused on the optimization of sintering temperature, sintering pressure and the percentage of Mg to improve the sintering behavior and mechanical properties of P/M Al-Cu-Mg alloys.

The mechanical properties of porous materials depend considerably on the amount of inherent porosity in the preforms left behind after sintering. Therefore, the plastic deformation of porous materials is essential to enhance the properties and/or to minimize uncertainties in mechanical properties by eliminating the porosity. Plastic deformation of porous materials improves metallurgical and mechanical properties which mainly depend on material geometry, die geometry, composition, IPRD, deformation temperature and strain rate. Thus, the other objective of the current research is to examine the influence of process parameters such as IPRD, extrusion ratio, die approach angle, deformation temperature and strain rate during hot extrusion of P/M components.

During plastic deformation, the material flow behavior is influenced by many factors such as deformation temperature, stress, strain and strain rate. Uniformity in metal flow can be observed in deformed materials using optimum process conditions. Flow stress is an important parameter which determines the extrusion difficulty. The flow stress of a material during deformation depends on process parameters such as deformation temperature, strain rate and IPRD. The alloys with low flow stress are commonly easy to extrude, whereas alloys with high flow stress are difficult to extrude. The constitutive model relations are often used to explain about plastic flow properties of any alloy and to describe the sensitivity of the flow stress at different processing conditions. Therefore, it is essential to formulate the constitutive modeling under different deformation conditions to explain the metal flow and flow stress behavior as a function of controlled amount of porosity present in the preforms and also to establish optimum processing variables. Hot deformation can affect the flow behavior, microstructure and the

energy required for deformation through WH, DRV and DRX. These can also affect the mechanical properties of hot deformed materials. Thus, the current study also concentrates on the DRX grains and their sizes during deformation and establishing the microstructural model to predict the accuracy with experimental DRX grain sizes.

The application of FEM in metal forming has been providing quality improvements and considerable cost savings to the industry. It has become an efficient tool for analysis and prediction of deformation and densification behavior of materials during metal forming. FE simulation can provide detailed information on load vs stroke curves, density variations, velocity, induced effective stress, effective strain and effective strain rate, etc. Thus, the present investigation confined itself to the application of FEM in analyzing and predicting the deformation and densification characteristics of preforms during hot extrusion. It also attempted to predict and optimize the percentage contribution of process parameters on final relative density, hardness and strength of extruded products using Taguchi analysis and RSM methodology.

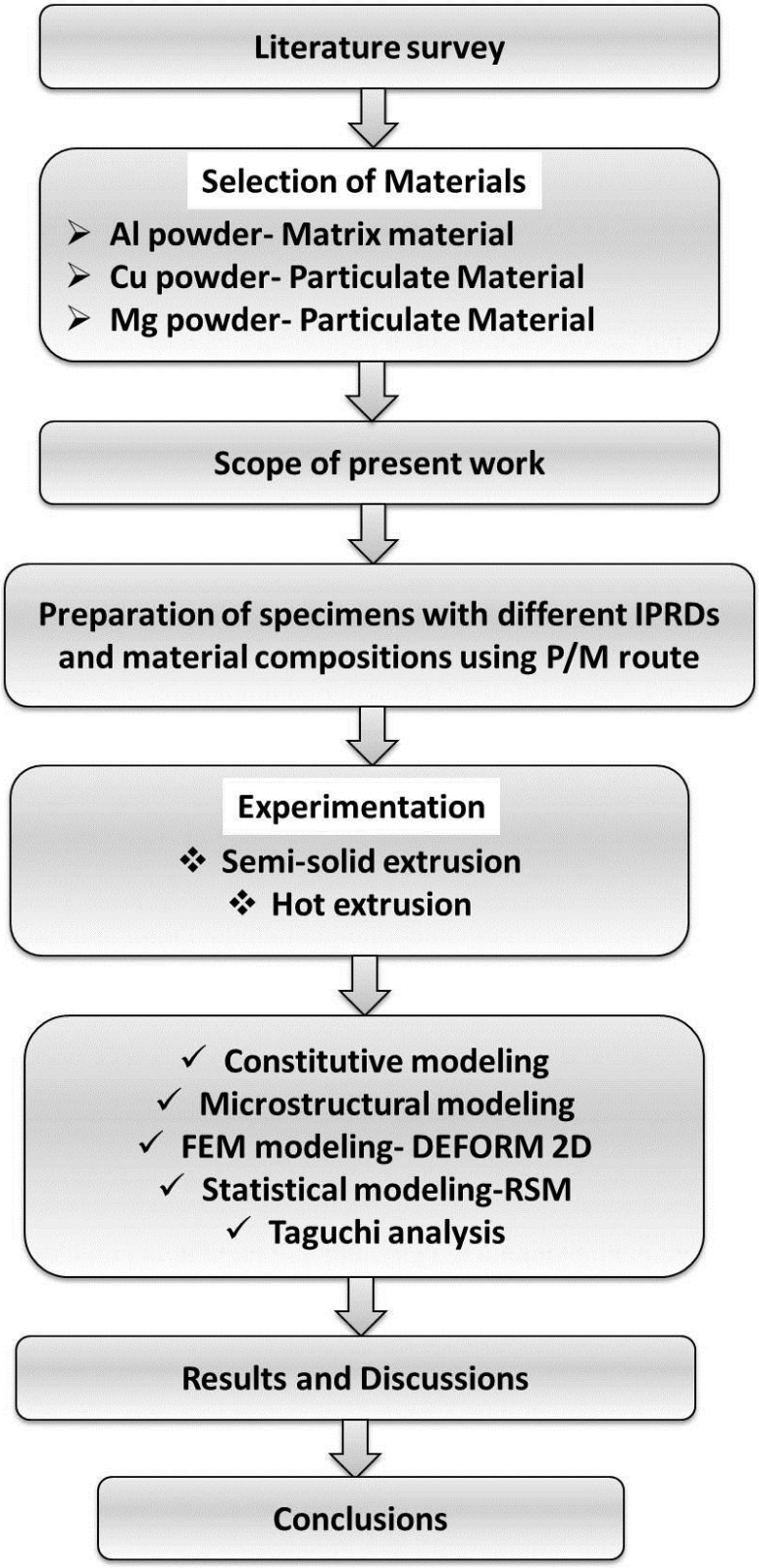

Fig. 3.1 Flow chart diagram showing the brief procedure of the present research investigations

CHAPTER 4

Methodology

The methodologies adopted in the current research to gather required information and analyze and evaluate the data to develop reliable conclusions are as follows:

1) Optimization of compaction pressure, sintering temperature and time and also Mg content in the Al-Cu alloys to develop highly densified preforms.
2) Evaluation of the effect of liquid and solid fraction, deformation temperature, and die geometries during semi-solid extrusion.
3) Identification of best processing temperature, extrusion ratio and die approach angle for the chosen composition for further investigations.
4) Conducting hot extrusion tests to explore the influence of IPRD, deformation temperature and strain rate on the microstructure and mechanical properties of P/M Al-Cu-Mg alloys.
5) Adopting Arrhenius-type constitutive equation and Zener-Hollomon equation to investigate the effect of temperature, strain rate and IPRD on deformation behaviour.
6) Adopting FE simulations to evaluate the influence of process parameters such as deformation temperature, strain rate and IPRD during hot extrusion of P/M Al-Cu-Mg preforms.
7) Employing RSM: Box-Behnken approach with hot extrusion to determine the density of the preforms after plastic deformation for different extrusion conditions.
8) Employing Taguchi L9 orthogonal array and ANOVA to optimize the best combination of process parameters for hardness and yield strength of hot extruded Al-Cu-Mg preforms.

The detailed experimental plans of the present investigation are shown as follows:

Experimental plan I

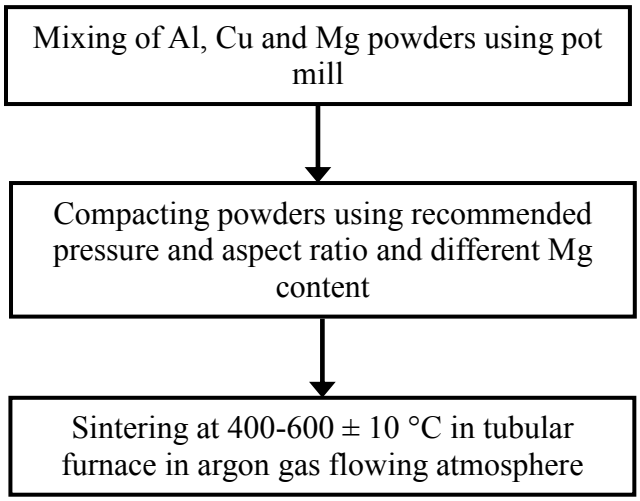

Fig. 4.1 Preparation of preforms through P/M route

Experimental plan II

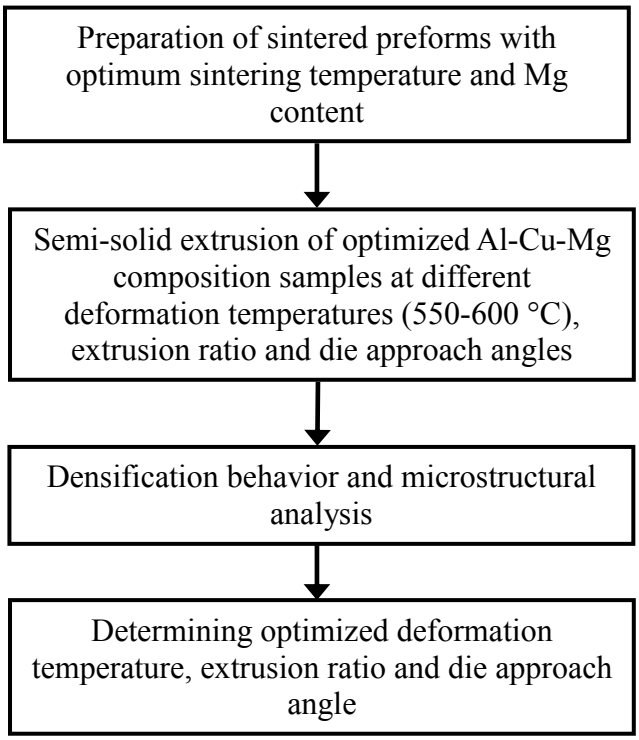

Fig. 4.2 Semi-solid extrusion of P/M Al-Cu-Mg preforms

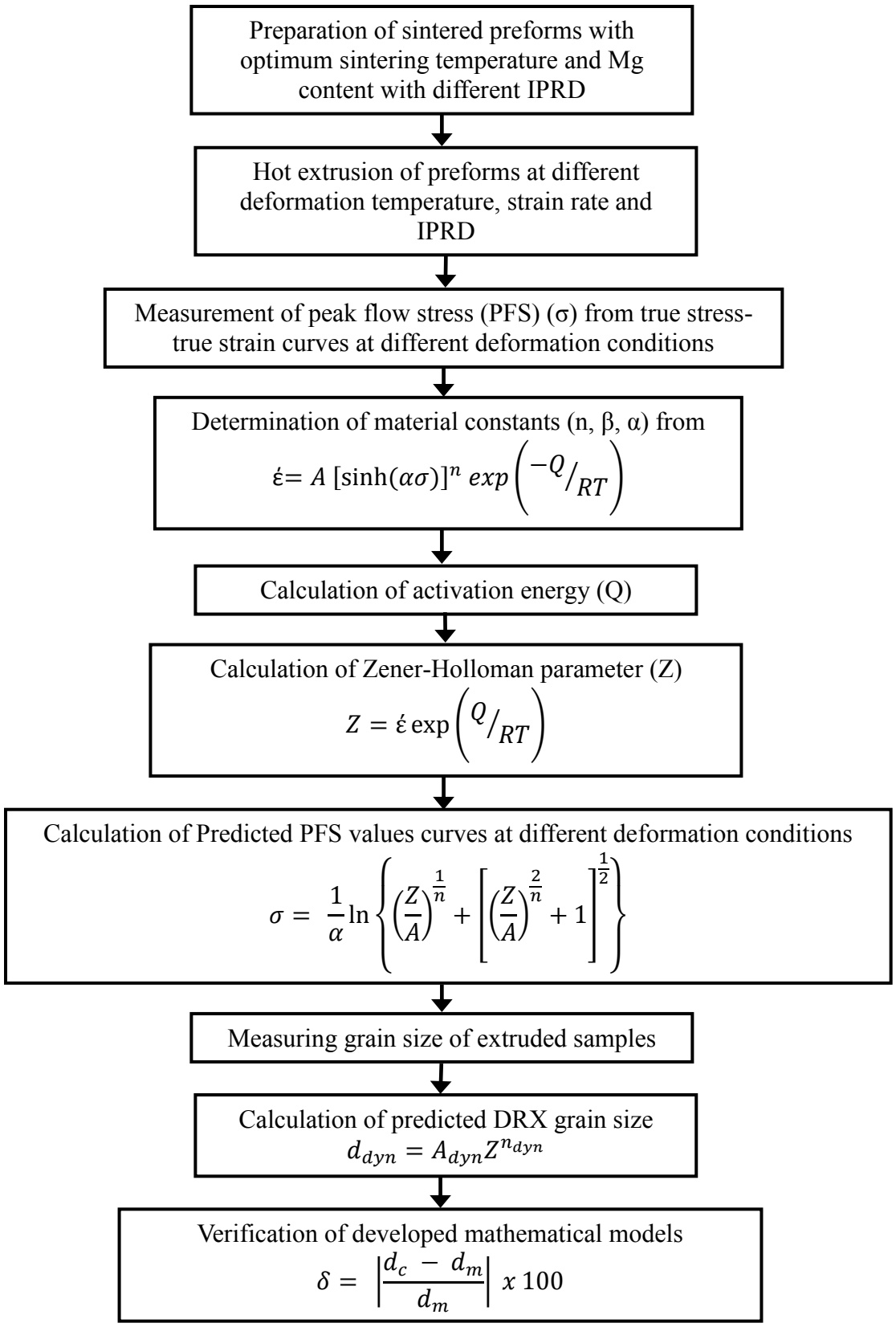

Fig. 4.3 Constitutive modeling and microstructural modeling of hot extruded preforms

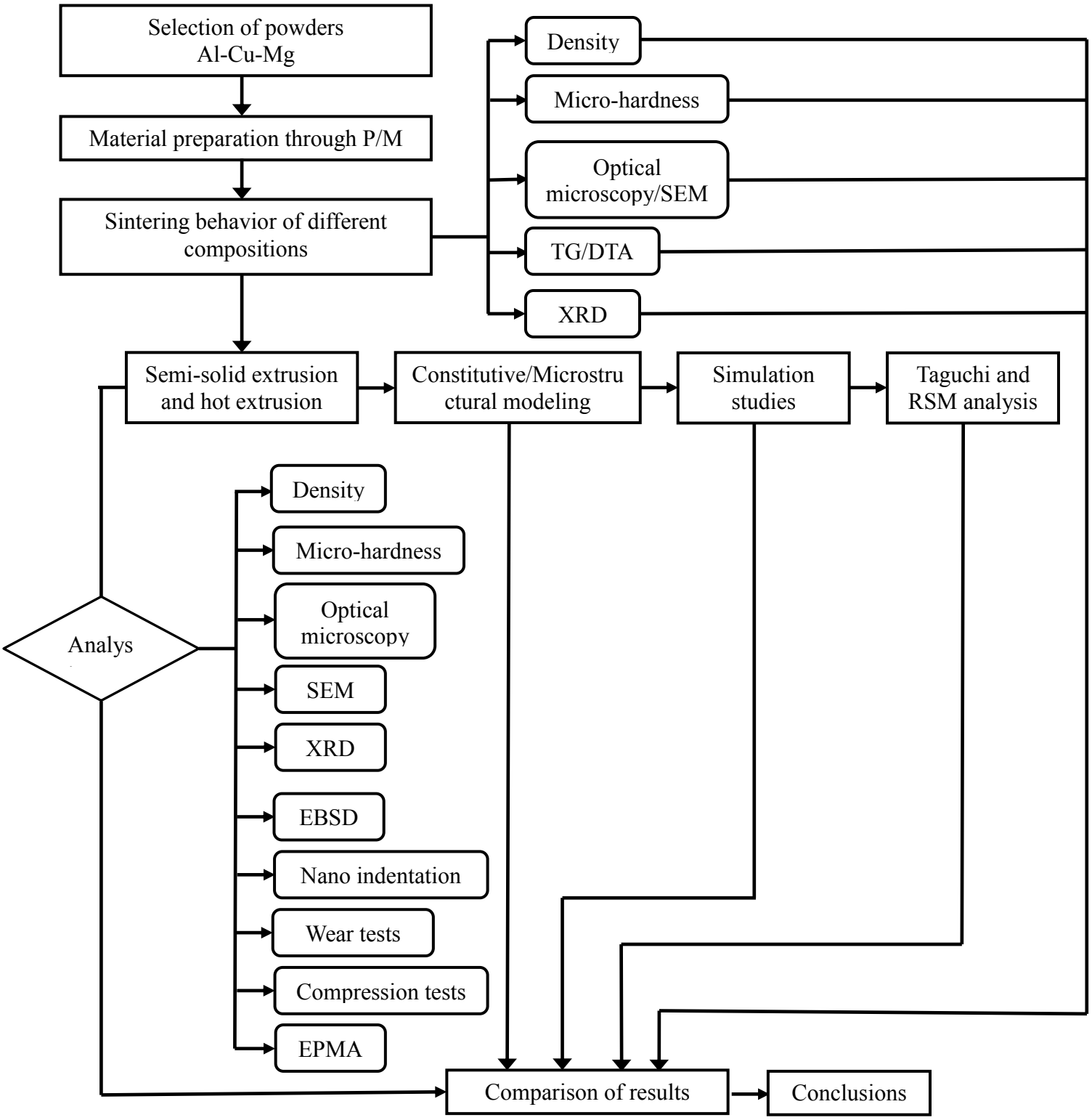

Fig. 4.4 Flow chart showing the detailed procedure of the present investigation

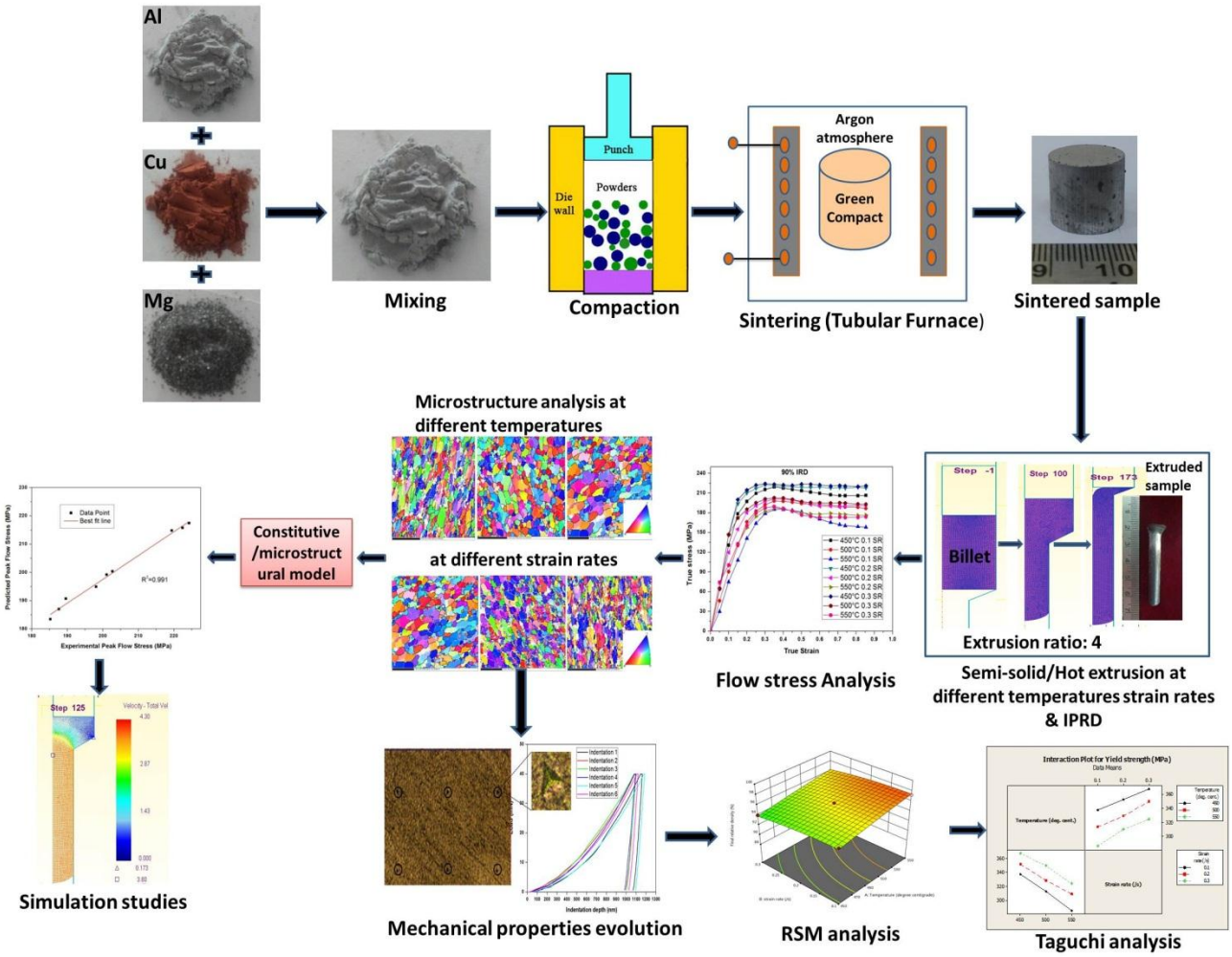

Fig. 4.5 Graphical representation of research work

CHAPTER 5

Experimental Details

This chapter describes the details of experiments conducted for the present research investigation which include material selection, sample preparation, hot extrusion test, metallurgical analysis by optical microscopy, SEM, EBSD, XRD and EPMA, and corresponding mechanical properties evaluation.

5.1 Selection of materials

The materials chosen for the present investigations were pure form of Aluminium (Al), Copper (Cu) and Magnesium (Mg). Al and Cu powders with 99.9% purity with a maximum of 0.5% insoluble impurities, and Mg powder with 99.96% purity with a maximum of 0.5% impurities were supplied by Alfa Aesaer, USA. The mesh sizes of Al, Cu and Mg were ~325, ~325 and ~36, respectively. The prime reason for selecting these materials was the extensive use of their alloys/composites in numerous structural applications such as aerospace, automotive, defence, transportation, building, architecture, etc. Moreover, literature studies related to the deformation and densification of the selected materials are scarce. P/M processed components have superior practical and industrial importance than the corresponding wrought materials with the same composition. In general, morphology of the raw powders plays a vital role in mechanical properties evolution of materials prepared by P/M process. Therefore, micrographs of Al, Cu and Mg powders are given in Fig. 5.1, 5.2 and 5.3, respectively. Al and Cu powders consist of particles with semi-rounded, spherical and irregular shapes. The average particle size (D) of Al was 16.11 µm (Fig. 5.1) and Cu was 19.51 µm (Fig. 5.2) respectively. Due to mechanical grinding operation, Mg powder particles look like flake shaped morphology with an average particle size (D) of 147.03 µm (Fig. 5.3).

5.2 Specimen preparation

5.2.1 Mixing

The required mass of Al, Cu and Mg powders was accurately weighed using electronic mass balance (± 0.01 mg repeatability) and mixed in a pot mill for 1 hour to get a homogeneous

mixture. Aluminum powder was mixed with copper (4 wt.%) and magnesium (0 wt.%, 0.25 wt.%, 0.5 wt.%, 0.75 wt.%, 1 wt.%) powders in order to produce light and strong Aluminum based powder metallurgy alloys. The homogeneous powder mix has the advantage of improving sinterability of the powder and making the ejection of compacts easy.

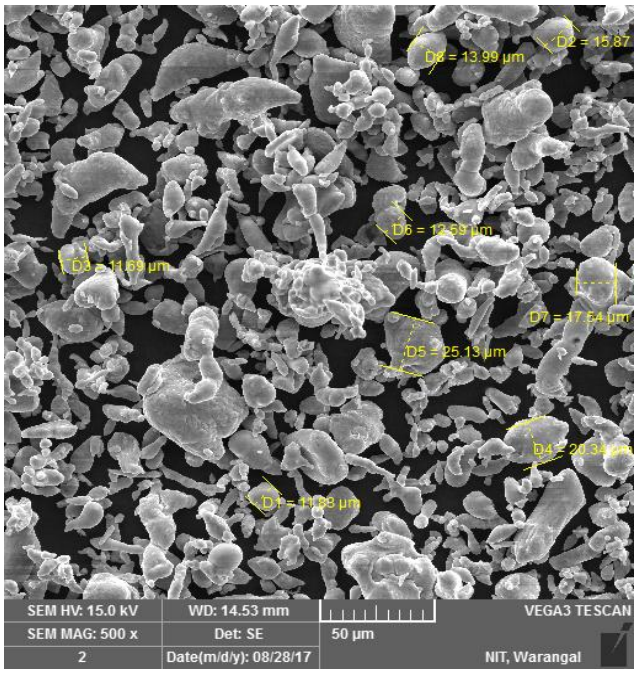

Fig. 5.1 SEM morphology of Aluminium powder

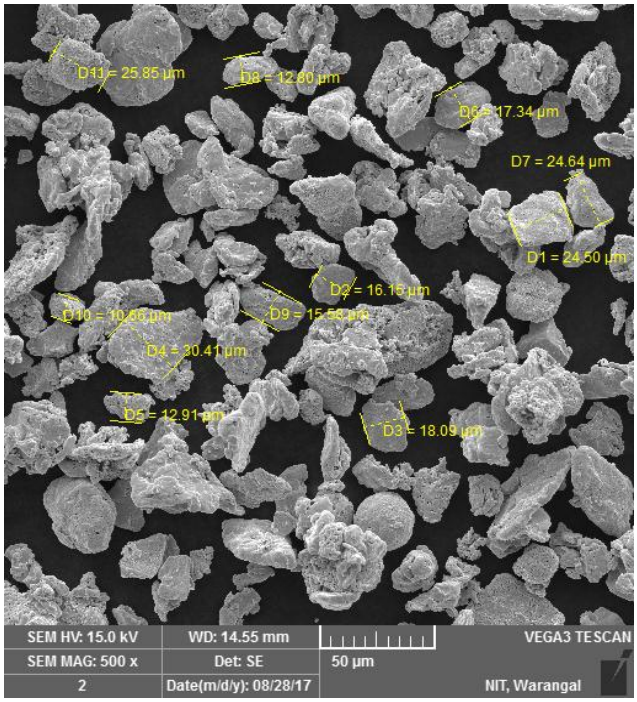

Fig. 5.2 SEM morphology of Copper powder

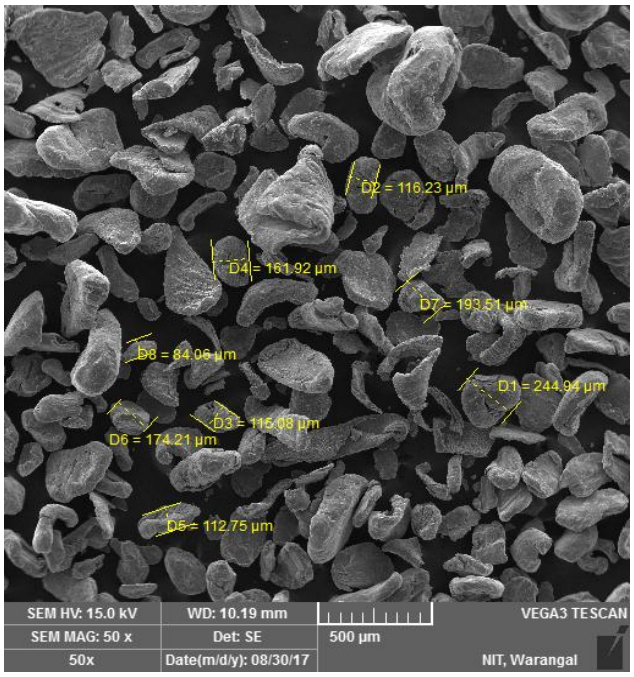

Fig. 5.3 SEM morphology of Magnesium powder

5.2.2 Compaction

Among several compaction methods, uniaxial die compaction was used for preparing powder compacts as it is by far most economical and important method. Uniaxial die compaction involves pressing of powder mix within a die cavity by the action of an upper punch at a constant velocity while the lower punch remains fixed. Fig. 5.4 shows the schematic diagram of uniaxial die compaction technique adopted in the current work for sample preparations. A hydraulic press of 25 ton capacity supplied by Kimaya Engineers, India, was used for preparing Al-Cu-Mg compacts. In this process, the required amount of the Al-Cu-Mg powder mix was properly poured into the die with its bottom punch inserted from the lower part of the die and top punch introduced from the upper side. All the green compacts were compacted by applying the recommended compaction pressures of 100 MPa to 450 MPa to the die assembly to achieve compacts with initial preform relative densities (IPRD) of 70%, 80% and 90%, respectively. Cylindrical green compacts with one aspect ratio (diameter of 15 mm and height of 15 mm) were prepared to obtain good dense compacts. Zinc stearate was applied on the die walls, punches and butts to minimize the interface friction between metal powders and die during compaction. After completion of compaction step, the green compacts were carefully ejected from the die by placing the die upside down and applying ejection load ranging from 50 MPa to 80 MPa. Zinc

stearate was expected to decompose during the sintering cycle due to low operating temperature/melting point, and small residues of zinc stearate left after sintering do not impart considerable effect on the final parts. Fig. 5.5 shows the 15 mm diameter high strength tool steel compaction die, punch and butt used for preparing powder compacts for hot extrusion tests.

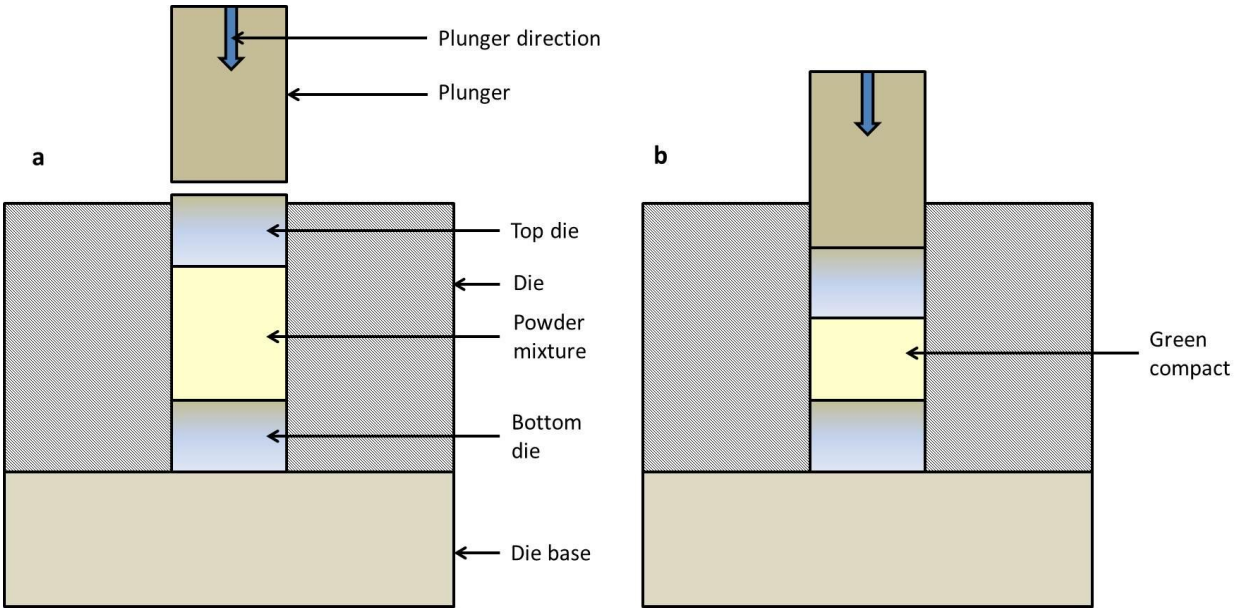

Fig. 5.4 The schematic diagram of uniaxial die compaction technique; a) before applied pressure and b) after applied pressure

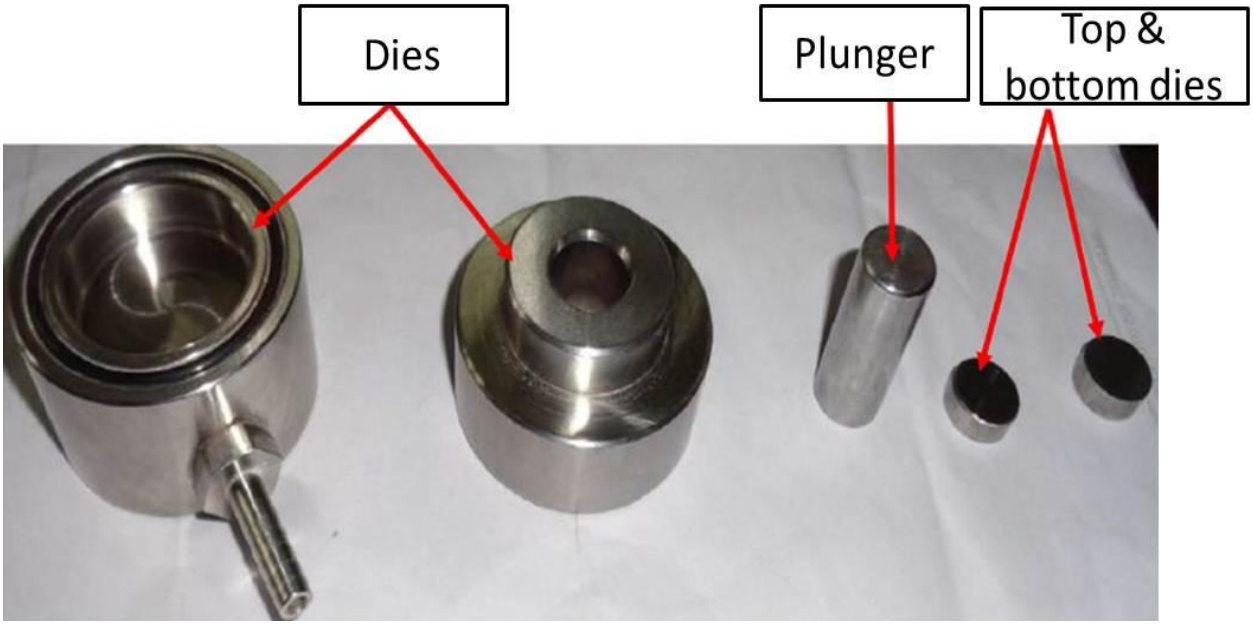

Fig. 5.5 Photographs of 15 mm die, top and bottom dies and plunger for preparing green compacts

5.2.3 Sintering

A tubular furnace with controlled atmosphere and cylinder containing argon gas was used for sintering green compacts as shown in Fig. 5.6. The tubular furnace specifications are given below.

Furnace specifications:

Inner diameter: 50-70 mm

Maximum temperature: 1100 °C

Working temperature: 1000 °C

Power requirement: 3 kW

Voltage: 220 V/ Single phase/60/50 Hz

Fig. 5.6 Tubular furnace used for sintering with argon gas attachment

Sintering of green compacts was done with the purpose of achieving all possible final strength, hardness and dimensions. Therefore, green compacts were placed in a stainless steel crucible and kept in the chamber. The green compacts were sintered at 400 °C, 450 °C, 500 °C, 550 °C and 600 °C at a heating rate of 10 °C/min and the specimen were allowed to sinter at these temperatures for 1 hour prior to furnace cooling. The chamber was then back-filled with 99.98% pure argon gas and maintained at a constant rate of flow throughout the sintering process to

avoid oxidation problems. The compacts were then allowed to attain room temperature inside the furnace after completion of the sintering schedule. During the sintering process, shrinkage in dimensions was observed that led to increase in the density of the consolidated body. The sintered density of the preforms was measured using Archimedes principles with an accuracy of ± 1%, and the photographs of a few sintered preforms are shown in Fig. 5.7. 550 °C temperature was used as optimized sintering temperature in all subsequent studies after the first study.

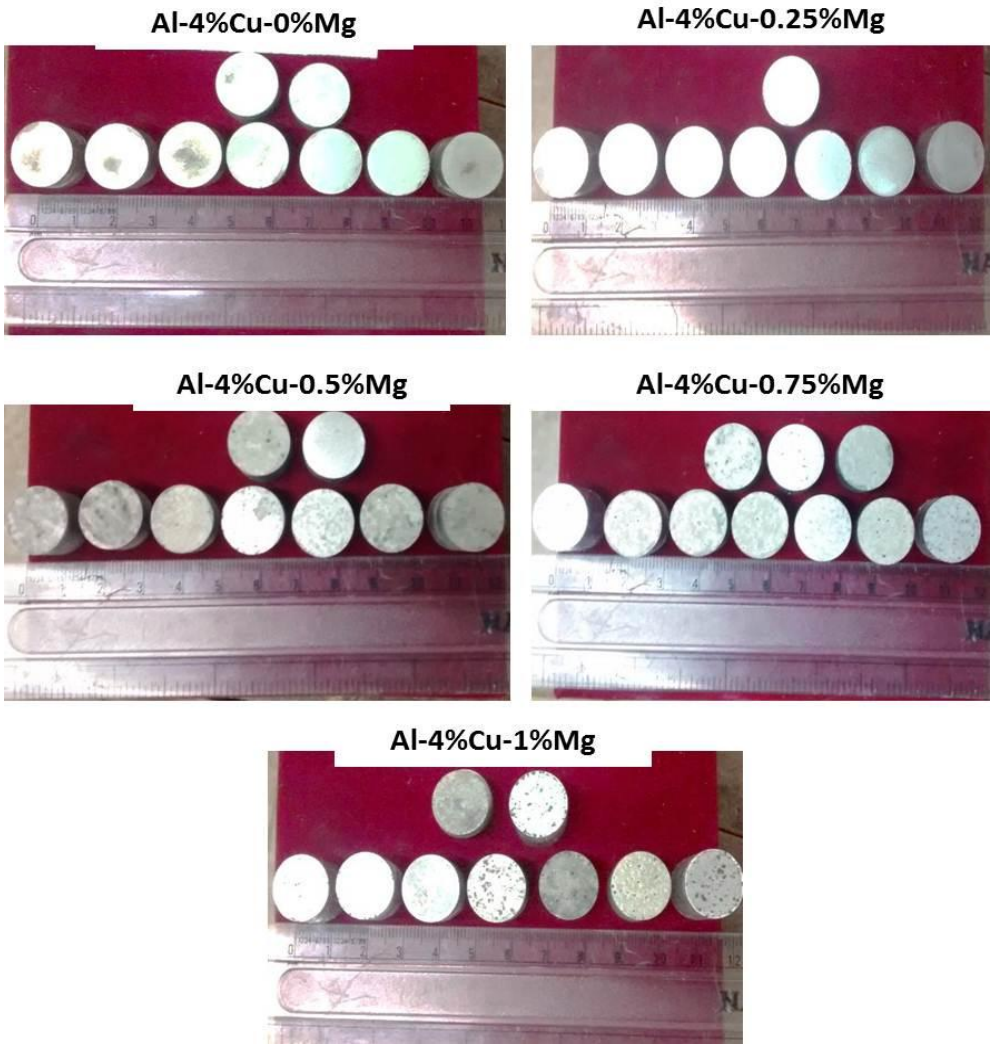

Fig. 5.7 Photographs of sintered samples at different temperatures with different compositions

5.3 Thermogravimetry/Differential thermal analysis (TG/DTA)

The semi-solid forming process requires 60-80% of solid fraction to produce the best quality products. The solid fraction of a material plays an important role that affects the viscosity of the

semi-solid slurry. The final product of the semi-solid extrusion coexists between solidus and liquidus temperatures. Therefore, TG/DTA was employed to identify the solidus and liquidus temperatures and the solidification interval of the Al-Cu-Mg preforms. Samples weighing 15 mg were cut and placed in the alumina pan in nitrogen gas atmosphere. The samples were then heated at a rate of 2.5 K/min between 200 °C and 700 °C. The curve obtained by TG/DTA was used to calculate the change in solid-liquid fractions with temperature. The semi-solid extrusion tests were performed in the temperature ranges between solidus and liquidus temperatures derived from TG/DTA analysis, in order to have a minimum to maximum solid fraction range in the samples. The percentage of solid fraction at any given temperature within the solidification limit is determined by Scheil equation, Eq. (2.1). Fig. 5.8 shows the photograph of TG/DTA instrument supplied by Ametek Scientific Instruments, USA (Software: Versa Studio 2.52.3).

Fig. 5.8 Photograph of TG/DTA instrument

5.4 Semi-solid extrusion/Hot extrusion test

Semi-solid extrusion tests were conducted to evaluate the effect of solid fraction and liquid fraction in the preforms during deformation, effect of extrusion ratio and also the die approach angle. A series of semi-solid extrusion tests were conducted on a hydraulic press of 50 ton

capacity supplied by SVS Hydraulics (P) Ltd, Hyderabad, India. Fig. 5.9 shows the photograph of hydraulic press used for extrusion tests.

Fig. 5.9 Hydraulic press of 50 ton capacity

At first, semi-solid extrusion testes were carried out on optimized Al-4%Cu-0.5%Mg P/M preforms within the temperature range between solidus (542.7 $^{\circ}$C) and liquidus (662.8 $^{\circ}$C) temperatures derived from the TG/DTA analysis. Extrusions of the sintered preforms were performed with extrusion ratios of 1.44, 2.55, and 4 and approach angles of 30°, 45°, and 60° for three different working temperatures of 550 °C, 575 °C, and 600 °C, respectively. Fig. 5.10 shows the photographs of extrusion dies with different extrusion ratios and die approach angles. An incremental load was applied till there was complete extrusion of sintered preforms. The deformation processes were carried out by fixing extrusion dies inside a split type electrical resistance furnace provided on the bed of hydraulic press. Two thermocouples were placed in the furnace to measure the furnace temperature and the preform temperature, in which one was placed inside the furnace and another was placed near the preform, respectively. A soaking time

of 20 minutes was kept to allow globularisation of the grains and to get uniform temperature throughout the furnace and sample after reaching the required test temperature before deformation. The deformation load and displacement were continuously monitored by the data acquisition system connected to the hydraulic press and the data was recorded after each extrusion test.

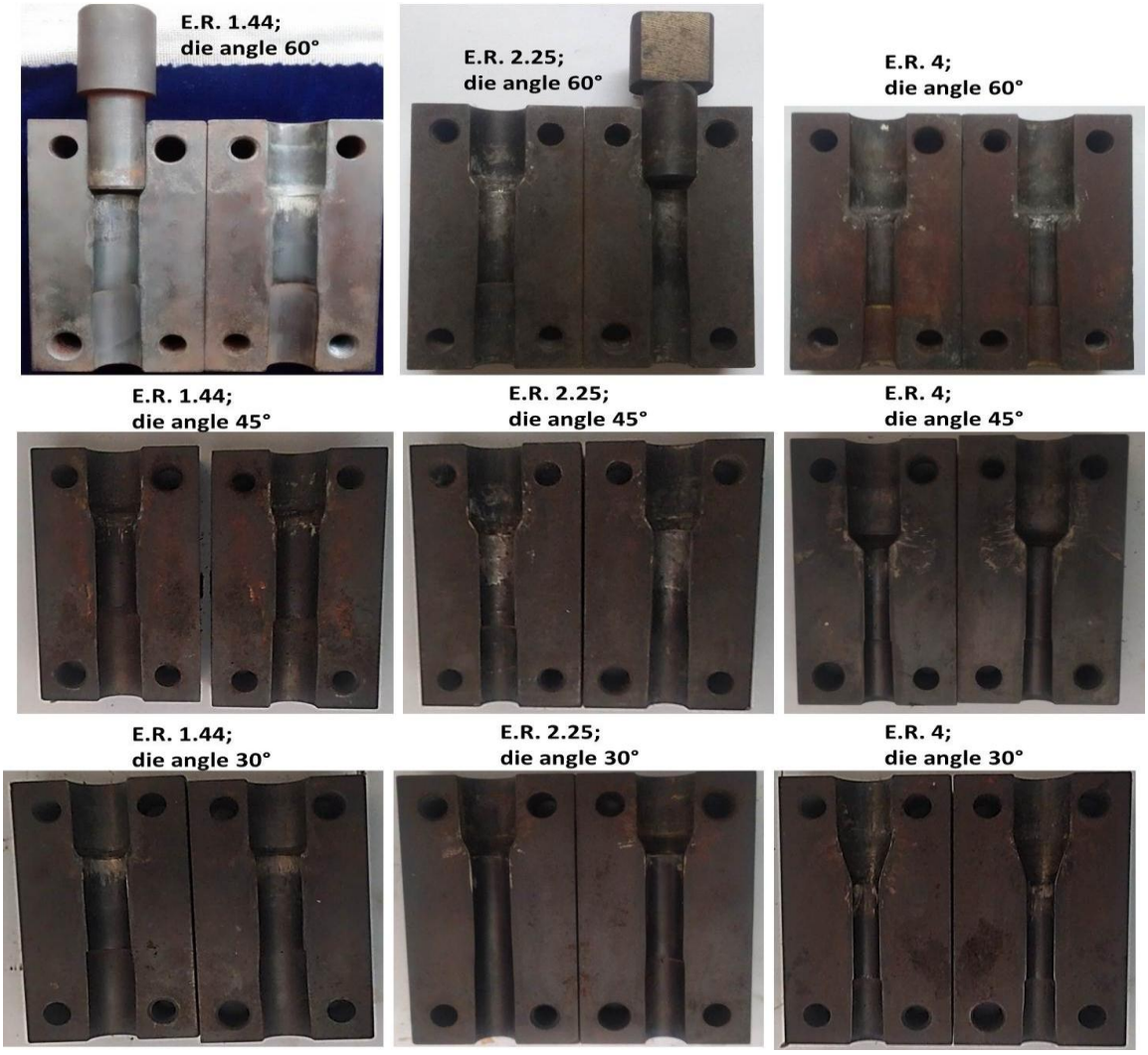

Fig. 5.10 Extrusion dies with different extrusion ratio and die approach angle

To reduce extrusion defects and increase the properties of extruded rods, the deformation temperature was reduced to below 550 °C and used die with extrusion ratio of 4 and approach angle of 30° for further studies of hot extrusion. Hot extrusion tests were performed at temperatures of 450 °C, 500 °C and 550 °C, strain rates of $0.1s^{-1}$, $0.2\ s^{-1}$ and $0.3\ s^{-1}$, and initial preform relative density (IPRD) of 70%, 80% and 90%, respectively. Prior to the test, a thin

layer of Molybdenum disulfide (MoS_2) and ethanol mixture was applied on the die walls and plunger to minimize the friction forces during extrusion tests.

5.5 Development of constitutive equations for modeling

Hot extrusion tests were conducted to evaluate the deformation behavior and to develop constitutive equation to predict the flow stress and to develop mathematical models to predict the DRX grain size for preforms of various IPRDs deformed at different deformation temperatures and strain rates. Cylindrical green pellets with one aspect ratio (diameter of 15 mm and height of 15 mm) were prepared to obtain good dense compacts. All the green pellets were compacted by applying recommended pressures to get samples with IPRD of 70%, 80% and 90%, respectively. Prior to extrusion, sintered preforms were soaked for 30 minutes at a test temperature to ensure a homogeneous temperature distribution. All the samples were then air cooled to obtain uniform microstructure and also to know the deformation degree on the DRX grain size. In order to explain the materials deformation behavior and to establish optimum processing variables, it was essential to investigate the constitutive modeling under different deformation conditions. Over many phenomenological constitutive models, the Arrhenius type model was chosen to explain the correlation between deformation temperature, strain rate and IPRD. The hot deformation activation energy (Q) and Zener-Hollomon parameter (Z-H) are very important physical parameters in the model in which activation energy acts as an energy barrier to dislocation motion on a slip plane while Z-H parameter depicts the relationship between flow stress of different materials and deformation parameters. These two parameters were calculated from the hyperbolic-sine constitutive equation i.e., an Arrhenius-type equation at different deformation temperatures, strain rates and IPRDs. Test parameters for constitutive modeling are presented in Table 5.1. Data logger was connected to the system and hydraulic machine to obtain true stress-strain plots during extrusion. Experimental results and constitutive modeling results were compared to observe the accuracy and reliability of the developed model for P/M processed Al-4%Cu-0.5%Mg preforms. A mathematical model for DRX grain size was also developed as a function of Z-H parameter for various IPRD to predict the DRX grain size.

Table 5.1 Material and experimental parameters

Alloy	Temperatures	Strain rate (s^{-1})	Initial Preform Relative Density (IPRD) (%)
Al-4%Cu-0.5%Mg	450 °C (723 K) 500 °C (773 K) 550 °C (823 K)	0.1 0.2 0.3	70 80 90

5.6 Microstructural investigation

Since most of the materials strength is derived by recrystallization, precipitates and dispersoids formed during sintering and deformation processes, all the sintered and extruded samples were examined by optical microscopy, SEM/EDS, EBSD, EPMA and XRD. All samples prepared for optical microscopic analysis were first polished by different grit size silicon carbide emery papers. Following this, samples were polished on disk polishing machine using different grade polishing clothes and diamond suspensions until they achieved mirror finishing surface. The polished samples were etched for 60 sec in a Keller's reagent. Optical metallography was done using a Quasmo ISI Microscope equipped with a micrometrics digital camera (Software: Quasmo iview 3.7) as shown in Fig. 5.11. A VEGA 3 LMU (TESCAN) SEM was used to capture the microstructures of polished samples where it was operated with a beam current of 10 mA and an accelerating voltage of 20kV. Elemental analysis was done by Energy Dispersive Spectroscopy (EDS) which was supplied by Oxford Instruments, UK (Software: INCA 5.03). Fig. 5.12 shows the scanning electron microscope with EDS connection.

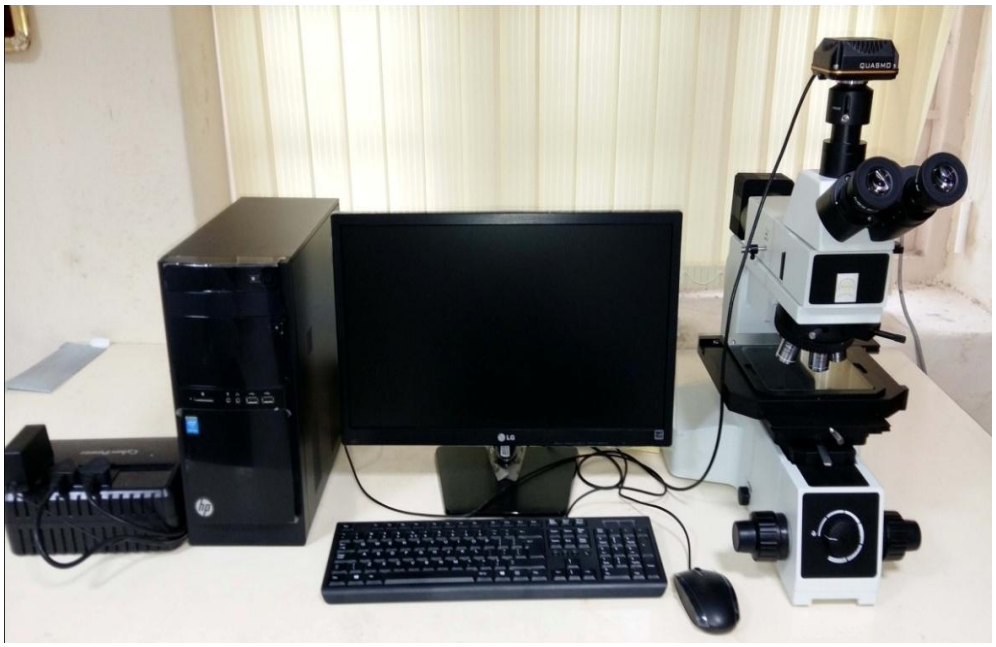

Fig. 5.11 Photograph of optical microscopy

Fig. 5.12 Photograph of scanning electron microscope

Microstructure analyses were performed by optical microscopy and SEM for extruded samples with different die extrusion ratio, approach angle, deformation temperature, strain rate and IPRD. The grain size of all the samples was measured by standard line intercept method. X-ray diffractometry (XRD) was also used to obtain qualitative analysis of the phases present in the

specimens. The XRD unit equipped with a copper X-ray source (CuKα) was operated at a voltage of 45 kV and current of 30 mA.

The specimens for EBSD were prepared by electro-polishing in a solution of 70% methonal and 30% nitric acid at -28 °C with a step size of 0.7 µm. EBSD data (IPF, LAM and ODF) was collected using TSL-OIM software in which low angle grain boundaries (LABs) were differentiated from high angle grain boundaries (HABs) by considering a critical misorientation angle of 15°. The extruded samples were further examined by electron probe micro analyzer (EPMA) to identify the grain boundary constituents and secondary phases formed in nanometer scale. Fig. 5.13 shows the photograph of electron probe micro analyzer. Samples were mirror polished and analyzed in un-etched condition. Elemental line scan, elemental distribution mapping and back scattered electron (BSE) images were analyzed by EPMA (make: CAMECA, model: SX-100) with an operating voltage of 20 kV and stabilized beam current of 20 nA.

Fig. 5.13 Photograph of electron probe micro analyzer (EPMA)

5.7 Mechanical properties evaluation

A systematic study was carried out to establish structure-property correlation of Al-Cu-Mg P/M alloys as a function of extrusion temperature and strain rate. Densities of as-sintered and extruded parts were measured by means of the Archimedes' principle with an error of ±1%. Shimadzu micro-hardness testing machine was used for the measurement of hardness of sintered and extruded samples by applying 500 g load with 15 seconds dwell time (test force time on sample). Room temperature compression tests were performed on the extruded samples to determine the mechanical properties on a computerized universal testing machine (UTM) at a cross-head velocity of 0.005 mm/min with a ratio of 1.5 L/D (length/diameter) according to ASTM-E9 standard [323]. The sintered and extruded samples were then polished and mounted for nanoindentation studies. Nanoindentation tests were performed in Anton Paar GmbH Nanoindentor, supplied by Santner Foundation, Austria, using a three-sided Berkovich tip made of diamond with Poison's ratio of 0.2 and elastic modulus of 865 GPa. Berkovich indenter was used to determine the hardness (H) and elastic modulus (E) in which data is generated from one complete cycle of loading and unloading [324]. The maximum load applied for nanoindentation tests was 40 mN with a loading/unloading rate of 80 mN/min and a dwelling time of 10s. A 3x2 indentation grid with a linear spacing of 200 μm was made on each sample surface, and the results were analyzed using Indentation 7.1.15 software. Nanoindentation data were used to measure the dislocation densities and residual stresses in extruded samples. Being a mechanical and non-destructive testing method, instrumented indentation was preferred over other techniques to measure the residual stresses [325]. The wear tests of optimized Al-4%Cu-0.5%Mg P/M extruded samples at different temperatures and strain rates were carried out on a pin-on-disc wear testing machine (Ducom, Bangalore, India; model: TR-20). The wear tests of extruded samples were carried out at an applied load of 15 KN, sliding distance of 1000 m and sliding velocity of 1.0 m/s. All the wear tests were conducted according to the ASTM G99 standards in dry sliding conditions. All the samples were prepared with φ 10 x 15 mm dimensions. All the samples were polished with emery papers for good surface finish prior to wear tests and then cleaned ultrasonically with ethanol before and after wear tests. The EN 31 grade tool steel disc with a hardness of 60 HRC was used as the counter body. Weight loss, coefficient of friction and wear rate were calculated from the data after every wear test. The morphology of the worn-out surface was observed by SEM-EDS to understand the wear mechanism of extruded samples.

5.8 FEM modeling

The FEM modeling of hot extrusion tests were carried out using DEFORM 2D software as illustrated in Fig. 5.14 for different stages of hot extrusion. An axisymmetric formulation of the billet was considered during modeling. A quadrilateral nodded 2000 elements with size ratio of 3, was used to mesh the billet. Optimized composition was selected as specimen in the present research subject. The diameter and length of the billet used for all the simulations had one aspect ratio (diameter of 15 mm and height of 15 mm). The simulation of hot extrusion process was executed in DEFORM 2D as it is reasonable to simplify the prototype as the plane model with 2D axisymmetry. The specimens were modeled as porous materials with various IPRD values (70%, 80% and 90%) given as input to the model, while die and stem were set as rigid body. Based on the flow stress curves obtained from the extrusion at different deformation temperatures, strain stress and IPRD, the flow stress constitutive equation was established by hyperbolic-sine relation (Arrhenius-type equation) and it was imported to DEFORM 2D software. Constant shear friction was considered between die and workpiece and coefficient of friction m=0.4 was assumed between top die to workpiece and workpiece to bottom die in all simulations. A die with extrusion ratio of 4 and approach angle of 30° were used in simulation studies as these yielded good experimental results in semi-solid extrusion. In order to verify the experimental results with simulation results, the same deformation temperature, strain rate and IPRD were used in simulation studies as were used in hot extrusion studies. The simulation parameters are shown in Table 5.2.

Table 5.2 Simulation parameters

Simulation parameter	**Value**
Temperature of the billet (°C)	450 °C, 500 °C, 550 °C
Temperature of the dies (°C)	450 °C, 500 °C, 550 °C
Strain rates	$0.1s^{-1}$, $0.2\ s^{-1}$, $0.3\ s^{-1}$
Extrusion ratio	4
Die approach angle	30°
Coefficient of friction	0.4

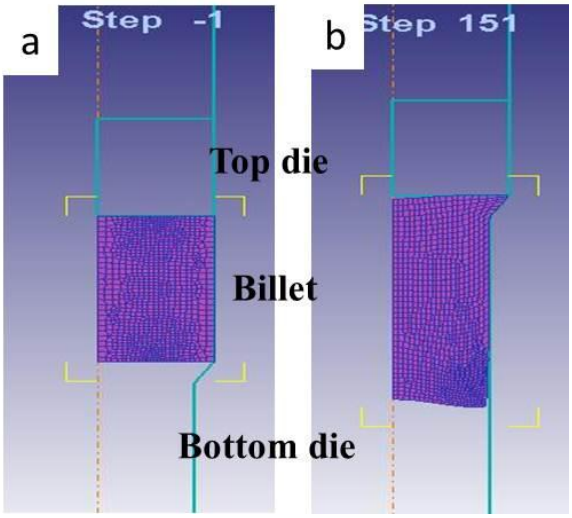

Fig. 5.14 FE modeling of P/M preform a) before deformation b) after deformation

5.9 Experimental plan for predicting the final relative density using RSM

5.9.1 Extrusion tests

Hot extrusion tests were conducted in between two parallel flat split die setup on a hydraulic press of 50 ton capacity. The tests were carried out on Al-4%Cu-0.5%Mg preforms of different IPRD such as 70%, 80% and 90%. All the extrusion tests were carried out at different deformation temperatures, 450 °C, 500 °C and 550 °C and strain rates, $0.1s^{-1}$, $0.2\ s^{-1}$ and $0.3\ s^{-1}$ according to the experimental design of RSM model. The densities of extruded samples were measured by means of the Archimedes' principle with an error of ±1%.

5.9.2 Modeling using RSM

RSM was used to investigate the influence of three independent variables, namely; deformation temperature, strain rate and IPRD, on the response function. The RSM design approach employed has been published elsewhere [313]. As BBD offers more advantages than CCD, a 17 experiment Box-Behnken experimental design was used to develop the mathematical model for determining the final relative density of the P/M extruded materials. The same parameters were used for RSM investigations as were used for experimental analysis. The input variables and their levels chosen for RSM investigation are given in Table 5.3.

Table 5.3 Input process parameters and their levels used for Box-Behnken design

Variables (Units)	Level 1	Level 2	Level 3
Deformation temperature (°C)	450	500	550
Strain rate (s^{-1})	0.1	0.2	0.3
Initial preform relative density (%)	70	80	90

Statistical software, Design-Expert 12 trial version was used to determine the mathematical mode. Based on the experimental design, the final relative density of the P/M Al-Cu-Mg preforms was measured after extrusion test for each experimental condition and given in Table 5.4.

Table 5.4 Box-Behnken experimental design matrix and experimental responses

		Factor 1	**Factor 2**	**Factor 3**	**Response 1**
Std	**Run**	**A:Temperature (°C)**	**B: Strain rate (/s)**	**C: Initial relative density (%)**	**Final relative density (%)**
6	1	500	0.1	70	89.90
15	2	500	0.2	80	96.05
5	3	500	0.2	80	96.05
7	4	500	0.2	80	96.05
13	5	500	0.2	80	96.05
16	6	450	0.1	80	94.00
11	7	500	0.3	70	91.60
2	8	550	0.2	70	93.01
14	9	450	0.2	90	96.40
9	10	500	0.3	90	97.40
8	11	450	0.2	70	89.00
3	12	500	0.2	80	96.05
10	13	450	0.3	80	95.25
1	14	550	0.2	90	98.24
4	15	550	0.3	80	97.24
12	16	500	0.1	90	97.06
17	17	550	0.1	80	95.97

5.10 Experimental plan to find the percentage contribution of parameters using Taguchi and ANOVA

The percentage contribution of each process parameter on the mechanical properties was determined using Taguchi and ANOVA techniques. MINITAB, statistical analysis software was employed for the experimental design and analysis, and to perform ANOVA analysis. Taguchi suggested a special design of orthogonal arrays (OA) (L9) with a small number of experiments, which helps to know the influence of process parameters on the results of hot extruded Al-Cu-Mg P/M alloy samples. Taguchi suggested this OA based on the number of degrees of freedom, which was determined from the number of factors, interactions, and levels of each factor. The main factors and interactions, if any, were assigned to the various columns after the acceptable OA was determined. The experimental results were then transformed in to signal-to-noise (S/N) ratio after the test strategy was established.

The main aim of the investigation was to identify the process parameters which would optimize the yield strength and hardness of hot extruded specimen. The control factors and their levels are shown in Table 5.5.

Table 5.5 Control factors and their levels

S.No	Control factors	Level 1	Level 2	Level 3
1	Deformation temperature (°C)	450	500	550
2	Strain rate (s^{-1})	0.1	0.2	0.3

ANOVA is a statistical methodology for determining the degree of similarity or difference between two or more groups of data based on the comparison of common component's average value. Pareto ANOVA [326] is a simplified ANOVA method used to measure the importance of each process parameter in hot extrusion experiments. Pareto ANOVA is a quick and simple technique to analyze results of the parameter design. This method identifies the important process parameters and analyzes the percentage contribution of each parameter on different quality characteristics. The use of both Pareto ANOVA method and S/N ratio approach makes it less cumbersome to analyze the results and hence it takes less time to attain the conclusion [327].

CHAPTER 6

Results and Discussion

6.1 Sintering behaviour of Al-Cu-Mg P/M alloys

In order to produce components with good sinterability and enviable mechanical properties, it is essential to control the sintering process parameters such as die compaction pressure, addition of elemental powders, sintering temperature, atmosphere, peak temperature holding time and heating rate. Besides this, microstructure and phase transformation of materials, and the mechanical properties are also be controlled by the above mentioned parameters. So the initial studies of present work concentrated on sintering behavior of Al-Cu-Mg alloys.

6.1.1 Laboratory compaction trials

Initial studies of this work focused on the aspect ratio of billets and sintering response of the Al-Cu-Mg alloys highlighting the effect of temperature on dimensional change and mechanical properties. It is essential to understand the microstructural characterization during sintering in order to control the mechanical properties of Al alloys processed by P/M. 4% of Cu was chosen as the primary alloying element which increases the strength and hardness of Al up to a maximum of 6% due to its solubility effect [11]. Mg is the other alloying element as adding Mg to Al-Cu alloys accelerates age-hardening at room temperature and also disrupts the oxide layer formed around the Al particles. Trial and error method was applied to prepare all samples with 1 aspect ratio (Φ 15 × 15 mm) with different weights of powders and compaction pressure. The reason behind selecting one aspect ratio is that the smaller length to diameter ratio compacts produces constant dense products because of faster stress transfer between powder particles. All the green compacts were compacted by applying the recommended compaction pressures of 100 MPa to 450 MPa to the die assembly to achieve compacts with 1 aspect ratio.

6.1.2 Effects of sintering temperature and Mg content in Al-Cu P/M alloys

6.1.2.1 Metallographic investigation of sintered preforms

To evaluate the effects of sintering temperature, Al-Cu-Mg alloys with different compositions such as Al-4%Cu, Al-4%Cu-0.25%Mg, Al-4%Cu-0.5%Mg Al-4%Cu-0.75%Mg and Al-4%Cu-1%Mg were consolidated at various temperatures between 400 °C and 600 °C. A heating rate of 10 °C/min and 1 hour soaking time were maintained for all compositions. Sintered samples were subjected to metallographic examination. Fig. 6.1 shows the samples sintered at 550 °C with varying Mg content from 0-1 wt.%. Visual inspection shows that the sintered samples were free from surface defects and porosity and showed good sinterability. Fig. 6.2 shows the SEM images of all compositional samples sintered at 550 °C. SEM Microstructures of different compositions showed different constituents including α-Aluminum grains, residual porosity, an intergranular secondary phase and intermetallic precipitates such as θ-Al_2Cu and ω-Al_7Cu_2Fe phases which also can be seen in XRD analysis (Fig. 6.4). Mg content is beneficial for forming liquid phase on an earlier stage of sintering which removes the oxide layers and promotes the atomic diffusion of Cu in Al matrix. The thickness of grain boundary increased with increasing Mg content which causes intergranular fracture and lowers the mechanical properties. This phenomenon was observed in samples above 0.5% Mg content i.e., Fig. 6.2d and 6.2e. Excess amount of Mg can lead to swelling and pores formation in the sintered samples. Secondary phase formation increased by up to 0.5 wt.% addition of Mg and then decreased with increasing Mg content. These secondary phases were dissolved into the matrix due to the higher liquid formation in >0.5 Mg wt.% compositions (Fig. 6.2d and 6.2e). The rate of diffusivity of Cu in Al might have also been affected by Mg content above 0.5% Mg which leads to less shrinkage during sintering. The above mentioned types of analyses were also observed and reported by Azim Gokce et al. [319]. They showed that as little as about 0.5% Mg addition to Al-Cu alloys is effective in improving aging characteristics and in increasing the strength. Fig. 6.3 shows the optical micrographs of Al-4%Cu-0.5%Mg samples sintered at different temperatures such as 400 °C, 450 °C, 500 °C, 550 °C, and 600 °C. The levels of porosity decreased with increasing sintering temperature which can be seen in Fig. 6.3a to 6.3e. At 600 °C, appreciable shrinkage was observed but it was identified as over sintering. Bulging and coarsening of grains were observed in sample sintered at 600 °C. The same phenomenon was observed in different compositional samples sintered at these temperatures.

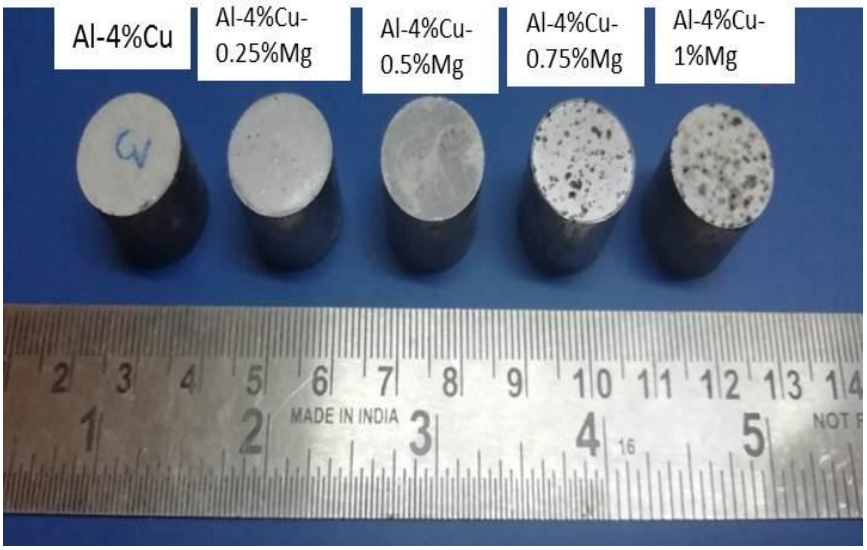

Fig 6.1 Samples of different compositions sintered at 550 °C

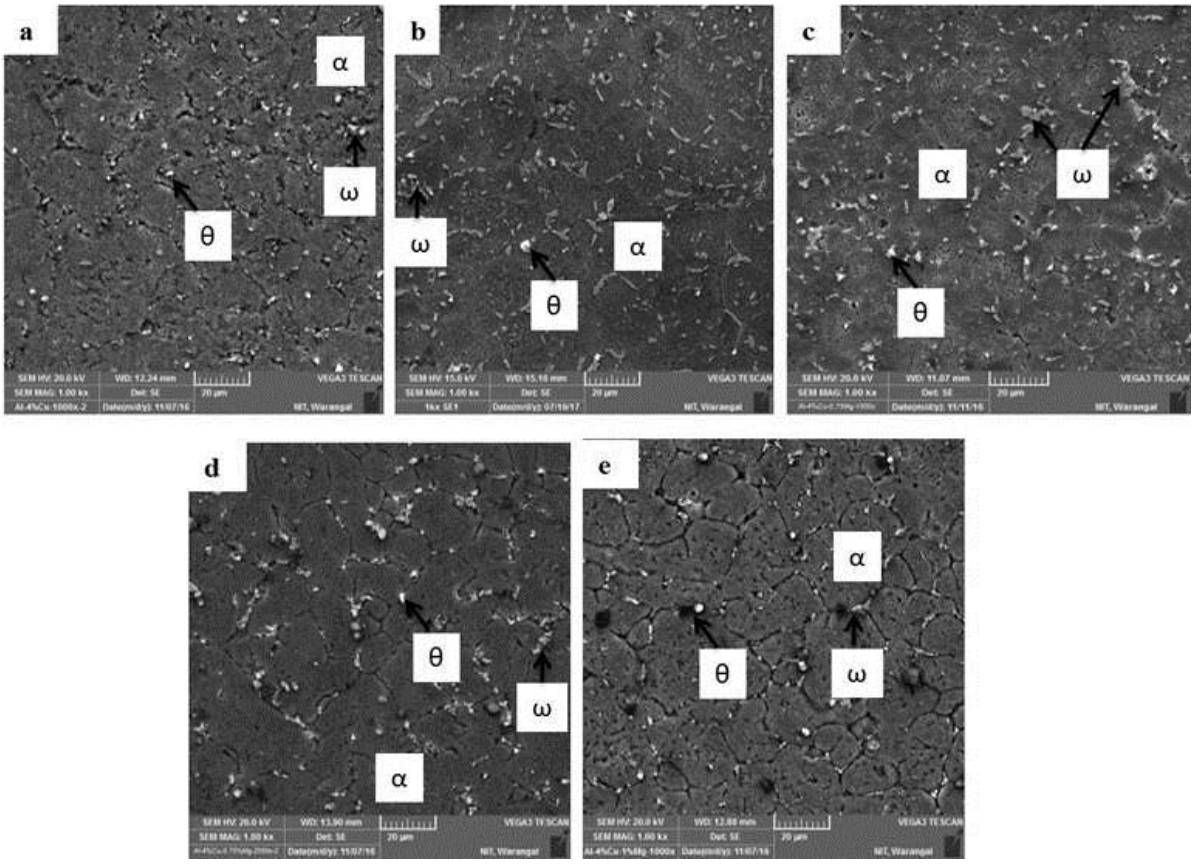

Fig. 6.2 SEM micrographs of all compositions sintered at 550 °C. a) Al4Cu, b) Al4Cu0.25Mg, c) Al4Cu0.5Mg, d) Al4Cu0.75Mg, e) Al4Cu1Mg (scale bar: 20 µm)

Metallography studies were followed by XRD analysis (Fig. 6.4) where the diffraction patterns showed the evidence of α-Al, Al_2Cu (θ) and Al_7Cu_2Fe (ω) phases which acts as precipitate strengthening agents. JCPDS cards for obtained Al cubic and tetragonal intermetallic compounds were 04-0787 for α-Al (space group: *Fm-3m*), 25-0012 for Al_2Cu (space group: *I4/mmm*), and 25-1121 for Al_7Cu_2Fe (space group: *P4/mnc*) which are in compliance with the literature data [328]. It is interesting to note that Mg as a trace alloying element resulted in its high diffusibility in Al during mixing stage. It was evident from SEM and XRD analysis that no individual Mg particles or peaks were identified in the analysis. No Mg phases were found because of low content and Mg is the first element that is incorporated into Al lattice. Cu peaks completely disappeared and it could be taken as a signal that all the quantity of this element had been employed to form Al_2Cu and Al_7Cu_2Fe as shown in SEM analysis. Al_2Cu phase formed uniformly in the matrix and along the grain boundaries which increases the mechanical properties of Al-Cu-Mg sintered preforms. The other secondary phase formed during the sintering process was Al_7Cu_2Fe (ω) which came from base Al and Cu powders during atomization process. This phase is also called dispersoid phase as it is utilized for the dispersoid strengthening of sintered and deformed materials. This phase was less distributed compared to the θ-Al_2Cu phase and formed as coarser (typically>5 μm) along the grain boundaries. Energy dispersive spectroscopy (EDS) elemental analyses were also used to examine the second phases formed in sintered samples and those were confirmed as Al_2Cu and Al_7Cu_2Fe (ω) as shown in Fig. 6.5. EDS analysis revealed that the secondary phases contain Al and Cu elements, and the atomic proportion of Al and Cu is approximately 2:1, which is very close to the Al_2Cu phase, as can be seen in Fig. 6.5b.

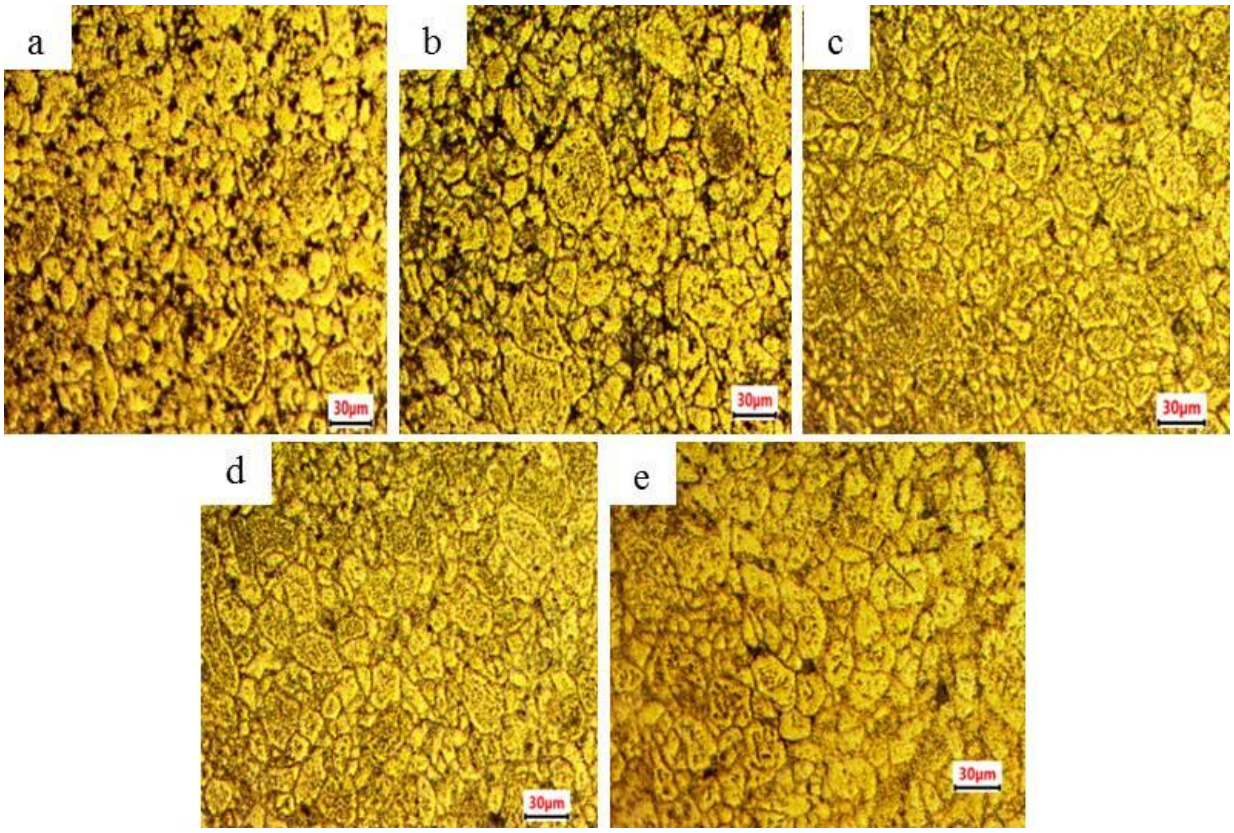

Fig. 6.3 Optical micrographs of Al4Cu0.5Mg samples sintered at a) 400 °C, b) 450 °C, c) 500 °C, d) 550 °C and e) 600 °C

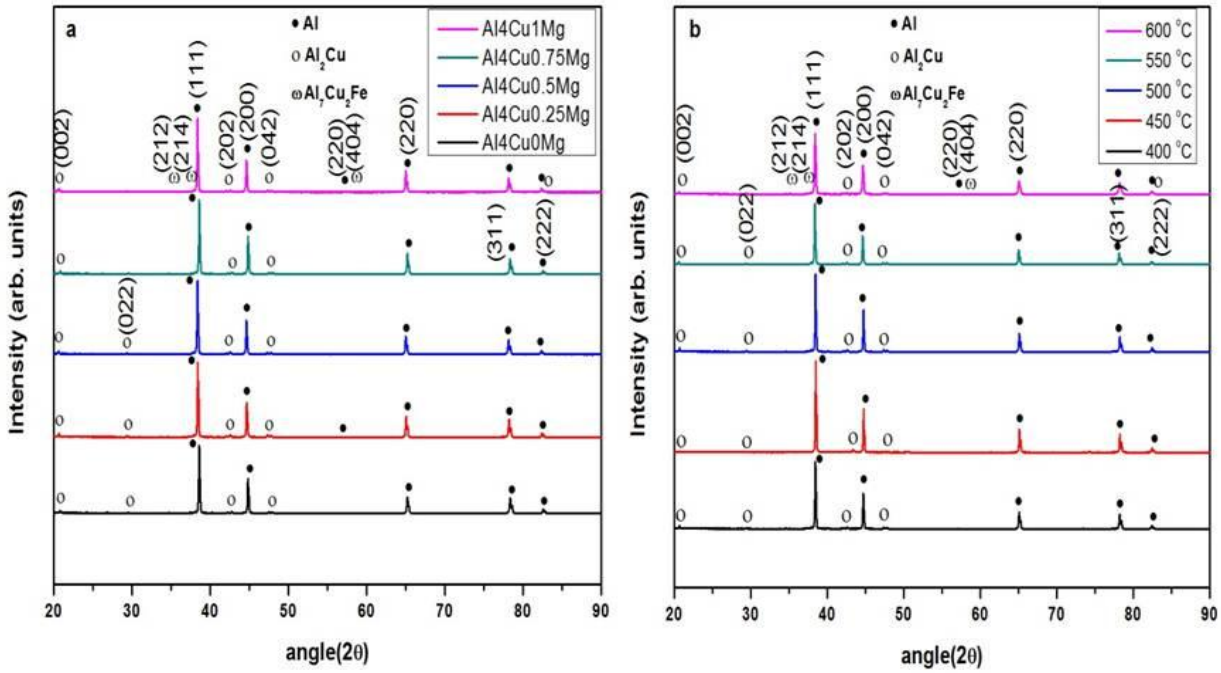

Fig. 6.4 XRD analysis of a) all compositions sintered at 550 °C and b) Al4%Cu0.5%Mg samples sintered at different temperatures from 400 °C to 600 °C

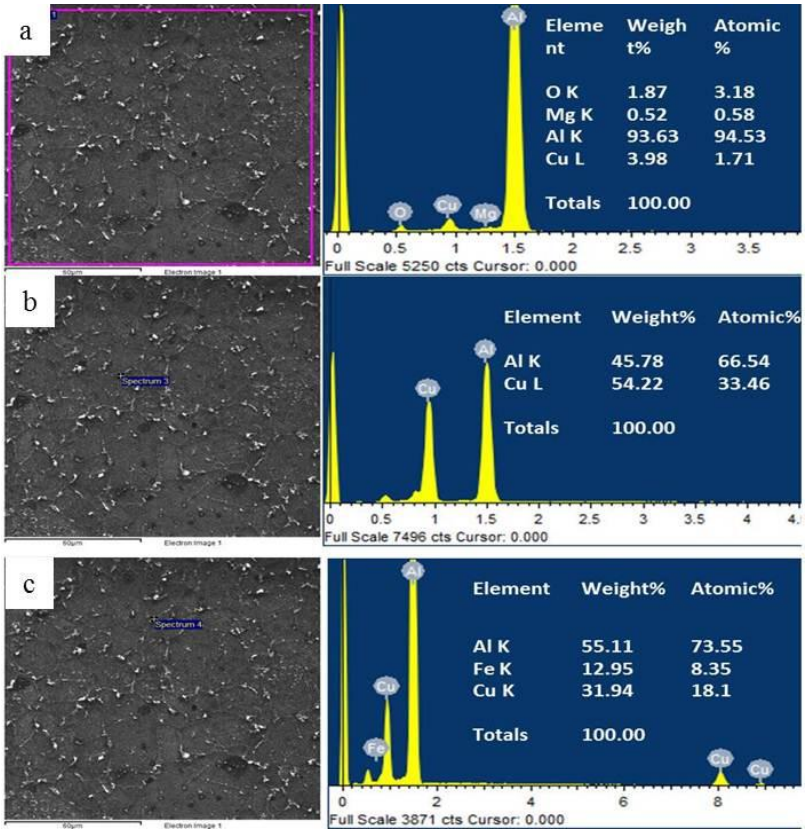

Fig. 6.5 EDS analysis of Al-4%Cu-0.5%Mg preform sintered at 550 °C

6.1.2.2 Dimensional changes of sintered preforms

It was noticed that, in terms of dimensional change, all compositions favored shrinkage. It is clearly seen from Fig. 6.6 that the length and diametric shrinkage increased with sintering temperature and there was no swelling. At 600 °C, appreciable shrinkage was observed but it was identified as over sintering and degradation of the samples. The effect of micro addition of Mg on the sintering behavior of Al alloys are shown in Fig. 6.6a and 6.6b. When Mg is added to Al powder, it causes shrinkage during sintering. The level of shrinkage increased with increase in Mg content and was shown to be maximum at 0.5% Mg. Though shrinkage was reduced with the addition of Mg in excess of 0.5 wt.% concentration, it affected the flowability of Cu and Al. The rate of diffusivity of Cu into Al might be affected by Mg above 0.5 wt.% addition which led to lower shrinkage compared to samples that had less than 0.5% Mg in the compositions.

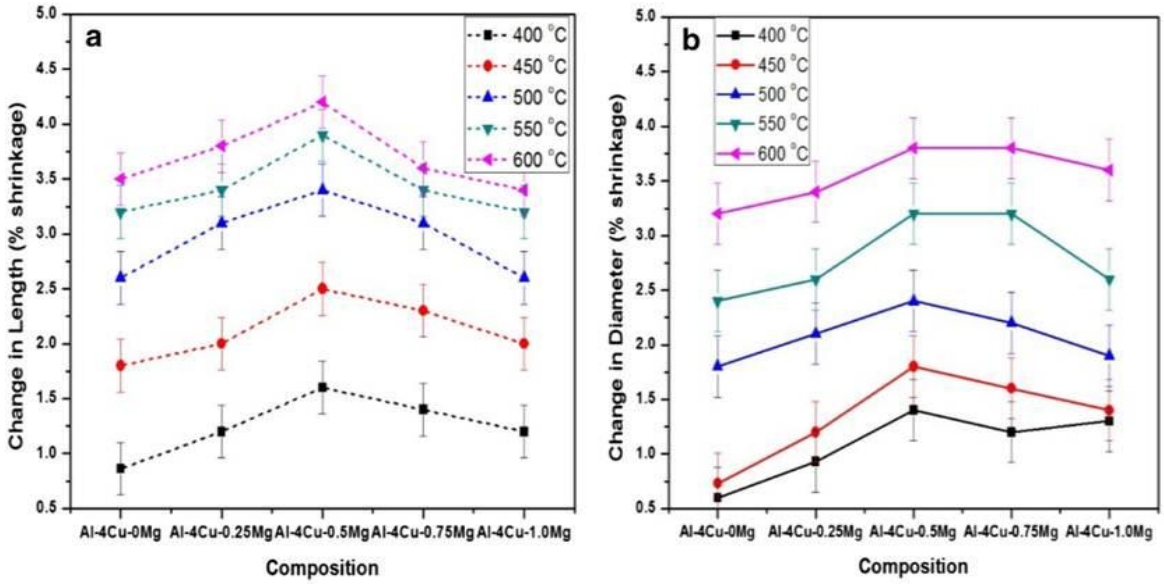

Fig. 6.6 Dimensional change after sintering, a) Change in length with composition for constant temperatures b) Change in diameter with composition for constant temperatures

6.1.2.3 Density of sintered samples

Sintering density can provide information about how well a material has sintered and the final density of materials depends on the shrinkage level. Sintering density trends of all compositions at different temperatures closely follow dimensional changes. The liquid phase produced by Mg content penetrates and diffuses into the oxide layers covering Al particles and improves the density of Al-alloys. The maximum sintered density of 2.63 g/cc or 95.38% of the theoretical density (theoretical density calculated as 2.76 g/cc) was observed at 550 °C in Al-4%Cu-0.5%Mg with comparable sintered densities of all other compositions sintered at 400 °C, 450 °C, 500 °C and 600 °C (Fig. 6.7). The density of sample sintered at 600 °C decreased due to bulging and degradation in sample.

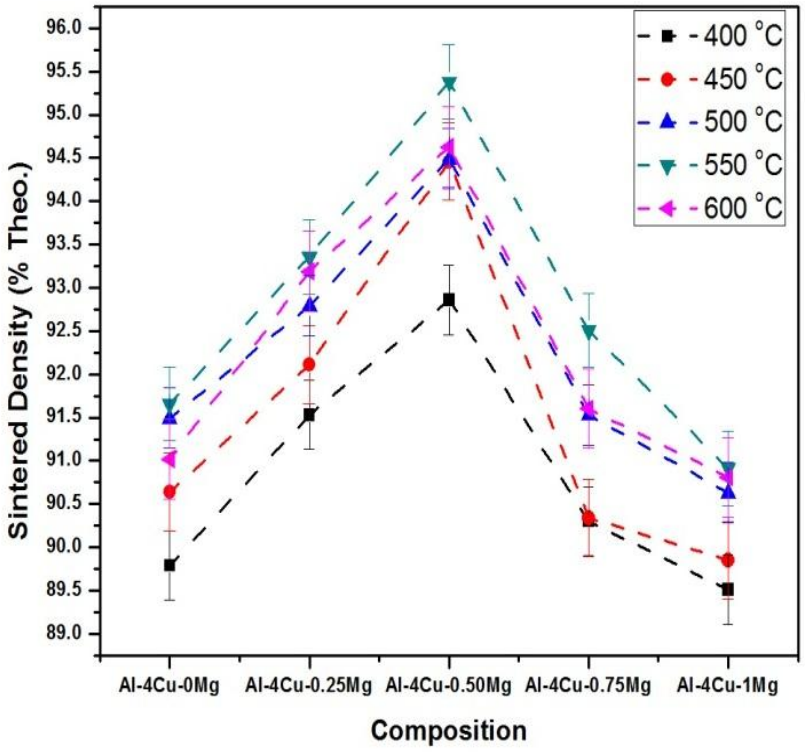

Fig. 6.7 Sintered densities as a function of composition at constant temperature

6.1.2.4 Hardness of sintered samples

Similar trends are also observed in the case of apparent hardness that reflected in the sintered density shown in Fig. 6.8. Hardness values of all compositional samples increased with increasing sintering temperature from 400 °C to 550 °C and then showed a decline at 600 °C which can be seen in Fig. 6.8. It was suspected to be the result of higher liquid formation and concomitant increase in the degree of microstructural coarsening which reduced hardness of Al-Cu-Mg P/M alloys sintered at 600 °C [329]. The second phase particles such as Al_2Cu and Al_7Cu_2Fe act as strengthening phases which are great carriers of plasticity and provoke to harden the material. Further use of 600 °C sintering temperature was avoided following of appreciable slumping in compacts. The hardness values were found to increase with the Mg content of up to 0.5%. Alloys above 0.5% Mg content showed a declining trend in hardness (Fig. 6.8), which was due to brittle and thicker grain boundaries, pores and less precipitate formation in SEM micrographs (Fig. 6.2). Many have reported that the oxide disrupting effect of Mg was maximized at < 1% Mg addition in Al-Cu alloys [92, 98, 330].

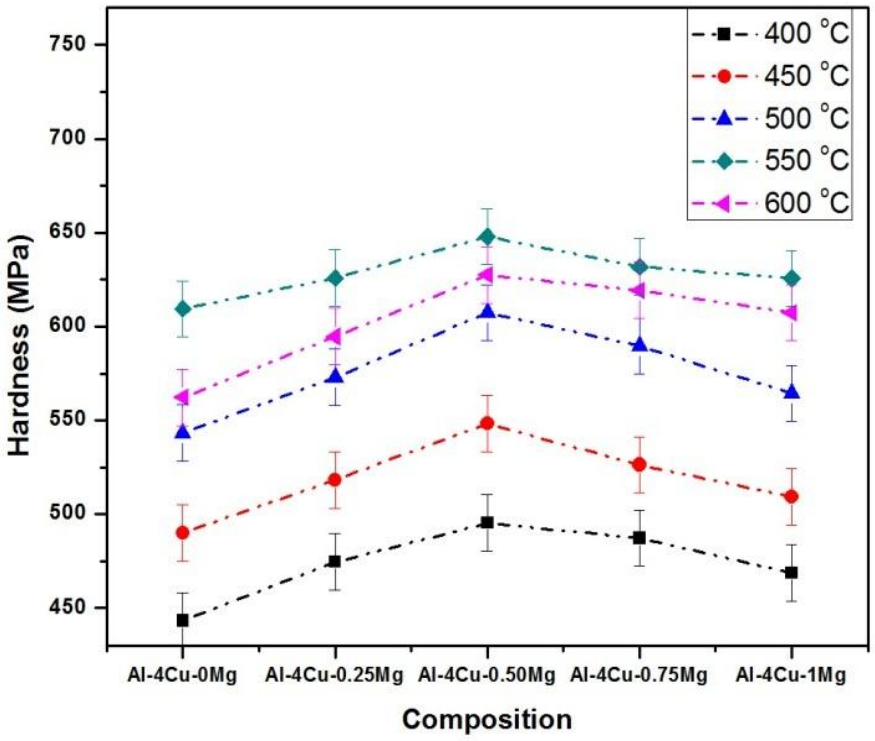

Fig. 6.8 Hardness plots as a function of composition at constant temperature

The 550 °C temperature and Al-4%Cu-0.5%Mg were optimized as sintering temperature and desired composition for all future studies which were confirmed by the balance of observed properties.

6.2 Semi-solid extrusion of sintered Al-Cu-Mg alloys

The purpose of this work was to study the deformation mechanism of aluminium alloy in the semi-solid state through experimentation. Semi solid metal forming is one such method in which favourable properties are obtained at high temperatures. The major advantages of semi-solid forming are flow stress reduction during shearing, reduced porosity, reduced operating temperature, low solidification shrinkage, and a minimal risk of hot tearing. As the mechanical behaviour and deformation mechanism of semi-solid metal is completely different from that of the solid state forming, it is necessary to investigate its nature at the semi-solid range. The final product of the semi-solid extrusion coexists between solidus and liquidus temperatures.

6.2.1 TG/DTA analysis for optimizing deformation temperatures

The TG/DTA analysis was used to identify the solidification interval and the solidus and liquidus temperatures of all compositions. The curve obtained by TG/DTA was used to calculate the solid-liquid fractions between solidus and liquidus temperature range. All the compositions sintered at optimum temperature i.e., 550 °C were used for TG/DTA analysis. According to the TG/DTA graph shown in Fig. 6.9, two endothermic reactions took place for Al-4%Cu alloy at 547.1 °C (solidus temperature) and 668.8 °C (liquidus temperature). When thermal analysis data was investigated with Al-Cu phase diagram shown in Fig. 6.10 (developed in Thermo-Calc software-2016b), it was observed that these two peaks were confirmed as the dislocation and reorientation of secondary phase (Cu) in Al matrix which is pointed as 'a' while the formation of the molten eutectics was pointed as 'b' in Fig. 6.10 above the solidus line for the Al-4%Cu alloy composition. As per the phase diagram, Al is continuously soluble in single liquid phase and the maximum solid solubility of Cu in Al is 5.65% at 548 °C. The eutectic (liquid) phase forms between Al and Al_2Cu [96]. At 550 °C, the formation of α-phase and liquid phase can be seen in Fig. 6.10. This liquid phase fills pores and results in high densification by capillary action. So, one should remember that the sintering temperature has to be above the solidus line to obtain sufficient density after sintering and no adverse effect can be seen if it is very low. 550 °C sintering temperature showed good microstructural properties due to the above mentioned reasons and the same temperature was optimized as sintering temperature for producing preforms for extrusion studies.

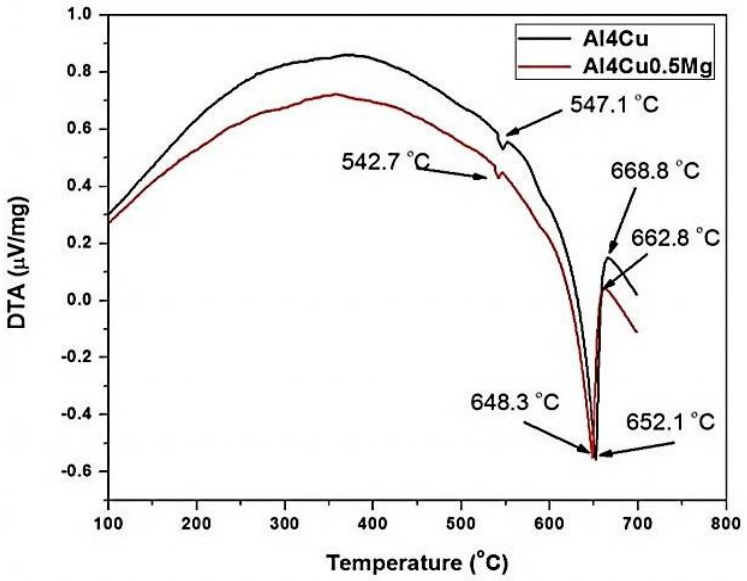

Fig. 6.9 Differential thermal analysis curves for Al4Cu and Al4Cu0.5Mg

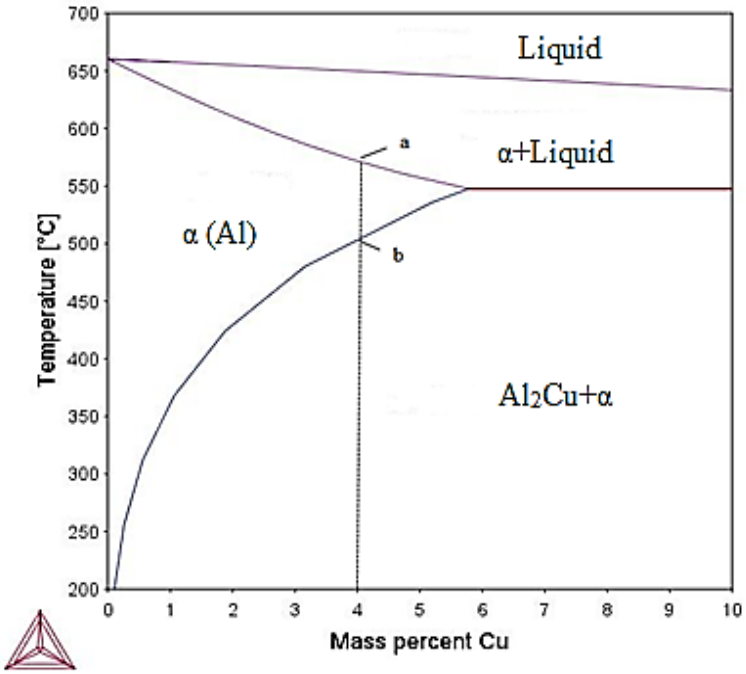

Fig. 6.10 Al-Cu binary phase diagram (rich side)

According to existing work [319], the liquid phase formed in Al-Cu alloy is transient and the formation temperature of this phase decreases with the addition of Mg content. So the formation of liquid phase for a given temperature increases with increasing Mg addition and causes thicker grain boundaries by filling the gaps between particles, which can be seen in Fig. 6.2.

Endothermic peaks of composition with 0.5% Mg (Fig. 6.9) sintered samples shifted to lower temperature compared with peaks attained for Al-4%Cu sintered sample. The dissolution temperature of Cu in Al matrix had reduced with the micro addition of Mg into Al-Cu alloy. TG/DTA analyses were helpful in identifying the sintering temperature of all alloys used in this work. It should be perceived from this work that the sintering temperature was just above the starting of the liquid phase. This was determined from the sintering behavior analyses since little amount of liquid formation was targeted to acquire sufficient densification.

Solidus and liquidus temperatures have to be determined to perform semi-solid extrusion at different temperatures. The deformation behavior of an alloy in semi-solid state is influenced by the percentage of solid fraction and the deformation temperature. The solidus temperature (542.7 °C) and liquidus temperature (662.8 °C) were identified for optimized Al-4%Cu-0.5%Mg alloy. The percentage of solid fraction at any given temperature within the solidification limit was determined using Scheil equation for Al-4%Cu-0.5%Mg alloy [114].

$$f_s = 1 - (T_s - T / T_s - T_l)^{(1/1-k)}$$

Where k = Partition coefficient = 0.17, T_s = Solidus temperature and T_l = Liquidus temperature

The working temperatures for the semi-solid extrusion test have been selected from solidus and liquidus temperatures so that the minimum to maximum solid fraction range can be achieved. The solid fractions of Al-4%Cu-0.5%Mg alloy at 550 °C, 575 °C and 600 °C were calculated as 0.96, 0.79 and 0.58 respectively from the Scheil equation. Between 623 and 631 °C, the sensitivity of the liquid fraction to temperature change was too high (>1.5 $°C^{-1}$) [331]. This was due to the difficulty in retaining a predetermined liquid fraction throughout the process. This is the reason working temperature below 600 °C was chosen for semi-solid extrusion.

The optimized compositional samples made of Al-4%Cu-0.5%Mg were prepared to study the densification and deformation properties. Semi-solid extrusion testes were carried out on optimized Al-4%Cu-0.5%Mg P/M preforms within the temperature range between solidus (542.7 °C) and liquidus (662.8 °C) temperatures derived from the TG/DTA analysis. Sintered preforms were prepared with an aspect ratio of 1 (φ 15 × 15 mm) for semi-solid extrusion. Extrusions of the preforms were conducted with extrusion ratios of 1.44, 2.55, and 4 and die

approach angles of 30°, 45°, and 60° for three determined working temperatures of 550 °C, 575 °C, and 600 °C, respectively.

6.2.2 Effect of deformation temperature/solid fraction during semi-solid extrusion

The solid and liquid fraction of the alloy is an important process condition and plays a vital role in producing higher quality products. The microstructural and mechanical properties of a material mainly depend on the amount of solid and liquid fractions during extrusion cycle. The percentage of solid and liquid fractions depends on the deformation temperature. The solid particles glide through the liquid matrix and make it easy to form due to the combination of solid and liquid particles during semi-solid extrusion. However, more liquid fraction than required results in liquid segregation in the workpiece. Fig. 6.11 shows the samples extruded at 550 °C, 575 °C, and 600 °C with die extrusion ratio of 4 and approach angle of 30°. Surface roughness, hot shortness and cracks on edges of extruded samples were increased with increasing deformation temperature due to increasing liquid fraction. High liquid fractions at the end of the extrusion process resulted in hot shortness and cracks propagation on walls and edges of the sample, which can be seen in Fig. 6.11a-6.11c. The samples extruded at 550 °C (Fig. 6.11a) showed no defects on walls and even at the edges as the samples were extruded with appropriate solid and liquid fractions.

Fig. 6.11 Semi-solid extruded samples at different temperature and die with same extrusion ratio and die approach angle; a) 550 ^{o}C, 4, 30^{o}, b) 575 ^{o}C, 4, 30^{o} and c) 600 ^{o}C, 4, 30^{o}

Fig. 6.12 shows the SEM microstructures of samples extruded at 550 °C, 575 °C, and 600 °C, respectively. The microstructures consist of equiaxed, elongated and fine grains. The mobility of grain boundaries during hot deformation increased with increasing deformation

temperature so that the equiaxed grain structure formation increased. The generation of dislocations, multiplication and rearrangement of dislocations can be decreased with increasing deformation temperatures. Therefore, the dislocation density resulting from work hardening and dynamic recovery was high at lower deformation temperature [211, 213]. Grain refinement in the microstructure was obtained due to the dynamic recrystallization (DRX). Clear description of DRX is presented in the coming sections. Distribution of secondary phases (Al_2Cu and Al_7Cu_2Fe) was observed even after deformation. These phases were uniformly distributed in matrix and along the grain boundaries which can improve the strength and hardness of extruded samples by precipitation hardening and dispersoid strengthening (Fig. 6.12). EDS elemental analysis and mapping were used to examine the second phase formed in extruded samples and these were confirmed as Al_2Cu and Al_7Cu_2Fe phases as shown in Fig. 6.13 and 6.14. Fig. 6.14a represents a SEM micrograph showing the distribution of secondary phases in the matrix and along the grain boundaries. Traces of Al, Cu, and Mg in the microstructure from elemental map scan are shown in Fig. 6.14b, c, and d, respectively. It can be seen that the secondary phase particles in the matrix and along the grain boundaries are associated with Al and Cu. EDS analysis (Fig. 6.13a and b) of semi-solid extruded samples revealed that the secondary phases contain Al and Cu elements, and the atomic proportion of elements is very close to the Al_2Cu and Al_7Cu_2Fe phase. Fig. 6.13a shows the EDS analysis of samples extruded using die with 45° die angle and 1.44 E.R at 550 °C and Fig. 6.13b shows the EDS analysis of samples extruded using die with 45° die angle and 4 E.R at 550 °C. Al_2Cu phase is very sensitive to elevated temperatures and easy to be cut by dislocations during extrusion at higher temperatures. Consequently, it was observed that the amount of Al_2Cu phase was reduced with increasing deformation temperature. The volume of secondary phases decreased with increasing deformation attributed to higher liquid fraction. The pinning effect of secondary phases on the grain boundaries was weakened by increasing deformation temperature, attributed to an increase in solubility of alloying elements in the matrix. This led to the dissolution of the secondary phase in the matrix, thereby merging and sliding of the grain boundaries. Dissolving of secondary particles in the matrix increased with increasing liquid fraction (temperature). The pinning effect of secondary phase particles is high at lower deformation temperature which can delay or restrict the grain growth during extrusion process, resulting in fine grain size.

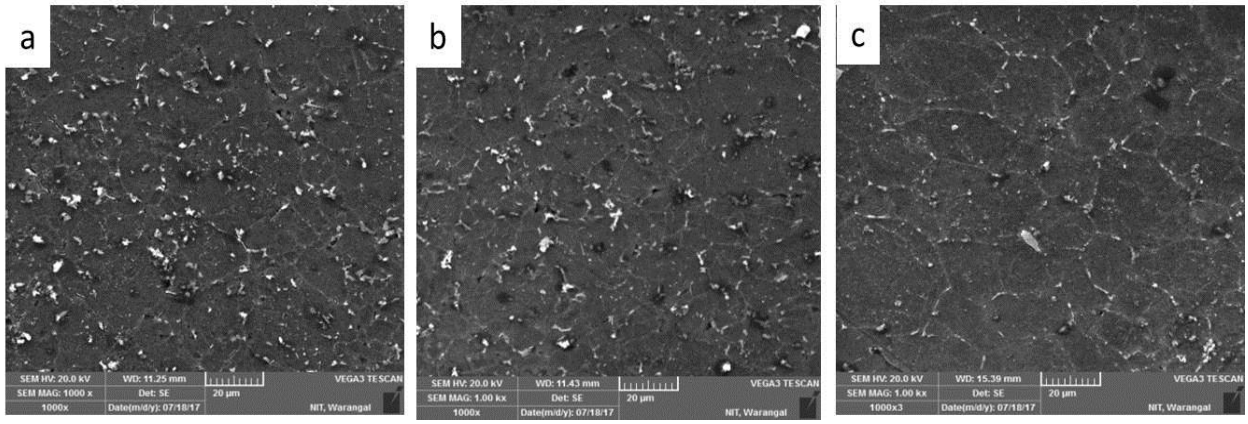

Fig. 6.12 SEM micrographs of semi-solid extruded samples at different temperature and die with same extrusion ratio and die approach angle; a) 550 ^{o}C, 4, 30^{o}, b) 575 ^{o}C, 4, 30^{o} and c) 600 ^{o}C, 4, 30^{o}

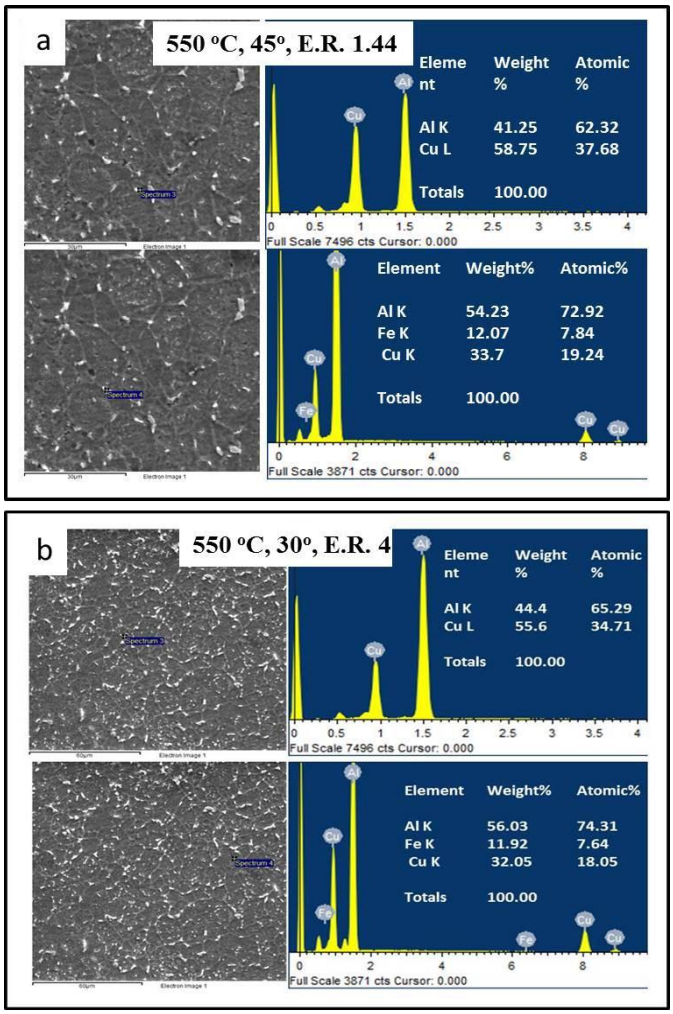

Fig. 6.13 EDS analysis of semi-solid extruded samples; a) 550 °C, 45°, 1.44 and b) 550 °C, 30°, 4

Fig. 6.15 shows the grain size distribution of samples extruded at 550 °C, 575 °C, and 600 °C, respectively. Microstructure coarsening increased with increasing deformation temperature so the grain size of the extruded samples increased with increasing deformation temperature which can be seen in Fig. 6.15a, 6.15b and 6.15c, respectively. The average grain size of samples deformed at 550 °C, 575 °C, and 600 °C were 7.77±3.2 µm, 8.48±4.1 µm, and 9.25±4.3 µm, respectively. The results indicated that the final average grain size of the semi-solid extruded samples increased with increasing deformation temperature irrespective of extrusion ratio and approach angle. The same type of results were observed for dies with other extrusion ratios and approach angles at 550 °C, 575 °C, and 600 °C temperatures, respectively. Irrespective of extrusion ratio and approach angle, the samples extruded at 550 °C were produced with good surface finish and refined grain structures with more volume of secondary phase particles.

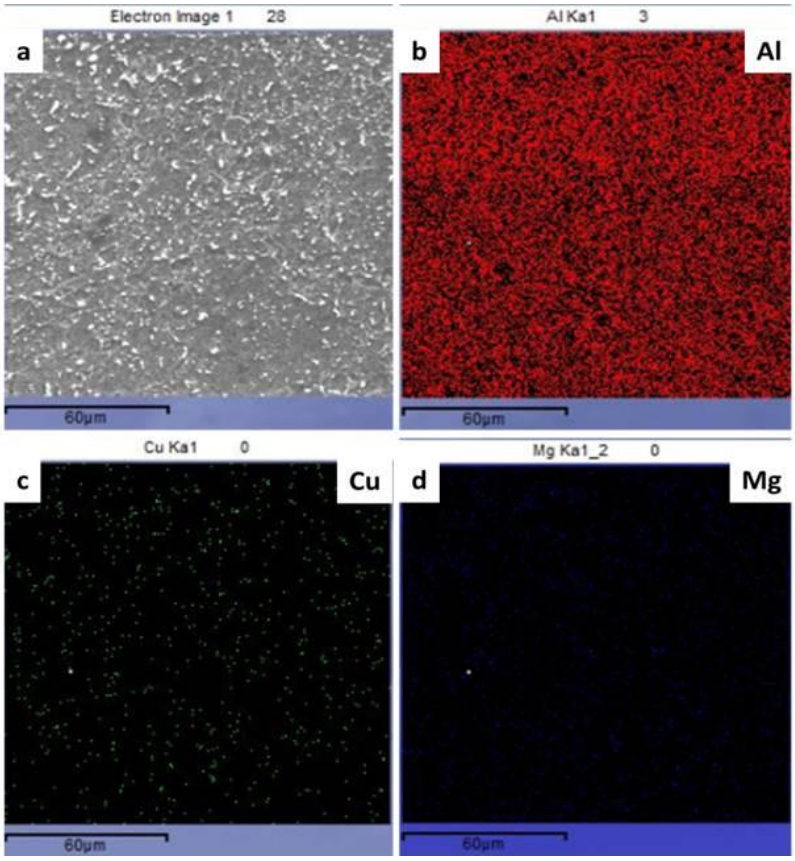

Fig. 6.14 Elemental analysis of an extruded sample at 550 °C and with E.R of 4 and die approach angle 30°; a) secondary electron micrograph, b) Al, c) Cu and d) Mg EDS maps of the SEM image shown in (a)

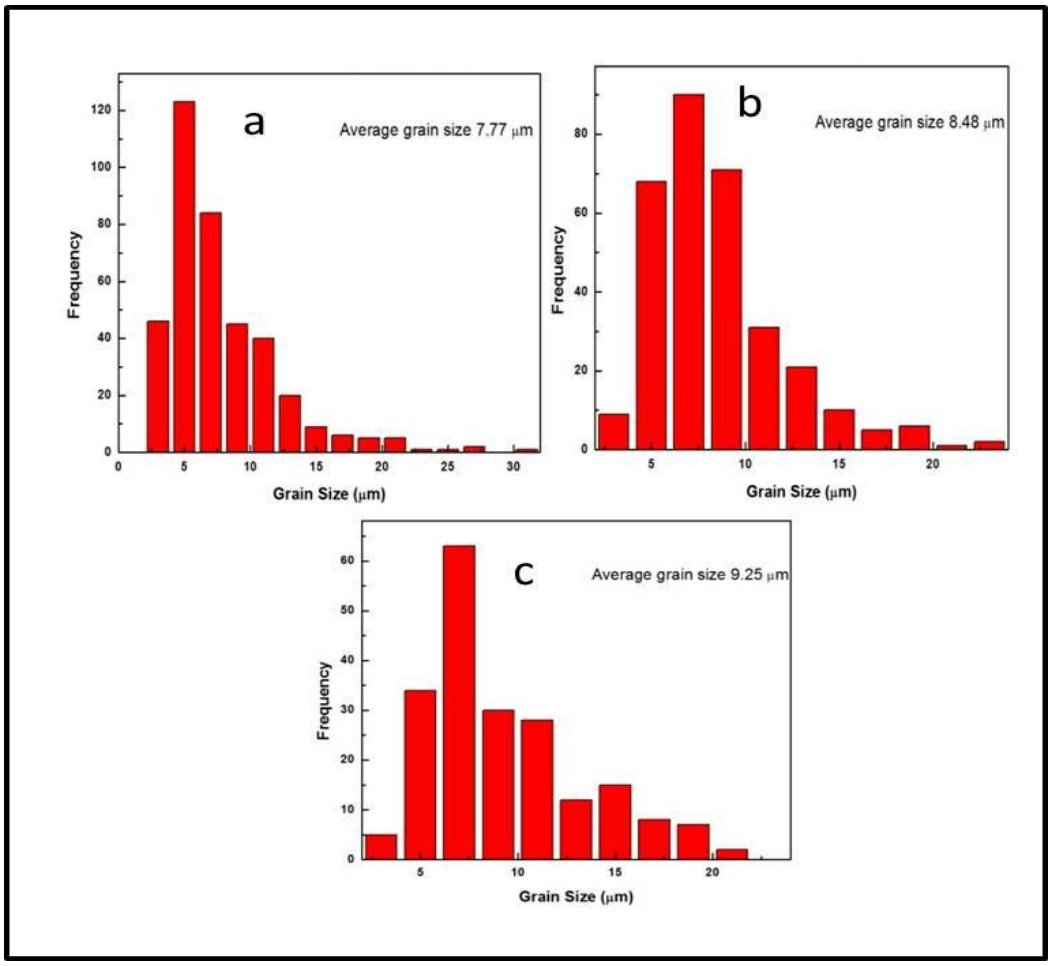

Fig. 6.15 Grain size distribution of semi-solid extruded samples at a) 550 °C b) 575 °C and c) 600 °C with fixed die approach angle of 30° and E.R. of 4

6.2.3 Effect of extrusion ratio

The extrusion ratio exercises enormous influence on the final components. Extrusion defects can be controlled by using optimum extrusion ratio. Fig. 6.16 shows the samples extruded with different extrusion ratios (E.R) such as 1.44, 2.25 and 4 with constant deformation temperature, 550 °C and a die approach angle of 30°. The extrudates diameter reduced while length increased with increasing E.R. The samples extruded at 550 °C were smooth and free of surface cracks and hot shortness. Smoothness increased with increasing extrusion ratio in samples extruded at 550 °C because of lower liquid fraction and lower liquid segregation. Surface cracks propagation was observed in samples extruded at 575 °C, and 600 °C even at lower extrusion ratio, which could be attributed to increasing fluidity/liquid segregation. Fig. 6.17 shows the microstructures of samples extruded at different extrusion ratios and with same temperature (i.e., 500 °C) and

approach angle (30°). The microstructures also consisted of α-Al matrix, Al_2Cu and Al_7Cu_2Fe phases. It was observed that the amount of elongated grains decreased with increasing E.R attributed to increasing deformation load with extrusion ratio (Fig. 6.17(a-c)). It was also observed that the average grain size decreased with increasing E.R (Fig. 6.18(a-c)). The distribution of grain size became more homogeneous with increasing E.R. With increasing E.R, uniform distribution of secondary phase particles was improved. The results indicated that the samples extruded at 4 E.R were given good microstructural results at all other parameters.

Fig. 6.16 Semi-solid extruded samples at different extrusion ratios and same die approach angle and temperature; a) 1.44, 30^{o,} 550 ^{o}C, b) 2.25, 30^{o} 550 ^{o}C, c) 4, 30^{o,} 550 ^{o}C

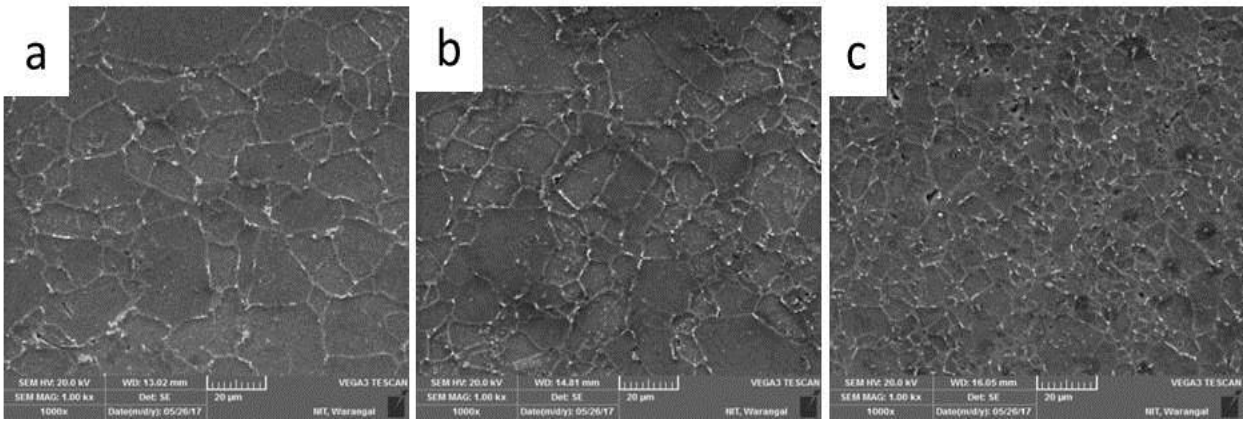

Fig. 6.17 SEM micrographs of semi-solid extruded samples at different extrusion ratios and same die approach angle and temperature; a) 1.44, 30^{o,} 550 ^{o}C, b) 2.25, 30^{o} 550 ^{o}C, c) 4, 30^{o,} 550 ^{o}C

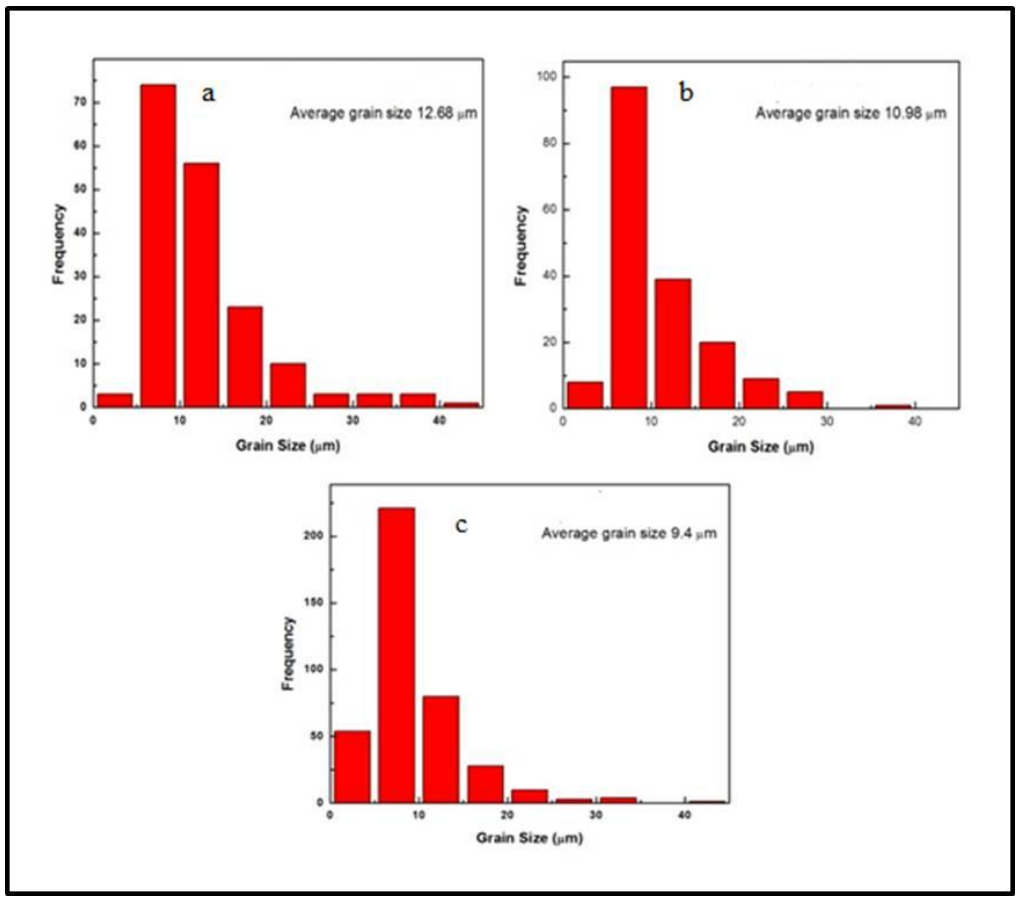

Fig. 6.18 Grain size distribution of semi-solid extruded samples at E.R. of a) 1.44 b) 2.25 and c) 4 with fixed die approach angle of 30° and extrusion temperature of 550 °C

6.2.4 Effect of die approach angle

The hot metal can slide down the die wall more easily when the metal approaches the die angle. Different die approach angles create varied frictional conditions at the die wall-metal interface. Shrinkage cavities can be reduced using a die with optimum guiding angle owing to the axial stress which changes from tensile to compressive in the central zone. Homogeneity in the structure can be increased by reducing dead metal zone using optimum die angle [332]. Fig. 6.19 shows the samples extruded with dies having extrusion angle of 30°, 45° and 60° and with the same deformation temperature (550 °C) and extrusion ratio (1.44). The load required for extrusion was decreased by increasing die angle. This was due to decreasing contact length between the die and billet which leads to lower frictional power losses with increasing die angle. Semi-solid extrusion with 30° die angle shown steady increase in extrusion load with ram displacement throughout the extrusion process. Small die angles give rise to the process of

adhesion with the die wall and preform, leading to higher load [152, 333]. Surface cracks and hot shortness defects increased with increasing die angle due to turbulent extrusion progression. The sample extruded at 60° die angle (Fig. 6.19c) was observed to have more cracks and higher roughness compared to other die angle extruded sample (Fig. 6.19 a and b). This was due to the frictional difference at the surface and central zone of preforms which led to differential velocities. Higher strain hardening might be other reason for the failure of samples at higher die angles [152]. The experimental results showed that extruding with lower angles was faster due to lower flow stress during hot extrusion process [334]. The shape and surface finish of the sample was affected by increasing the die angle from 30°-60° which lead to detrimental effect on mechanical properties.

Fig. 6.20 shows the microstructures of samples extruded with different die angles while keeping same extrusion ratio of 1.44 at 550 °C. Inhomogeneity in the microstructure was increased with increasing die angle (Fig. 6.20(a-c)). The deformation time increased with die angle which led to growth in the grain size and formation of elongated and coarse grains. The average grain size of the extruded samples increased with increasing die angle, shown in Fig. 6.21. Coarse and elongated grains formation was observed near the surface of samples extruded with 60° die angle (Fig. 20c). Dead metal zone formation increased with increasing die angle due to nonuniform friction. 30° extrusion die angle showed good results as compared to 45° and 60° irrespective of deformation temperature and E.R.

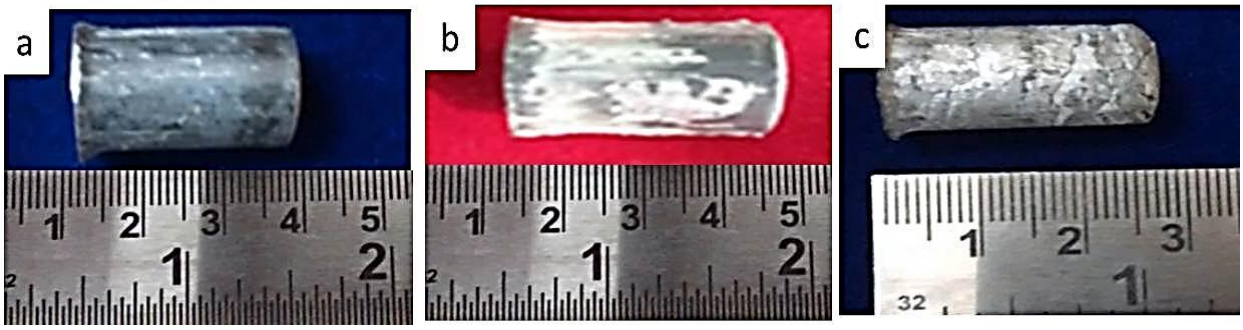

Fig. 6.19 Semi-solid extruded samples at different die approach angle and same extrusion ratio and deformation temperature; a) 30^{o}, 1.44, 550 ^{o}C, b) $45^{o,}$ 1.44, 550 ^{o}C and c) 60^{o} 1.44, 550 ^{o}C

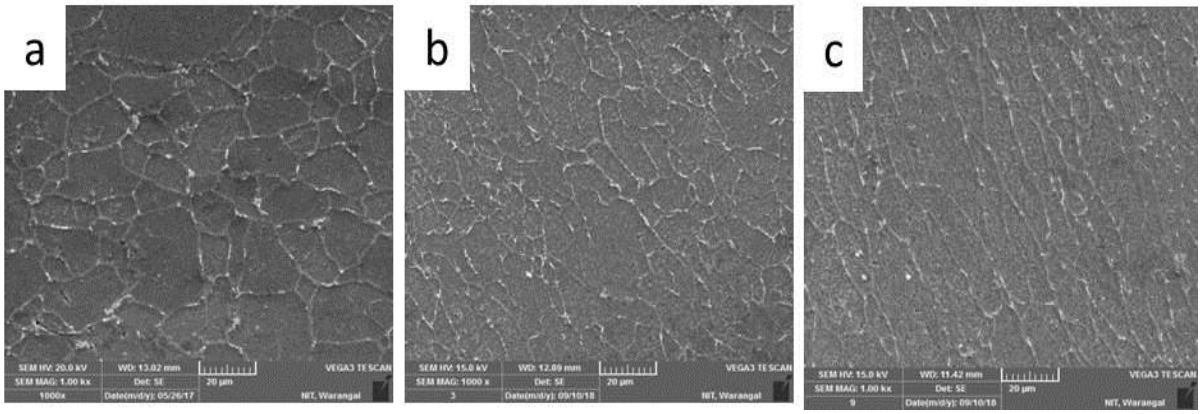

Fig. 6.20 Semi-solid extruded samples at different die approach angle and same extrusion ratio and deformation temperature; a) 30^{o}, 1.44, 550 ^{o}C, b) 45^{o,} 1.44, 550 ^{o}C and c) 60^{o} 1.44, 550 ^{o}C

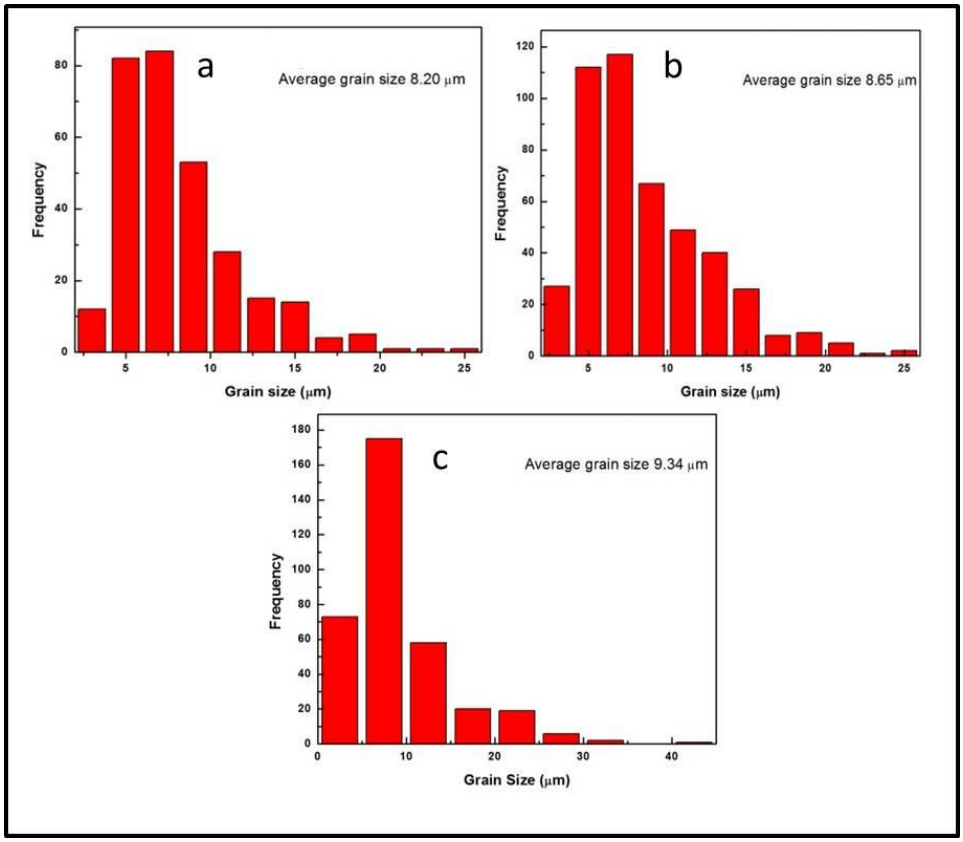

Fig. 6.21 Grain size distribution of extruded samples at different die approach angle of a) 30° b) 45° and c) 60° with fixed temperature 550 °C and E.R. of 4

6.2.5 XRD analyses of semi-solid extruded samples

XRD analyses were carried out in order to clarify the existence of different secondary phases in the microstructure of semi-solid extruded samples. XRD analyses of all samples with different

deformation conditions and die geometries are shown in Fig. 6.22. According to the XRD analyses, the only phases present in the samples were α-Al, θ-Al_2Cu and ω-Al_7Cu_2Fe. The equivalent crystallographic phases were also observed and marked in parentheses. The elemental Cu and Mg peaks were absent in all the cases as these elements were completely dissolved in the α-Al matrix during the primary mechanism of sintering. The quantity of θ phase decreased as the deformation temperature increased as it was dissolved in the matrix due to higher liquid fractions and easily cut through by dislocations at higher temperatures as shown in SEM results (Fig. 6.2).

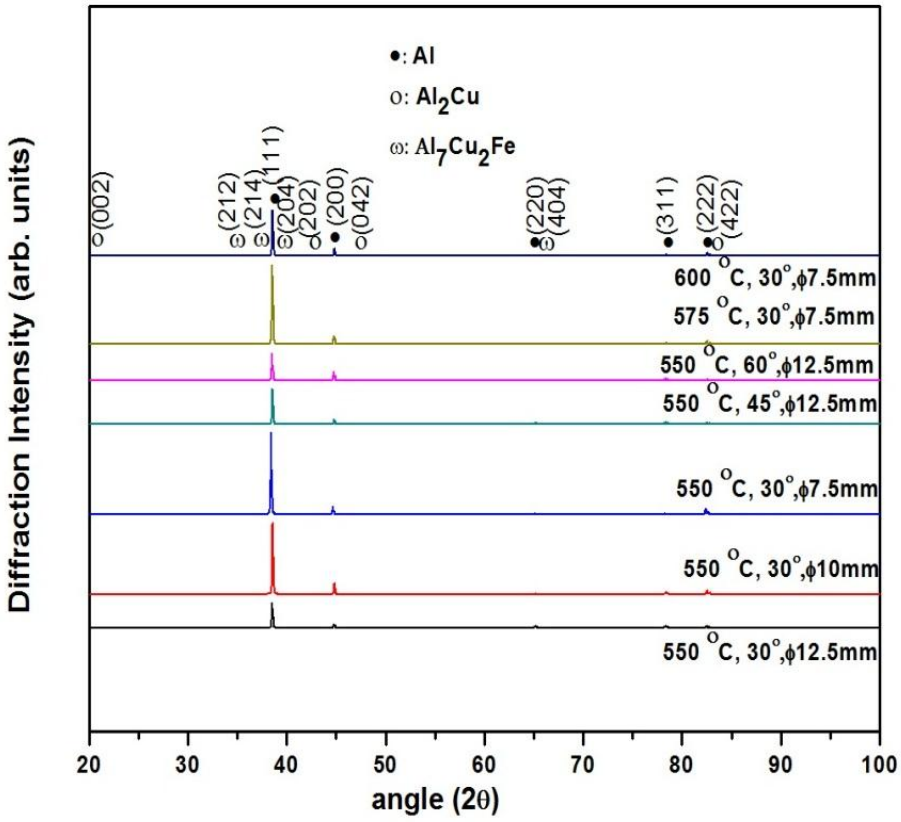

Fig. 6.22 XRD analyses of some of the semi-solid extruded samples at different parameters

6.2.6 Density and hardness of semi-solid extruded sample

The samples extruded at 575 °C and 600 °C showed lower density compared to the samples extruded at 550 °C (Fig. 6.23 and Fig. 6.24) because of crack propagation and hot shortness on the surface and edges of samples. The density of the semi-solid extruded samples decreased with increasing deformation temperature and die approach angle and decreasing E.R. The porosity decrease and uniform distribution of precipitates was observed after extrusion which led to

increase in the density of P/M Al-alloys. The results revealed a decrease in porosity and increase in grain refinement with increasing extrusion ratio and led to an increase in density (Fig. 6.23a). Samples extruded with 30° die angle showed higher densities at lower deformation temperatures (Fig. 6.24a).

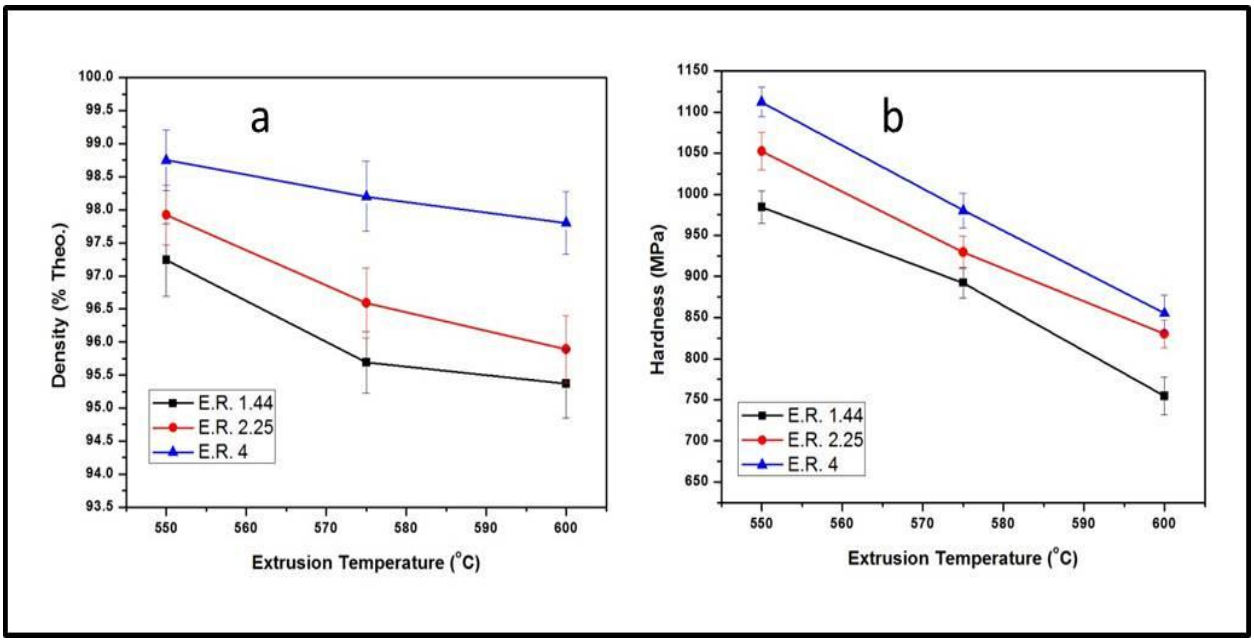

Fig. 6.23 Density and hardness of extruded samples at different temperatures and extrusion ratios with same approach angle 30°

The results of microhardness measurements are shown in Fig 6.23b and Fig. 6. 24b. It is seen that the hardness values after extrusion almost doubled from 647.85 MPa of sintered sample to 1121.9 MPa due to alloying, strain hardening and precipitation formation in the matrix and along the grain boundaries. Higher hardness could be attributed to the higher dislocation density in the samples due to thermal mismatch and difference in mechanical properties of alloying elements. This mismatch made plastic deformation more difficult by dislocation motion impedance, resulting in increasing the hardness. Hardness of extruded products could also be increased by uniform distribution of precipitates throughout the matrix and along the grain boundaries and due to strain hardening which impede the dislocation movement during extrusion. Microhardness increased with increasing extrusion ratio attributed to the grain refinement and uniform distribution of secondary phases (Fig. 6.23b). Hardness was reduced as the extrusion die angles enlarged from 30° to 60° (Fig. 6.24b) due to reduced contact length and

friction between preform and die, and also due to grain coarsening. Samples extruded at 550 °C showed higher hardness irrespective of die angle and E.R. Hardness reduced with increasing extrusion temperature due to grain coarsening and average grain size increment. 550 °C deformation temperature, 4 E.R and 30° die angle were optimized from the results as they showed good microstructure, density and hardness properties.

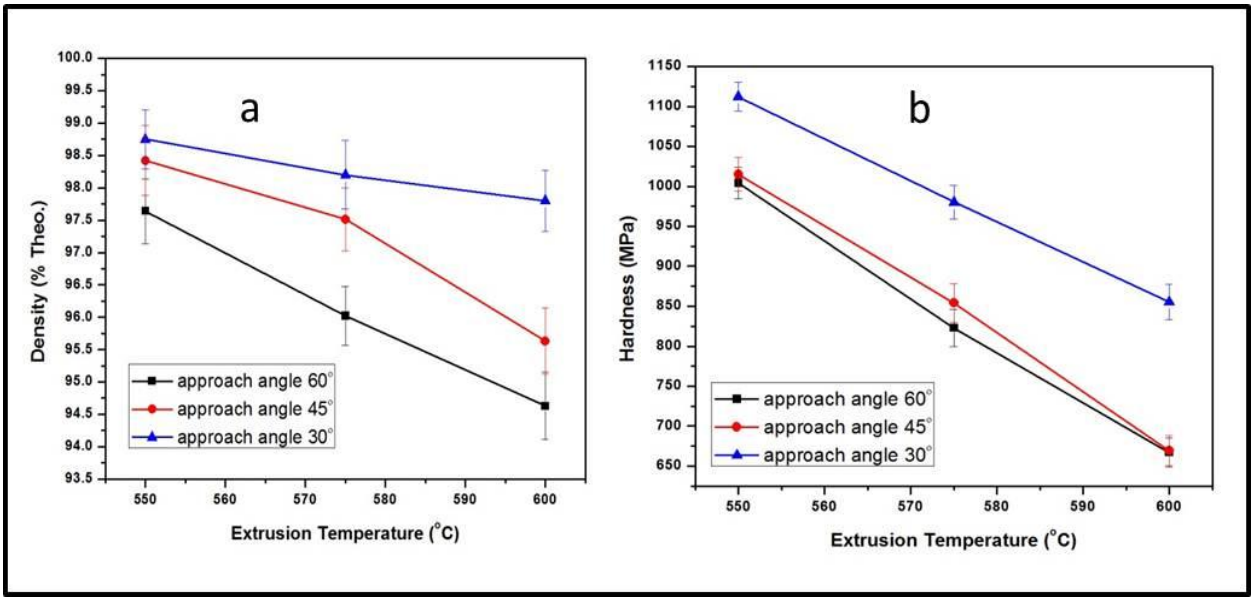

Fig. 6.24 Density and hardness of extruded samples at different temperatures and approach angles with same E.R. 4

6.2.7 Microstructural difference with in the sample during semi-solid extrusion

The temperature distribution within the material leads to varying physical and mechanical properties at different locations of the sample. So the extruded samples were demarcated into three regions: rear end, middle part and front end as shown in Fig. 6.25 to understand the temperature and microstructural changes that exist during the process of deformation. The microstructure features of demarcated semi-solid extruded Al alloys at three different temperatures are shown in the forming directions (Fig. 6.26, Fig. 6.27 and Fig. 6.28). Al_2Cu and Al_7Cu_2Fe phases were formed in the matrix and along the grain boundaries in all cases (Fig. 6.26 (d-f), Fig. 6.27 (d-f) and Fig. 6.28 (d-f)), which results in high strength and hardness. These phases started dissolving in the Al-matrix when the feedstock extruded above 550 °C which can be seen in SEM micrographs. The liquid phase was formed between Al and Al_2Cu because of

solid solubility of Cu in Al. This liquid is partly transient so that this could be seen only in few SEM micrographs of extruded alloys.

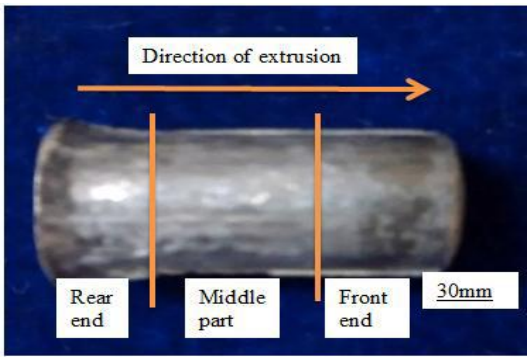

Fig. 6.25 Demarcation of sample for structural analysis

The optical micrographs of extruded samples are shown in Fig. 6.26 (a-c), Fig. 6.27 (a-c) and Fig. 6.28 (a-c) to distinguish the deformation behavior from front end to rear end of extruded sample at 550 °C, 575 °C and 600 °C. Liquid fraction increased with deformation temperature. It is interesting to notice that the deformation rate varied within the sample from front end to rear end because of change in liquid fraction during extrusion. Front end parts of all the samples extruded at 550 °C, 575 °C and 600 °C had little high liquid fraction and showed lower rates of deformation compared to other parts. Grains in the front end (first part of the extruded sample) were almost globular and this confirmed that the forming occurred in semi-solid state and with gliding of α-Al grains over one another. The eutectic phase fully penetrated into grain boundaries and two-third of the section of the samples featured with globular α-Al grains. On the other hand, the features in the rear end (last part of the extruded sample) were different and allowed the formation of fine and elongated grains. The α-Al solid solution matrix was dispersed with dark colored eutectic phase and seemed to be aligned in the direction of extrusion.

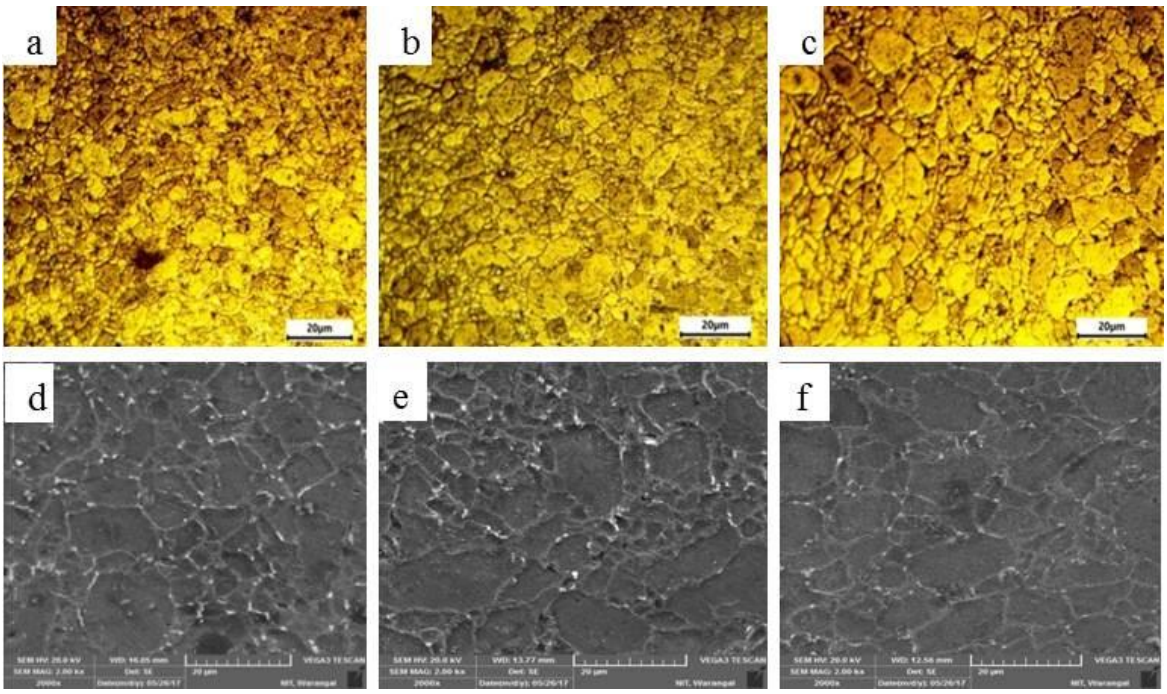

Fig. 6.26 Optical and SEM micrographs sample extruded at 550 °C with E.R of 4 and die angle of 30° a) and d) rear end, b) and e) middle part, c) and f) front end

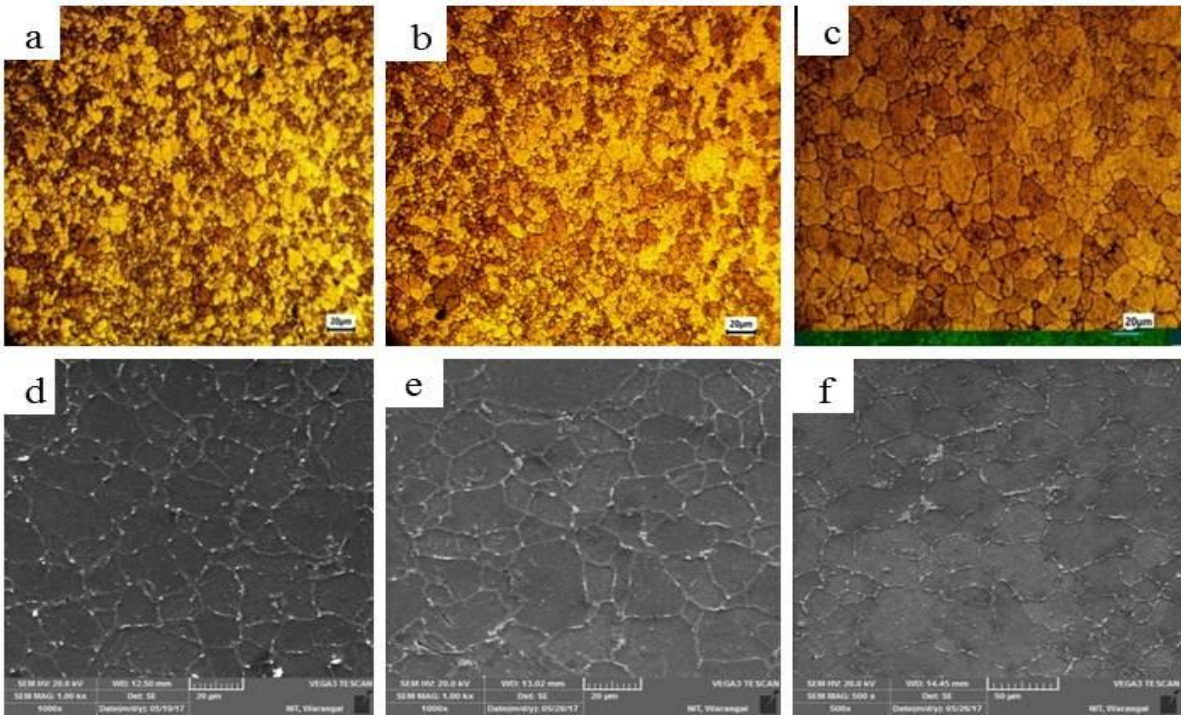

Fig. 6.27 Optical and SEM micrographs of sample extruded at 575 °C with E.R of 4 and die angle of 30° a) and d) rear end, b) and e) middle part, c) and f) front end

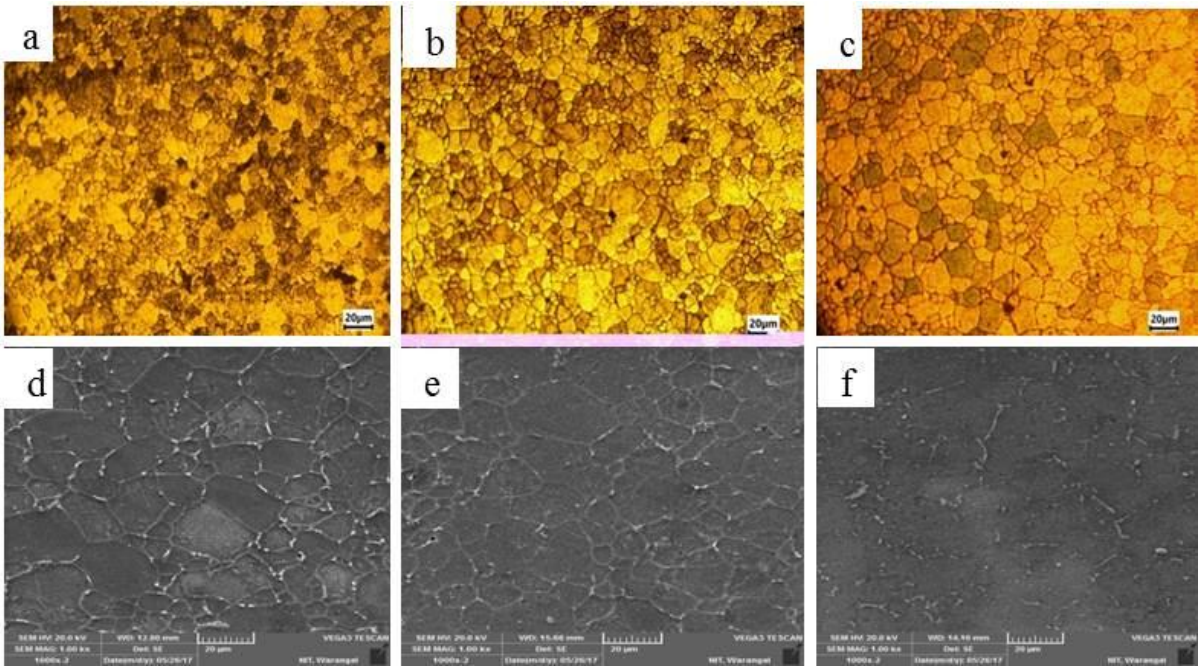

Fig. 6.28 Optical and SEM micrographs of sample extruded at 600 °C with E.R of 4 and die angle of 30° a) and d) rear end, b) and e) middle part, c) and f) front end

The non-presence of uniform grain structure and grain boundaries in the rear end samples imply that the liquid fraction was not sufficient enough to penetrate completely between the grain boundaries. This might be due to the temperature difference across the length of the sample during extrusion. The temperature drop in the rear end with time was due to heat exchange between the sample and the die. The rear end part of the extruded samples was seemingly not at adequate temperature and did not have sufficient liquid fraction to secure complete grain boundary wetting while it was passing into the forming zone. The rear end was drained of liquid whereas the liquid segregation and enrichment took place in the front end of the sample during extrusion. The rear end of all samples extruded at different temperatures experienced higher deformation because of low liquid fraction, as observed by the eutectic phase aligned in the direction of extrusion. The above mentioned types of analyses were also observed and reported by Birol et al. [113]. Homogeneity in microstructure increased with increasing temperature leading to formation of globular microstructure. Liquid segregation happens when the liquid medium flows towards the free surface of the die and initiates crack propagation on the sample surfaces during extrusion. This would be the prime reason for hot shortness and cracks propagation in some of the semi-solid extruded samples.

6.3 Hot extrusion of sintered Al-Cu-Mg alloys at various parameters

Extrusion defects like hot shortness and high surface roughness were observed in the semi-solid extruded rods above the 550 °C deformation temperature, diminishing the physical and mechanical properties. Extrusion ratio of 4 and an approach angle of 30° provided the best results in semi-solid extrusion process. To reduce these defects and increase the properties of extruded rods, the deformation temperature reduced to below 550 °C and used die having extrusion ratio of 4 and the approach angle of 30° for further studies on hot extrusion. Flow stress of sintered Al–Cu-Mg preforms also gets affected by the deformation conditions such as temperature, strain rate and initial preform relative density (IPRD) during the extrusion process. In addition, the IPRD of sintered Al-alloys may behave differently for various deformation conditions. Hence, it is necessary to study the flow behavior of aluminium and its alloys for a better understanding of metal forming processes. Very limited work is available which is related to hot extrusion behavior of Al-Cu-Mg sintered materials, considering the various IPRD and deformation conditions. Therefore, the main aim of this study was to estimate the effect of deformation temperature, strain rate, and IPRD on hot extrusion behavior to analyze the effect of IPRD on the hot deformation behavior, and to model and predict the flow stress of extruded samples using constitutive equations. Optimized composition comprising Al-4%Cu-0.5%Mg (theoretical density: 2.76 g/cc) green compacts was sintered at 550±10 °C to produce samples with an aspect ratio of one (Φ 15 × 15 mm) by trial and error method. Hot extrusion tests were performed at temperatures of 450 °C, 500 °C and 550 °C, strain rates of 0.1 s^{-1}, 0.2 s^{-1} and 0.3 s^{-1}, and IPRD of 70%, 80% and 90%. Some of the extruded samples with different extrusion conditions are shown in Fig. 6.29. Fig. 6.29a, b, and c show the samples extruded at 450 °C, 500 °C, and 550 °C with the same strain rate (0.1 s^{-1}). The liquid fraction in the samples increases with increasing deformation temperature [335]. All samples extruded at 450 °C, 500 °C and 550 °C (Fig. 6.29a, b and c) had shown a smooth surface without any cracks or shot shortness. But the bottom portion (first to extrude) of the samples extruded at 450 °C and 500 °C (Fig. 6.29a1 and b1) showed some cracks/fractures due to insufficient liquid fraction. The samples extruded at 550 °C showed no defects on edges and surfaces. The length of the extruded samples increased with increasing strain rate due to a reduction in deformation time (Fig. 6.29d and e). The length of the extruded samples was also decreased with decreasing IPRD due to high porosity at lower IPRD. Porosity in 70% IPRD samples was higher than that of 80% and 90%

IPRD samples. The length of 70% IPRD extruded samples was less compared to other IPRD extruded samples due to higher voids and blowholes in the sintered samples (Fig. 6.29f).

Fig. 6.29 Extruded samples at different temperatures and strain rates, a) 90% IPRD, 450 ^{o}C, 0.1 s^{-1} ; b) 90% IPRD, 500 ^{o}C, 0.1 s^{-1} ; c) 90% IPRD, 550 ^{o}C, 0.1 s^{-1}; d) 90% IPRD, 550 ^{o}C, 0.2 s^{-1}; e) 90% IPRD, 550 ^{o}C, 0.3 s^{-1}; f) 70% IPRD, 450 ^{o}C, 0.1 s^{-1}; g) 80% IPRD, 450 ^{o}C, 0.1 s^{-1}

6.3.1 True stress-true strain curves

Fig. 6.30 - Fig. 6.38 show the experimental true stress-strain plots for hot extrusion of Al-4Cu-0.5Mg sintered preforms under different temperatures, strain rates and IPRDs. True Stress and true strain curves were obtained during extrusion by data logger connected between the computer and hydraulic machine. It can be observed that the shape of true stress-true strain plots in hot extrusion tests was dependent on initial preform relative density (IPRD), deformation temperature and strain rates. Comparing these flow curves with one another, the peak flow stress (PFS) increased with decrease in deformation temperature and increase in strain rate or IPRD. This was due to the fact that the lower deformation temperature and higher strain rate provide less time for energy accumulation and less mobility of grain boundaries [197]. Flow stress of a material is a function of dislocation density [336]. The dislocation density is mainly affected by

the primary preform microstructure, deformation temperature and strain rate during hot deformation process. Before the peak flow stress is reached, the dislocation multiplication takes place drastically, and the WH prevails over the softening process. Consequently, the flow stress increases rapidly [197]. The flow stress increased as the strain rate increased which was due the increase in resistance offered by the material with increase in strain rate; hence a higher amount of load is required to deform the material. Every curve shown in Fig. 6.30-Fig. 6.38 exhibits PFS at a small value of strain and then remains constant or decreases gradually till it reaches high strain value, showing dynamic softening. Further, the experimental flow curves are composed of four different stages of deformation as seen in Fig. 6.39. Work Hardening (WH) is the deformation phenomena observed in the first stage (I) of deformation, where the flow stress rapidly increased to small strain values due to the faster rate of increase in dislocation generation, multiplication and accumulation and dislocation density [192, 193, 197]. It controls the behavior of true stress-strain curve before the onset of DRX. The flow curve transits from hardening to softening in second stage (II). In the third stage (III), the dynamic softening due to dynamic recovery (DRV) and dynamic recrystallization (DRX) occurs which reduces the WH effect. In the fourth stage (IV), two different types of plot variations can be observed as depicted by Quan et al. [337], (i) maintaining high PFS values which indicate the balance between WH and dynamic softening (450 °C, 500 °C and with all strain rates), (ii) flow stress drops continuously after reaching PFS where the dynamic softening dominates WH (550 °C and at all strain rates). WH, DRV and DRX play a vital role in microstructural changes of materials and their mechanical properties which have been explained in the later stages of this work. During plastic deformation, the work performed is the integral of stress and strain in the plastic deformation. The elimination or rearrangement of dislocations reduces the internal energy of the system and then there is a thermodynamic driving force for DRX process. Atomic diffusion takes place when the material is heated during deformation, reducing the number of dislocations and increasing the DRX grain formation.

A rapid rise in flow stress at initial stage of extrusion might be attributed to higher dislocation density as explained by Serajzadeh et al. [198]. Strain softening was observed at large strains in all the curves due to dynamic softening after reaching PFS. The dynamic softening phenomenon of material increases with increasing deformation temperature and decreasing strain rate [203]. The mobility of grain boundaries increases with softening of material and leads to

DRX. Increasing strain rate and decreasing deformation temperature prevent the occurrence of softening due to DRX and makes the deformed metals exhibit WH and DRV. It is concluded that work hardening and dynamic recovery were the dominant carriers at lower deformation temperatures and greater strain rates. In contrast, DRX was more perceptible at higher deformation temperatures and lower strain rates. The mobility of grain boundaries increased and accelerated the growth of DRX grain size with increasing deformation temperature and decreasing strain rate. Fig. 6.30 shows the relationship between true stress-true strain of sintered Al–4%Cu-0.5%Mg preforms with IPRD of 70% and strain rate of 0.1 s^{-1} for various temperatures 450 °C, 500 °C and 550 °C. It was observed that the flow stress decreased with increase in deformation temperature because of thermal softening. The same behavior was observed for other extruded samples irrespective of strain rates and IPRD of sintered Al–4%Cu-0.5%Mg preforms as shown in Fig. 6.30–Fig. 6.38. Irrespective of deformation temperature and strain rate, the flow stress increased with increasing IPRD due to dislocation decrement with increasing IPRD (Fig. 6.34-Fig. 6.38). Deformation difficulties increased with increasing IPRD and hence increased the load required to deform the preform.

The same behavior was observed in other IPRD of 80% and 90% preforms as shown in Fig. 6.33 – Fig. 6.38, respectively. It was noticed that the peak flow stress increased with increasing IPRD irrespective of the deformation temperature and strain rate attributed to decrease in dislocation motion with increasing IPRD, leading to increase in the deformation difficulties of preforms. Hence, the required load to deform the preform increased with increasing IPRD.

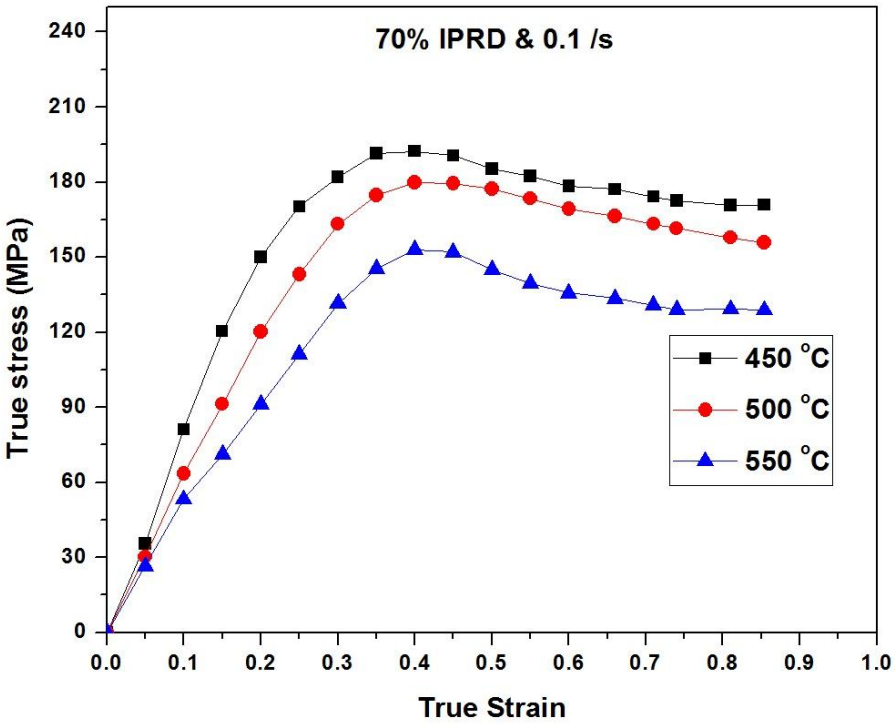

Fig. 6.30 True stress-true strain curves of P/M processed Al–4%Cu-0.5%Mg preforms during hot extrusion with 70% IPRD at strain rate of 0.1 s^{-1}

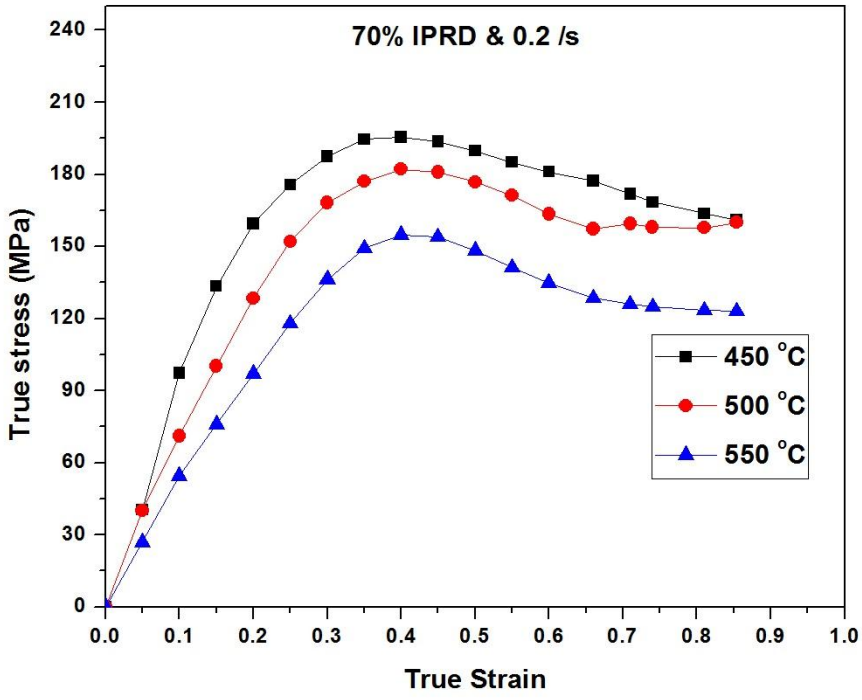

Fig. 6.31 True stress-true strain curves of P/M processed Al–4%Cu-0.5%Mg preforms during hot extrusion with 70% IPRD at strain rate of 0.2 s^{-1}

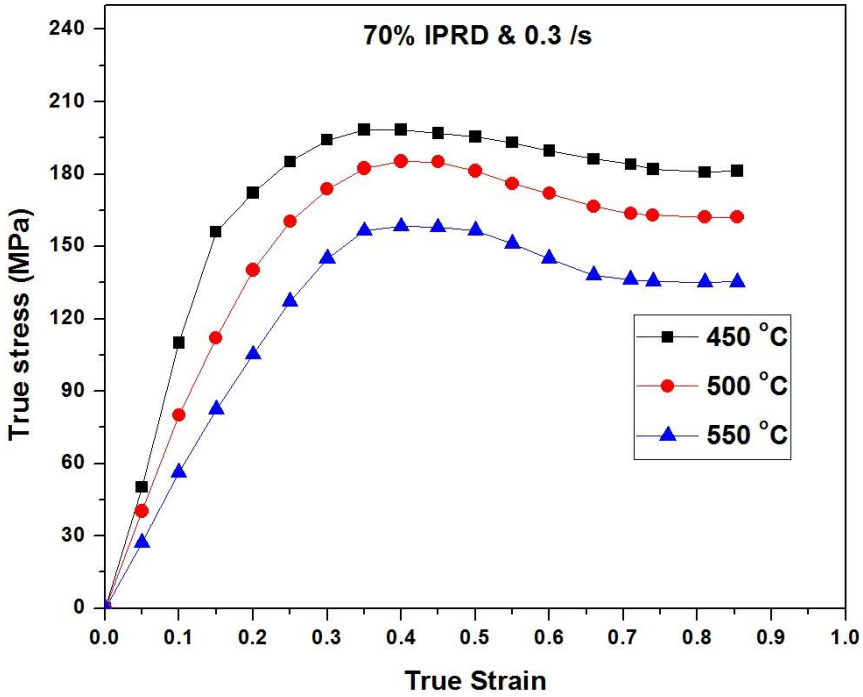

Fig. 6.32 True stress-true strain curves of P/M processed Al–4%Cu-0.5%Mg preforms during hot extrusion with 70% IPRD at strain rate of 0.3 s^{-1}

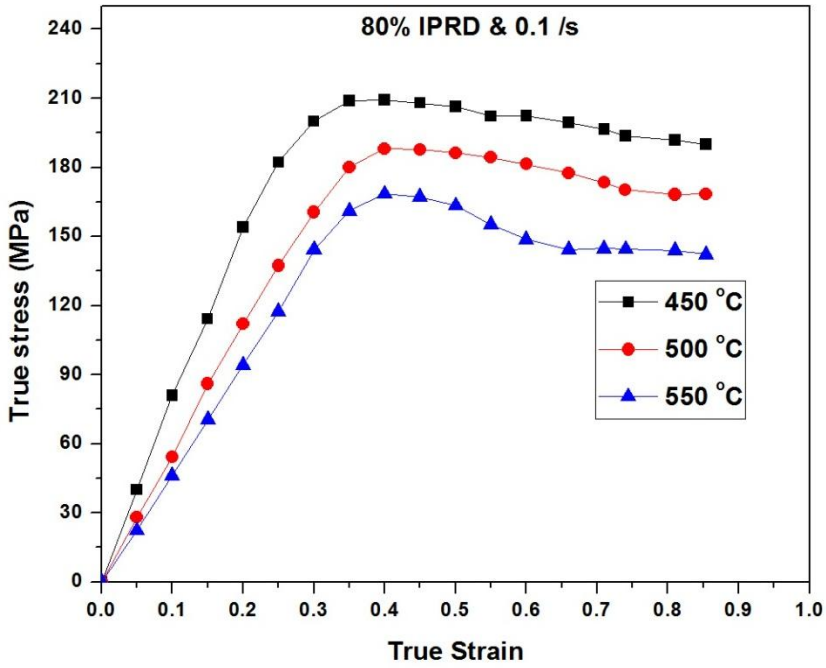

Fig. 6.33 True stress-true strain curves of P/M processed Al–4%Cu-0.5%Mg preforms during hot extrusion with 80% IPRD at strain rate of 0.1 s^{-1}

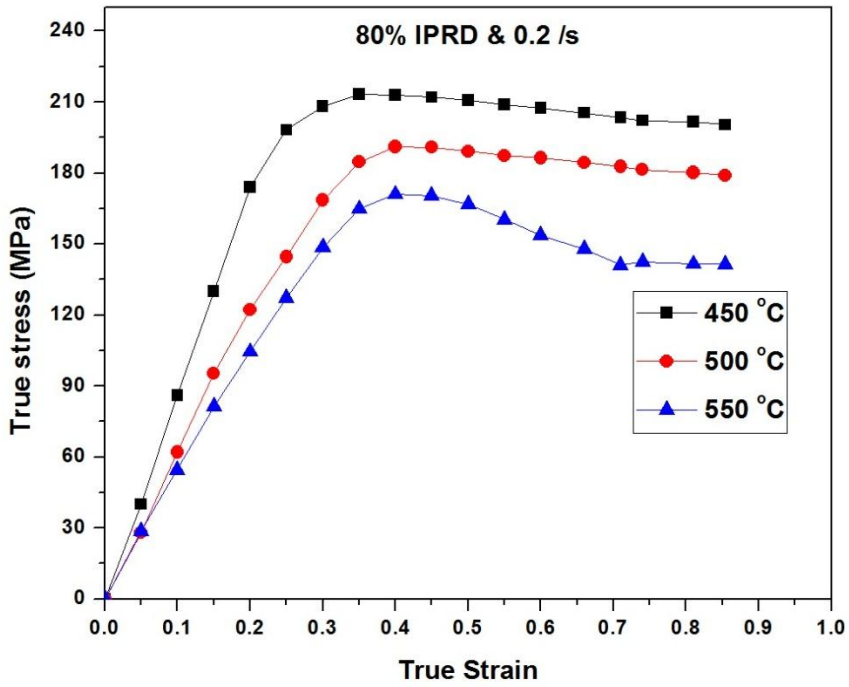

Fig. 6.34 True stress-true strain curves of P/M processed Al–4%Cu-0.5%Mg preforms during hot extrusion with 80% IPRD at strain rate of 0.2 s^{-1}

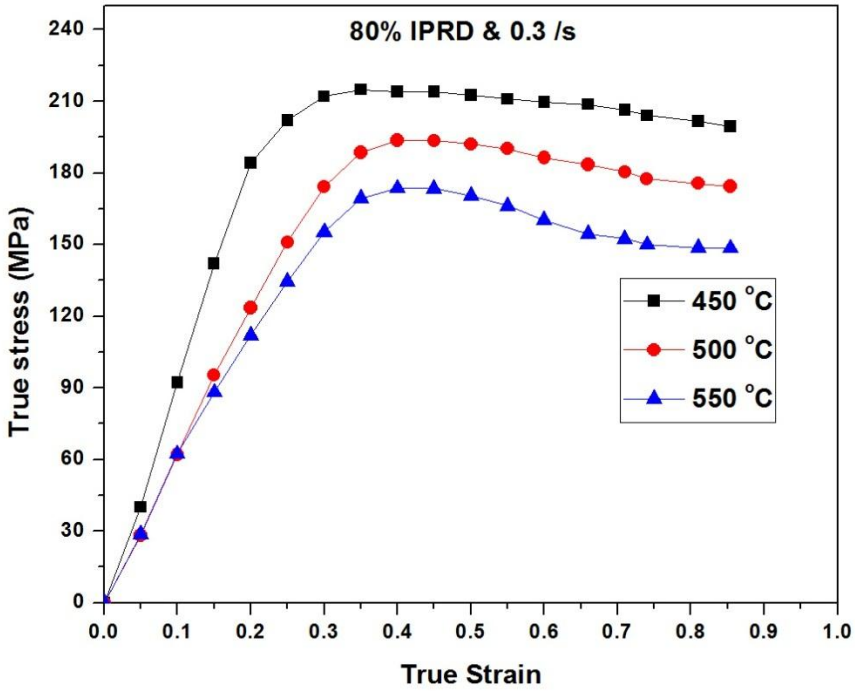

Fig. 6.35 True stress-true strain curves of P/M processed Al–4%Cu-0.5%Mg preforms during hot extrusion with 80% IPRD at strain rate of 0.3 s^{-1}

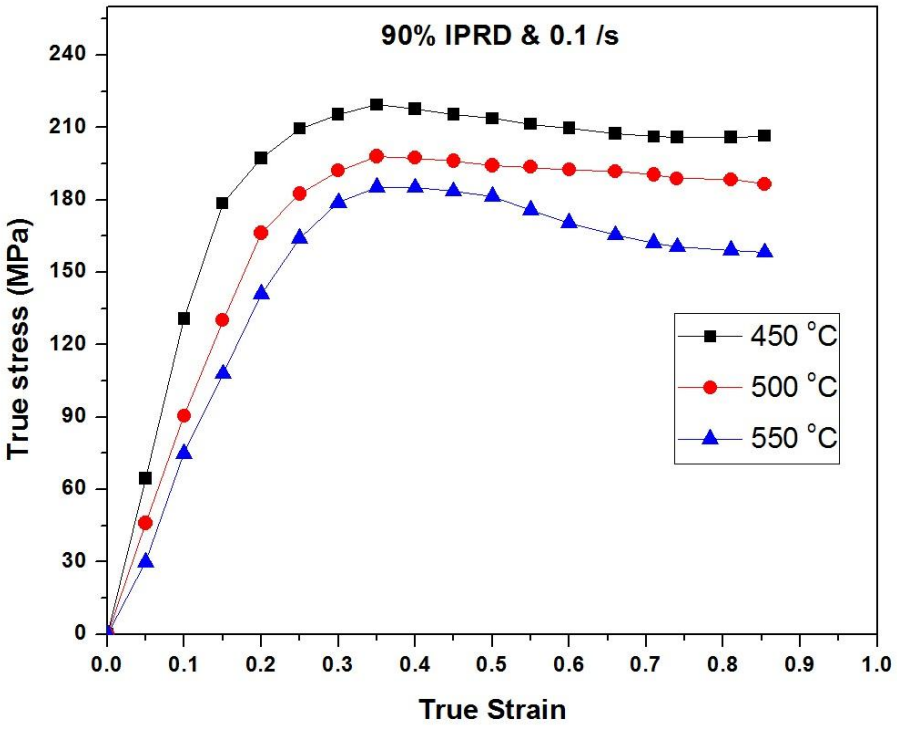

Fig. 6.36 True stress-true strain curves of P/M processed Al–4%Cu-0.5%Mg preforms during hot extrusion with 90% IPRD at strain rate of 0.1 s^{-1}

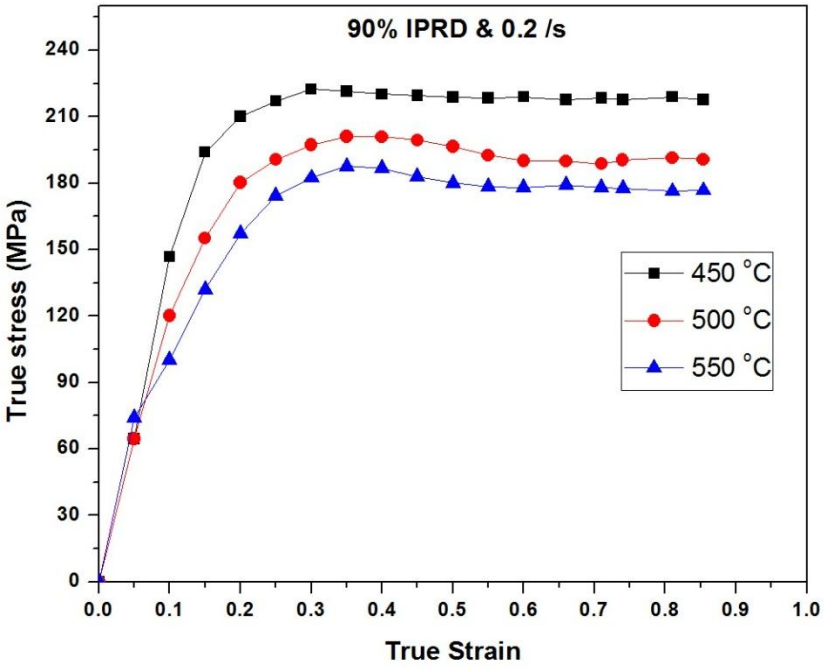

Fig. 6.37 True stress-true strain curves of P/M processed Al–4%Cu-0.5%Mg preforms during hot extrusion with 90% IPRD at strain rate of 0.2 s^{-1}

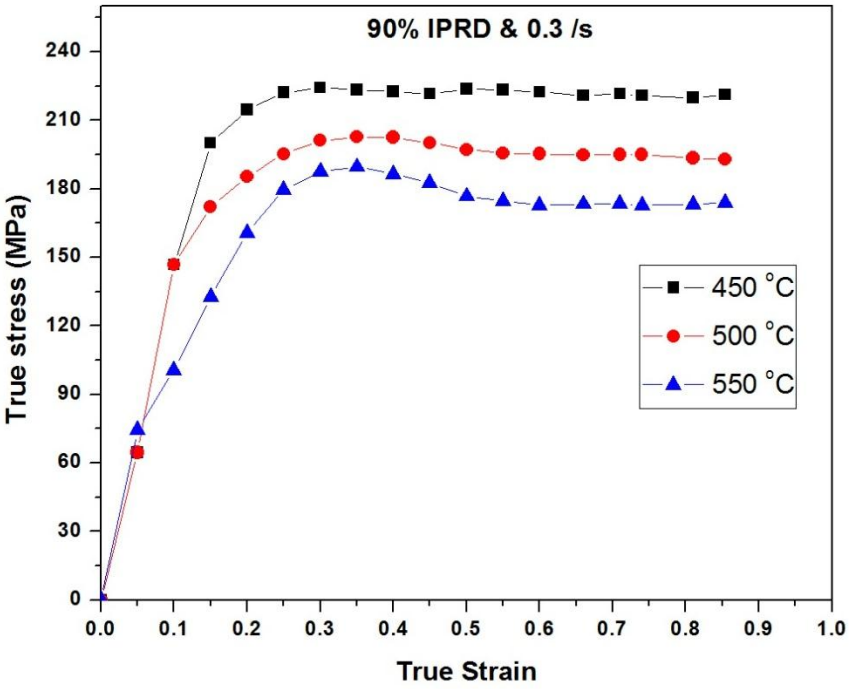

Fig. 6.38 True stress-true strain curves of P/M processed Al–4%Cu-0.5%Mg preforms during hot extrusion with 90% IPRD at strain rate of 0.2 s^{-1}

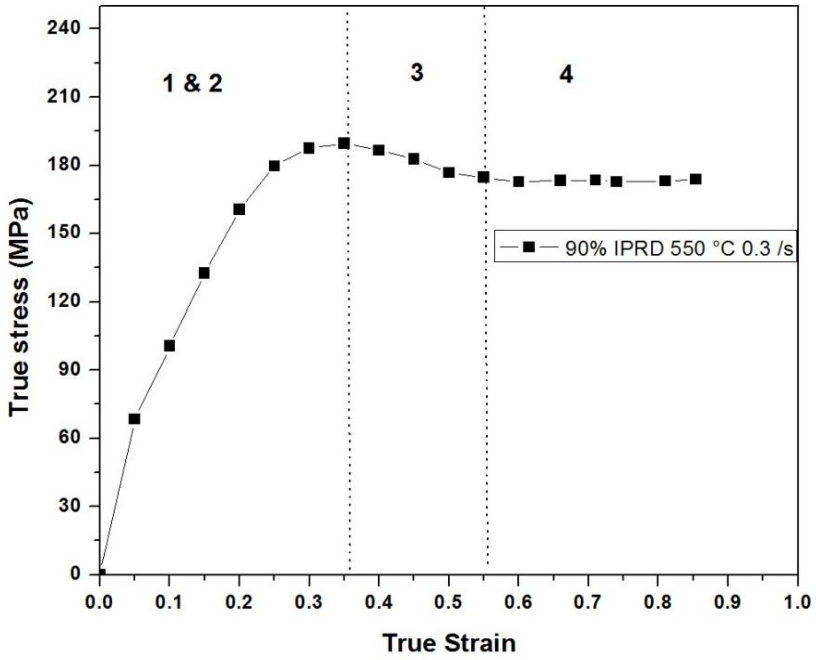

Fig. 6.39 Different deformation stages during hot extrusion (90% IPRD sample extruded at 550 °C and 0.3 s^{-1})

6.3.2 X-Ray difractrometry (XRD) analysis of hot extruded samples

XRD analyses were carried out in order to confirm the existence of different second phases in the hot extruded samples. XRD analyses of all hot extruded samples with different deformation conditions such as deformation temperature (450 °C, 500 °C and 550 °C), strain rate (0.1 s^{-1}, 0.2 s^{-1} and 0.3 s^{-1}) and IPRDs (70%, 80% and 90%) are shown in Fig. 6.40-Fig. 6.42. According to XRD analyses, the phases present in the samples are α-Al, θ-Al_2Cu and ω-Al_7Cu_2Fe. JCPDS cards obtained for Al cubic and tetragonal intermetallic compounds are the same as that written in section 6.1.2.1 (XRD analysis of sintered preforms). The equivalent crystallographic phases were also observed and marked in parentheses. The elemental Cu and Mg peaks are absent in all the cases as these elements were completely dissolved in the α-Al matrix during the primary mechanism of sintering. The XRD results indicate that the quantity of θ phase decreased with increasing deformation temperature and decreasing strain rate. IPRD of deformed samples did not affect the formation of secondary phases. The strength and hardness of deformed materials increase with fine distribution of above-mentioned phases among matrix and along the grain boundaries.

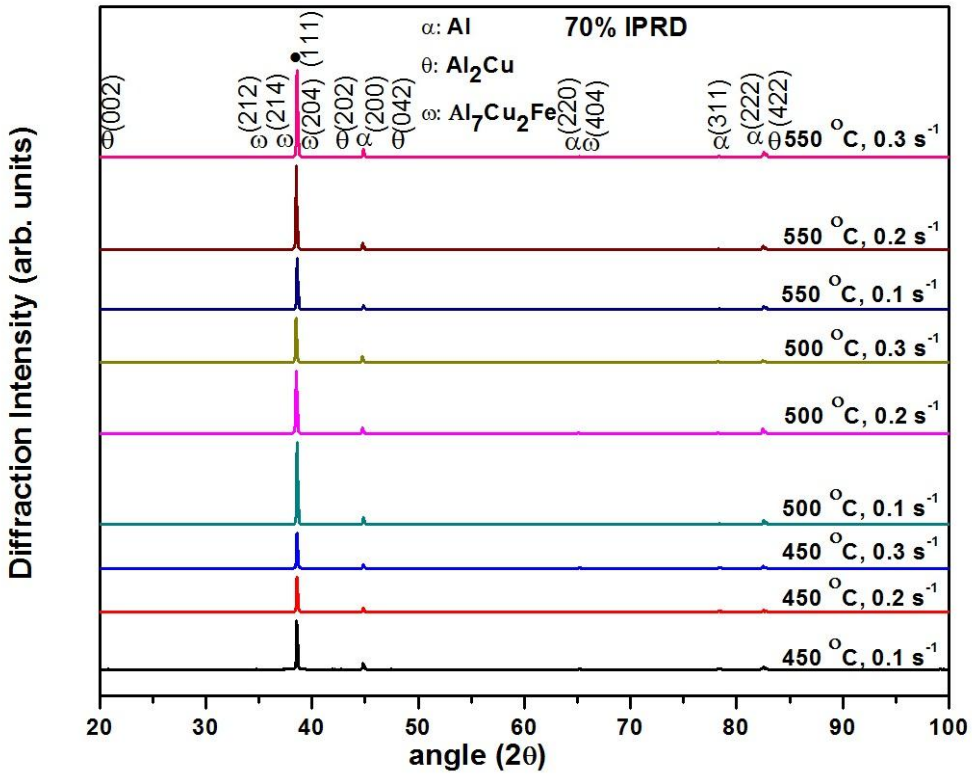

Fig. 6.40 XRD patterns of 70% IPRD samples extruded at different deformation temperatures and strain rate

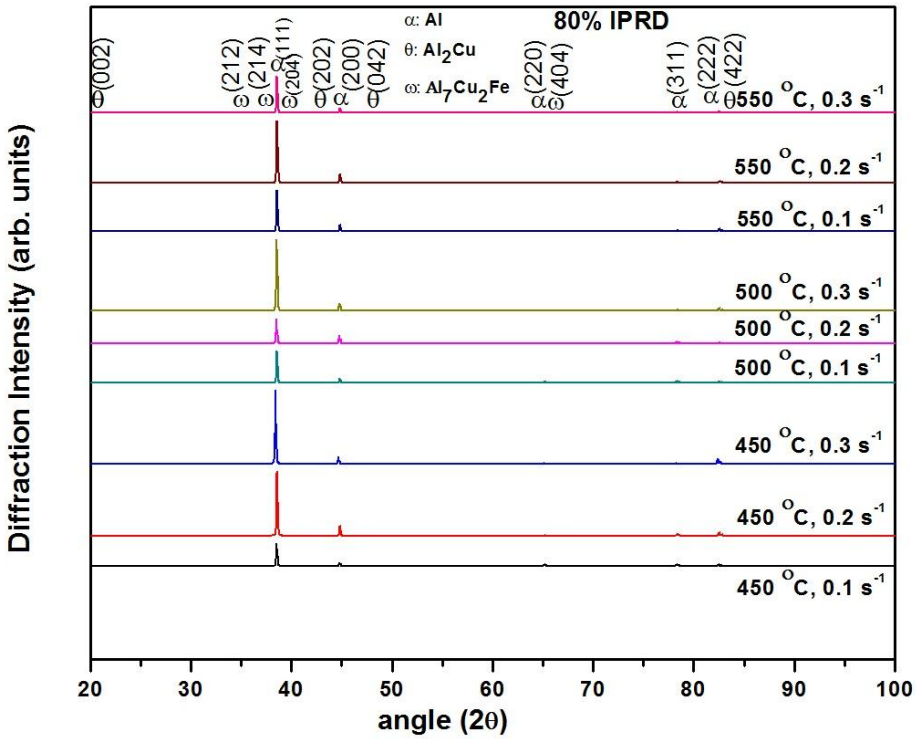

Fig. 6.41 XRD patterns of 80% IPRD samples extruded at different deformation temperatures and strain rate

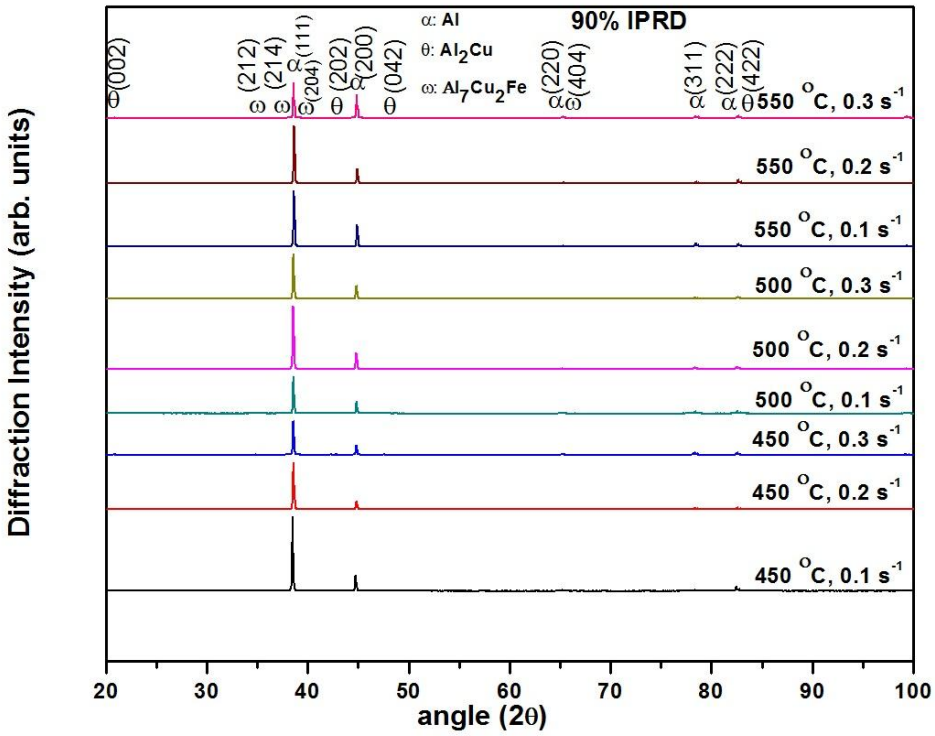

Fig. 6.42 XRD patterns of 80% IPRD samples extruded at different deformation temperatures and strain rate

6.3.3 Density of hot extruded samples

In the case of Al-Cu alloys, the micro addition of Mg induces liquid phase and reduces the temperature for eutectic reaction during sintering. The liquid phase penetrates and diffuses into the oxide layers that cover the Al particles and improves the density of Al-alloys [84]. The optimized composition of Al-4%Cu-0.5%Mg (theoretical density: 2.76 g/cc) alloy green compacts were sintered at 550±10 °C and produced with 70%, 80% and 90% IPRD and with an aspect ratio of one (Φ 15 × 15 mm) by trial and error method. The resultant density measurements for extruded samples at different temperatures and strain rates and with different IPRD are shown in Fig. 6.43. Due to low melting point of Mg (650 °C), it melts down, fills the gaps between extruded powder particles and therefore increases the density of specimens. The densities of extruded samples increased with increasing deformation temperature and IPRD, and reducing the strain rate. The chemical inhomogeneities of extruded samples were reduced by rapid diffusion with increasing deformation temperature. Porosity and blowholes were reduced by welding the cavities. The coarse columnar grains in the initial billets were broken down and refined into equiaxed recrystallized grains as explained in SEM analysis (section 6.5.1). The maximum density was attained in 90% IPRD sample extruded at 550 °C and 0.1 s^{-1} (98.75 % theoretical). The samples extruded at 550 °C showed higher density values compared to that of samples extruded at 450 °C and 500 °C for all strain rates (0.1-0.3 s^{-1}) and the samples extruded at 0.3 s^{-1} were revealed superior densification for all extrusion temperatures. The samples deformed with 90% IPRD showed higher densities compared to 70% and 80% IPRDs.

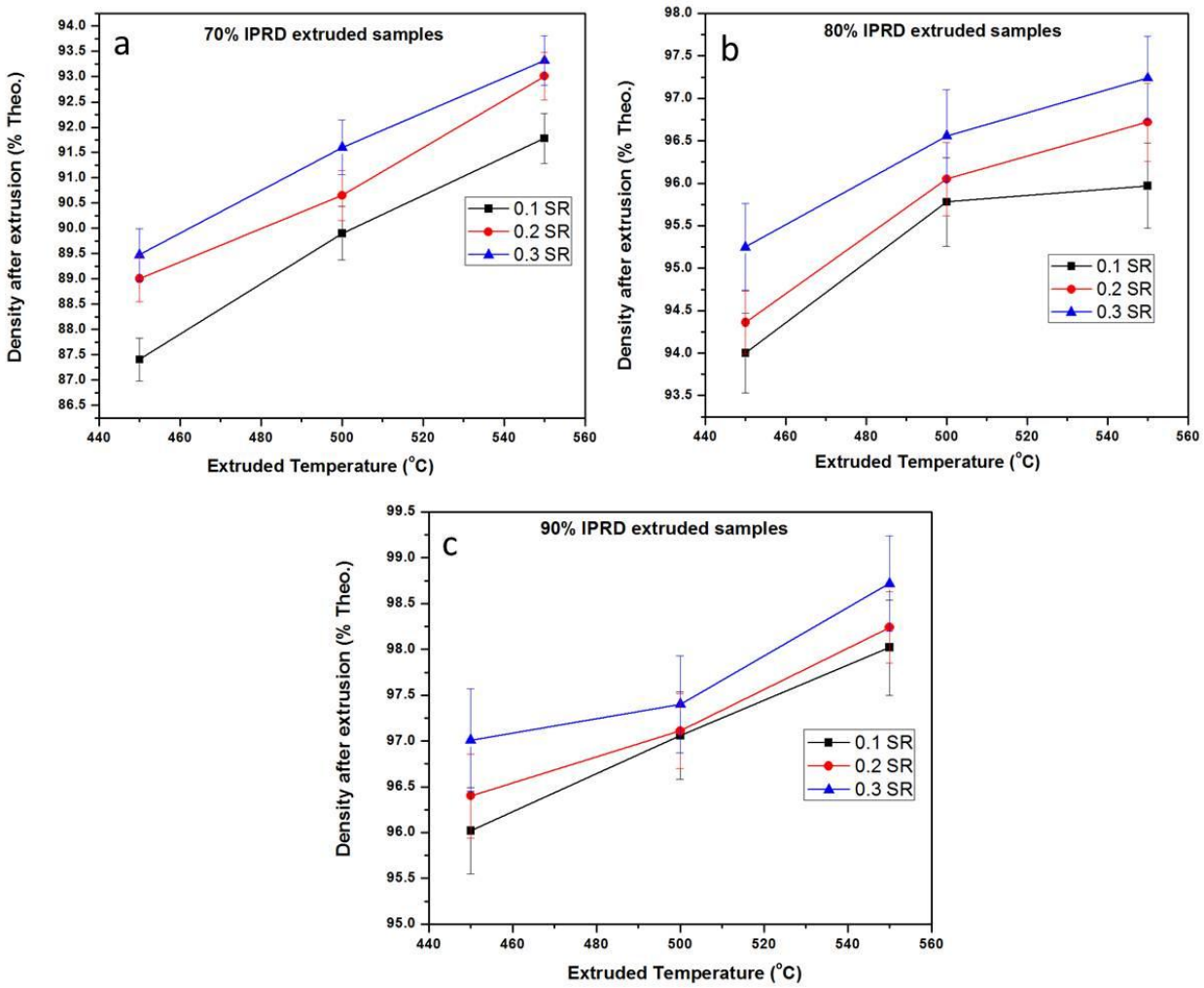

Fig. 6.43 Density of extruded samples at different temperatures, strain rates and IPRD

6.3.4 Hardness of hot extruded samples

The microhardness measurements of hot extruded Al-4%Cu-0.5%Mg sintered preforms at different temperatures and strain rates with different IPRDs are shown in Fig 6.44. The hardness values have almost doubled the sintered sample after extrusion due to alloying, strain hardening and precipitation formation within the matrix and along the grain boundaries. Higher hardness could be attributed to higher dislocation density in the samples due to thermal mismatch and difference in mechanical properties of alloying elements. This mismatch makes plastic deformation more difficult by dislocation motion impedance which results in increasing the hardness. Hardness of extruded products could also be increased by uniform distribution of precipitates throughout the matrix and along the grain boundaries and due to strain hardening which impede the dislocation movement during extrusion. Hardness was reduced with increasing

extrusion temperature due to grain coarsening and average grain size increment, and increased with increasing strain rate. 90% IPRD samples have shown higher micro-hardness values irrespective of deformation temperature and strain rate as shown in Fig. 644c.

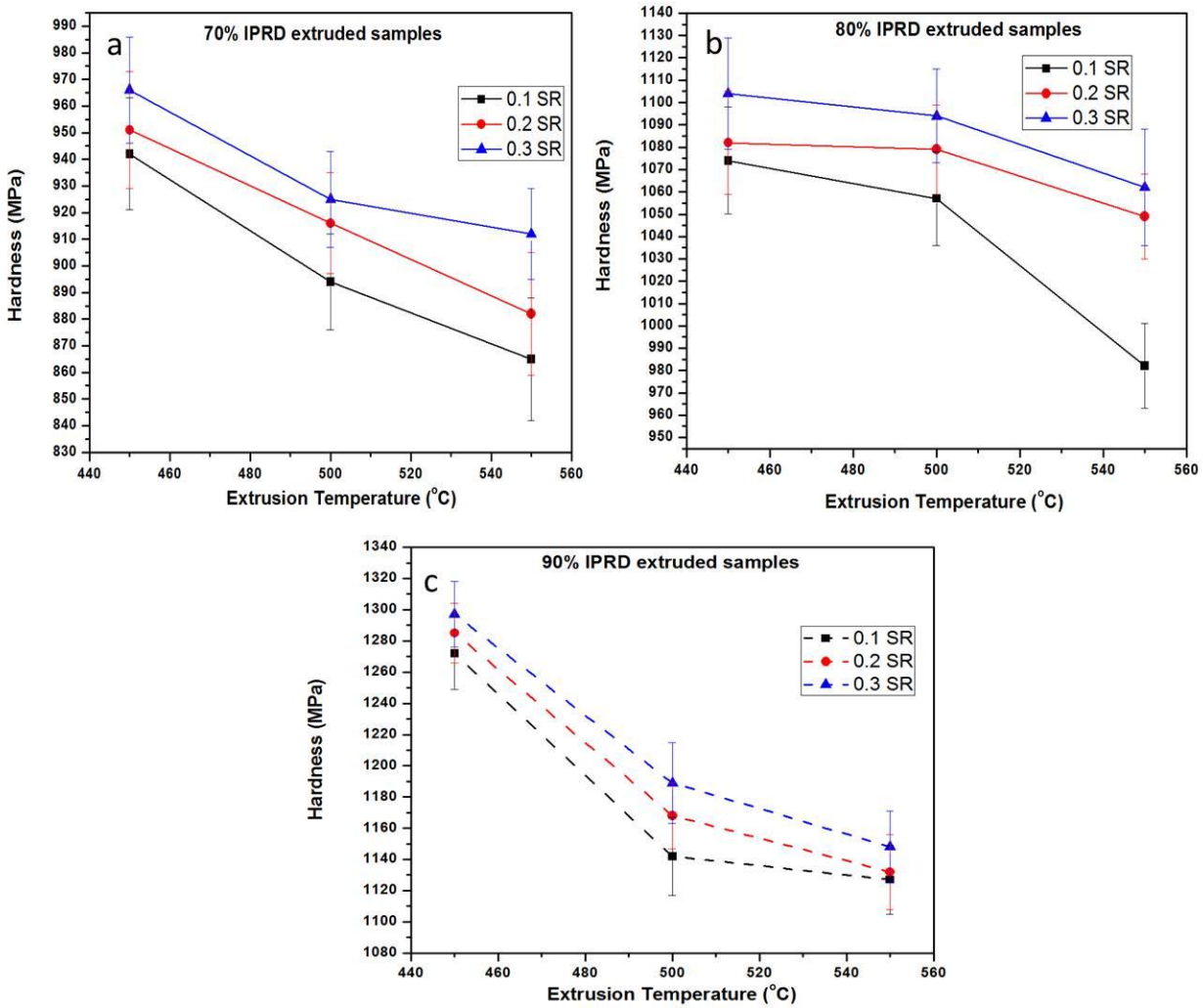

. **Fig. 6.44** Density of extruded samples at different temperatures, strain rates and IPRD

6.4 Development of constitutive model for hot extruded Al-Cu-Mg alloys

Constitutive equations proposed for P/M materials which take into account the influence of porosity are very limited. Therefore, it is fascinating to investigate the hot deformation behavior and develop constitutive equation to predict the flow stress by considering the influence of porosity and other process parameters such as deformation temperature and strain rate along with IPRD. In order to describe the material deformation behavior and to establish the optimum processing variables, it is essential to investigate the constitutive modeling. The constitutive

equations are expressed in terms of linear and non-linear relationships between process parameters, mainly, stress, strain, strain rate, temperature and IPRD of the materials. Several constitutive models have been suggested in the past to describe the hot deformation behavior of different materials. The most commonly used constitutive model is Arrhenius type equation (i.e., hyperbolic-sine equation), which can establish a relationship between flow stress (σ), deformation temperature (T), strain rate (έ), IPRD and the activation energy (Q). The true stress-strain data received from hot extrusion tests under different deformation temperatures, strain rates and IPRD (Fig. 6.30-Fig. 6.38) can be employed to find out the material constants of constitutive equation. The Arrhenius-type equation for all the stress levels can be written as [246]:

$$\acute{\varepsilon} = A\,[\sinh(\alpha\sigma)]^n\, exp\left(-Q/_{RT}\right) \tag{6.1}$$

Where A is the material constant; έ is the strain rate (s^{-1}); n is the material stress index; α is the stress multiplier; Q = the activation energy (kJ/mol); σ is the flow stress (MPa); T is the deformation temperature (K) and R is the universal gas constant (8.314 J/mol.K).

Substituting suitable functions into equation (6.1) leads to the subsequent power law (suitable for low stress levels (ασ< 0.8) and exponential law (suitable for high stress levels (ασ> 1.2) [246, 247].

$$\acute{\varepsilon} = A'\sigma^n \exp\left(-Q/_{RT}\right) \qquad [\alpha\sigma< 0.8] \tag{6.2}$$

$$\acute{\varepsilon} = A'' \exp(\beta\sigma)\ exp\ \left(-Q/_{RT}\right) \qquad [\alpha\sigma> 1.2] \tag{6.3}$$

In the above equations, A' and A'' are the material constants and α is expressed as β/n. Further, the influence of deformation temperature and strain rate on deformation behavior of materials can be expressed by an exponential type Zener-Holloman parameter [338].

$$Z = \acute{\varepsilon} \exp\left(Q/_{RT}\right) \tag{6.4}$$

where Q = Activation energy (KJ/mol); έ = Strain rate (s^{-1}); R = Universal gas constant (8.314 J mol^{-1} K^{-1}) and T = Absolute temperature (K).

Another form of Z parameter can be yielded when the Eq. (6.1) is substituted in Eq. (6.4) i.e.,

$$Z = A\,[\sinh(\alpha\sigma)]^n \tag{6.5}$$

6.4.1 Determination of material constants (n, β and α)

The material constants n, β and α should be derived to model the constitutive equation for hot extruded Al-4%Cu-0.5%Mg P/M processed preforms. Experimentally obtained true stress-strain data was used to derive the material constants of the constitutive equation. Here the Peak Flow Stress (PFS) is termed as σ, which is usually utilized for Al-alloys. The flow behavior (stress) in true stress-strain plots was almost persistent at higher strain values so that the influence of strain was not considered for hot extrusion experiments. In order to find n and β values, natural logarithm can be taken on both sides of Eq. (6.2) and Eq. (6.3) and given as Eq. (6.6) and (6.7), respectively.

$$\ln \acute{\varepsilon} = \ln A' + n \ln \sigma - \frac{Q}{RT} \tag{6.6}$$

$$\ln \acute{\varepsilon} = \ln A'' + \beta\sigma - \frac{Q}{RT} \tag{6.7}$$

Eq. (6.8) and (6.9) can be obtained from partial differentiation of Equation (6.6) and (6.7), when the hot extrusions are processed at constant temperatures.

$$n = \left[\frac{\partial ln\acute{\varepsilon}}{\partial ln\sigma}\right]_{T=const} \tag{6.8}$$

$$\beta = \left[\frac{\partial ln\acute{\varepsilon}}{\partial \sigma}\right]_{T=const} \tag{6.9}$$

The relation between flow stress (σ) and strain rate can be obtained by substituting flow stress values and corresponding strain rates for different IPRDs and deformation temperatures in Eq. (6.6) and (6.7). The plots shown in Fig. 6.45 and Fig. 6.46 illustrate the relation between ln σ-ln ἑ and σ-ln ἑ respectively. The n and β values for different IPRDs and temperatures were obtained from the slopes of every single line in Fig. 6.45 and Fig. 6.46, respectively by linear fit method. Table 6.1 shows the n, β and α average values for hot extruded Al-4%Cu-0.5%Mg sintered preforms with different IPRD samples extruded at different parameters.

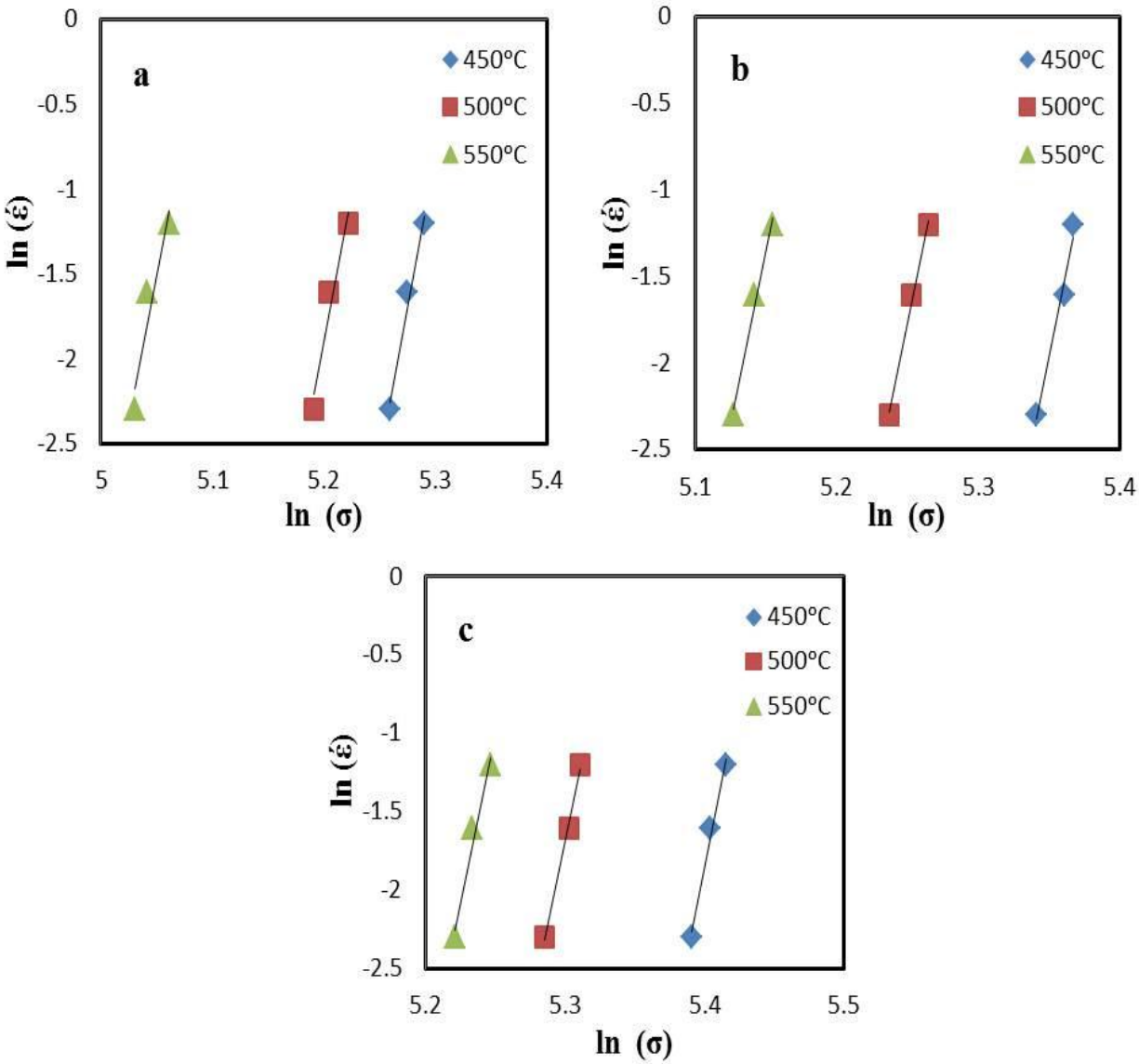

Fig. 6.45 Relationship between ln ε̇ –ln σ for Al–4%Cu-0.5%Mg preforms with initial preform relative densities: a) 70%, b) 80% and c) 90%

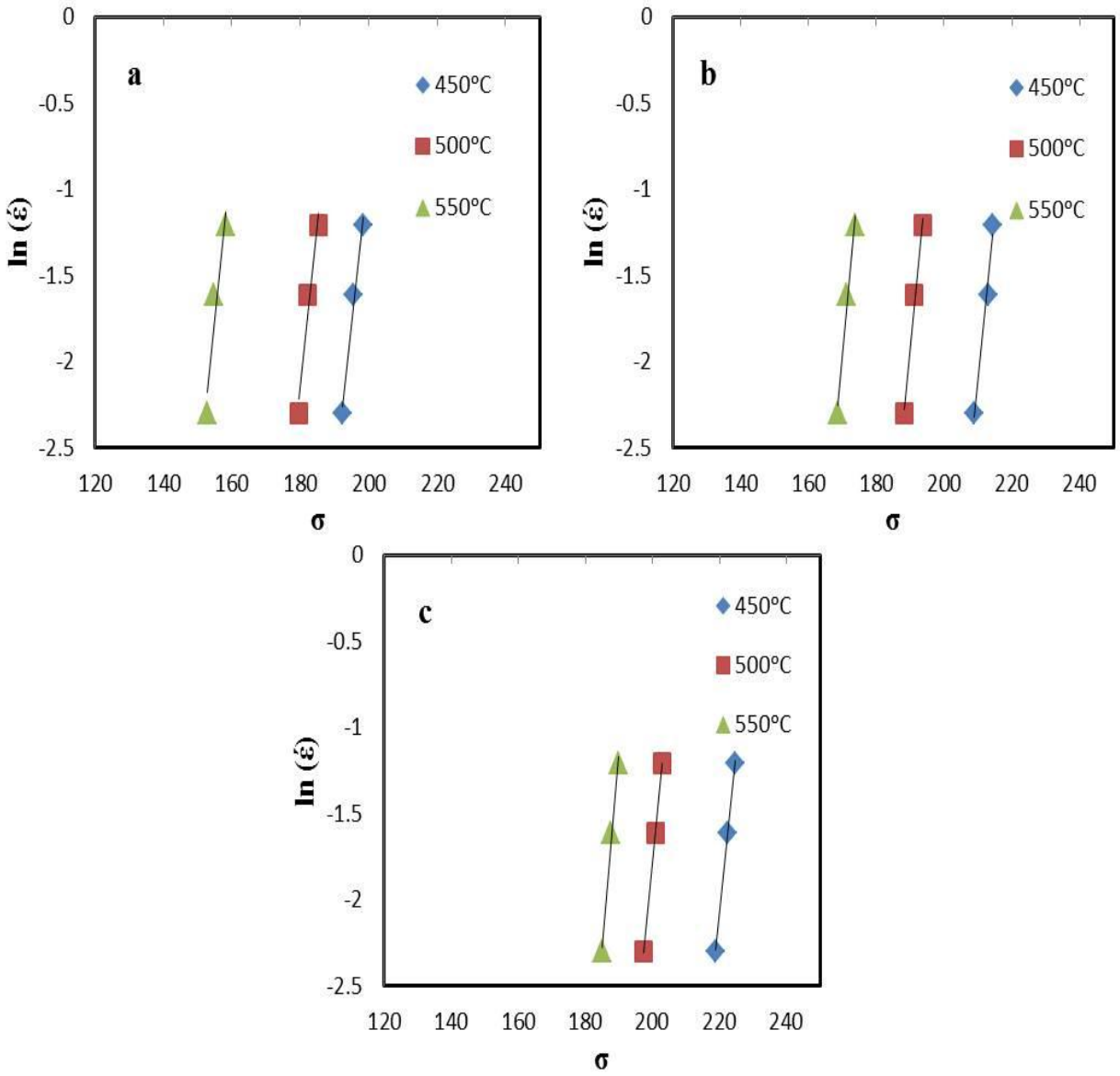

Fig. 6.46 Relationship between ln ε̇ -σ for Al–4%Cu-0.5%Mg preforms with initial preform relative densities: a) 70%, b) 80% and c) 90%

6.4.2 Calculation of activation energy (Q)

In order to calculate activation energy for hot extruded Al-alloy sintered preforms with different IPRDs and at a given strain rate, natural logarithm can be taken on both sides of Eq. (6.1)

$$\ln \dot{\varepsilon} = \ln A + n \ln[\sinh(\alpha\sigma)] - \frac{Q}{RT} \tag{6.10}$$

Differentiating Eq. (6.10) yields Eq. (6.11)

$$Q = R\left\{\frac{\partial \ln \dot{\varepsilon}}{\partial \ln[\sinh(\alpha\sigma)]}\right\}_{T=const}\left\{\frac{\partial \ln[\sinh(\alpha\sigma)]}{\partial\left(\frac{1}{T}\right)}\right\}_{\dot{\varepsilon}=const} \quad (6.11)$$

The slope of ln ἑ - ln[sinh(ασ)] at various deformation temperatures and the slope of plots ln[sinh(ασ)] – (1/T) at different strain rates for different IPRD are plotted and shown in Fig. 6.47(a-c) and Fig. 6.48(a-c). The values of ∂lnἑ/∂ln[sinh(ασ)] at various temperatures can be obtained by computing the slopes of straight lines shown in Fig. 6.47a to 6.47c. In the same way, the values of ∂ln[sinh(ασ)]/∂(1/T) can be derived from Fig. 6.48a to 6.48c. Therefore, the activation energy (Q) at varying IPRDs was calculated and is shown in Table 6.1. The Q of hot extruded Al-4%Cu-0.5%Mg sintered preforms increased with increasing IPRD due to the presence of pores in the sintered preforms, which reduce the deformation resistance of the material. Also, the average values of α decreased with increasing IPRD. The activation energy values shown in Table 6.1 are somewhat higher than that of pure Aluminium, i.e., 142 kJ/mol [339] and lower than homogenized 2026 Aluminium alloy i.e., 340.98 kJ/mol [45]. Usually, high values of Q have been found in heat-treatable alloys due to the existence of precipitates and other alloying elements. The alloying elements in a material obstruct the diffusion of other alloying elements; reduce the motion of grains, grain boundaries and dislocations in the recrystallization process, which can increase the activation energy (Q) of hot extruded materials. Irrespective of IPRD, the activation energy (Q) decreased with increasing extrusion temperature. Differences in activation energy (Q) between present alloy and other Al-alloys might be due to the dislocation pinning effect, and the effect of DRV, DRX and dynamic precipitation as explained in the microstructural evolution section (section 6.5 and 6.6).

Natural logarithm is taken on both sides of Eq. (6.5) to obtain Eq. (6.12)

$$\ln Z = \ln A + n \ln[\sinh(\alpha\sigma)] \quad (6.12)$$

Fig. 6.49(a-c) shows the slope of plots ln[sinh(ασ)]-lnZ which can give the values of ln*A* for different IPRDs. The values of ln*A* are 29.7, 31.82 and 33.02 for hot extruded Al-alloys with IPRDs of 70%, 80% and 90%, respectively. The Zener-Holloman parameter (Z) can be calculated by substituting Q values in Eq. (6.4). After estimating all the material constants from the above equations, the constitutive equation which is related to the flow stress (σ) and the

Zener-Holloman parameter (Z) could be written as in Eq. (6.13) by considering Eq. (6.1) and (6.4).

$$\sigma = \frac{1}{\alpha}\ln\left\{\left(\frac{Z}{A}\right)^{\frac{1}{n}} + \left[\left(\frac{Z}{A}\right)^{\frac{2}{n}} + 1\right]^{\frac{1}{2}}\right\} \tag{6.13}$$

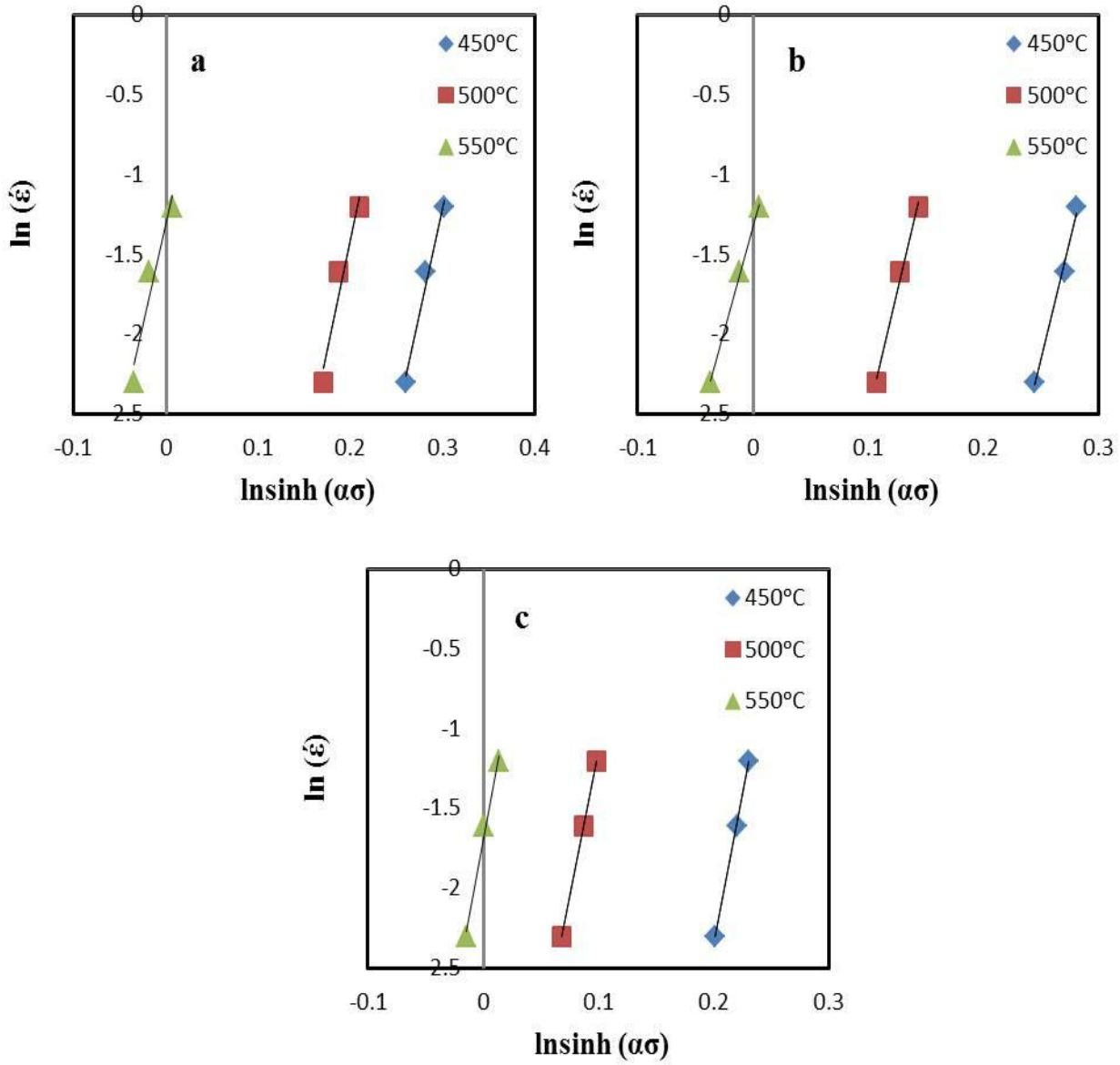

Fig. 6.47 Relationship between lnέ–ln[sinh(ασ)] for Al–4%Cu-0.5%Mg preforms with initial preform relative density: a) 70%, b) 80% and c) 90%

Table 6.1 The material constants for extruded samples with different initial preform relative densities

Initial Preform Relative Density (%)	β	n	α	Q (kJ/mol)
70	0.192	34.59	0.00557	217.83
80	0.201	39.88	0.00505	229.61
90	0.203	43.15	0.00472	238.01

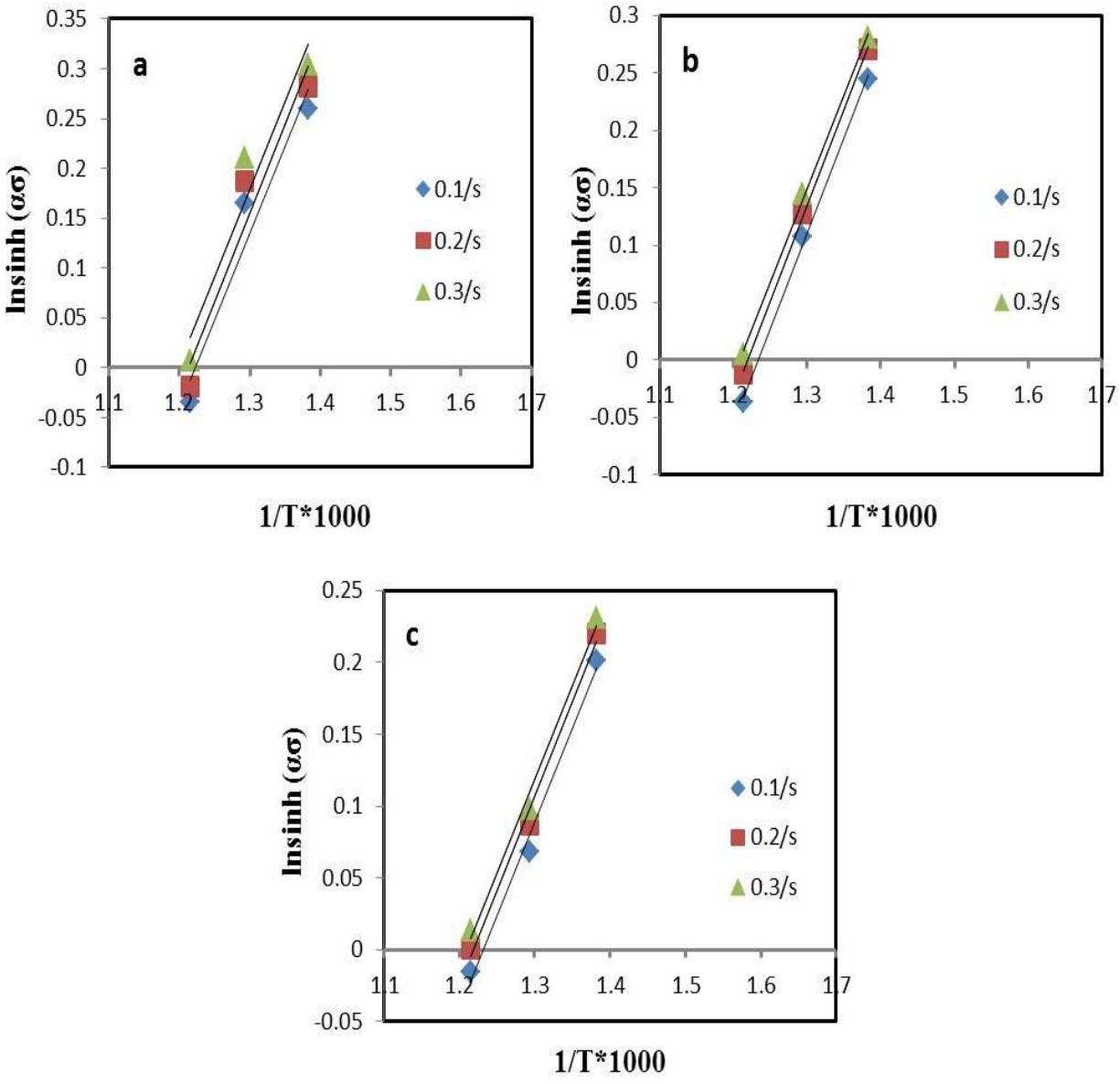

Fig. 6.48 Relationship between ln[sinh(ασ)]–1/T for Al–4%Cu-0.5%Mg preforms with initial preform relative density: a) 70%, b) 80% and c) 90%

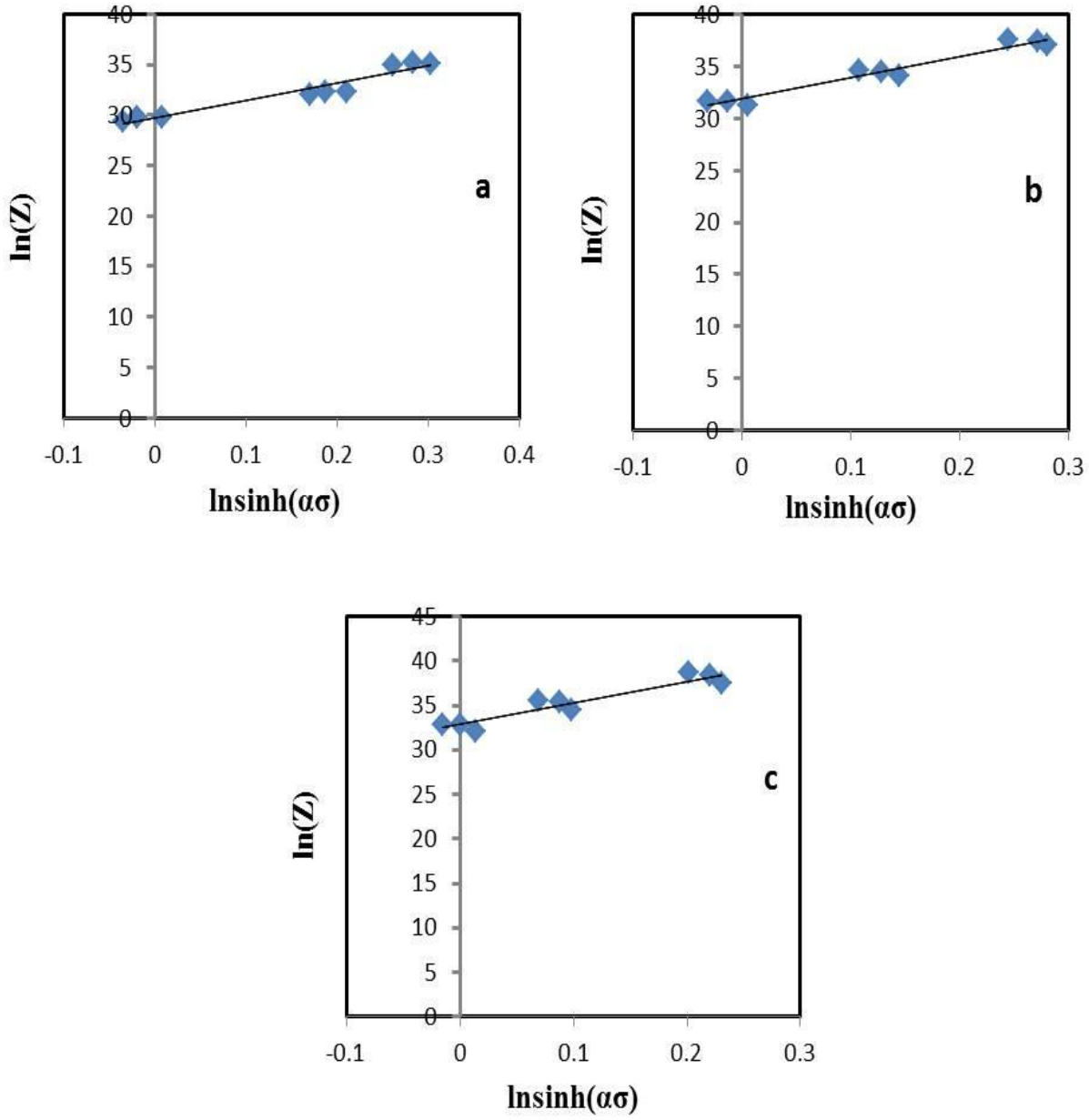

Fig. 6.49 Relationship between ln[sinh(ασ)] – lnZ for Al–4%Cu-0.5%Mg preforms with initial preform relative density: a) 70%, b) 80% and c) 90%

The values of n, α, Q and ln*A* were used to fit into the third-order polynomial functions, which show the evolution of material constants. The relationship between these values and IPRD is shown in Fig. 6.50 (a-d). Thus, the variation of α, n, Q and ln*A* with IPRD for P/M processed Al-4%Cu-0.5%Mg compacts during hot extrusion would be expressed as:

$$n = -0.0101IPRD^2+2.044IPRD-59 \quad (6.14)$$

$$\alpha = 5E\text{-}7IPRD^2\text{-}1.25E\text{-}4IPRD+0.0119 \quad (6.15)$$

$$Q = -0.0169IPRD^2+3.713IPRD+40.73 \quad (6.16)$$

$$\ln A = -0.0046IPRD^2+0.902IPRD-10.9 \quad (6.17)$$

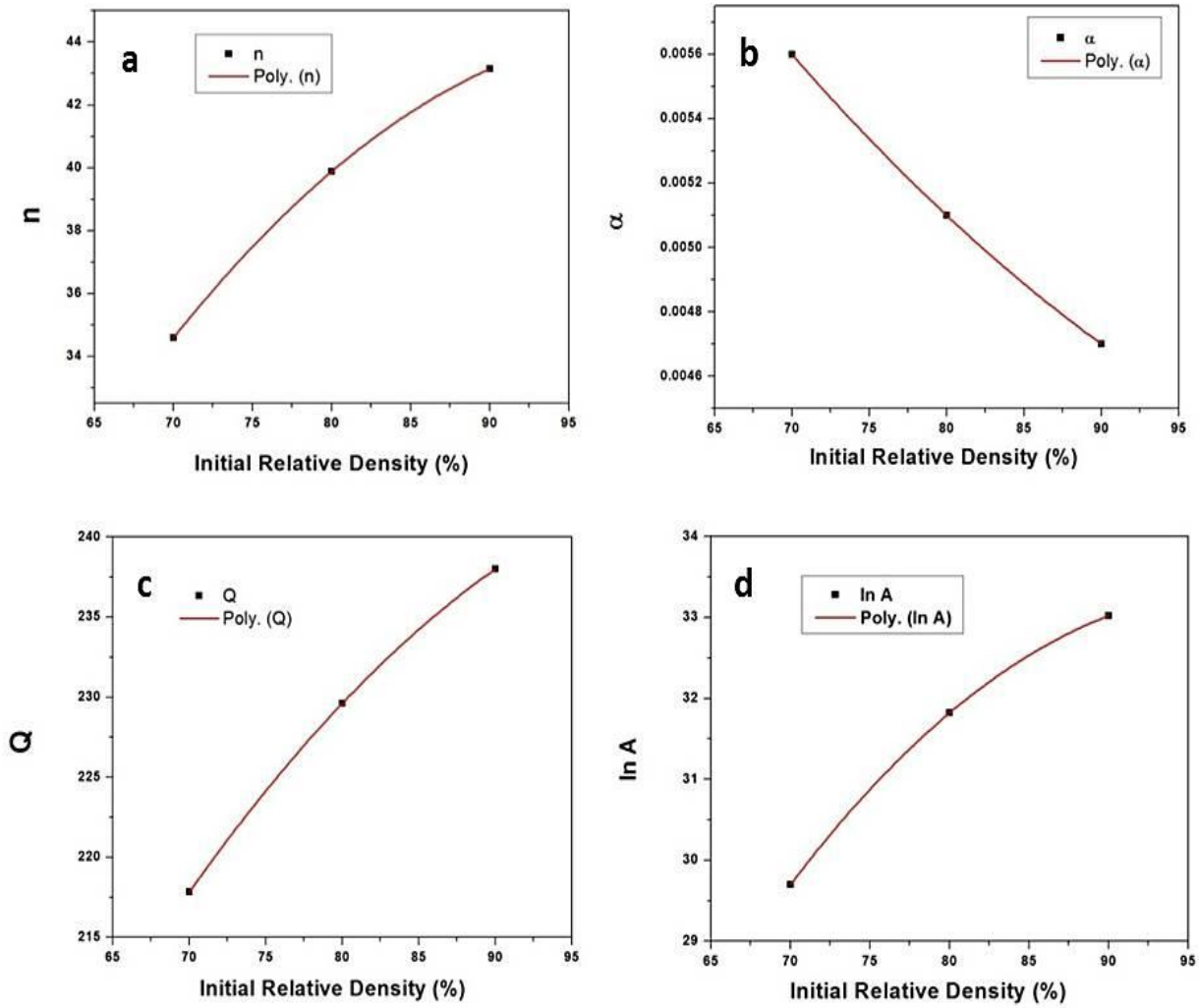

Fig. 6.50 Relationship between (a) n, (b) α, (c) Q and (d) ln A and initial preform relative density of hot extruded Al–4%Cu-0.5% Mg preforms

6.4.3 Verification of developed constitutive modelling

In order to evaluate the constitutive equations developed for hot extruded Al-4%Cu-0.5%Mg sintered preforms, the flow stress for different extrusion temperatures (450 °C, 500 °C and 550 °C) and strain rates (0.1 s^{-1}, 0.2 s^{-1} and 0.3 s^{-1}) with different IPRDs were calculated using Eq. 6.13. The comparison between predicted (calculated) values of flow stress and experimental flow stress values at different processing conditions and for different IPRDs are shown in Fig. 6.51 to Fig. 6.53. It is clearly seen from the figures that most of the predicted data points and experimental values lie close to the best fit line and show the perfect correlation between the results. The correlation coefficient (R) is a statistical parameter and commonly used to represent the strength of the linear relationship between predicted and measured values [340]. The R values were 0.969, 0.989 and 0.991 for IPRDs of 70%, 80% and 90%, respectively, as shown in Fig. 6.51-6.53. The prediction capability and correlation coefficient were increased with increasing IPRD.

Other standard statistical parameters, namely, absolute error (δ) and AARE (Average Absolute Relative Error) were also determined to further evaluate the accuracy and predictability of the developed constitutive equation [340].

$$\delta = \left|\frac{\sigma_P - \sigma_{Ex}}{\sigma_{Ex}}\right| X\ 100 \tag{6.18}$$

$$AARE = \frac{1}{N}\sum_{i=1}^{N}\left|\frac{\sigma_P - \sigma_{Ex}}{\sigma_{Ex}}\right| X\ 100 \tag{6.19}$$

Where σ_{Ex} is the measured (experimental) flow stress, σ_P is the calculated (predicted) flow stress and N is the number of data employed in the investigation. Table 6.2 shows the list of experimental and predicted peak flow stress values for hot extruded Al-4%Cu-0.5%Mg sintered preforms at different extrusion temperatures and strain rates with different IPRDs. The results revealed that the developed constitutive equation reflects excellent predictability and accuracy. The maximum observed AARE is 6.14% which is acceptable for deformation behavior of porous materials. Therefore, the results demonstrate excellent agreement between experimental peak flow stress values with predicted ones, which confirms the reliability and accuracy of the developed constitutive equation for hot deformation of Al-4%Cu-0.5%Mg sintered preforms.

Table 6.2 Predicted and experimental PFS of powder metallurgy Al-4%Cu-0.5%Mg preforms during hot extrusion

Extrusion temperature (K)	Strain rate (1/s)	IPRD = 70%				IPRD = 80%				IPRD = 90%			
		Exp. PFS	Calc. PFS	Error (δ (%))	AARE (%)	Exp. PFS	Calc. PFS	Error (δ (%))	AARE (%)	Exp. PFS	Calc. PFS	Error (δ (%))	AARE (%)
723	0.1	192.34	190.25	1.08		208.78	208.46	0.14		219.38	214.83	2.07	
723	0.2	195.46	191.23	2.16	**2.22**	212.94	209.67	1.53	**1.23**	222.41	215.78	2.97	**2.68**
723	0.3	198.34	191.53	3.43		214.39	210.04	2.02		224.22	217.47	3.00	
773	0.1	179.78	167.89	6.61		188.11	184.65	1.83		198.08	194.89	1.60	
773	0.2	182.11	172.93	5.04	**5.94**	191.17	185.16	3.13	**2.81**	201.05	199.18	0.92	**3.67**
773	0.3	185.32	173.88	6.17		193.63	186.91	3.47		202.71	200.36	1.15	
823	0.1	153.03	145.97	4.61		168.55	159.02	5.65		185.24	183.45	0.96	
823	0.2	154.9	147.04	5.07	**5.6**	171.06	160.79	5.99	**6.14**	187.64	186.99	0.34	**0.62**
823	0.3	158.39	147.10	7.12		173.65	161.86	6.78		189.62	190.69	0.56	

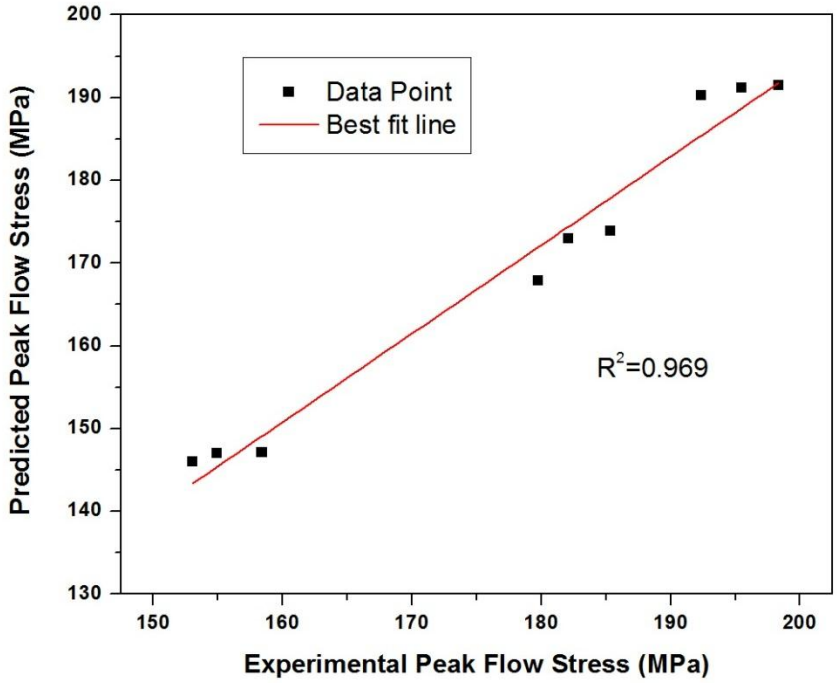

Fig. 6.51 Correlation between experimental and predicted Peak flow stresses of 70% IPRD hot extruded samples at given process parameters

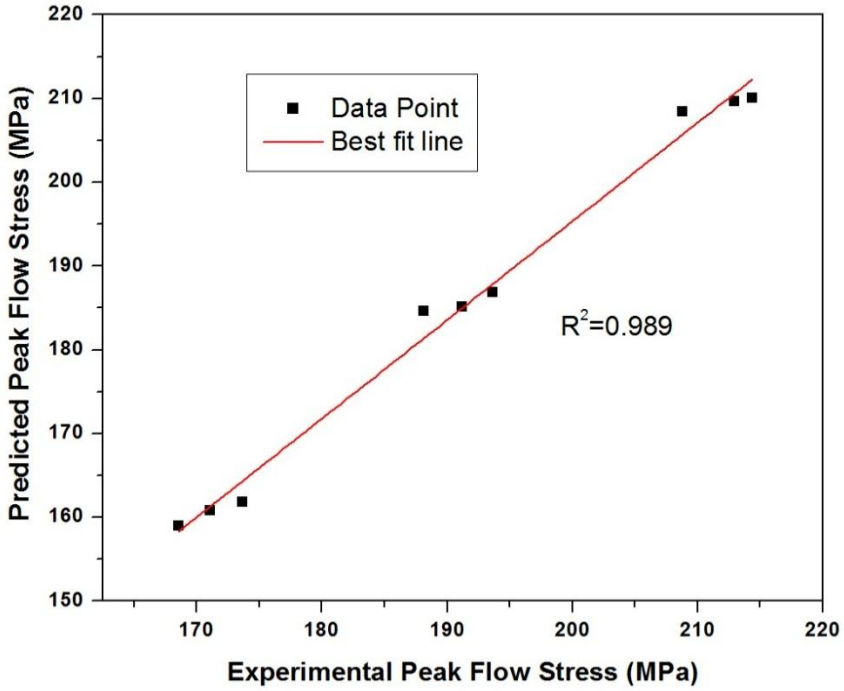

Fig. 6.52 Correlation between experimental and predicted Peak flow stresses of 80% IPRD hot extruded samples at given process parameters

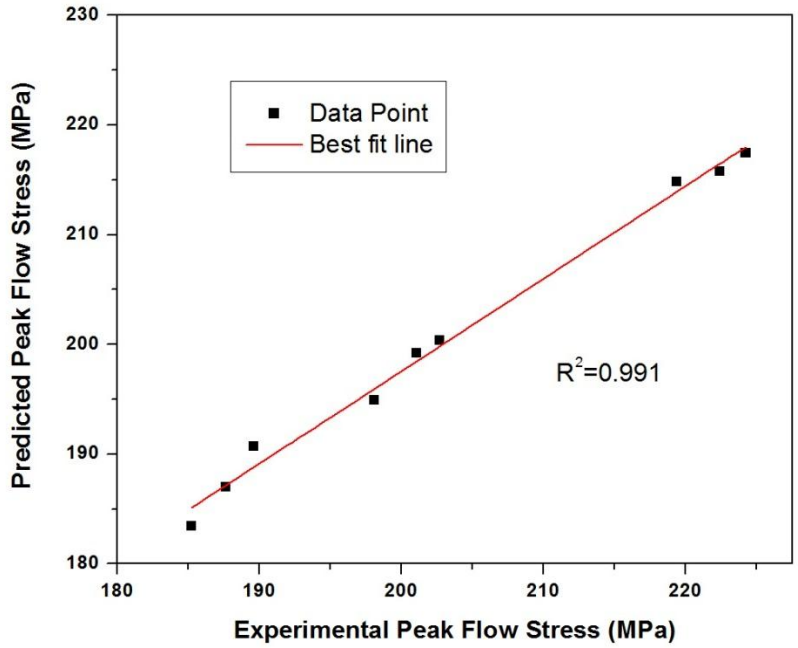

Fig. 6.53 Correlation between experimental and predicted Peak flow stresses of 90% IPRD hot extruded samples at given process parameters

6.5 Microstructural modeling of sintered Al-4%Cu-0.5%Mg P/M preforms during hot extrusion

6.5.1 Microstructural Evolution during Hot deformation

Fig. 6.54, Fig. 6.57 and Fig. 6.59 show the optical and SEM microstructures of hot extruded Al-4%Cu-0.5%Mg P/M processed preforms at various temperatures, strain rates and IPRDs. It is necessary to study the microstructural evolution and structural property correlation accompanying DRV and DRX respectively. Irrespective of IPRDs, the flow softening of hot extruded materials increased with increasing deformation temperature and decreasing strain rate.

6.5.1.1 Effect of deformation temperature on microstructure

Fig. 6.54 (a-c) shows the optical micrographs of hot extruded Al-4%Cu-0.5%Mg alloys under different deformation temperatures (450 °C-550 °C) and fixed strain rate of 0.1 s^{-1}. No porosity was observed in any of the microstructure. Therefore, the extrusion ratio, approach angle, and process parameters used for extrusion were high enough to produce fully densified products from powder compacts. The microstructures consisted of equiaxed, elongated and fine grains. The mobility of grain boundaries during hot deformation increased with increasing temperature so

that the equiaxed grain structure formation increased, which indicates the occurrence of DRX. DRX begins when the strain hardening and dynamic recovery can no longer store more immobile dislocations. These DRX grains can form by the growth, rotation and coalescence of subgrains and show a high contrast with the matrix as shown in Fig. 2.4. This mechanism is called as continuous dynamic recrystallization (CDRX). The grain boundary migration increases with the hot extrusion temperature, which increases the DRX and homogeneity in the microstructure. Further, the recrystallized grain size increased with increasing deformation temperature, as can be seen in Fig. 6.54a, b and c respectively. From the above analysis, the flow stress could be decreased with increase in temperature due to DRX as shown in true stress-true strain plots (Fig. 6.30 - Fig. 6.38). The generation of dislocations, multiplication and rearrangement of dislocations decreases with increasing deformation temperatures. Therefore, the dislocation density resulting from WH and DRV is higher at lower deformation temperature [213, 341]. Due to high efficiency of WH and DRV, new grains were not formed by nucleation but the subgrains transformed into new grains progressively within the deformed original grains (Fig. 6.54a). Fully DRXed microstructure with increased grain size could be seen in the case of deformation at 550 °C (Fig. 6.54c). Fig. 6.55 shows thee grain size distribution of 90% IPRD samples extruded at 450 °C, 500 °C and 550 °C, respectively at a strain rate of 0.1 s^{-1}. The average grain size of sintered samples (14.2 µm) was refined to 9.89 µm, 11.91 µm and 12.67 µm, respectively for the sample extruded at 450 °C, 500 °C and 550 °C, respectively. It is concluded that the DRX grains size of extruded samples increased with increasing deformation temperature.

SEM analyses (Fig. 6.54d, e and f) show the distribution of secondary phase particles during hot extrusion of Al-alloy preforms at a certain strain rate of 0.1 s^{-1} and the deformation temperatures of 450 °C, 500 °C and 550 °C, respectively. In these microstructures, Al (α) matrix appears in grey colour and the Al_2Cu and Al_7Cu_2Fe phases show good contrast with the surrounded α matrix. These high density secondary phases act as sufficient boundary drag pressure to prevent nucleation of discontinuous dynamic recrystallization (DDRX). Hence, accelerate the CDRX in extruded samples. High stacking fault energy (HSFE) metals, such as Al-alloys, ferritic steels, beta-titanium alloys, etc. undergo CDRX rather than discontinuous dynamic recrystallization (DDRX) during hot deformation process [203, 204]. These secondary phases can reduce the movement of dislocations during deformation [342]. It is clearly seen in the SEM analysis that the quantity of secondary phase particles in the matrix and along the grain

boundaries decreased with increasing temperature. EDS elemental analyses were used to examine the second phases formed in hot extruded samples and confirm them as Al_2Cu and Al_7Cu_2Fe phases as shown in Fig. 6.56. It can be seen that the secondary phase particles in the matrix and along the grain boundaries are associated with Al and Cu. EDS analysis revealed that these secondary phases contain Al and Cu elements, and the atomic proportion of Al and Cu is very close to the Al_2Cu and Al_7Cu_2Fe phases. The SEM analysis (Fig. 6.54d, e and f) shows that the subgrain structure formation is increased with increasing temperature which might be attributed to a decrease in dislocation density [243, 246]. These subgrains usually merge with other subgrains and grow into new grains with increasing temperature during deformation. It is apparent that the DRX grains can be possibly formed by the sequence of microstructural changes: the dislocations generation and rearrangement, WH, dislocation self-annihilation, and their absorption by grain boundaries (dynamic recovery), and nucleation and growth of new recrystallized grains (DRX grains) [249, 251]. These DRX grains can be seen as high contrast (HC) grains with the matrix in optical microstructures. The same phenomenon was observed in microstructures of extruded samples at other strain rates (0.2 s^{-1} and 0.3 s^{-1}) and IRD (70% and 80%) with varying temperatures.

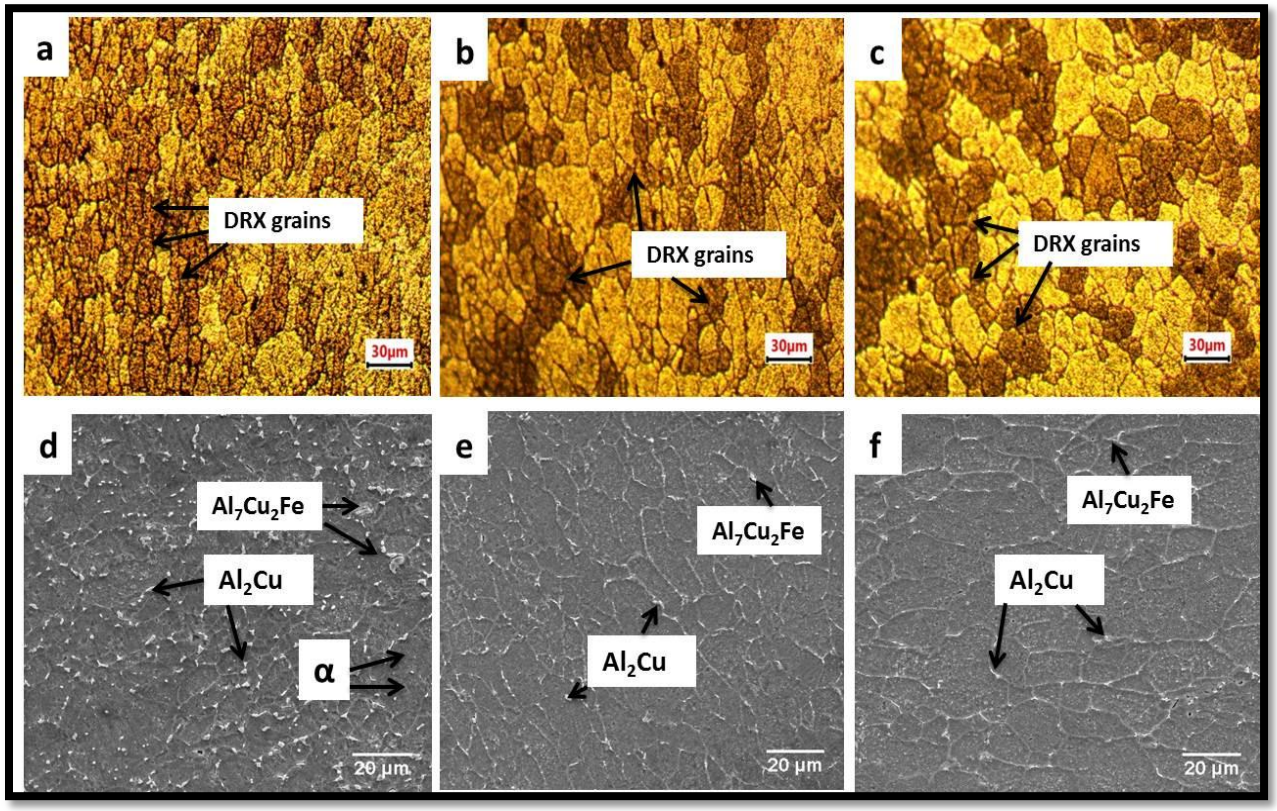

Fig. 6.54 Optical and SEM Micrographs of deformed Al-4%Cu-0.5%Mg P/M preforms with 90% IPRD deformed at 0.1 s^{-1} and different temperatures a) 450 ^{o}C b) 500 ^{o}C and c) 550 ^{o}C

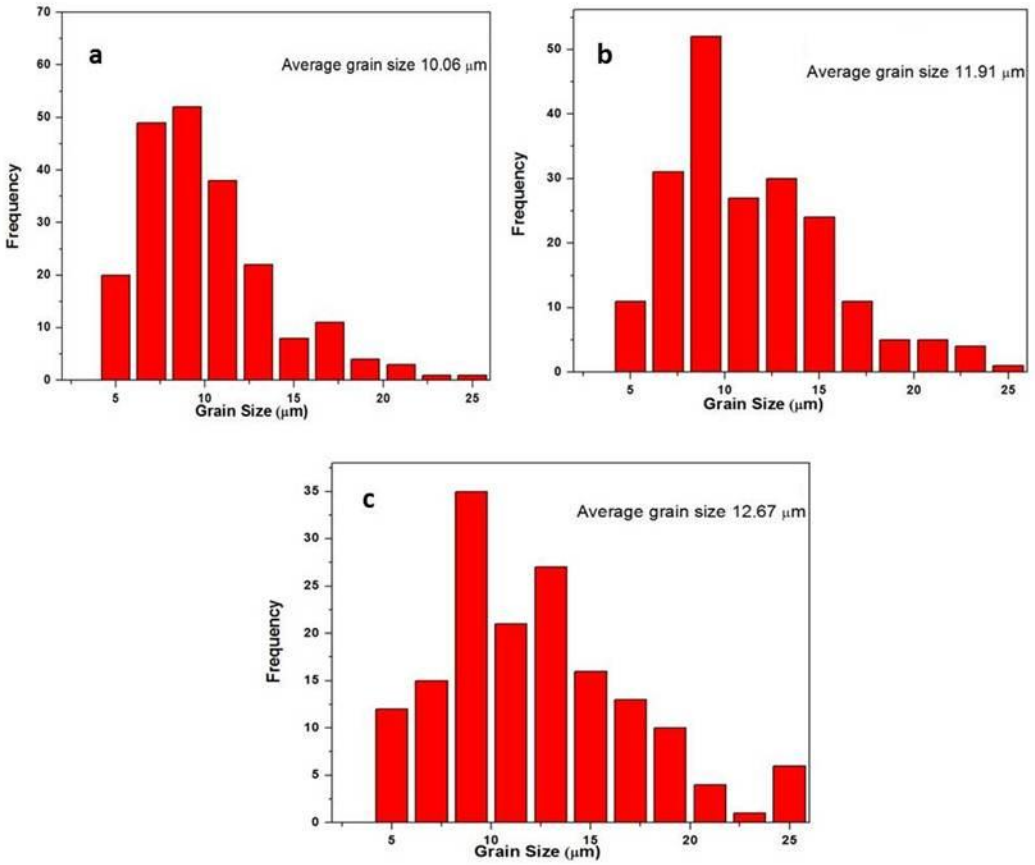

Fig. 6.55 Average DRX grain size distribution of deformed Al-4%Cu-0.5%Mg P/M preforms with 90% IPRD deformed at 0.1 s^{-1} and different temperatures a) 450 ^{o}C b) 500 ^{o}C and c) 550 ^{o}C

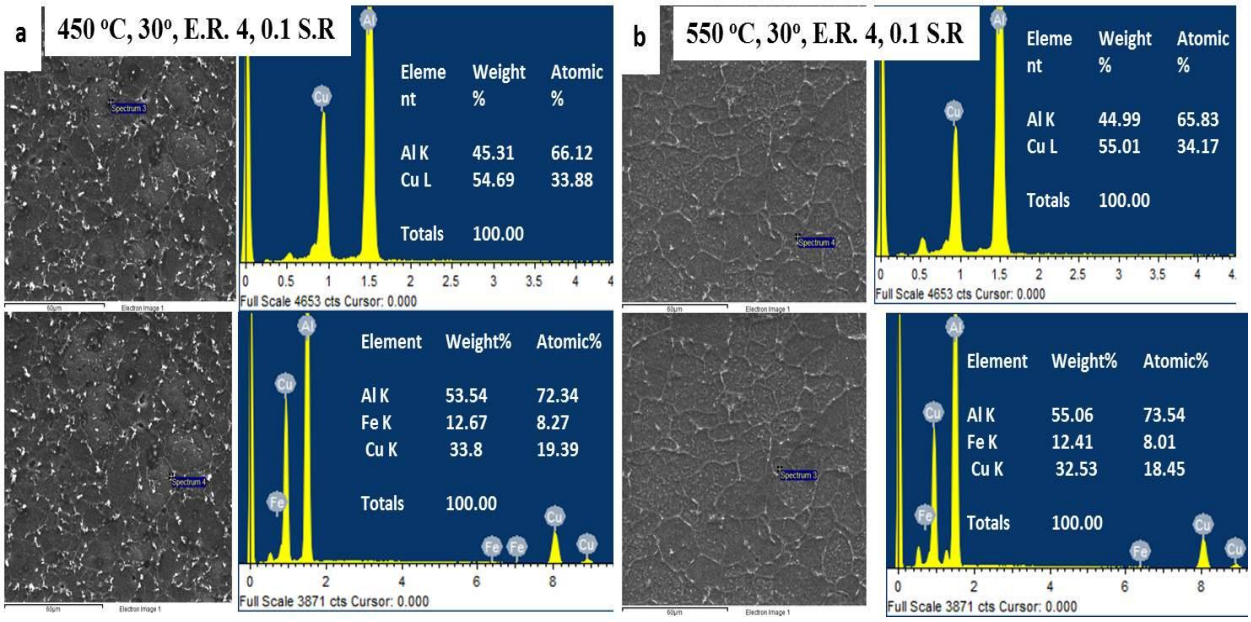

Fig. 6.56 EDS analysis of Al-4%Cu-0.5%Mg P/M 90% IPRD preforms extruded at same extrusion ratio, die angle, strain rate and different deformation temperatures a) 450 °C and b) 550 °C

6.5.1.2 Effect of strain rate on microstructure

Fig. 6.57 shows the microstructures of hot extruded Al-4%Cu-0.5%Mg sintered 90% IPRD preforms under the same deformation temperature (550 °C) and at three different strain rates of 0.1 s^{-1}, 0.2 s^{-1} & 0.3 s^{-1}, respectively. The results in Fig. 6.57 (a-c) show that the DRX grain size decreases with increasing strain rate due to shorter grow-up time and increasing migration energy stored in grain boundaries. Grain grow-up time is decreased with increasing strain rate at constant temperature. Fig. 6.58 shows the grain size distribution of 90% IPRD samples extruded at 0.1 s^{-1}, 0.2 s^{-1} and 0.3 s^{-1} and at same temperature of 550 °C. The average grain size of extruded samples was decreased with increasing strain rate. The dislocation propagation and multiplication are faster at higher strain rates so the mobility of grain boundaries decreased with increase in strain rate. The dislocation density increases with increasing strain rate whereas the dynamic recovery rate decreases, resulting in more nucleation rate in deformed structures [266, 343, 344]. The flow stress increased with increasing strain rate which might be attributed to increasing dislocation density (Fig. 6.30-Fig. 6.38) [337]. In contrast, the deformation time for dynamic softening is higher at low strain rates which leads to the annihilation of dislocation (Fig. 6.57a). So that the recrystallization grain size is higher at lower strain rate. On the other hand, fine DRX grains were observed at higher strain rate which was attributed to the higher nucleation and lower diffusion rate. At the strain rate of 0.1 s^{-1} and deformation temperature of 550 °C, the microstructure showed complete recrystallized microstructure with homogenous grain formation (Fig. 6.57a). According to the microstructural analysis, the deformation should take place at lower strain rates in order to obtain good microstructures without residual dislocations inside the grains. DRX is also easier to form when the sample deforms at lower strain rates. SEM analyses have also shown the same phenomena as optical microstructures which are not included here. SEM microstructures were observed with distribution of secondary phases and their uniformity in matrix increased with increasing strain rate. The same types of results were observed for other deformation temperatures (450 °C and 500 °C) and IPRDs (70% and 80%).

From the above results, it is concluded that the DRX grain size of the sintered Al-alloys is very sensitive to the deformation temperature and strain rate during deformation. Generally, Zener-Holloman Parameter (Z) is used to study the combined effect of deformation temperature and strain rate in case of deformation. The grain size of the deformed Al-4%Cu-0.5%Mg sintered

preforms also depends on the Z parameter, that is, a decreasing Z leads to more adequate proceedings of DRX.

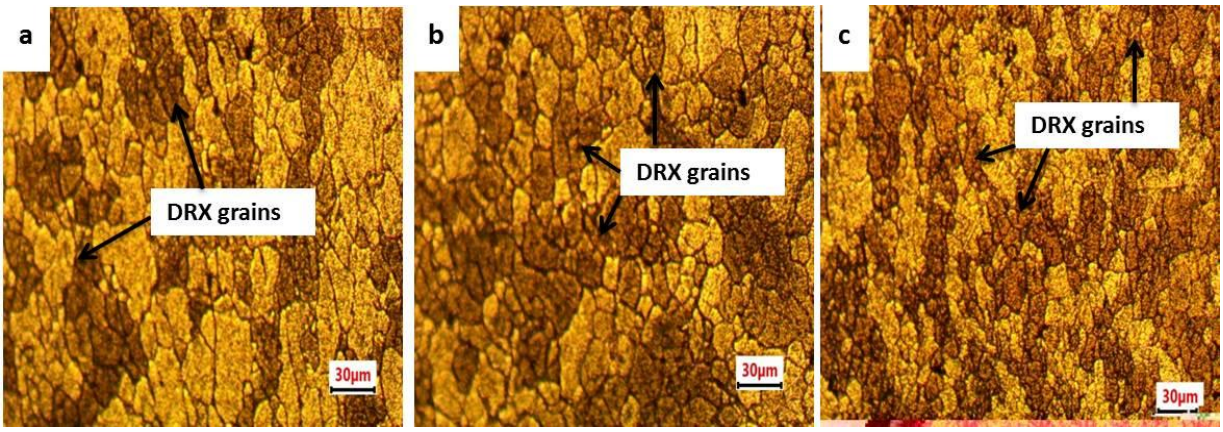

Fig. 6.57 Optical Micrographs of deformed Al-4%Cu-0.5%Mg P/M preforms with 90% IPRD deformed at 550 ^{o}C and different strain rates a) 0.1 s^{-1} b) 0.2 s^{-1} and c) 0.3 s^{-1}

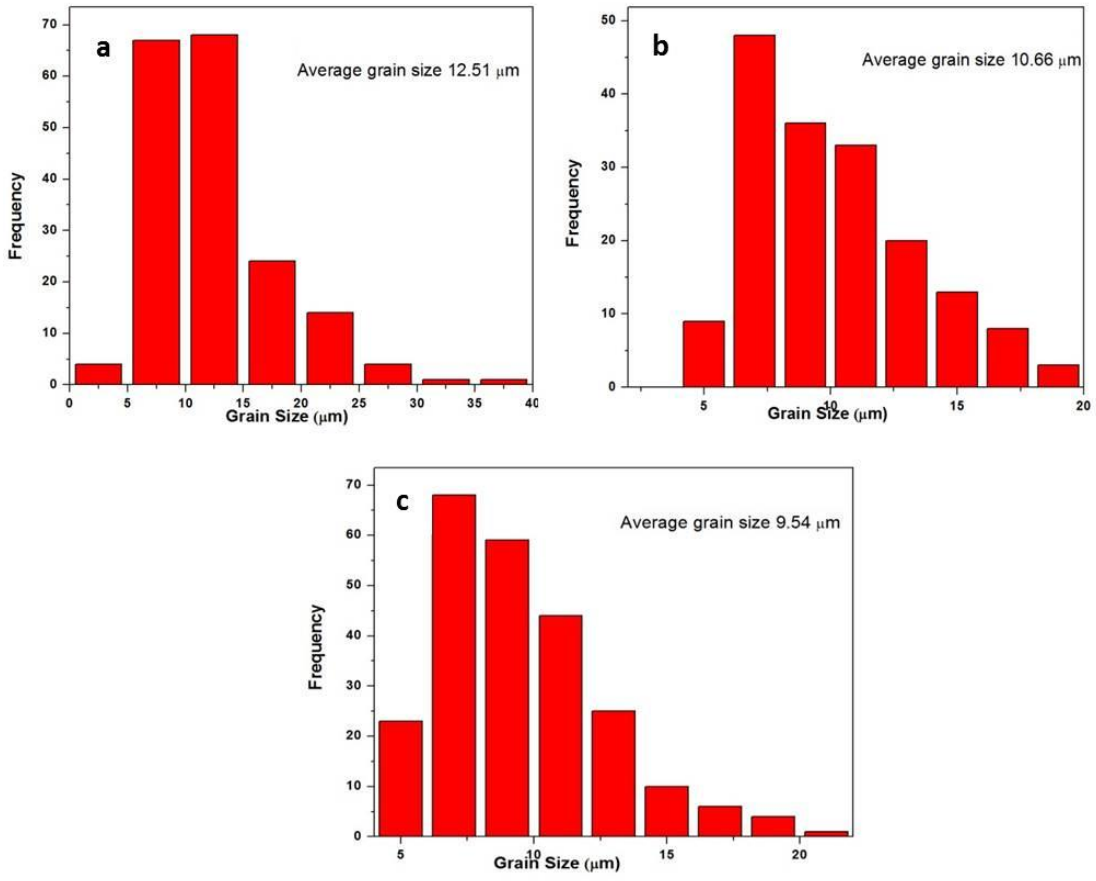

Fig. 6.58 Grain size distribution of deformed Al-4%Cu-0.5%Mg P/M preforms with 90% IPRD deformed at 550 ^{o}C and different strain rates a) 0.1 s^{-1}, b) 0.2 s^{-1} and c) 0.3 s^{-1}

6.5.1.3 Effect of initial preform relative density (IPRD) on microstructure

The effect of IPRD on microstructure changes of extruded Al-4%Cu-0.5%Mg sintered preforms at different process conditions was studied. Fig. 6.59 shows the optical micrographs of extruded samples with 70%, 80% and 90% IPRDs at a fixed deformation temperature (550 °C) and strain rate (0.1 s^{-1}). In addition to matrix work hardening, geometric work-hardening or densification hardening takes place during hot deformation of different IPRD powder preforms and this enhances the flow stress of the material as shown in Fig. 6.30-Fig. 6.38 [28]. IPRD of P/M materials plays a vital role in modifying microstructure and mechanical properties of different parts in automobile and aerospace industries. The level of porosity decreased with increasing IPRD of preforms which facilitates faster diffusion rate of grains during hot extrusion. Therefore, the average DRX grain size increased with increasing IPRD. The DRX grain size increased with increase in IPRD due to higher initial preform density which provides higher deformation time. A homogeneous grain formation was observed in samples extruded with higher IPRD. Fig. 6.60 shows the plots of average DRX grain size of 70%, 80% and 90% IPRD samples deformed at 550 °C and 0.1 s^{-1}. The average DRX grain size of 70%, 80% and 90% IPRD samples extruded at 550 °C and 0.1 s^{-1} were 9.89 µm, 12.45 µm, and 12.67 µm, respectively.

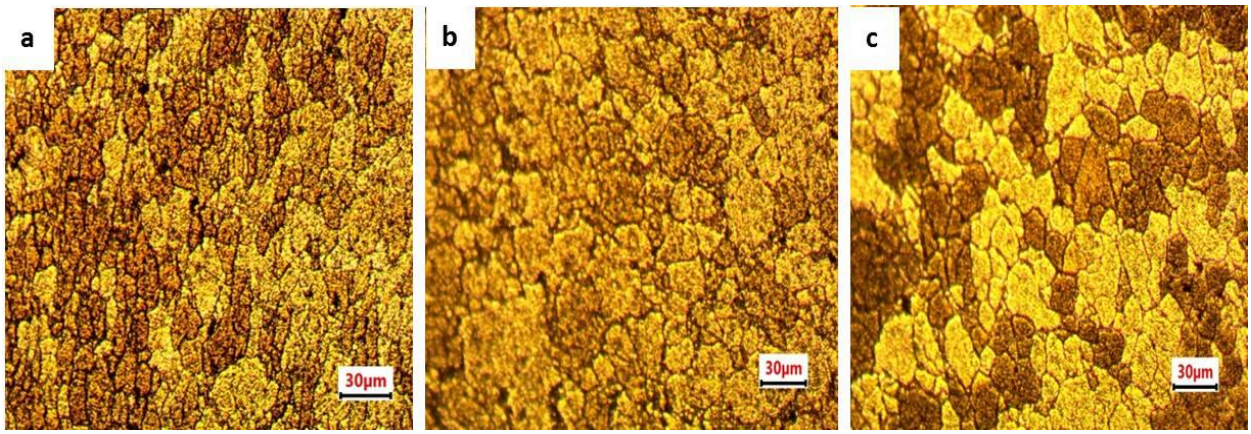

Fig. 6.59 Optical Micrographs of Al-4%Cu-0.5%Mg P/M preforms deformed at constant temperature 550 ^{o}C and strain rate 0.1 s^{-1} at different IPRDs a) 70% b) 80% and c) 90%

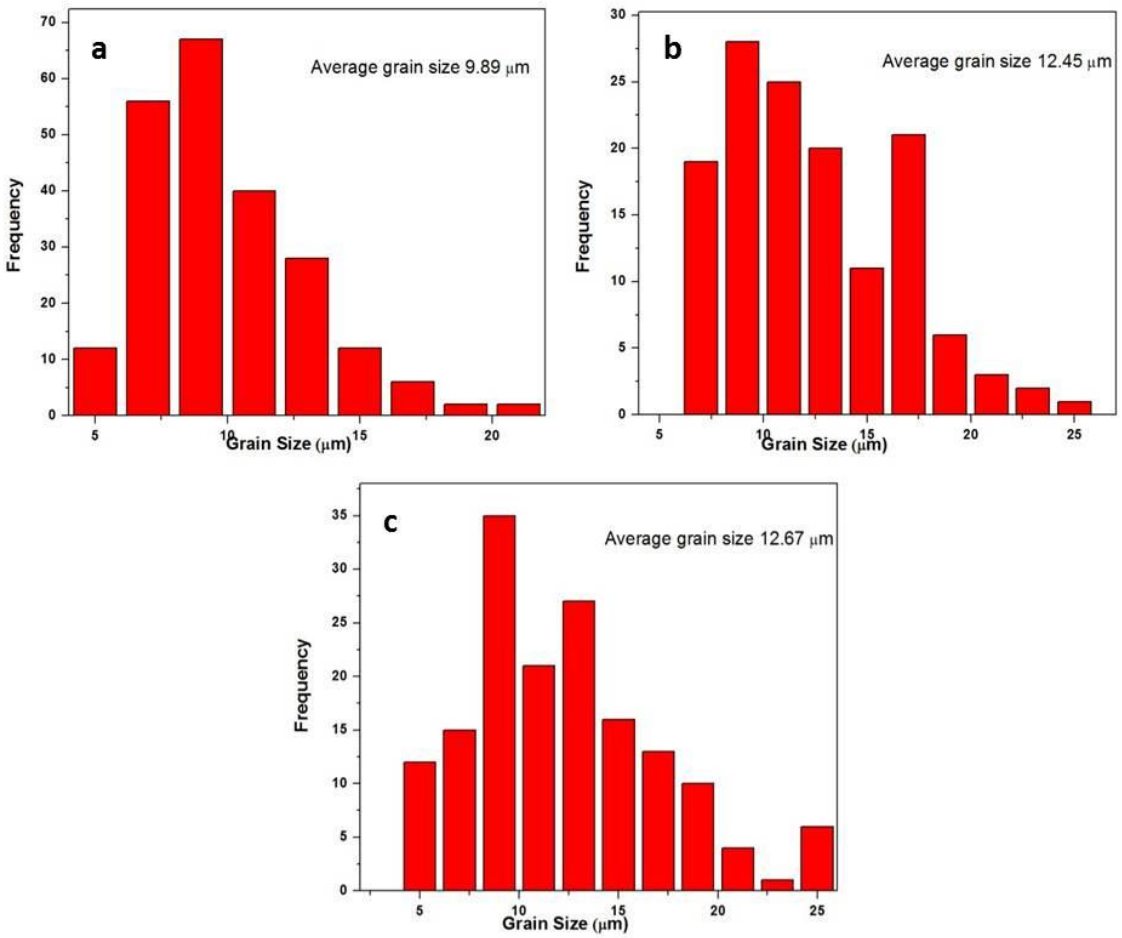

Fig. 6.60 Average DRX grain size distribution of Al-4%Cu-0.5%Mg P/M preforms deformed at constant temperature 550 ^{o}C and strain rate 0.1 s^{-1} at different IPRDs a) 70% b) 80% and c) 90%

6.5.2 Development of microstructure model for hot extruded samples

The microstructure and DRX grains behavior of the cast/wrought material (fully dense) are different from porous materials despite the same chemical compositions because of the geometry of the preforms, friction conditions and densification behavior [47]. Therefore, it is interesting to study the grain size evolution and the modeling aspects to predict the DRX grain size of powder preforms with different deformation parameters, such as temperature strain rate and IPRD. In general, the grain size of any material has the direct impact on its mechanical properties and performance. So the grain size control of any material plays significant role in the hot extrusion process. Thus, the aim of the present work is to study the DRX behaviour of Al-Cu-Mg alloy during the hot extrusion tests. The mathematical models of DRX needed to be developed as a function of Zener-Holloman parameter for various IPRDs to predict the DRX grain size.

6.5.2.1 Analysis of flow curves during hot extrusion

Experimental works were performed on sintered Al–4%Cu-0.5%Mg preforms with 70%, 80% and 90% IPRD over temperature ranges of 450 °C – 550 °C and strain rates range of 0.1-0.3 s^{-1}. True stress-true strain curves of Al–4%Cu-0.5%Mg P/M alloys deformed at deformation temperatures of 450 °C, 500 °C and 550 °C and strain rates of 0.1 s^{-1}, 0.2 s^{-1} and 0.3 s^{-1} with IPRDs of 70%, 80% and 90% are shown in Fig. 6.61 - Fig. 6.63. The flow stresses of all the materials decreased with increase in deformation temperature and decrease in strain rate irrespective of IPRD. It is noticed that the flow stress of these materials is very sensitive to the deformation temperature and strain rate. With increasing deformation temperature, the rate of vacancy diffusion and motion of dislocation is increased [345]. Thereby, the grain boundaries mobility was increased and accelerated the growth of DRX grains [346]. In contrast, the DRX grain size decreased with increase in strain rate due to the less time to deform the material. The dynamic softening of material increased with decreasing strain rate and then reduced the flow stress (Fig. 6.61 - Fig. 6.63). It is also observed that the effect of IPRD on flow stress plays a significant role for all tested deformation conditions.

It is observed that the flow stress increased with increasing IPRD irrespective of deformation temperature and strain rate. Initial preform density of 90% IPRD samples was high which facilitated higher diffusion rate of grains during extrusion. The deformation difficulties of the preforms increase as the dislocation movement decreases with increasing IPRD. Therefore, the load required to deform the material increased with increasing IPRD. Applying higher loads overcomes the deformation difficulties and increases the dislocation movement in the preforms during extrusion. As shown in Fig. 6.61- Fig. 6.63, the flow stress curves increased rapidly to a certain strain value and then held constant until they reached higher strain values (PFS). This happened due to the higher dislocation density in the initial stages of deformation and dynamic equilibrium between work hardening and dynamic softening in the next stage. Work-hardening which is caused by the dislocation density is the dominant carrier at lower strain values. The dynamic softening due to dynamic recovery (DRV) and dynamic recrystallization (DRX) occurs finally which neutralize the WH with increasing strain. As a result, the true stress-true strain curves become flat with nearly zero slopes at higher strains.

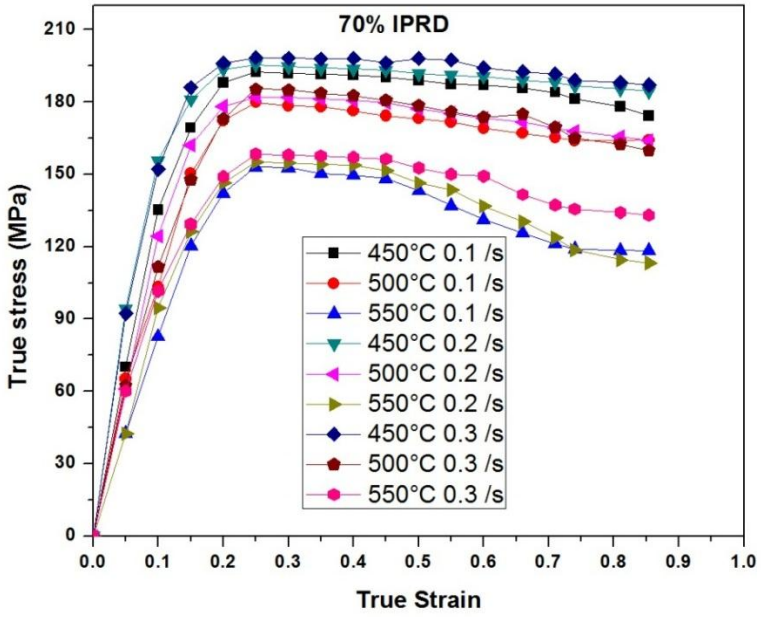

Fig. 6.61 True stress–true strain curves of Al–4%Cu-0.5%Mg P/M alloys for various deformation temperatures and strain rates with IPRD of 70%

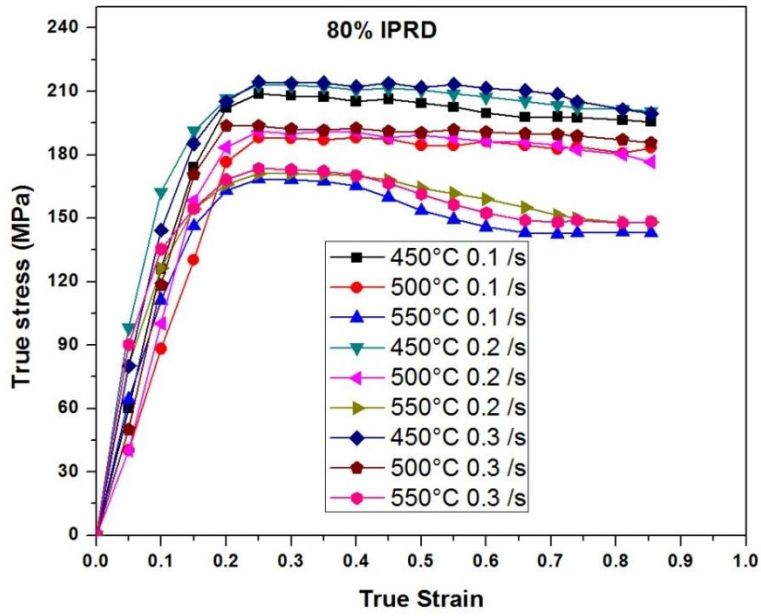

Fig. 6.62 True stress–true strain curves of Al–4%Cu-0.5%Mg P/M alloys for various deformation temperatures and strain rates with IPRD of 80%

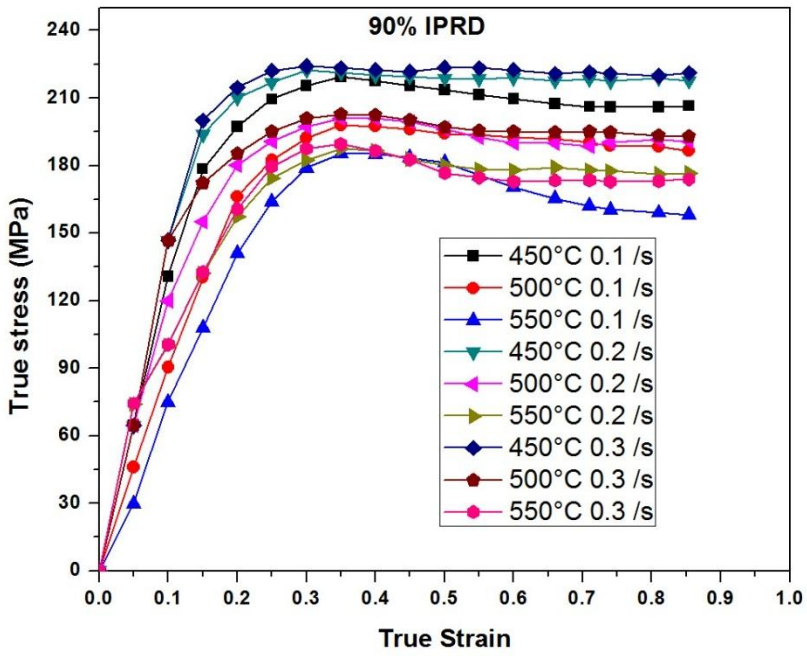

Fig. 6.63 True stress–true strain curves of Al–4%Cu-0.5%Mg P/M alloys for various deformation temperatures and strain rates with IPRD of 90%

6.5.2.2 Calculation of activation energy (Q) and Zener-Hollomon parameter (Z)

As reported by Shaban et al. [266], the DRX grain size mainly depends on deformation parameters such as temperature and strain rate. Accordingly, Zener-Hollomon parameter is used to describe the combined effect of deformation temperature and strain rate [338].

$$Z = \acute{\varepsilon} \exp\left(Q/_{RT}\right) \tag{6.20}$$

where Q is the activation energy (kJ/mol); $\acute{\varepsilon}$ is the strain rate (s^{-1}); R is the universal gas constant (8.314 J mol^{-1} K^{-1}) and T is the absolute temperature (K).

Activation energy (Q) should be calculated first to find the Zener-Hollomon parameter. Activation energy is commonly used to evaluate the hot workability and optimize the hot working process of materials as it indicates the degree of difficulties during hot deformation [347, 348]. The constitutive equation, which includes the responses of flow stress, deformation temperature and strain rate is derived using activation energy. For aluminium and its alloys, the activation energy is affected notably by the initial preform microstructure because the solute atoms are able to diffuse to dislocation cores and are pinned at the dislocation [212, 255]. Arrhenius type constitutive equation is the most commonly used model to calculate the

activation energy of material during hot deformation. The Arrhenius-type equation for all the stress levels can be written as [349]:

$$\acute{\varepsilon} = A\,[\sinh(\alpha\sigma)]^n\, exp\left(-Q/_{RT}\right) \tag{6.21}$$

Where A = material constant; έ = strain rate (s^{-1}); n = material stress index; α is the stress multiplier; Q = the activation energy (kJ/mol); σ is the flow stress (MPa); T is the deformation temperature (K) and R is the universal gas constant (8.314 J/mol.K).

The procedure to calculate the activation energy and Zener-Hollomon parameter is clearly explained in section 6.4. The activation energy and Zener-Hollomon parameter values of sintered Al-4%Cu-0.5%Mg preforms deformed at different conditions are represented in Table 6.3. As can be seen from Table 6.3, the activation energy decreased with increasing deformation temperature and strain rate. In general, the hot deformation activation energy for metals and alloys can qualitatively represent the energy barrier to dislocation motion during hot deformation. The presence of higher value of hot deformation activation energy denotes the presence of higher dragging forces to the motion of the dislocations in hot deformation [341]. The activation energy parameter for a material provides prime information about the deformation mechanisms involved in microstructure evolution, in particular the movement of dislocation, dynamic recovery, dynamic recrystallization and the grain boundary motion [247].

Table 6.3 Activation energy and Zener-Hollomon parameter values of sintered Al-4%Cu-0.5%Mg preforms deformed with different deformation parameters

Deformation temperature (K) (°C)	Strain rate (s^{-1})	70% IPRD		80% IPRD		90% IPRD	
		Q (kJ/mol)	Z (s^{-1})	Q (kJ/mol)	Z (s^{-1})	Q (kJ/mol)	Z (s^{-1})
723 (450)	0.1	223.88	1.49E+15	238.15	1.6E+16	246.36	6.25E+16
723 (450)	0.2	221.15	1.89E+15	232.78	1.31E+16	240.58	4.78E+16
723 (450)	0.3	218.42	1.8E+15	227.90	8.7E+15	232.88	1.99E+16
773 (500)	0.1	220.47	7.87E+13	235.36	7.98E+14	243.69	2.92E+15
773 (500)	0.2	217.78	1.04E+14	230.05	6.98E+14	237.98	2.4E+15
773 (500)	0.3	215.09	1.02E+14	225.22	4.94E+14	230.37	1.1E+15
823 (550)	0.1	217.20	6.08E+12	230.73	4.39E+13	243.06	2.66E+14
823 (550)	0.2	214.55	8.25E+12	225.53	4.1E+13	237.36	2.31E+14
823 (550)	0.3	211.90	8.41E+12	220.80	3.08E+13	229.76	1.14E+14

6.5.2.3 Development of microstructural modeling for deformed Al P/M preforms

The relation between average DRX grain size and Z parameter is shown as [350],

$$d_{dyn} = A_{dyn} Z^{n_{dyn}} \quad (6.22)$$

Where d_{dyn} refers to the DRX grain size, A_{dyn} and n_{dyn} represent material constants.

The above equation used to develop a mathematical model and also to predict the DRX grain size of extruded preforms. The correlation between Z parameter and average DRX grain size of hot extruded P/M Al-4%Cu-0.5%Mg alloy was established by fitting power law in the form of Eq. (6.22) for different IPRDs as shown in Fig. 6.64-Fig. 6.66. For different IPRDs, such as 70%, 80% and 90%, mathematical models were developed between Z parameters and average DRX grain size (measured from microstructures of samples). These average DRX grain sizes of samples for different conditions were taken from section 6.5.1 for developing a mathematical

model. The correlation between Z parameter and average DRX grain size is expressed as follows.

The developed mathematical models are:

For 70% IRD $d_{dyn} = 18.44Z^{-0.026}$ $R^2 = 0.936$ (6.23)

For 80% IRD $d_{dyn} = 24.848Z^{-0.0268}$ $R^2 = 0.942$ (6.24)

For 90% IRD $d_{dyn} = 26.498Z^{-0.028}$ $R^2 = 0.965$ (6.25)

It is noticed from Fig. 6.64 - Fig. 6-66 that the DRX grain size is inversely proportional to the Z parameter. The average DRX grain size of extruded materials increased with increasing deformation temperature and decreasing strain rate as shown in Fig. 6.55 and Fig. 6.58. According to Eq. (6.22), the Z parameter decreased with increasing deformation temperature and decreasing strain rate. Hence, the DRX grain size decreased with increasing Z parameter as shown in Fig. 6.64 - Fig. 6.66. The mobility of DRX grain boundaries increased with increasing deformation temperature and decreasing strain rate. The growth of DRX grains increased with decreasing strain rate due to the availability of deformation time. Therefore, it is observed that the DRX grain size and Z parameter were dependent on deformation temperature and strain rate. The microstructures with a great amount of precipitates developed and were associated with the Z values. Lower distribution of precipitates in the grain interior and matrix, and high formation of DRX grains was observed at lower Z values and/or higher temperature (Fig. 6.54f). At high Z values, high dislocation density and considerably finer precipitates were observed (Fig. 6.54d). These precipitates developed serrations in the grain boundaries and resulted DRV and DRX due to dynamic flow softening. DRX is easily occurred with lowering the Z values which means large extent of dynamic softening happened.

The material constants such as A_{dyn} and n_{dyn} are determined from the mathematical models developed earlier (Eq. 6.23-6.25) for 70%, 80% and 90% IPRDs as shown in Table 6.4. It is observed that the material constant n_{dyn} decreased with increasing IPRD. As already explained, decreasing the Z parameter leads to increase in average DRX grain size and the Z parameter values increased with increasing IPRD (Table 6.3). Hence, the average DRX grain size increased with increasing IPRD (Fig. 6.60). The level of porosity decreased with increasing IPRD of preforms which facilitated faster diffusion rate of grain during hot extrusion. Time for

deformation of preforms increased with increasing IPRD, leading to increase in DRX grain size with increasing IPRD during extrusion (Fig. 6.59 & Fig. 6.60). The developed mathematical models can also be utilized to calculate the DRX grain size of deformed Al-4%Cu-0.5%Mg P/M preforms for different IPRDs.

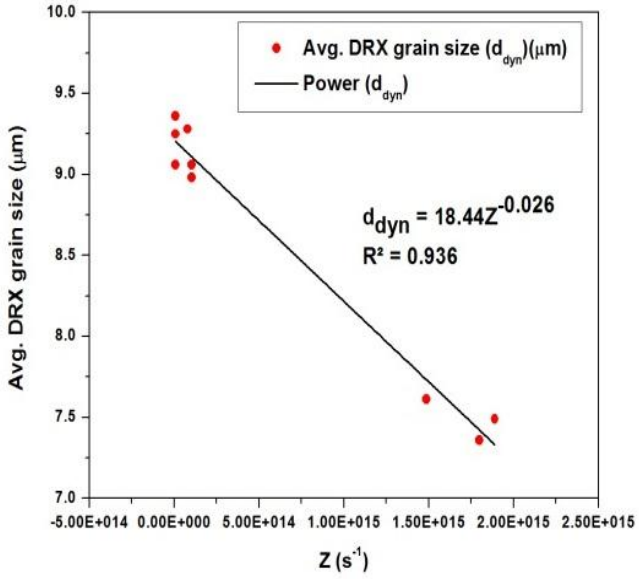

Fig. 6.64 Correlation between Z parameters and average DRX grains size of 70% IPRD Al–4%Cu-0.5%Mg P/M alloy deformed at different temperature and strain rate

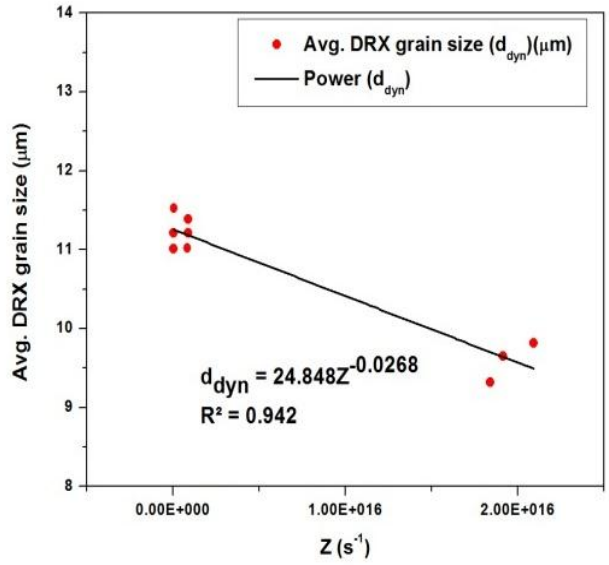

Fig. 6.65 Correlation between Z parameters and average DRX grains size of 80% IPRD Al–4%Cu-0.5%Mg P/M alloy deformed at different temperature and strain rate

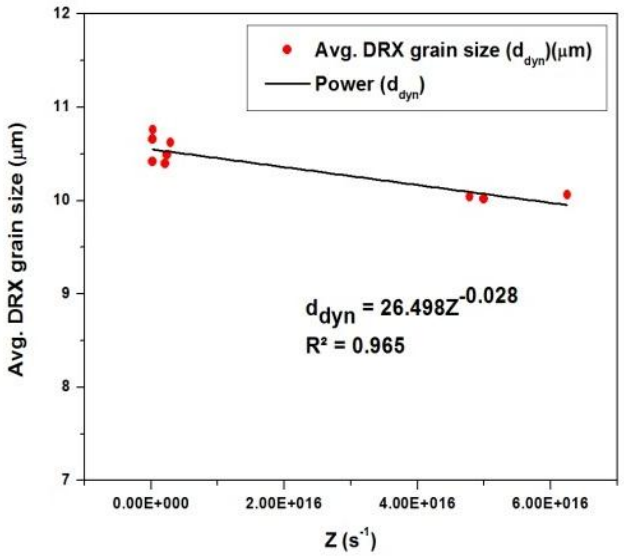

Fig. 6.66 Correlation between Z parameters and average DRX grains size of 90% IPRD Al–4%Cu-0.5%Mg P/M alloy deformed at different temperature and strain rate

Table 6.4 A_{dyn} and n_{dyn} values of deformed samples with different IPRDs

IPRD (%)	A_{dyn}	n_{dyn}
70	18.44	-0.0260
80	24.84	-0.0268
90	26.49	-0.028

6.5.2.4 Verification of developed microstructural model

In order to evaluate the developed microstructure model for hot extruded Al-4%Cu-0.5%Mg P/M preform, the average DRX grain size of extruded samples at different deformation temperatures (450 °C, 500 °C and 550 °C) and strain rate of 0.1 s^{-1}, 0.2 s^{-1} and 0.3 s^{-1} with different IPRDs were measured and shown in Fig. 6.55, Fig. 6.58 and Fig. 6.60. The DRX grain size for all the deformation conditions were calculated using the model developed, as shown in Table 6.5. The comparison between experimental (measured) DRX grain size (d_m) and mathematically calculated DRX grain size (d_c) at different processing conditions with different IPRDs is shown in Fig. 6.67 to Fig. 6.69. These plots show the accuracy of developed microstructure model for sintered Al-4%Cu-0.5%Mg alloy deformed at different deformation parameters. It is clearly observed from the figures that most of the calculated data points and measured data points lie very close to the best fit line and show the perfect correlation between the results. The R^2 values between calculated and measured DRX grain size were found to be

0.946, 0.955 and 0.957 for 70%, 80% and 90% IPRDs, respectively. The prediction capability and correlation coefficient (R^2) increased with increasing IPRD.

The accuracy of the developed model was also confirmed by standard statistical parameters - absolute error (δ) and mean absolute error (δm). These parameters were determined from measured and calculated average DRX grain size values using Eq. (6.26).

$$\delta = \left|\frac{d_c - d_m}{d_m}\right| \times 100\% \tag{6.26}$$

Table 6.5 shows the measured and calculated average DRX grain size and mean absolute error values for hot extruded Al-4%Cu-0.5%Mg sintered preforms at different deformation conditions. The absolute error for different conditions did not exceed 9.96% while the mean absolute error did not exceed 8.34% as shown in Table 6.5. The developed model is reliable and accurate as these values did not exceed 10% [351]. The results also depict that the measured and calculated average DRX grain size are in good agreement with each other. Therefore, the results revealed that the developed microstructure model reflects excellent predictability and accuracy for hot extruded Al-4%Cu-0.5%Mg sintered preforms for different deformation conditions.

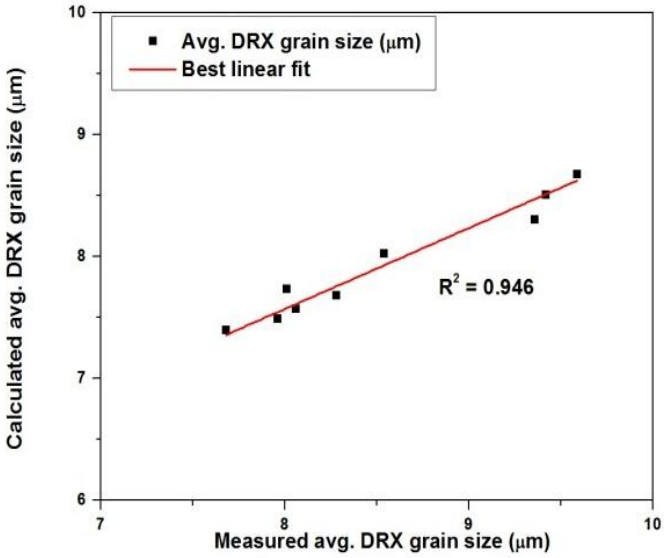

Fig. 6.67 The relationship between calculated and measured average DRX grain size of sintered Al-4%Cu-0.5%Mg alloy preforms deformed with 70% IPRD

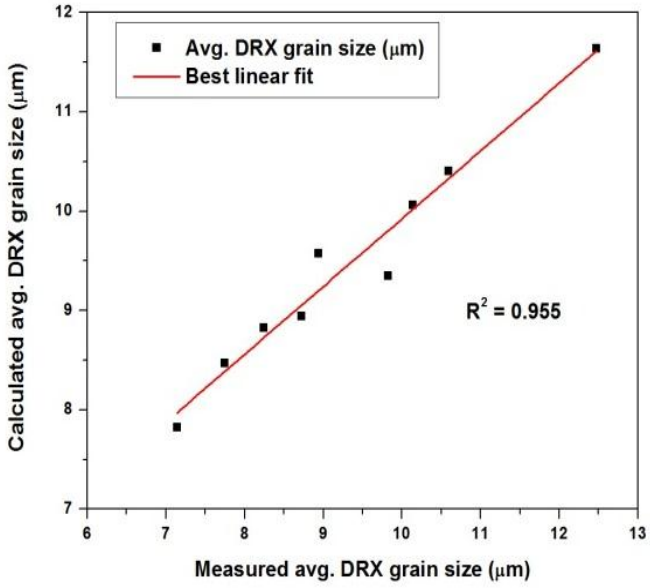

Fig. 6.68 The relationship between calculated and measured average DRX grain size of sintered Al-4%Cu-0.5%Mg alloy preforms deformed with 80% IPRD

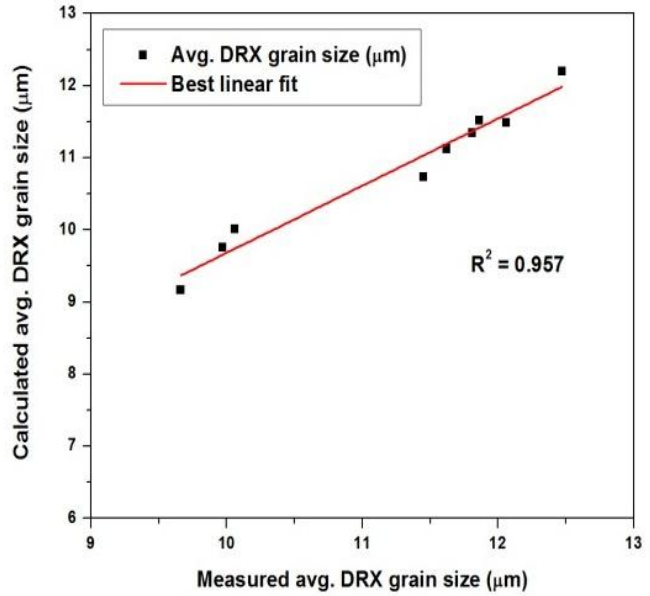

Fig. 6.69 The relationship between calculated and measured average DRX grain size of sintered Al-4%Cu-0.5%Mg alloy preforms deformed with 90% IPRD

Table 6.5 Measured and calculated DRX grain size of P/M Al-4%Cu-0.5%Mg preforms during hot extrusion at different parameters

Extrusion temperature (K)	Strain rate (1/s)	IPRD = 70%				IPRD = 80%				IPRD = 90%			
		d_m	d_c	δ (%)	δm (%)	d_m	d_c	δ (%)	δm (%)	d_m	d_c	δ (%)	δm (%)
723	0.1	8.01	7.43	7.17	**5.01**	9.82	9.35	4.75	**7.14**	10.06	9.26	7.93	**6.79**
723	0.2	7.49	7.38	1.34		8.24	8.82	7.09		9.27	9.03	2.50	
723	0.3	6.85	7.29	6.54		7.14	7.82	9.59		7.43	8.17	9.96	
773	0.1	8.74	8.02	8.17	**6.08**	10.59	9.84	7.07	**7.80**	11.91	10.84	8.94	**8.34**
773	0.2	7.92	7.96	0.61		8.94	9.57	7.10		10.49	9.82	6.31	
773	0.3	7.28	7.97	9.48		7.75	8.46	9.25		8.72	9.57	9.78	
823	0.1	9.89	8.97	9.22	**6.95**	12.47	11.64	6.64	**4.77**	12.67	11.70	7.64	**5.90**
823	0.2	8.24	8.51	3.27		10.14	10.66	5.13		10.66	10.49	1.56	
823	0.3	7.48	8.11	8.36		8.72	8.94	2.55		9.54	10.35	8.51	

6.6 Simulation studies of hot extruded Al-Cu-Mg P/M alloys

Extensive finite element analysis (FEA) based simulation studies were performed to examine the metal flow, the stress behaviour and the corresponding strain induced,. The quality of a material can be analyzed by extensive finite element studies at different process parameters. FEM based simulations were conducted on Al-Cu-Mg alloys extruded at different temperature, strain rate and IPRD. The process parameters used for FEM studies were same as hot extrusion studies such as:

I. Die temperature (550 ^{o}C, 575 ^{o}C, and 600 ^{o}C)
II. Strain rate (0.1 s^{-1}, 0.2 s^{-1}, and 0.3 s^{-1})
III. Extrusion ratio (4)
IV. Die approach angle (30^{o})
V. IPRD (70%, 80% and 90%)

DEFORM-2D simulation software was used as a tool to simulate the hot extruded Al alloy samples. The workpieces with cylindrical shape (Φ 15×15 mm) were used for simulation studies. Axisymmetric analyses were used for the FEM simulation to decrease the simulation time. An Arrhenius type constitutive equation was used in all simulation studies i.e., $\dot{\varepsilon} = A[\sinh(\alpha\sigma)]^{n}\exp[-$

Q/RT]. All the constant values were taken from the constitutive modeling studies (section 6.4) for simulation studies and shown in Table 6.6-6.8. The workpiece was set as porous for all three temperatures, strain rates and IPRDs. The bottom and top die were set as rigid. Constant shear friction was considered between die and workpiece and coefficient of friction m=0.4 was assumed between top die to workpiece and workpiece to bottom die in all simulations.

Table 6.6 Constant values used for simulation of 70% IPRD sample at different deformation parameters

Temperature (K)	**έ (/s)**	**n'**	**m**	**Q**	**Z**
723	0.1	16.42	1.64	223.88604	1.49E+15
723	0.2	16.42	1.62	221.15573	1.89E+15
723	0.3	16.42	1.6	218.42541	1.8E+15
773	0.1	16.17	1.64	220.4773	7.87E+13
773	0.2	16.17	1.62	217.78856	1.04E+14
773	0.3	16.17	1.6	215.09981	1.02E+14
823	0.1	15.93	1.64	217.20491	6.08E+12
823	0.2	15.93	1.62	214.55607	8.25E+12
823	0.3	15.93	1.6	211.90723	8.41E+12

Table 6.7 Constant values used for simulation of 80% IPRD sample at different deformation parameters

Temperature (K)	έ (/s)	n'	m	Q	Z
723	0.1	19.58	1.46	238.15902	1.6E+16
723	0.2	19.58	1.43	232.78701	1.31E+16
723	0.3	19.58	1.4	227.90337	8.7E+15
773	0.1	19.35	1.46	235.36144	7.98E+14
773	0.2	19.35	1.43	230.05254	6.98E+14
773	0.3	19.35	1.4	225.22626	4.94E+14
823	0.1	18.97	1.46	230.73936	4.39E+13
823	0.2	18.97	1.43	225.53471	4.1E+13
823	0.3	18.97	1.4	220.80321	3.08E+13

Table 6.8 Constant values used for simulation of 90% IPRD sample at different deformation parameters

Temperature (K)	έ (/s)	n'	m	Q	Z
723	0.1	23.15	1.28	246.36045	6.25E+16
723	0.2	23.15	1.25	240.58638	4.78E+16
723	0.3	23.15	1.21	232.88761	1.99E+16
773	0.1	22.9	1.28	243.69997	2.92E+15
773	0.2	22.9	1.25	237.98825	2.4E+15
773	0.3	22.9	1.21	230.37263	1.1E+15
823	0.1	22.84	1.28	243.06145	2.66E+14
823	0.2	22.84	1.25	237.3647	2.31E+14
823	0.3	22.84	1.21	229.76903	1.14E+14

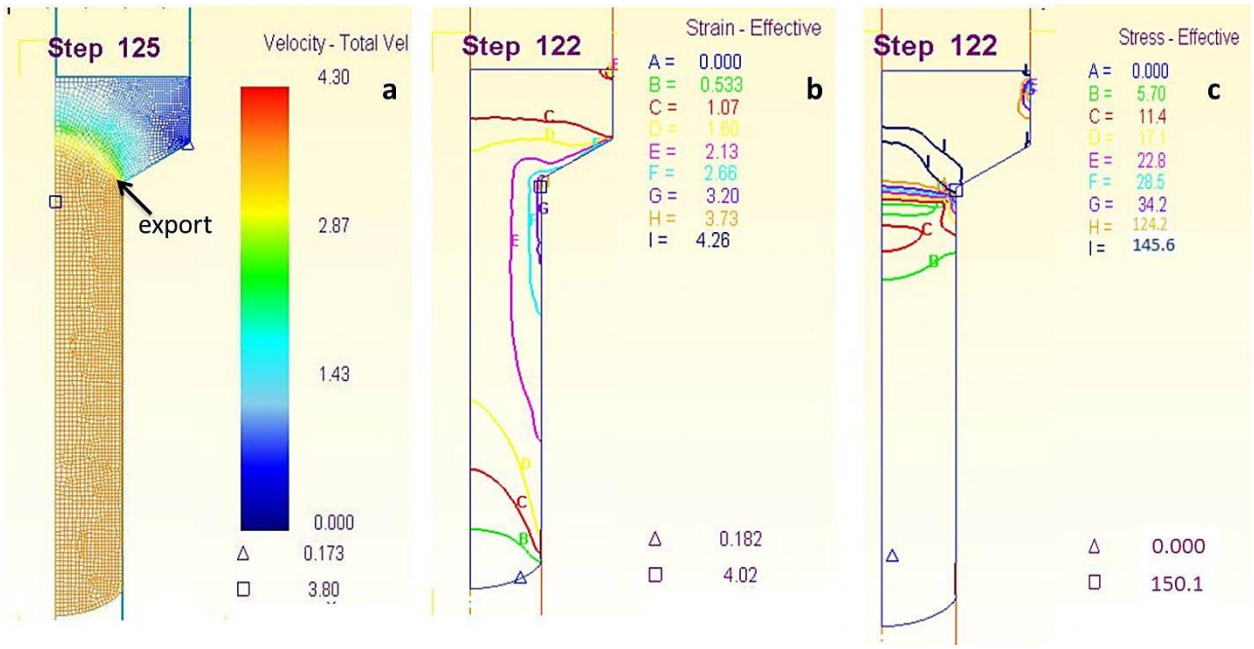

Fig. 6.70 Extrusion process with billet and die temperature 550˚C, Strain rate of 0.1 s^{-1} with 90% IPRD (a) velocity contour line at 125 step (b) effective strain contour line at 122 step (c) effective stress contour line at 122 step

Fig. 6.70 shows the velocity, effective strain and stress distribution of 90% IPRD sample extruded at a deformation temperature of 550˚C and strain rate of 0.1 s^{-1}. The metal near skin flows slowly due to the friction between billet and container/die. The velocity at the centre of the billet was higher compared to skin. The maximum velocity of the material was higher at the entrance of export and the flow resistance of material was lower when the billet comes down to export (Fig. 6.70a). The progression of the top die across the bottom die created different deformation zones, such as, centre zone, rigid zone, dead zone and shear zone as shown in Fig. 6.71. The shear zone was found along the wall of the extrusion die and mainly at the export. The metal near the die angle hinders the flow due to the friction and forms dead metal zone. Velocity of the material was low at dead metal zone. The velocity of the material increased with increasing deformation temperature and strain rate. The formation of dead zone and shear zone in the extruded samples was decreased with increasing temperature and strain rate and formed homogeneous and uniform microstructure as explained earlier. The effective strain distribution (Fig. 6.70b) was non-uniform in extruded products. The effective strain progressively increases from the centre to the skin of the material. This was because the flow velocity gradient of the material near the skin was higher than at the centre which increased the strain. The centre of the extruded rod always has 3 dimensional compression stresses. The metal near the export is easy to

deform and the deformed zone becomes larger with increasing stem stroke. The metal near the skin forms elongated grains in particular conditions (point 2 in Fig. 6.71). The effective-stress during extrusion is high at the entrance of the export (Fig. 6.70c). The same stress shows from skin to centre of the billet but this starts decreasing in the material when the material goes down to export. The effective stress and strain decreased with increase in deformation temperature (Fig. 6.72) and decrease in strain rate and IPRD (Fig. 6.73). At 550 ^{o}C, the effective stress in 90% IPRD material extruded at 0.1 s^{-1} is lower than at other temperatures and was 187.2 MPa (Fig. 6.72c).

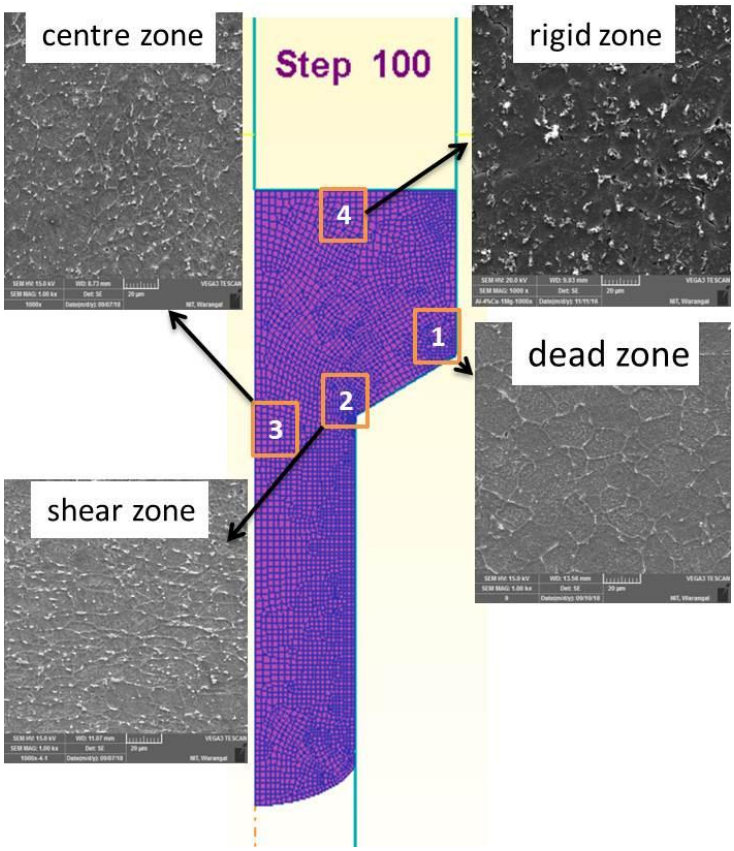

Fig. 6.71 Different deformation zones formed during the extrusion

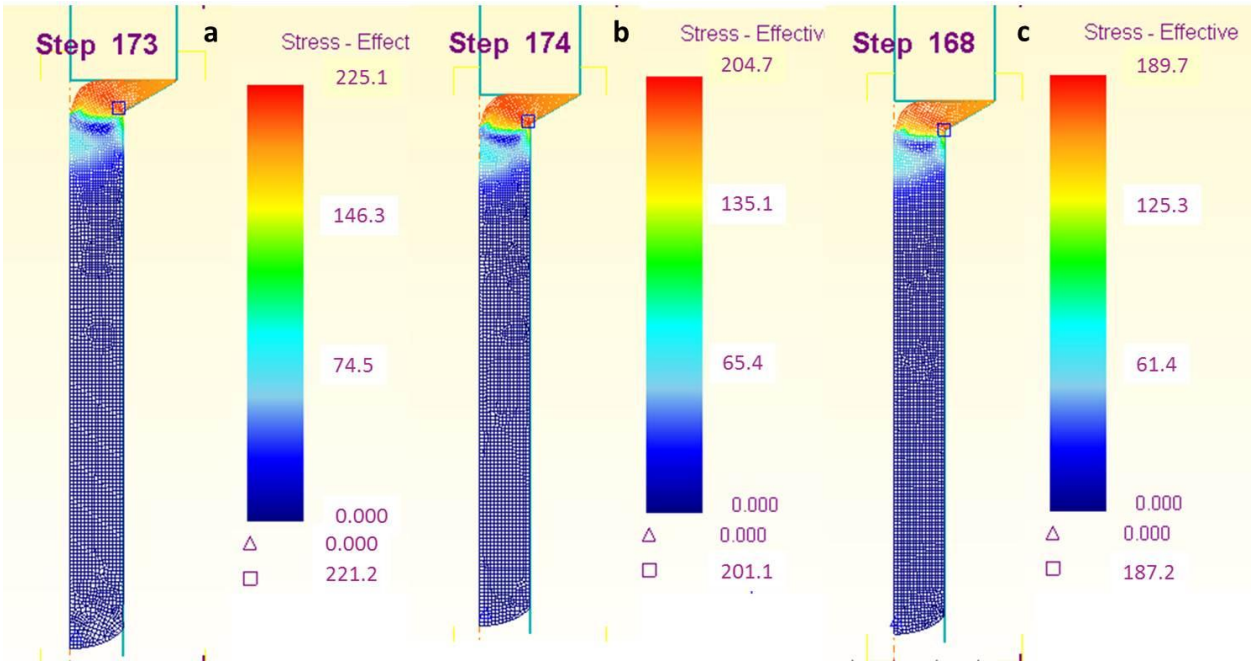

Fig. 6.72 Effective stress distribution of extruded samples at a) 450 ^{o}C, b) 500 ^{o}C, c) 550 ^{o}C with 0.1 s^{-1} strain rate and 90% IPRD

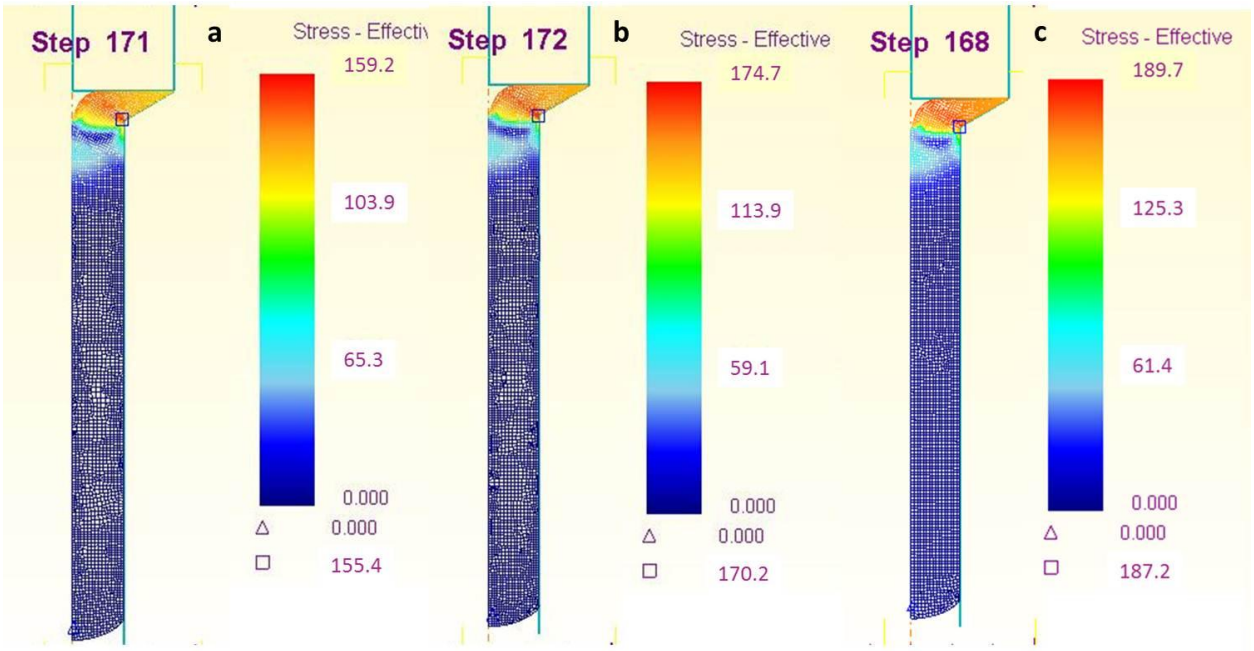

Fig. 6.73 Effective stress distribution of extruded samples with different IPRDs a) 70%, b) 80%, c) 90% deformed at 550 ^{o}C and 0.1 s^{-1}

The distribution of strain is uniform in case of samples extruded at 550 ^{o}C due to high liquid fraction compared to the other two temperatures (Fig. 6.74). Softness is increased and

resistance to deformation is decreased with increasing temperature, so that effective strain is reduced with increasing deformation temperature. The experimental flow stress results (taken from section 6.3.1) were verified with the simulation results. Fig. 6.75 shows the correlation between experimental flow stress values and simulation flow stress values. Most of the measured and calculated peak flow stress values are close to the best fit line which reflects the accuracy of the experimental and simulation results. The R^2 values between measured and simulated results are found to be 0.969, 0.989 and 0.991 for IPRDs of 70%, 80% and 90%, respectively, which indicates the simulated flow stress values agreed well with the experimental flow stress values for the deformation conditions tested for the purpose.

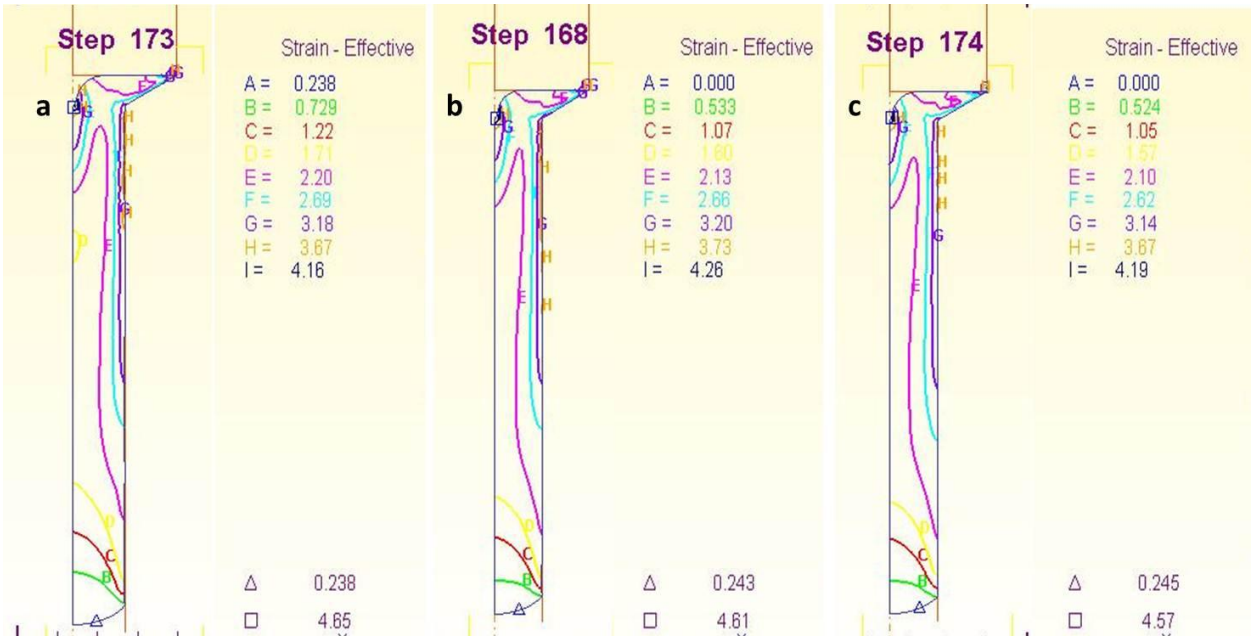

Fig. 6.74 Effective strain distribution of 90% IPRD extruded samples at a) 450 ^{o}C, b) 500 ^{o}C, c) 550 ^{o}C with 0.1 s^{-1} strain rate

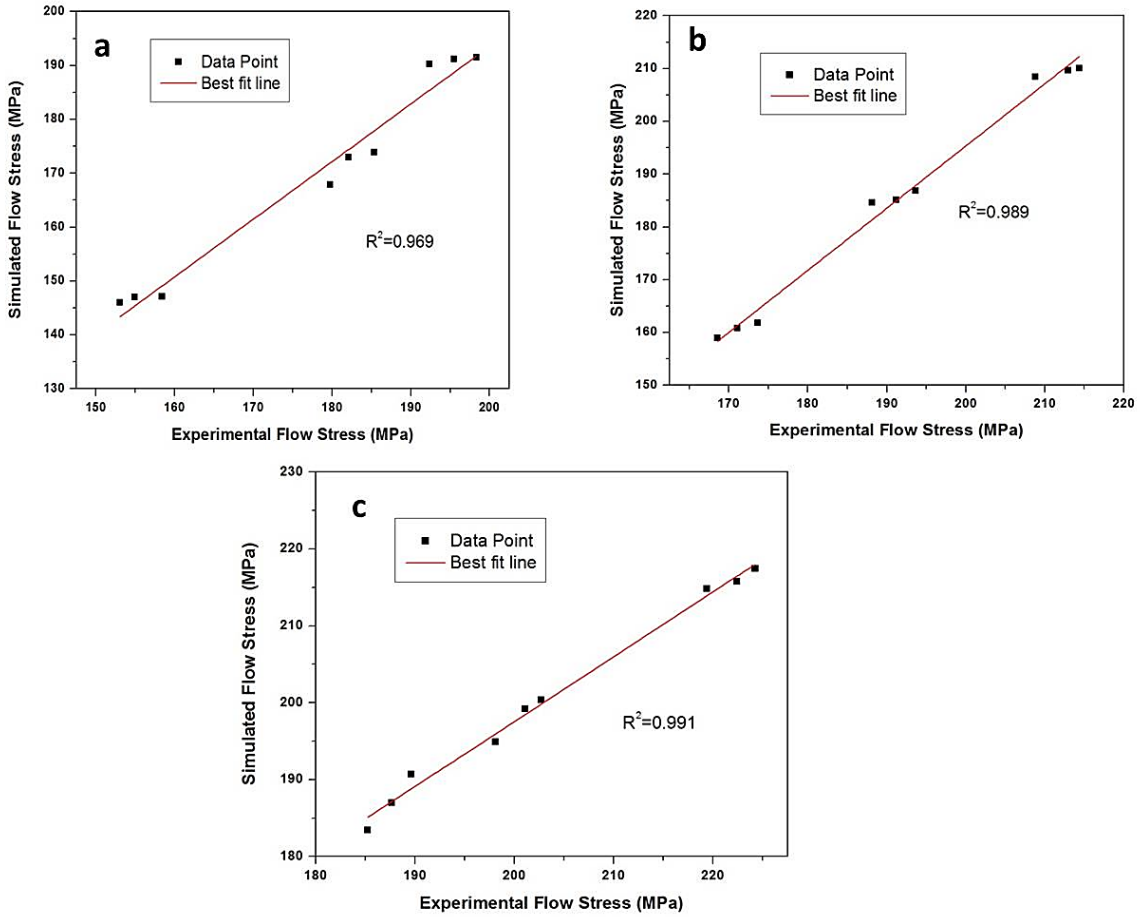

Fig. 6.75 Correlation between experimental and simulated flow stresses: a) 70% IPRD, b) 80% IPRD and c) 90% IPRD

6.7 Microstructure and mechanical properties evolution of hot extruded samples

A systematic study was carried out to establish a structure-property correlation of Al-Cu-Mg P/M alloys as a function of extrusion temperature and strain rate. Only 90% IPRD samples were chosen for these analyses as they showed higher density (Fig. 6.43) and micro-hardness values (Fig. 6.44) after hot extrusion. Samples extruded at 450 °C, 500 °C and 550 °C and strain rates of 0.1 s^{-1}, 0.2 s^{-1} and 0.3 s^{-1} with 90% IPRD were taken into consideration for these analyses.

6.7.1 Microstructure evolution of the hot extruded samples

6.7.1.1 Evolution of microstructures: SEM study

SEM microstructures of the extruded samples at different temperatures and strain rates are illustrated in Fig. 6.76 & Fig. 6.77. No porosity was observed in any of the microstructures. Therefore, the extrusion ratio, approach angle, and parameters used for extrusion were high enough to produce fully densified products from powder compacts. The initial microstructure (sintered) of Al-4%Cu-0.5%Mg with coarser and non-uniform grains has been shown in Fig. 6.76a. Fig. 6.76 (b-d) show SEM microstructures of the samples extruded at 450 °C-550 °C with a fixed strain rate of 0.1 s^{-1}. The microstructures comprised elongated and fine equiaxed grains. The alloying addition, especially Mg, retards the DRV by reducing stacking fault energy (SFE) of Al. Besides, the solute drag effect of Mg reduces the dislocation mobility which is necessary for the occurrence of recovery. As a consequence, Mg hampers the recovery and promotes the recrystallization directly. The grain boundary migration (growth kinetics) increased with increasing deformation temperature which increased the rate of DRX and eventually led to a homogenized microstructure. Further, the size of the recrystallized grain increased with increasing temperature. Coarse and partially recrystallized grains can be observed in the case of sample extruded at 450 °C with 0.1 s^{-1} (Fig. 6.76b). The dislocation density in the subgrains and boundary decreased with increasing deformation temperature and the subgrains began to change from elongated shape to equiaxed shape with decreasing dislocation density as shown in Fig. 6.76c & d. The dynamic recrystallization prevailed with increasing deformation temperature. Accordingly, microstructure with more or less fully DRX grains was produced in the sample deformed at 550 °C with 0.1 s^{-1} (Fig. 6.76d). The average DRX grain size increased with increasing deformation temperature as shown in Fig. 6.76 (e-g). The average grain size of samples deformed at 450 °C, 500 °C and 550 °C were 10.66±4.1 µm, 11.91±4.9 µm, and 12.67±5.3 µm, respectively. The grain refinement during deformation at elevated temperatures occurs by the deformation-induced continuous reaction in Al-alloys which is very similar to continuous DRX [352]. CDRX occurs by the accumulation of dislocations in subgrains, resulting in increasing misorientation angle. These subgrains (LABs) merge and convert into HABs after reaching a critical value of misorientation during deformation. Driving force for the migration of grain boundaries increased with increasing deformation temperature and hence resulted in accelerated CDRX. In addition, geometric dynamic recrystallization (GDRX) might have taken

place during deformation. Uniformly dispersed solutes and fine particles within the matrix interacted with dislocations which would have reduced the DRV and thus the stored energy might have increased the DRX process during hot deformation. This DRX process led to grain refinement, leading to GDRX as defined by Doherty et al. [206]. The presence of precipitates and high-density fine particles acted as an effective barrier to the dislocation movement and consequently prevented the occurrence of discontinuous dynamic recrystallization (DDRX) in all deformation temperatures from 450 °C-550 °C. A wide distribution of precipitates and dispersoid phases can be observed in microstructures shown in Fig. 6.76 & Fig. 6.77 (white arrows). All these phases were analyzed by EDS and EPMA and confirmed as α-Al, Al_2Cu (θ) and Al_7Cu_2Fe (ω) shown in Fig. 6.78 and Fig. 6.83, respectively. Fig. 6.78b and c show the elemental analysis of θ and ω phases. These secondary phase particles play a vital role in the evolution of microstructure and mechanical properties during deformation. Al_2Cu phase formed uniformly in the matrix increases the mechanical properties of Al-Cu-Mg deformed materials. This phase is very sensitive to elevated temperatures and easy to be cut by dislocations during extrusion at higher temperatures. Consequently, it was observed that the amount of Al_2Cu phase was reduced with increasing deformation temperature.

Another secondary phase formed during the deformation process was Al_7Cu_2Fe (ω) which came from the base Al and Cu powders during the atomization process. This phase is also called dispersoid phase as it is utilized for the dispersion strengthening of deformed materials. This phase was less distributed compared to the phase formed by precipitate hardening (θ-Al_2Cu) and formed as coarser grains (typically>5 μm) along the grain boundaries (Fig. 6.76 & 6.77). The pinning effect of secondary phases on the grain boundaries was weakened by increasing deformation temperature, attributed to an increase in solubility of alloying elements in the matrix. This led to the dissolution of the secondary phase in the matrix, thereby grain boundary merging and sliding. The DRX grain size increased with deformation temperature due to the above phenomenon (Fig. 6.76 (e-g)).

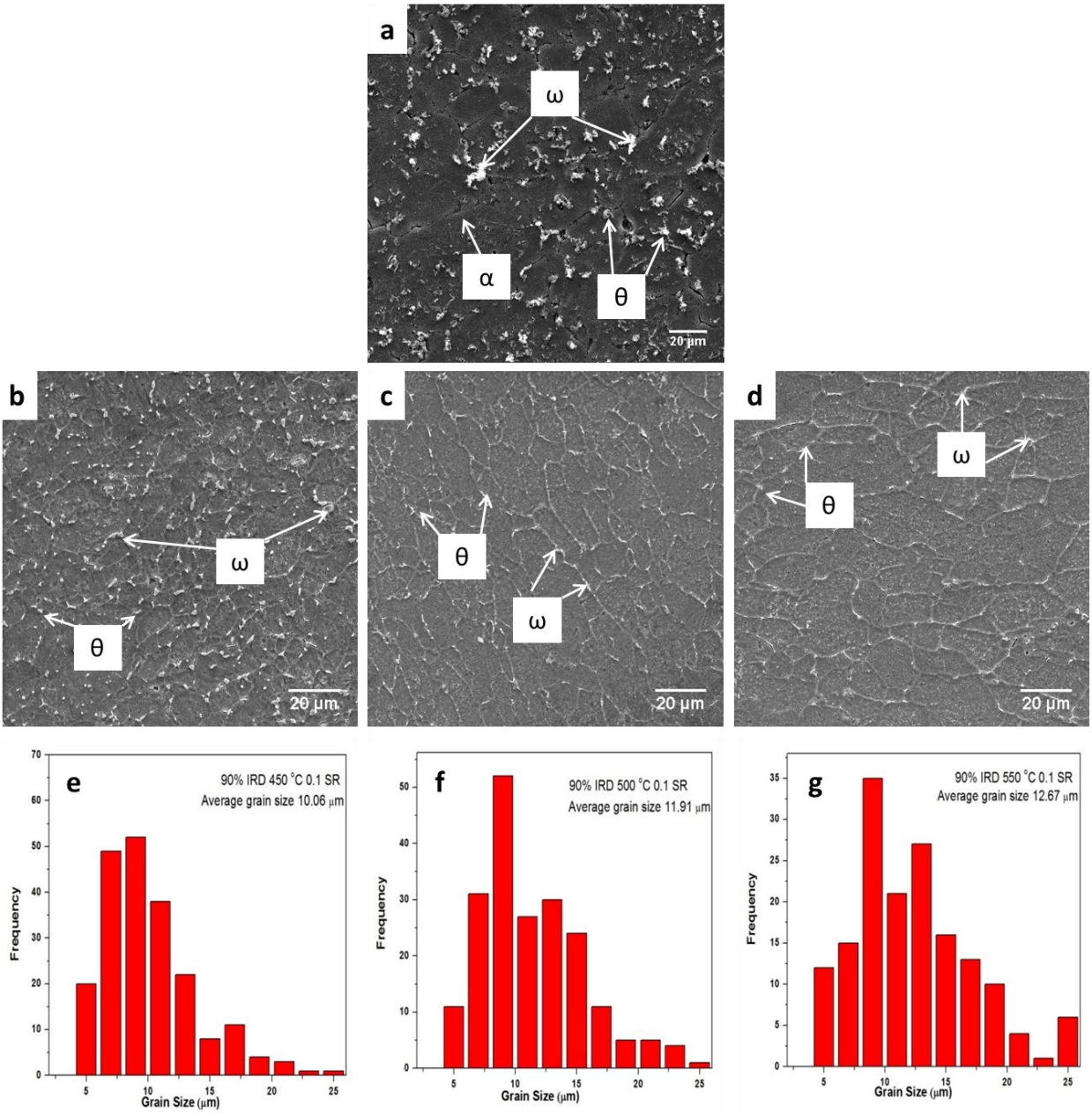

Fig. 6.76 SEM micrographs and corresponding grain size analysis of sintered and extruded samples at different temperatures and same strain rate: **a**. sintered sample, **(b, e)** 450 ^{o}C, 0.1 s^{-1}, **(c, f)** 500 ^{o}C, 0.1 s^{-1}, **(d, g)** 550 ^{o}C, 0.1 s^{-1}

SEM microstructures of samples extruded at 0.1 s^{-1}, 0.2 s^{-1}, and 0.3 s^{-1} strain rates and 550 °C have been shown in Fig. 6.77(a-c). The more significant DRX was observed with lowering strain rates at a given temperature. The DRX was also in close relation with deformation time. The deformation time was reduced with increasing strain rate. Both CDRX and GDRX (migration of original grain boundaries) were possible at a lower strain rate and this

was observed in the sample deformed at 0.1 s^{-1}. On the other hand, fewer and smaller DRX grains were observed due to a rapid increase in stored energy in the samples deformed at 0.3 s^{-1} strain rate (Fig. 6.77c). Deformation at a lower strain rate, coalescence of precipitates and also substantial softening of materials was occurred due to higher deformation time. The strain-induced precipitation was enhanced at a higher strain rate (0.3 s^{-1}), because of higher dislocation density and less coalescence of precipitates due to less available time. During extrusion, the degree of refinement of the microstructure increased with increasing strain rate. The grains were subsequently segmented and formed a higher amount of DRX grains due to higher imposed shear at higher strain rates. From Fig. 6.77(d-f), it can be found that the average recrystallized grain size of samples extruded with strain rates of 0.1 s^{-1}, 0.2 s^{-1}, and 0.3 s^{-1} were 12.51 µm, 10.66 µm, and 9.54 µm respectively. Similar microstructures were observed in the samples extruded at 450 °C and 500 °C deformation temperatures with all strain rates, which are not included in this paper.

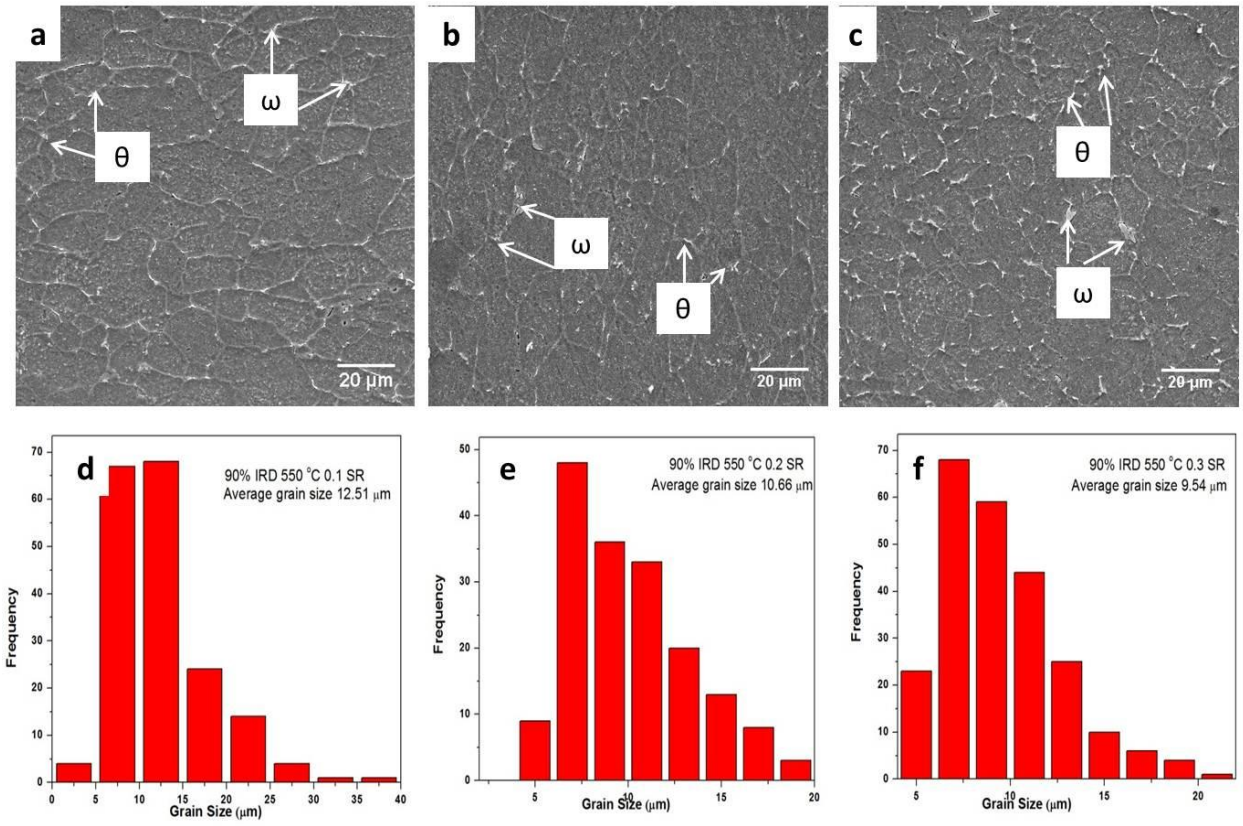

Fig. 6.77 SEM micrographs and corresponding grain size analysis of extruded samples at different strain rates and same deformation temperature: **(a, d)** 550 ^{o}C, 0.1 s^{-1}, **(b, e)** 550 ^{o}C, 0.2 s^{-1}, **(c, f)** 550 ^{o}C, 0.3 s^{-1}

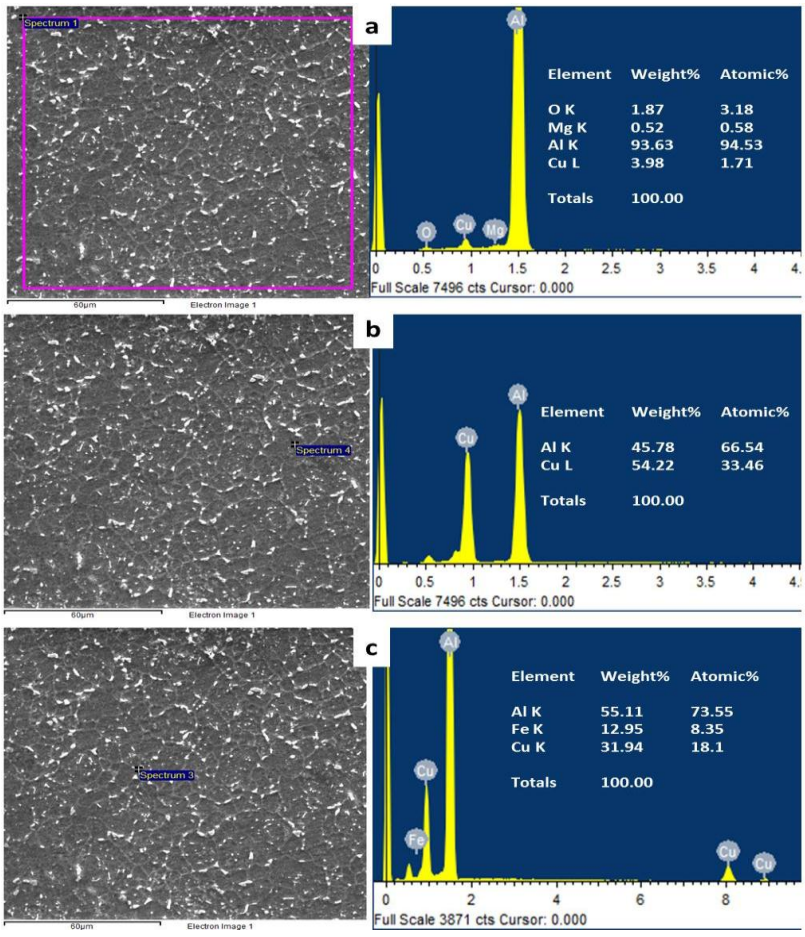

Fig. 6.78 Elemental analysis of extruded sample (450 ^{o}C, 0.1 s^{-1}) at different regions, a. specified region of sample, b. Al_2Cu (θ) phase and c. Al_7Cu_2Fe (ω) phase

6.7.1.2 Evolution of microstructures: EBSD study

The insufficient spatial resolution of optical microscopy (OM) and scanning electron microscopy (SEM) restricts its capability to resolve the finer details of the substructure. Therefore, the electron backscatter diffraction (EBSD) was realized to institute more insight into grain size distribution, recrystallized grain orientation, texture, and phases present in the Al-alloys [353]. Inverse pole figures (IPF) were generated by analyzing the EBSD data to gain more insights into the evolution of microstructures during the hot extrusion process (Fig. 6.79 & 6.80), where grey and black lines represent LABs (misorientation angle: 2°-15°) and HABs (misorientation angle: >15°), respectively. IPFs of extruded samples revealed elongated as well as fine equiaxed grains in their microstructures. Exaggerated interaction between the dislocations led to active annihilation and rearrangement of dislocations, commonly called as “repeated polygonization”

[213], when the material was deformed at 550 °C. This repeated polygonization facilitated the formation of coarse subgrains at 550 °C and equiaxed grains formed eventually, as can be seen in Fig. 6.79c. The original (parent) grains were disintegrated progressively by LABs and formed strain-free grains surrounded by HABs. More prominent DRX was observed in the specimens deformed at 550 °C than those deformed at 450 °C and 500 °C, Fig. 6.79 (a-c). At 450 °C and a strain rate of 0.1 s^{-1}, higher amount of DRV and a few dynamic recrystallized grains were observed along the grain boundaries. Also, small grains with high angle grain boundaries, flat and less equiaxed grains were observed (Fig. 6.79a). The misorientation angle between subgrains increased with increasing deformation temperature as depicted in Fig. 6.79 (d-f). Misorientation between subgrains in sample deformed at 450 °C was minute, as compared with the samples deformed at 500 °C and 550 °C. The average misorientation angle increased with increasing deformation temperature. Consequently, the LABs were transformed into HABs with increasing temperature. The corresponding LABs were 72.5%, 56.7%, and 45.36% in samples deformed at 450 °C, 500 °C, and 550 °C with a strain rate of 0.1 s^{-1}. The same phenomenon was observed when the strain rate increased to 0.2 s^{-1} or 0.3 s^{-1} for all deformation temperatures (not shown in the thesis).

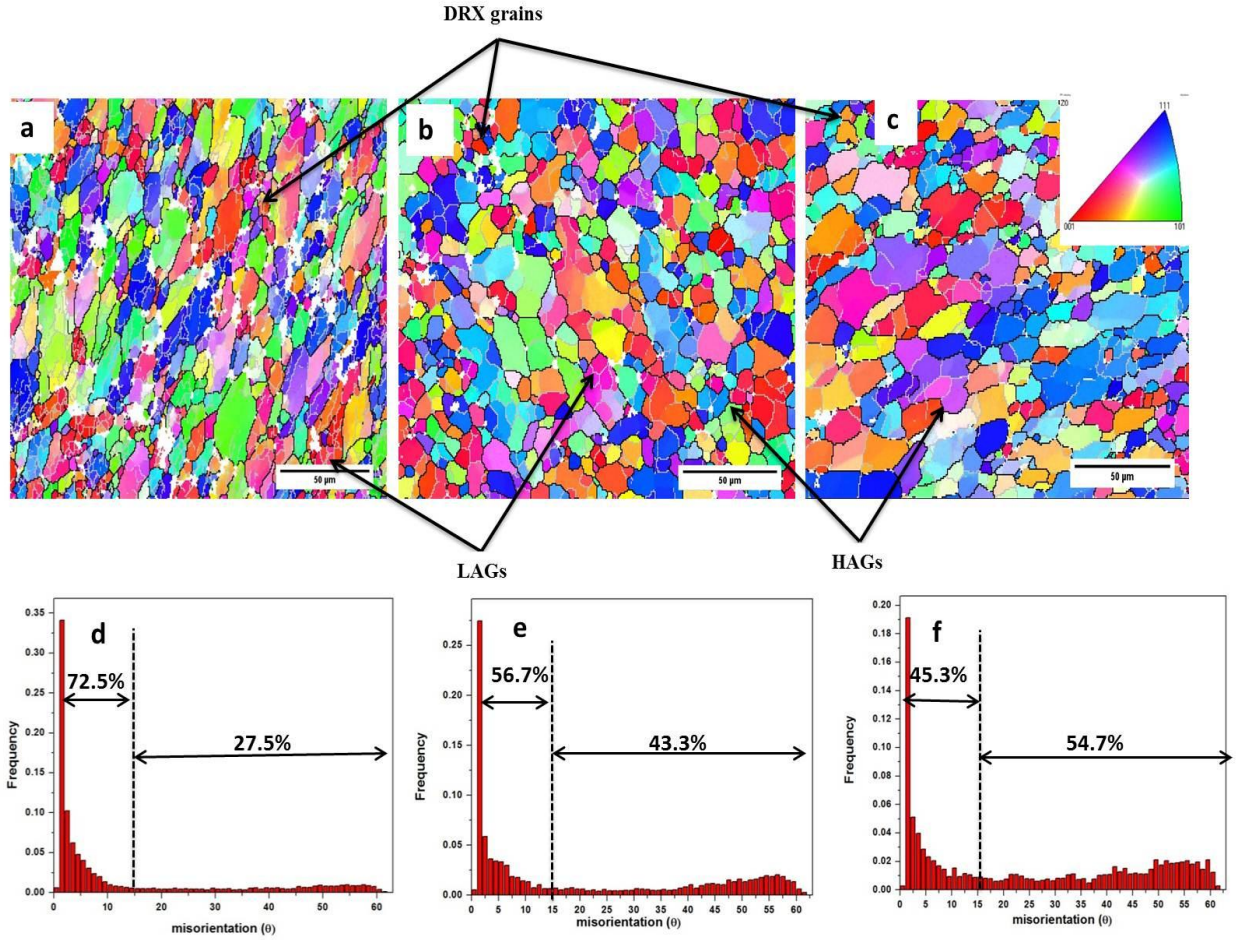

Fig. 6.79 EBSD (IPF-ND) imaging maps and corresponding grain boundaries misorientation angles distribution of samples extruded at different deformation temperatures and same strain rate: **(a, d)** 450 ^{o}C, 0.1 s^{-1}, **(b, e)** 500 ^{o}C, 0.1 s^{-1}, **(c, f)** 550 ^{o}C, 0.1 s^{-1}

The IPF images of deformed samples at 550 °C with strain rates of 0.1 s^{-1}, 0.2 s^{-1}, and 0.3 s^{-1} are shown in Fig. 6.80 (a-c). A low dislocation density and a high amount of DRX grains with fewer subgrains were observed in the specimen deformed at 0.1 s^{-1} as shown in Fig. 6.80a. Low strain rate allowed sufficient time for the movement and rearrangement of dislocations to attain lower energy configuration. Consequently, the intergranular dislocation density decreased substantially and the formation of DRX grains increased with lower strain rate, Fig. 6.80a. Grain boundary migration became less due to a high amount of stored energy and precipitation with increasing strain rates. The fraction of DRX grains gradually decreased with increasing strain rate. The deformation time decreased with increasing strain rate which restrained dislocation annihilation. This led to more number of nucleation sites and thereby restrained the growth of the recrystallized grains as shown in Fig. 6.80c. The distribution of grain boundary misorientation

shifted towards a lower angle as the strain rate of deformation increased, Fig. 6.80 (d-f). The corresponding LABs for samples deformed at 0.1 s^{-1}, 0.2 s^{-1} and 0.3 s^{-1} were 45.36%, 59.5% and 74.67%, respectively.

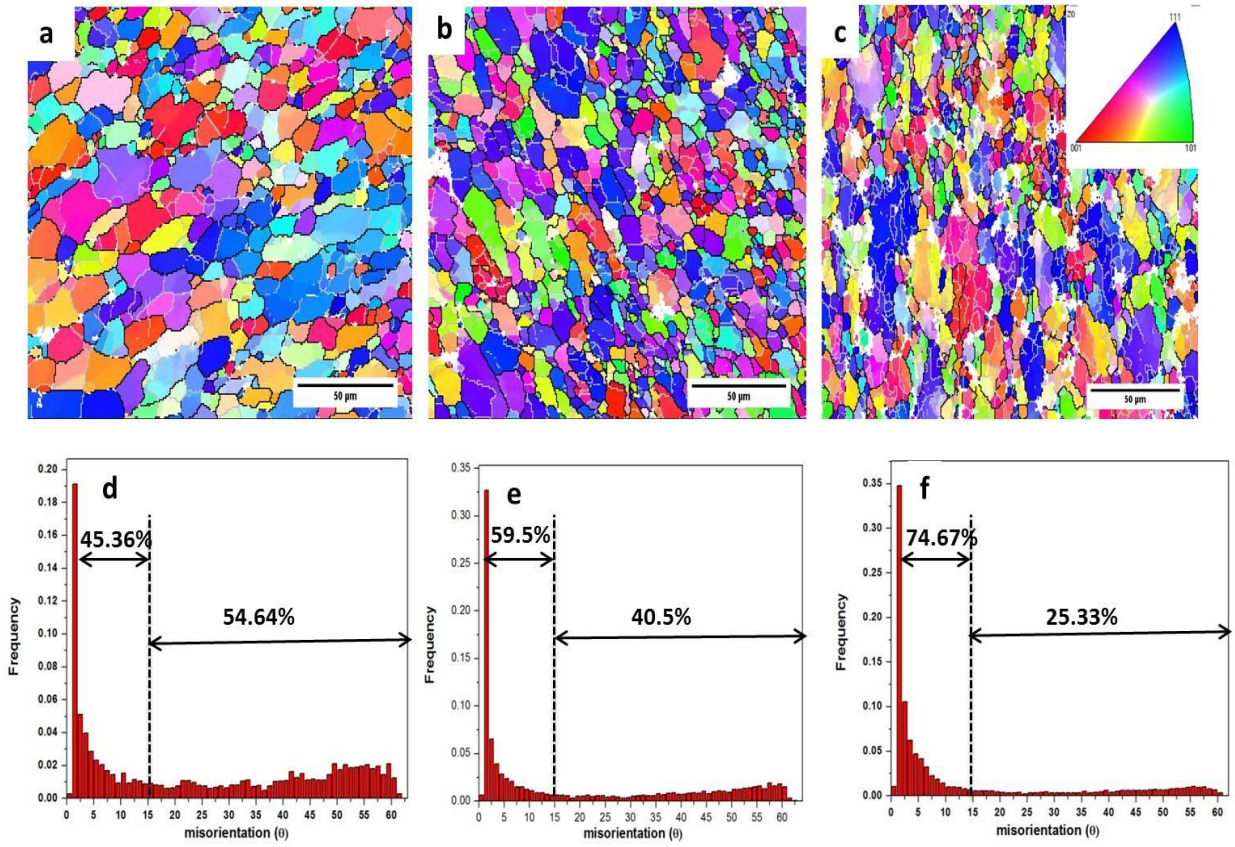

Fig. 6.80 EBSD (IPF) imaging maps and corresponding grain boundaries misorientation angles distribution of samples extruded at different strain rates and same deformation temperature: **(a, d)** 550 ^{o}C, 0.1 s^{-1}, **(b, e)** 550 ^{o}C, 0.2 s^{-1}, **(c, f)** 550 ^{o}C, 0.3 s^{-1}

6.7.1.3 Local Average Misorientation (LAM)

The color-coded LAM maps generated from EBSD data analyses, Fig. 6.81, represent the lattice strain at a local scale by considering point-to-point misorientation. LAM is depicted as the misorientation angle that corresponds to the averaged nearest-neighbor pairs within a Kernal [354]. These maps indicated that the hot extrusion resulted in an increase in local strain throughout the bulk of the samples. The maps in Fig. 6.81 (a-c) turned from green/yellow (large local misorientation) to more blue (small local misorientation). The average misorientation decreased with increasing deformation temperature from 450 °C-550 °C. The hot extrusion process resulted in strain accumulation in the grain boundaries. In LAM maps, coarse and

partially recrystallized grains at 450 °C completely transformed to equiaxed and fully recrystallized grains at 550 °C as depicted by SEM micrographs as well as IPF map analyses. With increasing strain rates, the maps turned from more blue to more green/yellow as it had less deformation time (Fig. 6.81(c-e)).

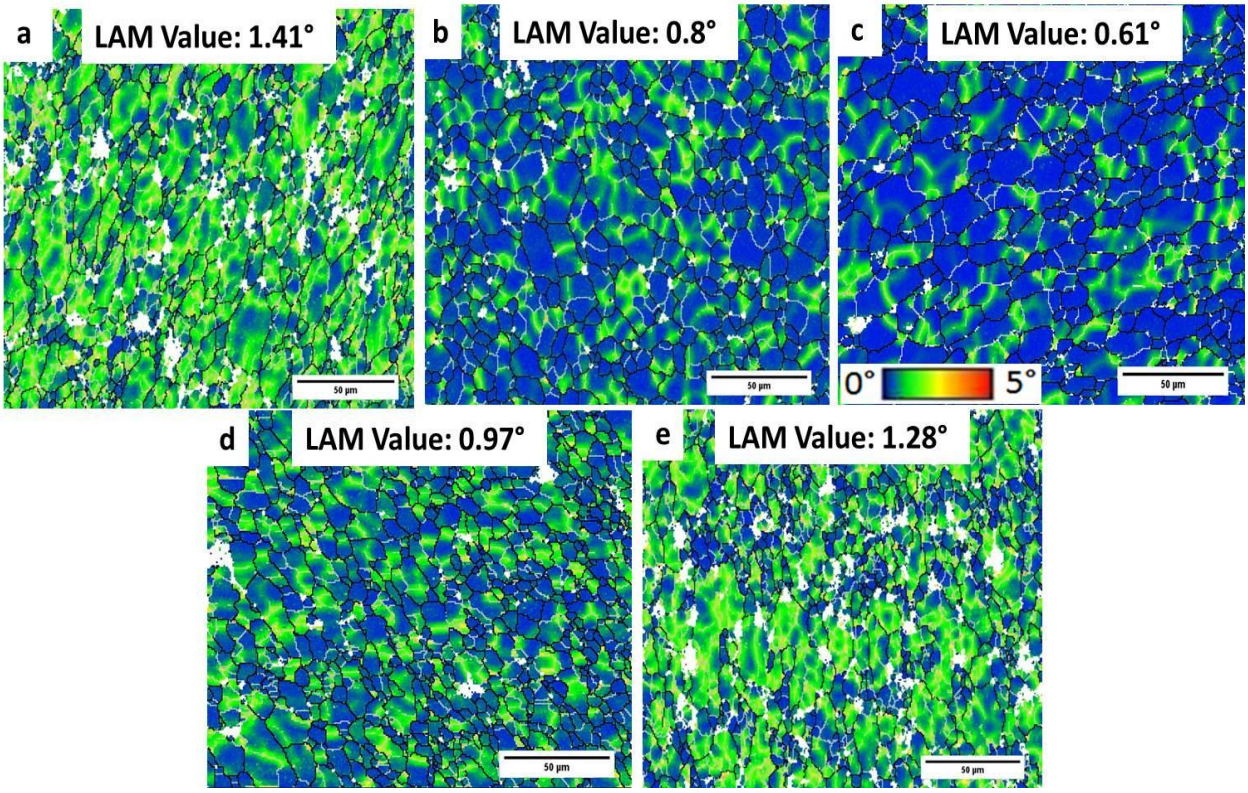

Fig. 6.81 The Local Average Misorientation (LAM) maps in the range of 0-5° misorientation for sample extruded at **a**. 450 ^{o}C, 0.1 s^{-1}, **b**. 500 ^{o}C, 0.1 s^{-1}, **c**. 550 ^{o}C, 0.1 s^{-1}, **d**. 550 ^{o}C, 0.2 s^{-1}, **e**. 550 ^{o}C, 0.3 s^{-1}

6.7.1.4 Evolution of crystal orientation: Micro-texture measurements

The orientation distribution function (ODF) was calculated from the samples extruded at different temperatures and strain rates (Fig. 6.82). The ODFs were determined following Bunge notation in the Euler angle range between 0°-90° for φ_1 and φ, and 0°-45° for φ_2. Several textures commonly develop in Al-alloys such as Brass {110}<112>, Cube {100}<001>, Copper {112}<111>,Goss {110}<001> and S {123}<634> orientations during dynamic recrystallization [74]. Fig. 6.82a shows the ODF of the sample extruded at 450 °C and 0.1 s^{-1}, showing the presence of Brass {110{<112>, Copper {112}<111> and S {123}<634> type of orientations due to extrusion and Cube {100}<001> and Goss {110}<001> orientations due to deformation

temperatures with maximum intensities of 7.04 times of any random orientation. An overall similar texture (maximum 6.82) was observed in the sample deformed at 550 °C and 0.1 s^{-1} with a weaker Cu {112}<111> and Goss {110}<001> orientations as shown in Fig. 6.82b. The deformation texture transformed during recrystallization due to a series of constructional/deconstructional events in the microstructure at a higher deformation temperature associated with the nucleation of new grains and their growth. On the other hand, the presence of incoherent precipitates (Al_2Cu) and dispersoids (Al_7Cu_2Fe) simulate recrystallization and favor the random deformation texture. Cube {100}<001> and rotated cube texture {001}<110> transformed to Cu, Brass and S-type textures during deformation process [208]. Fig. 6.82c and d depict the ODF of the samples extruded at 450 °C with 0.2 s^{-1} and 0.3 s^{-1} strain rates, respectively. The presence of strong Cu, Brass, and Goss-type textures and weak Cube textures was also evident with maximum intensities of 12.47 and 14.07 at 0.2 s^{-1} and 0.3 s^{-1}, respectively. This combination of textures produces materials with superior yield strength [208].

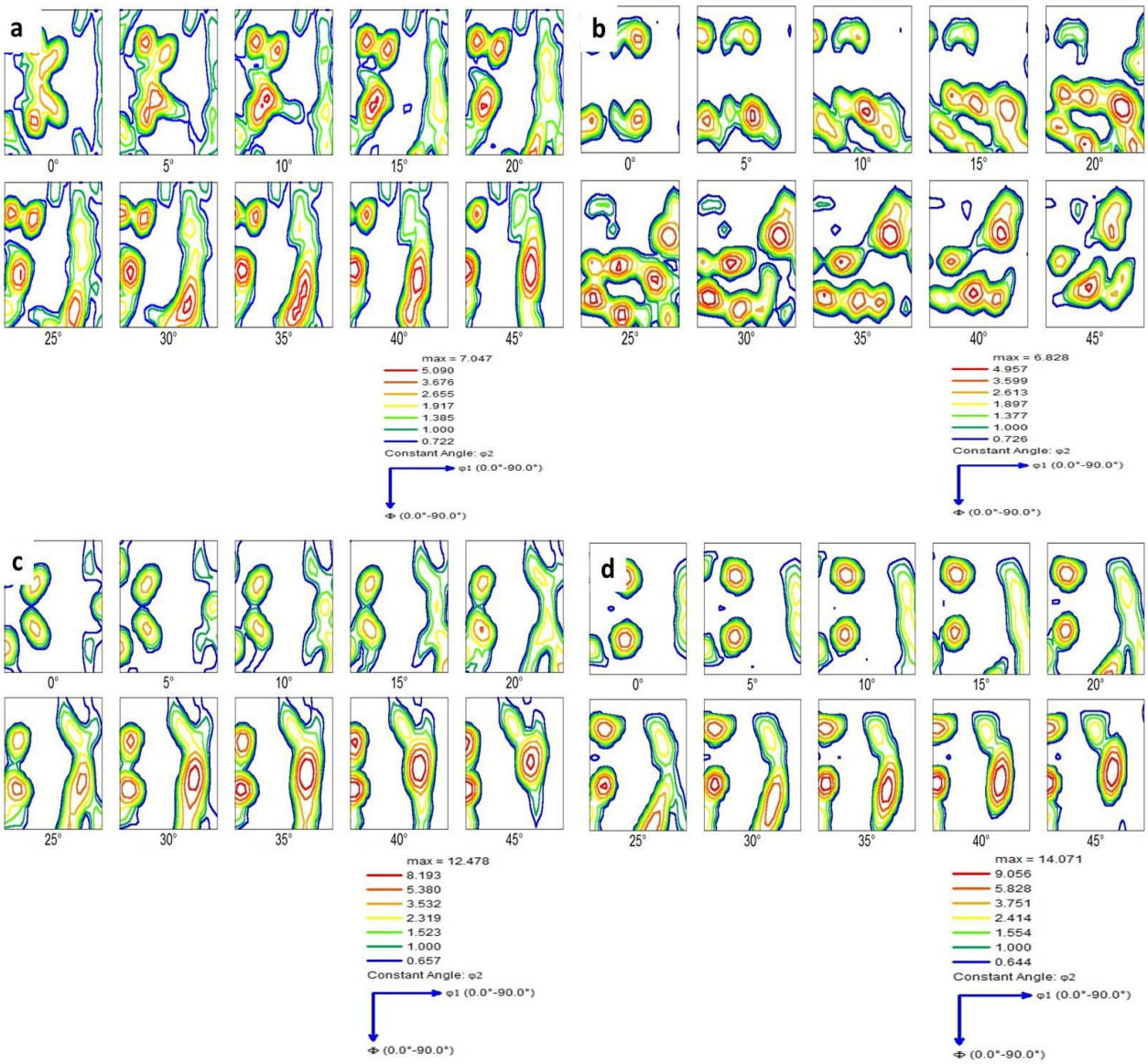

Fig. 6.82 The orientation distribution function (ODF) maps extruded samples: **a**. 450 ^{o}C, 0.1 s^{-1}, **b**. 550 ^{o}C, 0.1 s^{-1}, **c**. 450 ^{o}C, 0.2 s^{-1}, **d**. 450 ^{o}C, 0.3 s^{-1}

6.7.1.5 EPMA analysis

EPMA analyses generated X-ray elemental mappings of Al, Cu, Mg, and Fe of sample extruded at 450 °C and 0.1 s^{-1} strain rate under un-etched conditions as shown in Fig. 6.83. Elemental distribution mapping revealed that the grain boundaries to be enriched with Cu and a small amount of Fe in Fig. 6.83c and e. On the other hand, uniform distribution of Mg was observed in the matrix (Fig. 6.83d). EPMA results are tabulated in Table 6.9. From Fig. 6.83a-points 1 & 2, the white phase contains some amount of Fe. These phases containing Fe-rich were believed to

be Al_7Cu_2Fe as witnessed in the microstructure. Fe is a common impurity that forms dispersoid in Al-alloys. According to the study of Jose et al. [355], Fe can easily diffuse into the liquid phase and form as an insoluble intermetallic (dispersoid) phase (ω- Al_7Cu_2Fe). These Fe impurities develop materials with higher hardness. Point 3 in Fig. 6.83a shows that Cu and Mg elements were dissolved uniformly throughout the matrix phase. It is interesting to observe that the minor alloying element (Mg) was mechanically alloyed due to high diffusivity in Al during the powder mixing stage. There were no individual Mg particles visible in X-ray mapping (Fig. 6.83d). The intergranular zones (points 4 and 5) were identified as Cu rich zones and confirmed as θ-Al_2Cu phases as shown in Table 6.9. It is interesting to know that the Cu content in grain boundaries was higher than that in grain interior. These phases (θ and ω) were also evidenced with XRD analyses as discussed in the next section. Similar types of secondary phases were observed even in the remaining samples with varying percentages. The results obtained by EPMA were in good agreement with those observed in the microstructural analysis.

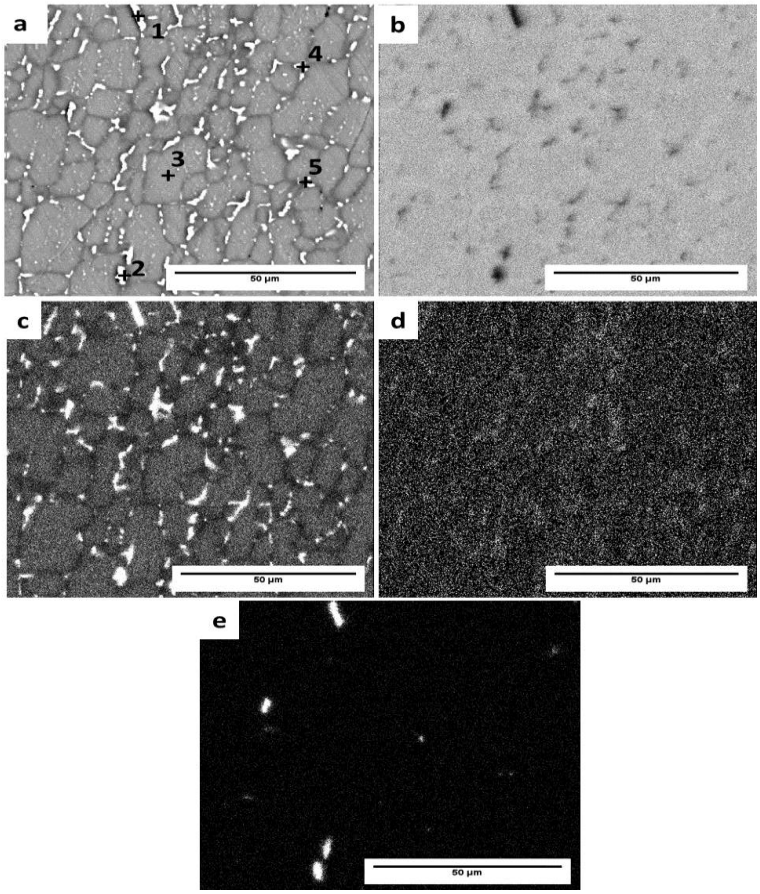

Fig. 6.83 EPMA elemental mapping of extruded sample at 450 ^{o}C, 0.1 s^{-1}: **a**. BSE, **b**. Al, **c**. Cu. **d**. Mg, **e**. Fe

Table 6.9 EPMA analysis results of the points shown in **Fig. 6.83**

Alloy	Point	Elements (Weight %)			
		Al	**Cu**	**Mg**	**Fe**
Al-4%Cu-0.5%Mg	1	56.93	30.7	0.13	12.24
	2	55.84	29.71	0.28	14.17
	3	95.56	4.01	0.41	0.02
	4	63.8	36.13	0.04	0.03
	5	65.32	34.59	0.07	0.02

6.7.2 X-ray diffractometry (XRD) analysis

XRD analyses were also carried out in order to identify different second phases in the microstructure of extruded samples. XRD analyses of all the samples with different deformation conditions are shown in Fig. 6.84. According to the XRD analyses, the only phases present in the samples were that of α-Al, θ-Al_2Cu and ω-Al_7Cu_2Fe. JCPDS cards obtained were same as that indicated in section 6.1.2.1 (XRD analysis of sintered preforms). The equivalent crystallographic phases were also observed and marked in parentheses. The XRD results indicate that θ is the major precipitate in all the extruded samples, but the quantity of θ phase decreased as the deformation temperature rises and strain rate decreases as shown in SEM analysis (Fig. 6.76 & 6.77). It was also confirmed that the atomic weights of Al, Cu, Mg, and Fe resulting from EPMA are very close to θ and ω-type. The strength and hardness of materials increase with a fine distribution of the above-mentioned phases among matrix [328]. The XRD results are in good agreement with SEM and EPMA analyses.

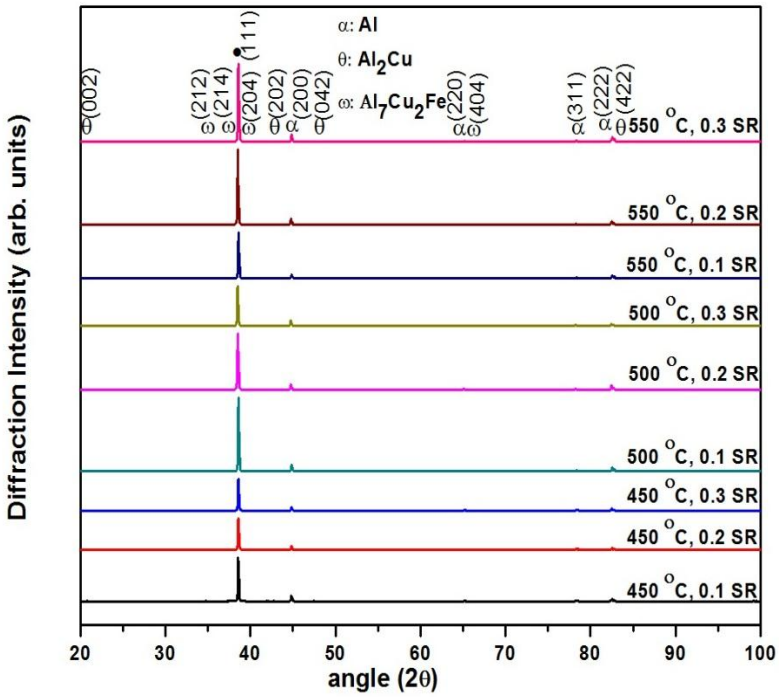

Fig. 6.84 X-ray diffraction patterns of extruded samples with different conditions

6.7.3 Evolution of Mechanical properties

6.7.3.1 Compressive behaviour

Taking into account the aforementioned, in addition to microstructural analysis, mechanical properties were also measured. Microstructural refinement during hot extrusion leads to improvement of mechanical properties of Al alloys [42, 223]. SEM micrographs showed severe orientation of grains facilitated by the extrusion process which enhance the strength of materials. Fig. 6.85 depicts the room temperature compressive properties of extruded alloys deformed at different temperatures and strain rates. Yield strength calculations were performed by the offset method with a 0.2% gauge length from the true stress-strain curves. 70% reduction in overall length of the sample was done to perform compression tests. Generally, yield strength and young's modulus decrease with increasing extrusion temperature [356] as shown in Fig. 6.85 (a & b). DRV and DRX along with strain hardening show the relation between microstructures and mechanical properties of materials. The increment in strength is attributed to the strain hardening which takes place during plastic deformation but it decreases with increasing deformation temperature [222]. Strain hardening was high at 450 °C compared to that at 500 °C and 550 °C due to factors such as high dislocation density and high precipitate distribution which constrain

the plastic flow of material. DRX grain size also plays a vital role in strength properties where in the yield strength decreased as DRX grain size increased. Since a large number of grain boundaries in the fine-grained material impede dislocation motion, higher mechanical properties were observed in the sample extruded at 450 °C due to the fine-grained structure. The yield strength of a material increases with decreasing grain size according to the Hall-Petch equation [357, 358]. The strength of materials also improved by the presence of uniformly-dispersed second phase particles in the matrix (Fig. 6.76 and 6.77). Al_2Cu and Al_7Cu_2Fe were the two secondary phase particles formed uniformly in the microstructures (Fig. 6.76 and 6.77) and increased the strength of materials after deformation. As explained, Al_2Cu is soft, easy to be cut through by dislocations and dissolves into the matrix during the deformation at high temperatures [181]. Thus, the precipitate distribution was lower in the case of sample extruded at 550 °C compared to 450 °C and 500 °C as shown in Fig. 6.76 (a-c). The precipitate strengthening mechanism was reduced with increasing deformation temperature which led to a reduction in mechanical properties. Compression yield strength of the sample extruded at 450 °C was higher than that of the sample extruded at 500 °C and 550 °C due to the formation of fine DRX grains and higher distribution of second phase particles. Yield strength and young's modulus values of all the extruded samples are tabulated in Table 6.10 to show the clear difference at different extrusion conditions. On the other hand, the size of the DRX grains decreased with increasing strain rate due to the higher imposed shear. This might have increased the yield strength and young's modulus of samples with increased strain rate (Fig. 6.85). The maximum yield strength and young's modulus were observed in the sample extruded at 450 °C and 0.3 s^{-1} strain rate i.e., 367.24 MPa and 69.48 GPa, respectively. These values are higher than the sintered sample i.e., 186 MPa and 61 GPa due to the grain boundary strengthening and dispersion strengthening. Improvement of mechanical properties in hot extruded samples can also be attributed to the enhancement in bonding between Al-Cu-Mg powder particles during hot deformation.

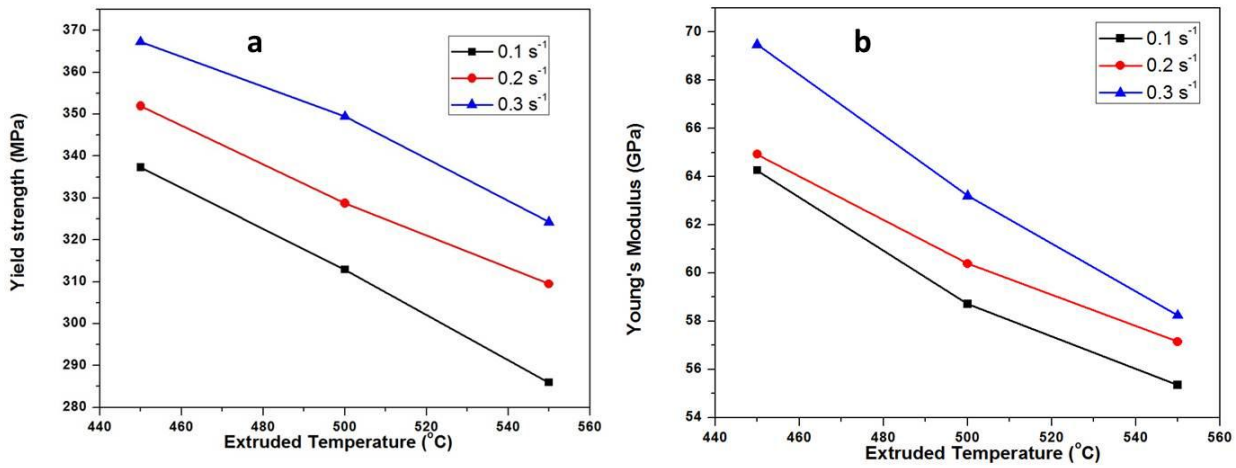

Fig. 6.85 Compressive properties of extruded samples: **a**. extrusion temperature *vs* yield strength at different strain rates, **b**. extrusion temperature *vs* young's modulus at different strain rates

Table 6.10 Mechanical properties of all extruded samples at different conditions

Deformation temperature (°C)	**Strain rate (s^{-1})**	**Yield strength (MPa)**	**Young's modulus (GPa)**	**Hardness (MPa)**
450 °C	0.1	337.31	64.26	1225.06
450 °C	0.2	351.92	64.93	1262.74
450 °C	0.3	367.24	69.48	1305.06
500 °C	0.1	312.91	58.72	1206.83
500 °C	0.2	328.74	60.39	1219.89
500 °C	0.3	349.44	63.21	1282.91
550 °C	0.1	285.93	55.35	1153.50
550 °C	0.2	309.47	57.15	1182.68
550 °C	0.3	324.25	58.24	1201.18

6.7.3.2 Nano-indentation experiments

The conventional hardness measurement method is less accurate when an indentation is made on a surface as it is very difficult to determine the contact area between the indenter and the surface area of the sample accurately and therefore the hardness value [359]. Nanoindentation test (DSI) is a sophisticated method to measure the hardness, dislocation densities, and residual stresses at a local scale [360]. A grid of 3x2 indentations on the sample surface extruded at 450 °C and 0.1 s^{-1} and their loading-unloading curves can be seen in Fig. 6.86a. The hardness can be calculated from the load (P)-penetration depth (h) curve using Eq.6.27 [361].

$$H = \frac{P_{max}}{A_c} \tag{6.27}$$

where P_{max} is the peak indentation load and A_c is the projected contact area that relies on geometry and contact depth of the indenter. Fig. 6.87 shows the hardness plots of extruded Al-

Cu-Mg P/M alloy at various temperatures and strain rates. These hardness values are also tabulated in Table 6.10. The samples for nanoindentation test are cut in transverse direction and all the indentations are made on the core (center zone) of the samples to measure hardness. The hardness values are decreased with increasing deformation temperature and decreasing strain rate as explained earlier. The maximum hardness values were observed in the sample extruded at 450 °C for all the strain rates. The highest hardness among all the samples i.e., 1305.06 MPa was observed in the sample extruded at 450 °C and 0.3 s^{-1} which is more than twice the hardness of the sintered sample i.e., 680.39 MPa. This is due to the severe plastic deformation (strain hardening) and higher volume fraction of precipitate dispersion within the grains and along the boundaries as seen in SEM microstructures (Fig. 6.76 and 6.77). This was also attributed partly to the densification during deformation. The hardness value decreased with an increase in deformation temperature due to the formation of coarser DRX grains. This was just the opposite in case of strain rate, where the hardness increased with increasing strain rate.

The maximum penetration depth (h_{max}) was varied from 9014 nm at 450 °C to 1094 nm at 550 °C extrusion temperature which is shown in load (P)-penetration depth (h) curve (Fig. 6.86b). The opposite scenario was observed with strain rate analysis where the h_{max} value decreased with increasing strain rate (Fig. 6.86c) due to a decrease in DRX grain size and an abundance of precipitates.

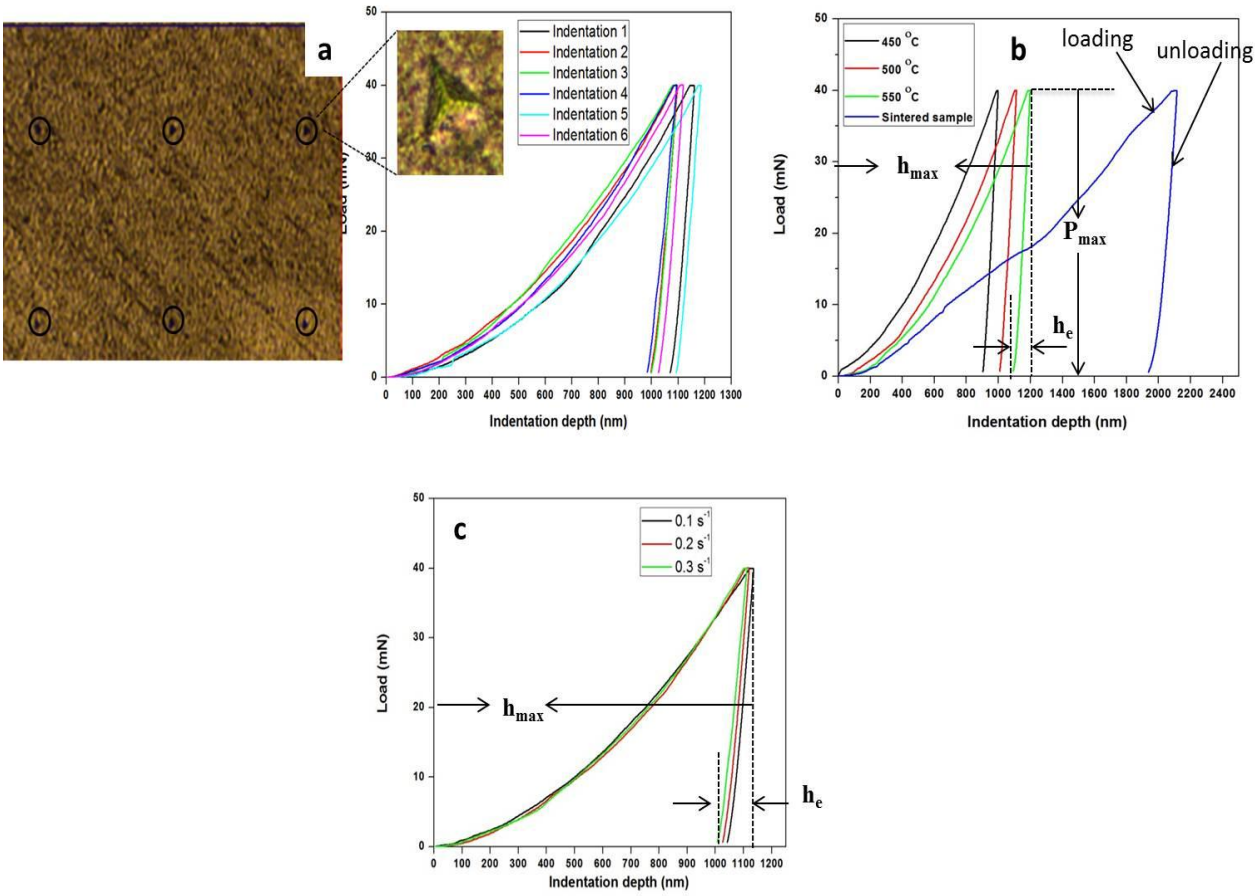

Fig. 6.86 Load (P)-penetration depth (h) curves of extruded samples: **a**. loading-unloading curves of 3x2 grid indentations, **b**. Loading-unloading curves for sintered samples and extruded samples at different temperatures and same strain rate (0.1 s^{-1}), **c**. Loading-unloading curves for sample extruded at different strain rates and same deformation temperature (550 °C)

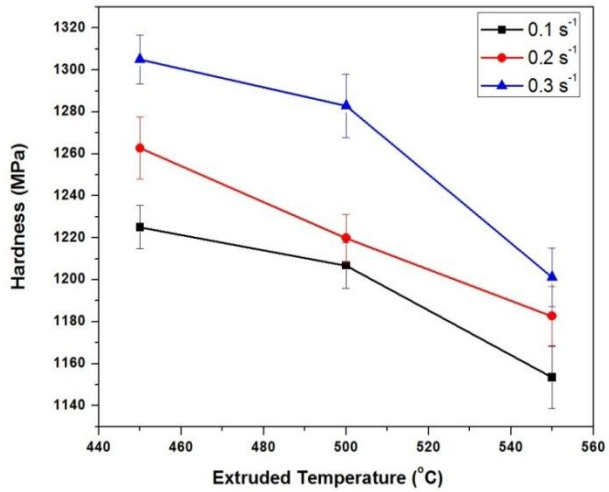

Fig. 6.87 Hardness plot for samples extruded at different deformation temperatures and strain rates

Nix and Gao model was followed to calculate the dislocation density of extruded samples [362, 363].

$$\rho_s = \frac{3}{2}\frac{1}{f^3}\frac{tan^2\,\theta}{bh^*} \tag{6.28}$$

where ρ_s is the dislocation density in the lattice, b is the Burgers vector of the dislocation, θ is the angle between the indenter surface and materials surface, and f is the correction factor for plastic zone size. The calculated value of θ for Berkovich tip is 18.85°, f is 1.9 [364] and b is 0.8553 nm which is considered from the lattice parameter of face-centered cubic (FCC) ((Al-alloys) as 0.6066 nm). The dislocation density decreased with increasing extrusion temperature and decreasing strain rate as seen in the SEM and EBSD analyses, Fig. 6.88. The maximum dislocation density was observed in the sample extruded at 450 °C and 0.3 s^{-1} i.e., $1.43x10^{4}$ m^{-2} and minimum at 550 °C and 0.1 s^{-1} i.e., $9.93x10^{13}$ m^{-2}.

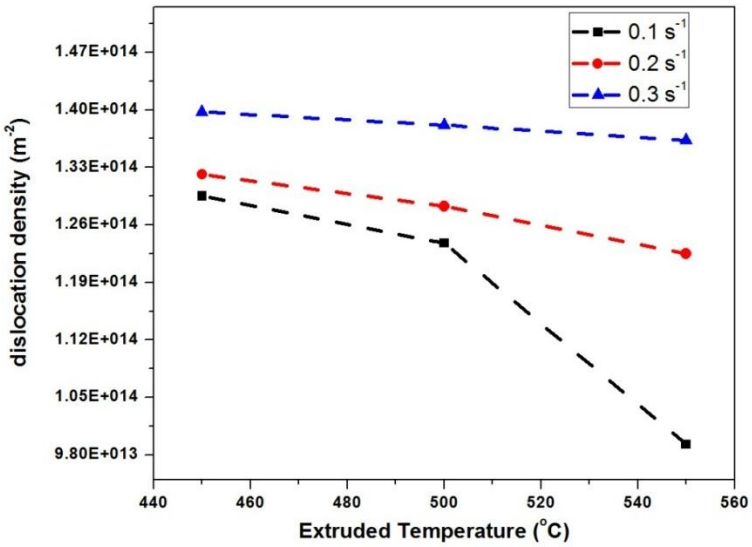

Fig. 6.88 Dislocation density plot for samples extruded at different deformation temperatures and strain rates

Suresh et al. [365] proposed a model to calculate the residual stress more accurately from nanoindentation experiments. A correlation between the residual stresses and projected contact areas (A_{c0}/A_c) was established by the following equation [365].

$$\frac{A_{c0}}{A_c} = 1 + \frac{f_g.\sigma_r}{H} \tag{6.29}$$

where, A_{c0} and A_c are the true projected contact areas without and with residual stresses at indentation depth h_{max}; f_g is the geometric factor where f_g=sin θ for compressive residual stresses and f_g=1 for tensile residual stresses; θ is the included angle of the indenter tip (θ=π/2-α; 2α=142.3° in the present study); and H is the hardness that remained unchanged under residual stress state. Compressive residual stresses (higher elastic recovery) can be expected when the unloading curve of the deformed sample shifts left to the unloading curve of the initial (undeformed) sample, whereas tensile residual stress (lower elastic recovery) shifts the unloading curve to the right [360]. Therefore, f_g=sin θ was considered in this study as the unloading curves of all the deformed materials shifted to the left side, revealing higher elastic recovery. Fig. 6.89 shows the residual stress plot calculated by following the above approach. The residual stresses decreased with increasing temperature and decreasing strain rate. The highest possible residual stress i.e., 1267.6 MPa (compressive) was observed in the specimen extruded at 450 °C and 0.3 s^{-1}.

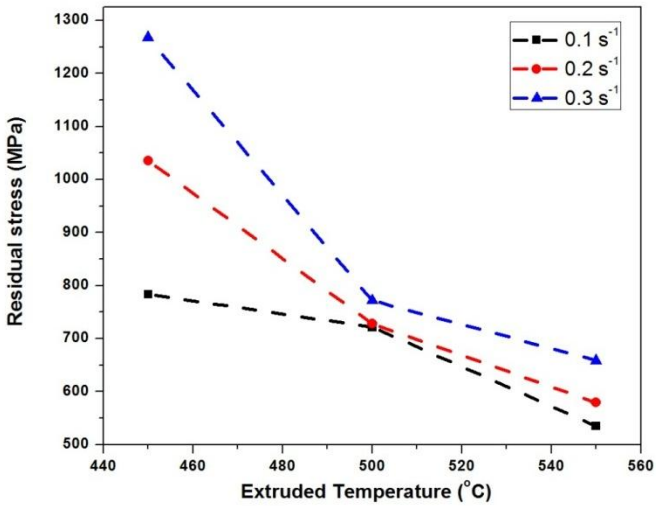

Fig. 6.89 Residual stress plot for samples extruded at different deformation temperatures and strain rates

The piling-up and sinking-in behavior at the indenter periphery depends on the residual stress state of the tested specimen and is defined by the ratio of the true contact area (A_c) to the geometrical area (A_g), which can be computed from the penetration depth from the geometry of the indenter. The power-law relationship developed between h_e/h_{max} and A_c/A_g is as follows [361].

$$\frac{h_e}{h_{max}} = \alpha \left(\frac{A_c}{A_g}\right)^{\beta} \tag{6.30}$$

where, α and β are the constants which were derived by E/σ_y ratio. The following equations were developed by best fit to the data obtained by Xu et al. [328].

$$\alpha = 1.0483\left(\frac{E}{\sigma_y}\right)^{-0.4533}, \qquad R^2 = 0.9931$$

For μ=0 (6.31)

$$\beta = -0.9651 \times 10^{-3}\,\frac{E}{\sigma_y} - 1.4136, \qquad R^2 = 0.9761$$

$$\alpha = 0.7043\left(\frac{E}{\sigma_y}\right)^{-0.409}, \qquad R^2 = 0.9931$$

For μ=0.2 (6.32)

$$\beta = -1.0455 \times 10^{-3}\,\frac{E}{\sigma_y} - 1.98825, \qquad R^2 = 0.9761$$

where R^2 is the coefficient of determination taken above 0.97 [361]. For piling-up behavior, the ratio $A_c/A_g>1$; for no piling-up or sinking-in behavior, $A_c/A_g=1$ and for sinking-in behavior, $A_c/A_g<1$ [361]. Sinking-in behavior was observed in all the materials extruded at different temperatures and strain rates i.e., $A_c/A_g<1$ (Fig. 6.90). Xu et al. [361] reported that the materials with sinking-in behavior would lead to superior mechanical properties than the materials showing piling-up behavior. The sinking-in behavior was reduced with increasing temperature due to the softening of the material during deformation and increased with increasing strain rate due to severe plastic deformation and lowering of DRX grain size. Friction also exercised notable influence on the piling-up or sinking-in behavior of materials. The coefficient of friction was considered as μ = 0 (frictionless) and μ = 0.2 (frictional) between indenter and sample as depicted by Xu et al. [361]. All the A_c/A_g-h_e/h_{max} curves with varying E/σ_y values moved towards a more sinking-in direction when friction was taken into account (μ = 0.2). Therefore, the nanoindentation method can be a useful method to predict the piling-up or sinking-in behavior and contact area of indentation other than hardness, dislocation density, and residual stresses of elastic-plastic materials.

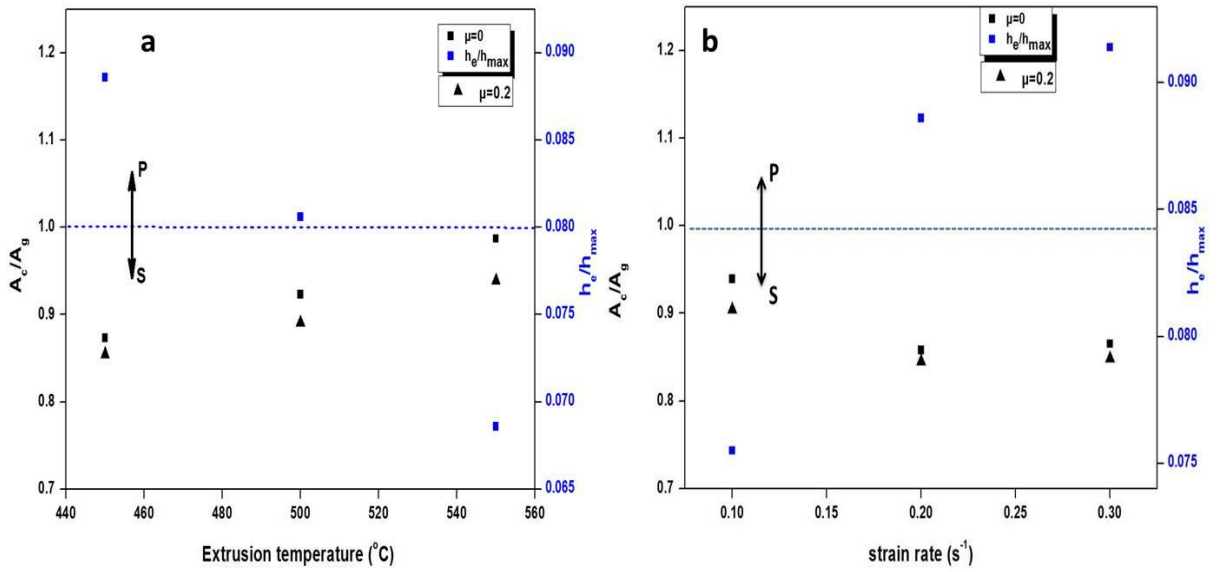

Fig. 6.90 Piling-up and sinking-in behavior and h_e/h_{max} ratio of extruded samples: **a.** at different temperatures, **b.** at different strain rates

6.7.3.3 Wear behaviour of hot extruded samples

The wear test of optimized Al-4%Cu-0.5%Mg P/M extruded samples at different temperatures and strain rates were carried out on a pin-on-disc wear testing machine. The wear tests of extruded samples were carried at an applied load of 15 KN, sliding distance of 1000 m and the sliding velocity of 1.0 m/s. All the wear tests were conducted according to the ASTM G99 standard in dry sliding conditions. Wear resistance depends primarily on hardness of the material. The worn surface of hot extruded Al-alloy revealed grooved line features and represent abrasion wear as the predominant wear mechanism. The SEM microstructures (Fig. 6.91 - Fig. 6.93) of worn surfaces of hot extruded Al-4%Cu-0.5%Mg P/M alloys show the presence of wear grooves. Since the hot extruded samples are mainly composed of Al_2Cu (θ) and Al_7Cu_2Fe (ω) phases, and hardness of EN31 steel counter body is higher than pin material, the abrasive wear might have taken place either by any intermetallic pullout particle or hard steel counter body. Wear resistance of a material also depends on the microstructure after hot deformation. Fine and uniform recrystallized microstructure was observed after hot extrusion at different processing parameters (Fig. 6.76 (b-d) and Fig. 6.77 (a-c)). Softness and grain boundary migration of material increased with increasing deformation temperature and then resulted in increasing grain size of hot extruded P/M preforms. No presence of porosity in microstructures was observed

after hot extrusion; therefore they resulted in enhanced hardness and improved wear resistance. Samples extruded at 450 °C deformation temperature were seen with finer grain structure and higher hardness because of which samples showed higher wear resistance (Fig. 6. 91). The wear rate of deformed samples increased with increasing deformation temperature which might be attributed to decreasing hardness and increasing grain size. At higher deformation temperature (Fig. 6.93), the worn surface was observed with much deeper groves and more surface damage when compared with the worn surface of the sample extruded at lower deformation temperature (Fig. 6.91). It was found that abrasion is the dominant wear mechanism in the samples extruded at 450 °C, whilst a combination of abrasion and delamination seems to be the governing wear mechanisms at 550 °C for hot extruded samples. The SEM of the worn surfaces of all the hot extruded samples hardly shows the presence of wear debris.

The SEM-EDS elemental analysis of worn surfaces revealed the presence of oxygen and iron along with Al, Cu and Mg (Fig. 6.91d, Fig. 6.92d, and Fig. 6.93d). The box regions indicate the formation of an oxygen layer i.e., FeO with the presence of oxygen content. This oxygen layer acts as a lubricant and protects the material surface increasing the wear resistance of material. The fragmentation of oxide layer during wear test increased with increase in sample deformation temperature which in turn increased the delamination of material surface. The specific wear rate of hot extruded samples was calculated based on the weight loss measurement of tested samples. The specific wear rate and coefficient of friction (CoF) was increased with increasing deformation temperature (Fig. 6.94 and Table 6.11). The difference in wear behavior can also be related to the presence of intermetallics in the samples such as Al_2Cu (θ) and Al_7Cu_2Fe (ω) in our case. In particular, the presence of high amount of intermetallics in the sample extruded at 450 °C contributed to higher hardness and subsequently wear resistance. The volume of intermetallics decreased with increasing deformation temperature; therefore the friction between pin and disc increased which then increased the wear rate.

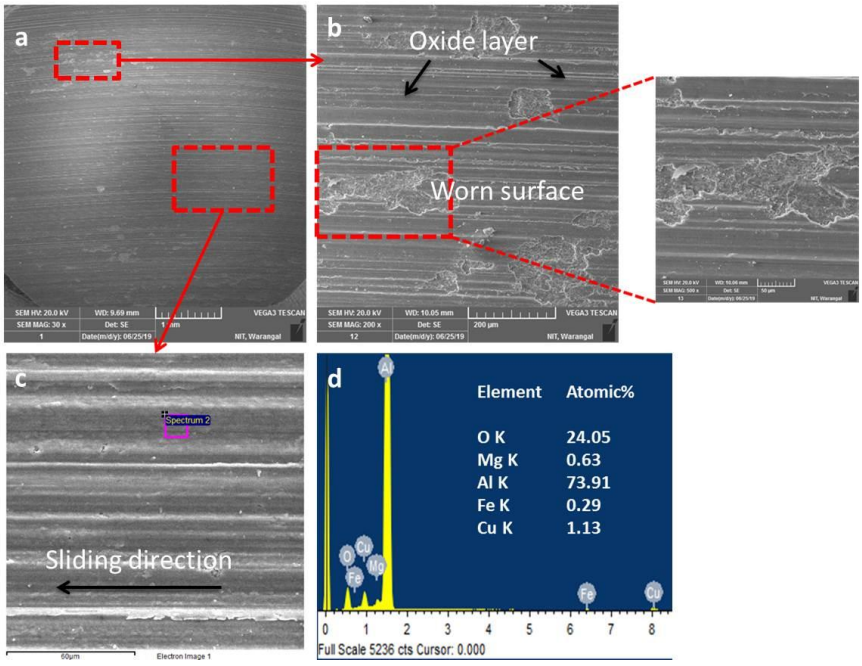

Fig. 6.91 SEM micrographs of worn surfaces of the 90% IPRD extruded sample at 450 °C and 0.1 s^{-1}; a) overview of extruded worn sample surface, b) high worn surface and high magnification worn surface shown in an inset, c) low worn surface and d) EDS of corresponding inset

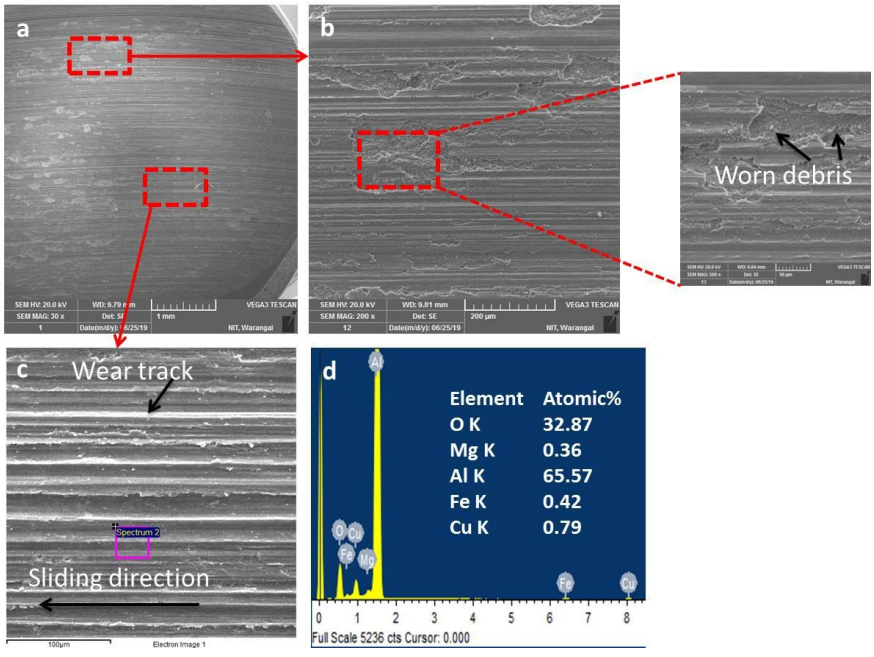

Fig. 6.92 SEM micrographs of worn surfaces of the 90% IPRD extruded sample at 500 °C and 0.1 s^{-1}; a) overview of extruded worn sample surface, b) high worn surface and high magnification worn surface shown in an inset, c) low worn surface and d) EDS of corresponding inset

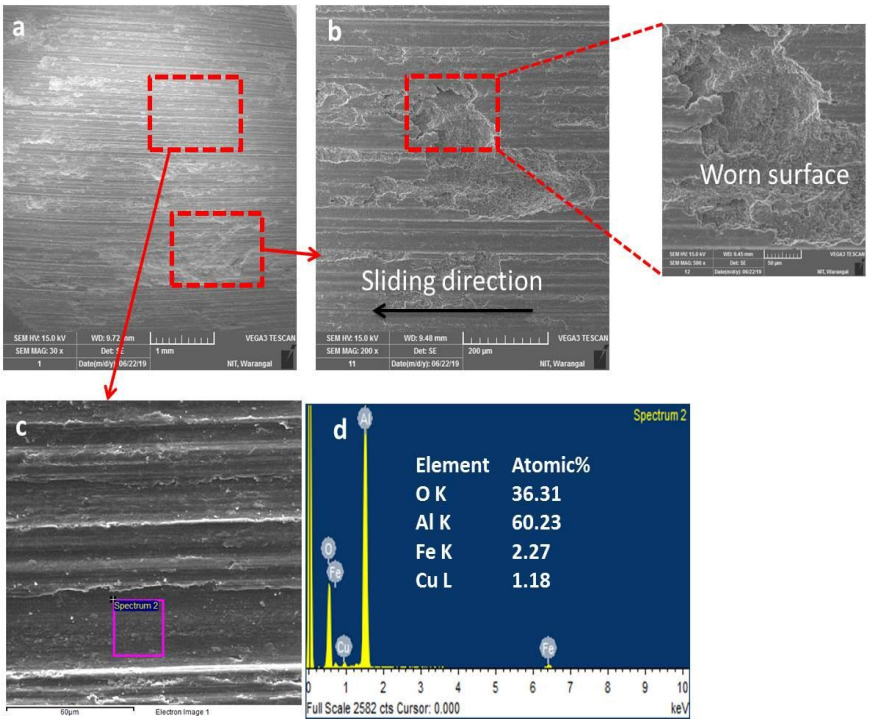

Fig. 6.93 SEM micrographs of worn surfaces of the 90% IPRD extruded sample at 550 °C and 0.1 s^{-1}; a) overview of extruded worn sample surface, b) high worn surface and high magnification worn surface shown in an inset, c) low worn surface and d) EDS of corresponding inset

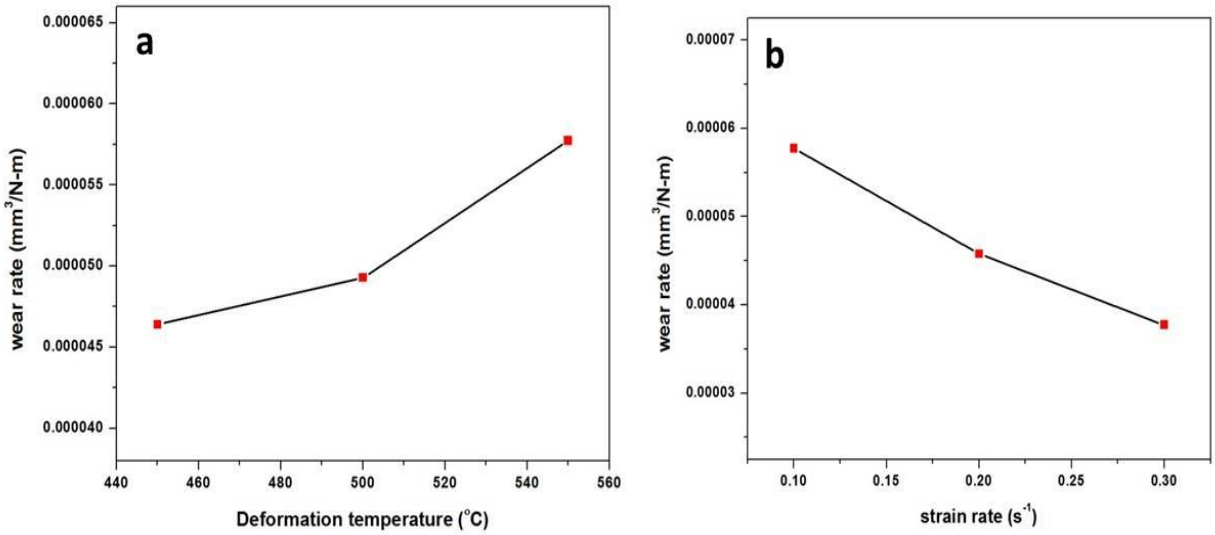

Fig. 6.94 Wear rate of 90% IPRD extruded samples; a) different temperatures and at 0.1 s^{-1} strain rate; b) different strain rates and at 550 °C

Table 6.11 Coefficient of friction of 90% IPRD extruded samples

Temperature (°C)	Strain rate (s^{-1})	Coefficient of friction (μ)
450	0.1	0.25132±0.02
500	0.1	0.27238±0.04
550	0.1	0.30083±0.02
550	0.2	0.29078±0.04
550	0.3	0.25602±0.02

The samples extruded from the pre-sintered powder compacts showed fine and uniform recrystallized microstructures resulting in an excellent combination of mechanical properties. No porosity was present in the microstructures (Fig. 6.76 and 6.77) of the extruded samples which thus resulted in enhanced compression yield strength and hardness of the extruded products compared to sintered products. The wear resistance of the P/M Al-4%Cu-0.5%Mg samples also improved after hot extrusion. The improvements observed in mechanical properties were also attributed to work hardening, precipitate hardening, and dispersion strengthening effects associated with the extrusion process. It is worth noting that these results are in good agreement with a number of previous investigations [366, 367].

6.8 Prediction of density of hot extruded samples using RSM

The mathematical model was developed using Box-Behnken experimental design (BBD) for the determination of final relative density of the P/M extruded materials. The final relative density of extruded samples was measured for each experimental condition based on the experimental design and given in Table 5.4. Box-Behnken experimental design was adopted to study the influence of deformation temperature, strain rate and IPRD on the final relative density of the extruded samples.

6.8.1 Establishing the mathematical model

RSM technique creates the relation between the response and input process parameters, and thereby the performance of the measured response was evaluated by analyzing the response

which mainly depends on input process parameters. It was also used to find the location of optimum conditions in a precise estimation. The relationship between the measured response and input process parameters is described as:

$$Y = f(x_1, x_2, x_3, \ldots\ldots x_k) + \epsilon \tag{6.33}$$

Where Y= Response (output=final relative density), f= the response function, x_1, x_2, x_3,…..and x_k are the input process parameters such as deformation temperature, strain rate and IPRD and ϵ is the noise or error observed in the response Y.

Lower order polynomial (linear) and higher-order polynomial are the two models in which any one model can be used to develop the RSM model. First-order polynomial (Eq. 6.34) is employed when the response is well modelled by a linear function of independent variables and when a linear relationship exists between input variables and output. On the other hand, higher-order polynomial (Eq. 6.35) is employed, if there is any curvature or non-linearity in the system. The main aim of the RSM is to move towards the region of optimization by improving the path. The path improvement is performed by developing a suitable model. The two models used in RSM are

Low-order polynomial (first-order model):

$$Y = \beta_0 + \beta_1 x_1 + \beta_2 x_2 + \cdots + \beta_k x_k + \epsilon \tag{6.34}$$

Where β_0 is a constant coefficient, β_1 is the slope of linear effect of the input factor, x_1 and ϵ are errors.

Higher-order model (non-linearity):

$$Y = \beta_0 + \sum_{i=1}^{k} \beta_i x_i + \sum_{i=1}^{k} \beta_{ii} x_i^2 + \sum_{i<j}^{k} \beta_{ij} x_i x_j + \epsilon \tag{6.35}$$

Where x_i is the input variable, $x_i x_j$ is the interaction effect between two parameters, β_{ii} is the linear (square term) by linear interaction effect between input factors x_i and β_{ij} is the quadratic (interaction terms) effect of the input factors.

The input variables and experimental density values shown in Table 6.12 were given in the system to select a suitable model. For a given set of input parameters and readings, the

system itself recommended quadratic model i.e, higher-order polynomial (Eq. 6.35) and selected 17 runs as shown in Table 5.4.

Table 6.12 Input variables and experimental results used for RSM analysis

Extrusion temperature (°C)	Strain rate (s^{-1})	Extruded sample density (%)		
		70% IPRD	80% IPRD	90% IPRD
450	0.1	89.47	95.25	97.01
450	0.2	89.00	94.36	96.4
450	0.3	87.40	94.00	96.02
500	0.1	91.6	96.56	97.4
500	0.2	90.65	96.05	97.11
500	0.3	89.9	95.78	97.06
550	0.1	93.32	97.24	98.72
550	0.2	93.01	96.72	98.24
550	0.3	91.78	95.97	98.02

6.8.2 Results of ANOVA

From the regression statistics, since the cubic model was aliased, it was not considered for the analysis. Quadratic model was suggested by the system as a significant model because it showed higher regression coefficient (R^2), adjusted R^2 and predicted R^2. The regression coefficient (R^2) for the selected quadratic model describes the prediction capability of the model and it is found to be 99.57% (Table 6.13), which is very close to 100% and desirable. In the present work, the difference between predicted R^2 and adjusted R^2 values is within the permissible limit as predicted R^2 and adjusted R^2 are observed as 98.06% and 99.01%, respectively. It indicates as an adequate signal and thus, the model can be used to navigate the design space. The summary of the regression statistics is presented in Table 6.13.

Table 6.13 Regression statistics

Std. Dev.	0.2641
Mean	95.02
C.V. %	0.2779
R^2	0.9957
Adjusted R^2	0.9901
Predicted R^2	0.9806
Adeq Precision	43.6890

ANOVA was analyzed to determine the significance and adequacy for the prediction of response/output (Table 6.14). P-values (probability-value) should be less than 0.05 to indicate the model terms as significant while the terms having >0.05 are insignificant. P-value is calculated based on the 95% confidence in trouble (Confidence Interval) [312]. The ANOVA table (Table 6.14) shows that the process variables; namely, deformation temperature, strain rate and IPRD are statistically significant as their P-values are lower than 0.05. According to the ANOVA results, IPRD is the most significant factor as it has the greatest influence on densification, followed by temperature and strain rate. F-value (Fisher-value) shows whether the variance between input parameters over a output is significantly different or not. F-value should be as maximum as possible. The F-value for the model is 178.45, which is quite high and shows the model is adequate. According to Davidson et al. [368], there is only 0.01 percent probability that noise causes a "model F-value". "Lack of Fit test" was used to compare the residual error to pure error from replicated design points in order to validate the model. The lack of fit value obtained is 0.48 which is shown to be insignificant by the system.

The mathematical model developed to determine the response i.e., final relative density is given in Eq. 6.36. This equation is developed as per the quadratic (higher-order polynomial) equation and can be used to make predictions about the final relative densities for given levels of each factor.

Final relative density = -105.33475+0.163705(Temperature) -20.21375(strain rate) +3.60319 (IPRD) -0.001050(Temperature * strain rate) -0.001084(Temperature * IPRD) +0.340000(strain rate * IPRD) -0.000052(Temperature^2) -30.40000(strain rate^2) -0.017560(IPRD^2) (6.36)

Table 6.14 ANOVA for final relative density

Source	Sum of Squares	df	Mean Square	F-value	p-value		% contribution
Model	111.99	9	12.44	178.45	< 0.0001	significant	99.56437
A-Temperature	12.02	1	12.02	172.38	< 0.0001	significant	10.68634
B-strain rate	2.60	1	2.60	37.26	0.0005	significant	2.311522
C-IRD	81.84	1	81.84	1173.63	< 0.0001	significant	72.7596
AB	0.0001	1	0.0001	0.0016	0.0094	significant	8.89E-05
AC	1.17	1	1.17	16.84	0.0046	significant	1.040185
BC	0.4624	1	0.4624	6.63	0.0367	significant	0.411095
A^2	0.0720	1	0.0720	1.03	0.0034	significant	0.064011
B^2	0.3891	1	0.3891	5.58	0.0500	significant	0.345928
C^2	12.98	1	12.98	186.19	< 0.0001	significant	11.53983
Residual	0.4881	7	0.0697				0.433944
Lack of Fit	0.4881	3	0.1627			insignificant	0.433944
Pure Error	0.0000	4	0.0000				0
Core Total	112.48	16					100

The model was further validated by the examination of residuals/outputs, which is the difference between the experimental response and predicted response. Fig. 6.95 shows the normal probability plot, perturbation plot, residual vs run plot and predicted vs actual for the response, respectively. All the data points are distributed relatively close to the best fit line, as shown Fig. 6.95a, demonstrates the model's adequacy.

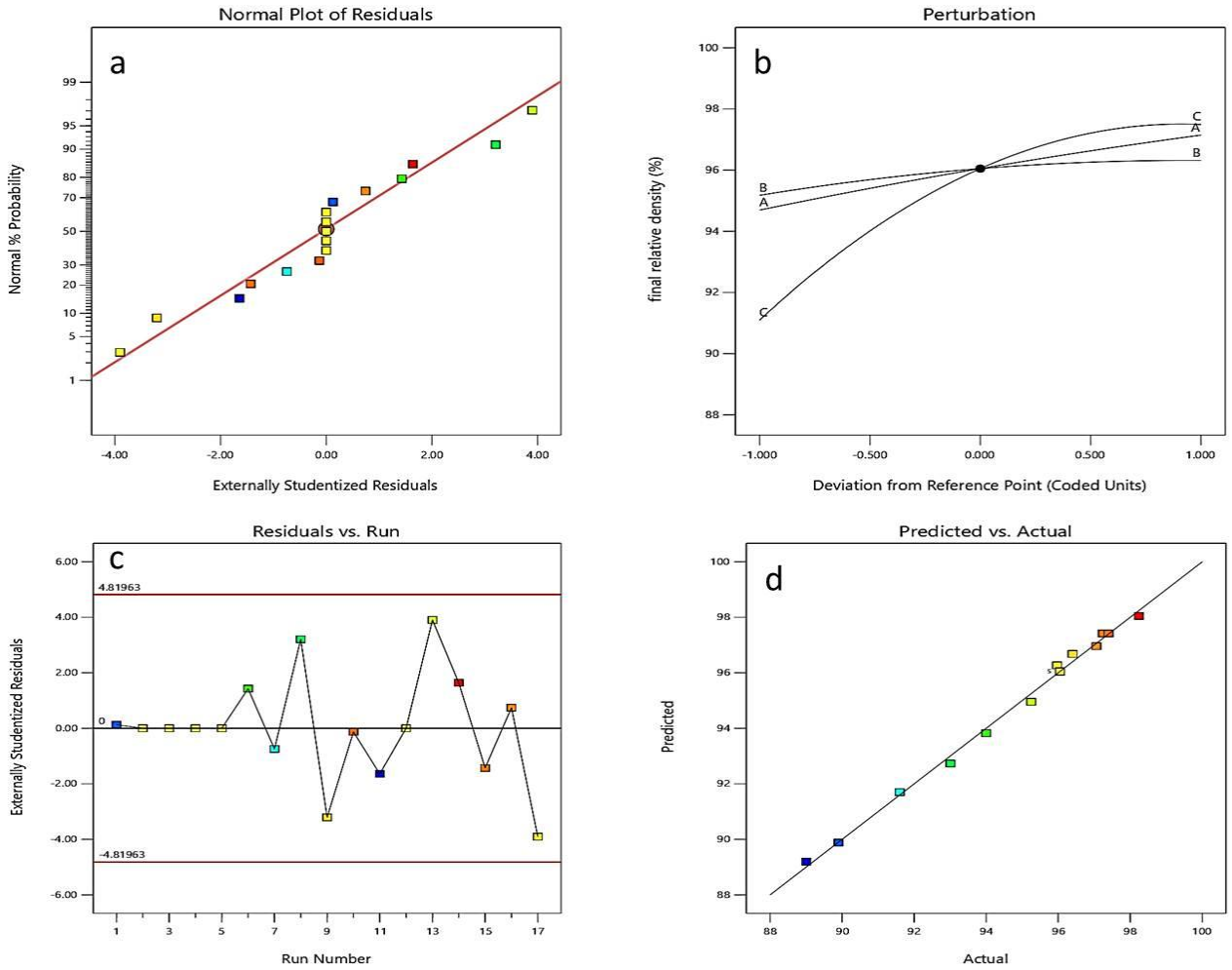

Fig. 6.95 Plots of a) normal probability plot, b) perturbation plot, c) residual vs run plot and d) predicted vs actual

Perturbation plot is useful for comparing the effects of all the input factors (parameters) at a certain point in the design space. Only one factor is changed over the range to depict the response, while all other factors remain constant. This plot shows the variation of all inputs selected for analysis in the experiments. A, B and C lines shown in the perturbation plot represent temperature, strain rate and IPRD, respectively. The plot (Fig. 6.95b) shows that the density of the extruded samples increased with increasing deformation temperature, strain rate and IPRD as observed in experimental results. The point at which all the three coincide is the ideal condition. Residual versus run plots check the lurking variables that may have influenced the response during the experiment. This plot should show random scatter. Upper and lower limit are formed automatically and all the residual are within the limits which shows the accuracy of the experimental results (Fig. 6.95c). Fig. 6.95d shows the plot of predicted relative density

versus actual relative density of the hot extruded samples. The coefficient determination (R^2) is found to be 0.992, which reveals an excellent fit between predicted data points and experimental values. All the values are scattered and fitted uniformly over the 45° straight line.

6.8.3 Interaction effects (3D surfaces) of process parameters on final relative density

Surface plot is a 3-Dimensional plot that is drawn between two input parameters and one output parameter. These plots show a functional relationship between a designated dependent variable i.e., final relative density and either of two independent variables; deformation temperature, strain rate and IPRD. The inputs considered in Fig. 6.96 are temperature and strain rate and the output is final relative density. The final relative density of hot extruded samples should be as maximum as possible so that the 3D plots obtain maximum curves, as shown in Fig. 6.96, Fig. 6.97 and Fig. 7.98. With increase in deformation temperature, a linear increase in final relative density is observed in Fig. 6.96 and Fig. 6.98. The same type of linear increment is observed with increasing strain rate (Fig. 6.96 and Fig. 6.97). On the other side, a nonlinear increment in final relative density is observed with increasing IPRD that is shown in Fig. 6.97 and Fig. 6.98. The 3D surface shown in Fig. 6.96 is a planar/linear surface as the final relative density varied linearly (straight line) with changing deformation temperature and strain rate. Whereas the plots in Fig. 6.97 and Fig. 6.98 show a ridge surface in which a linear change in final relative density was observed with a change in strain rate and temperature and a nonlinear change (curve line) in final relative density is observed with change in IPRD. The interaction effect between the three input parameters produced higher final relative densities. Using these response plots, one can identify that the response plots are fitted based on the developed model as the developed ANOVA model shown as significant.

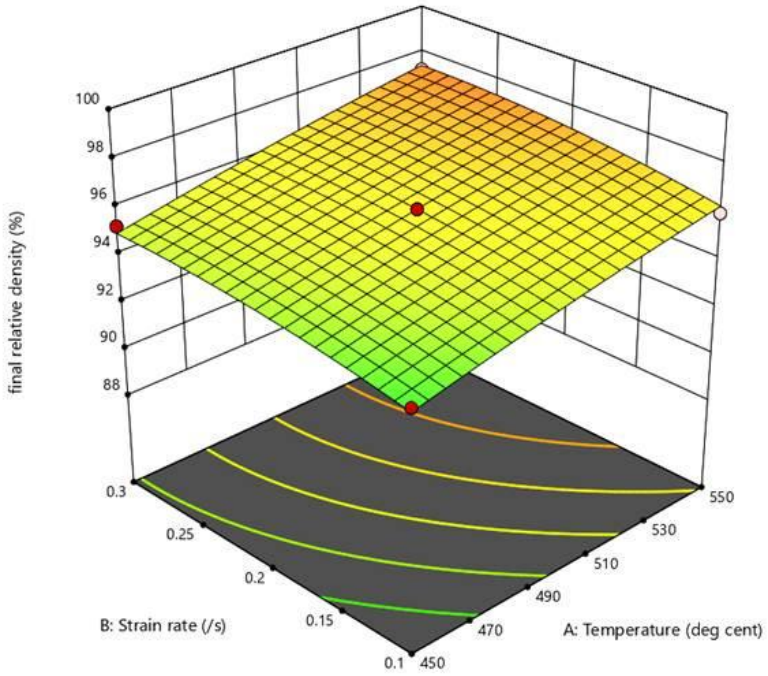

Fig. 6.96 A 3D surface plot showing the effect of deformation temperature and strain rate on final relative density for deformed samples

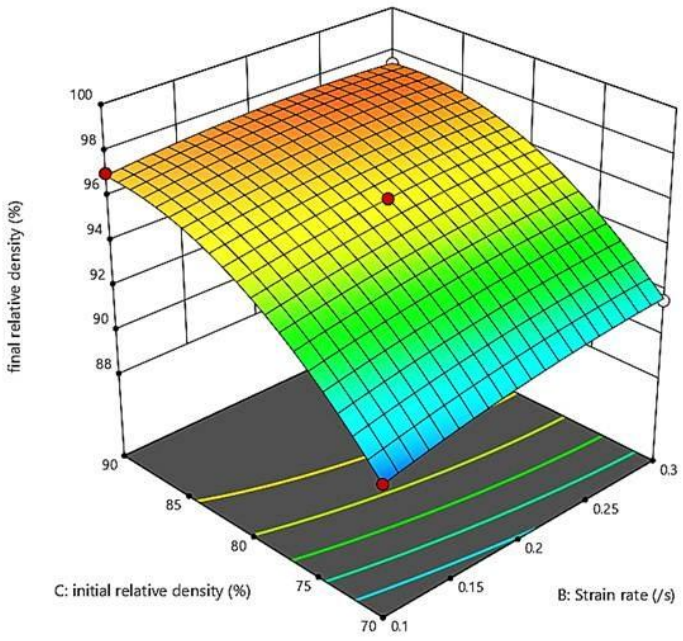

Fig. 6.97 A 3D surface plot showing the effect of deformation temperature and strain rate on final relative density for deformed samples

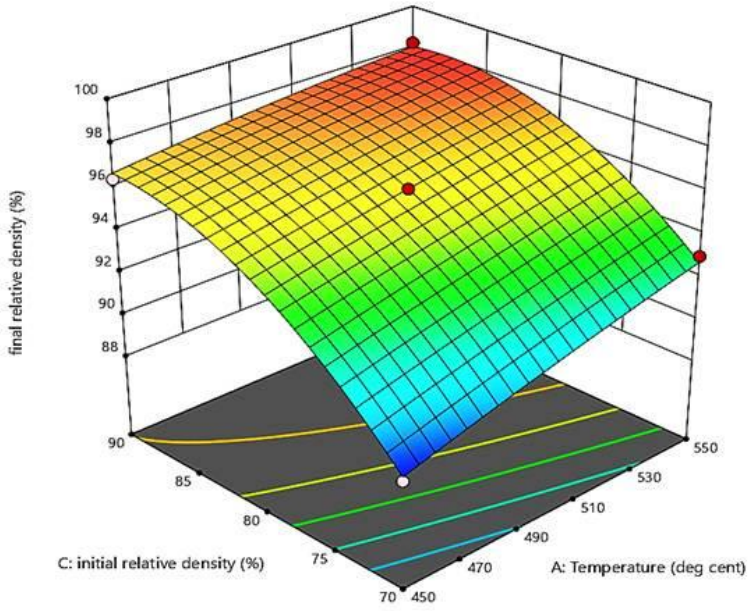

Fig. 6.98 A 3D surface plot showing the effect of deformation temperature and strain rate on final relative density for deformed samples

6.8.4 Confirmation test of developed model

The prediction capability of the developed model was further confirmed and listed in Table 6.15. The difference between experimental and predicted final relative density values was expressed as a percentage residual error. The maximum error was 0.29 percent, which is very minimal, indicating the ability of the model to successfully predict the final relative density of hot extruded Al-Cu-Mg P/M preforms for different combinations of the input process parameters, namely, deformation temperature, strain rate and IPRD.

Table 6.15 Experimental and predicted data and their associated percentage of error

Run	A:Temperature (°C)	B: Strain rate (/s)	C: IPRD (%)	Final relative density (%)		Residual /Error (%)
				Experimental	Predicted	
1	500	0.1	70	89.90	89.88	0.0183
2	500	0.2	80	96.05	96.05	0.0000
3	500	0.2	80	96.05	96.05	0.0000
4	500	0.2	80	96.05	96.05	0.0000
5	500	0.2	80	96.05	96.05	0.0000
6	450	0.1	80	94.00	93.82	0.1761
7	500	0.3	70	91.60	91.70	0.1015
8	550	0.2	70	93.01	92.73	0.2776
9	450	0.2	90	96.40	96.68	0.2776
10	500	0.3	90	97.40	97.42	0.0183
11	450	0.2	70	89.00	89.20	0.1944
12	500	0.2	80	96.05	96.05	0.0000
13	450	0.3	80	95.25	94.95	0.2959
14	550	0.2	90	98.24	98.05	0.1944
15	550	0.3	80	97.24	97.42	0.1761
16	500	0.1	90	97.06	96.96	0.1015
17	550	0.1	80	95.97	96.27	0.2959

6.9 Prediction of influence of process parameters on mechanical properties of hot extruded samples using Taguchi

The main aim of the present investigation is to identify the percentage influence of process parameters which would optimize the yield strength and hardness of hot extruded specimen. The experimental results are transformed into signal to noise (S/N) ratio after the test strategy is established. S/N ratio is a measure of quality characteristics that are changing from or approaching to the intended value. As indicated below (Eq. 6.37, Eq. 6.38 and Eq. 6.39), three different S/N ratios available based on the quality characteristics: lower the better (LTB), nominal the better (NTB) and higher the better (HTB) [369]. In the present work, higher the better quality characteristics were used since yield strength and hardness need to be high for hot extruded products.

Lower the better: It is used where the lower output value is desired

$$\frac{S}{N} ratio = -10log\left(\frac{1}{n}\sum_{i=1}^{n} y_i^2\right) \quad (6.37)$$

Larger the better: It is used where the higher output value is desired

$$\frac{S}{N} ratio = -10log\left(\frac{1}{n}\sum_{i=1}^{n} 1/y_i^2\right) \quad (6.38)$$

Nominal the best:

$$\frac{S}{N} ratio = -10log\left(\frac{\bar{y}}{s_{\bar{y}}^2}\right) \quad (6.39)$$

Where y_i= observed response value and n=number of replications

The experimental results such as yield strength and hardness values are shown in Table 6.10 for Taguchi analysis. The control factors and their levels for the analysis are shown in Table 5.5. According to Taguchi design of experiments, L9 orthogonal array was selected for 2 parameters and 3 levels. S/N ratios for yield strength and hardness of hot extruded samples for different combination of process parameters were calculated by Eq. 6.38 and shown in Table 6.16 and 6.17, respectively. All the experimental works are repeated 3 times for better results of hardness and yield strength. Table 6.18 and 6.19 are the response tables which show the mean S/N ratio values for yield strength and hardness for each level. Delta values shown in Table 6.18 and 6.19 are the difference between higher mean S/N ratio and lower mean S/N values which give the ranking of the influence of processes parameters. The main effect plots (Fig. 6.99 and 6.100) were drawn from the response tables. These main effect plots show the effect of control factors (process parameters) on the yield strength and hardness in terms of S/N ratios. These plots are also used to determine the optimum condition for improving mechanical properties. The yield strength and hardness decreased with increase in deformation temperature and decrease in strain rate as observed in experimental results. The mean S/N ratio reduced with increasing temperature and decreasing strain rate. So, the yield strength and hardness for hot extruded P/M Al-alloys are high at higher mean S/N ratio values as shown in Fig. 6.99 and 6.100. From the main effect plots, 450 °C deformation temperature and 0.3 s^{-1} strain rate were shown to have higher S/N ratios. So, this combination of process parameters produces higher yield strength and hardness as observed in experimental results.

Table 6.16 Experimental yield strength and their S/N ratios

Extrusion temperature (°C)	Strain rate (s^{-1})	Yield Strength (MPa)	S/N ratio (Yield strength)
450	0.1	337.31	50.56
450	0.2	351.92	50.92
450	0.3	367.24	51.29
500	0.1	312.94	49.90
500	0.2	328.74	50.33
500	0.3	349.44	50.86
550	0.1	285.93	49.12
550	0.2	309.47	49.81
550	0.3	324.25	50.21

Table 6.17 Experimental yield strength and their S/N ratios

Extrusion temperature (°C)	Strain rate (s^{-1})	Hardness (MPa)	S/N ratio (Hardness)
450	0.1	1225.06	61.7631
450	0.2	1262.74	62.0263
450	0.3	1305.06	62.3126
500	0.1	1206.83	61.6329
500	0.2	1219.89	61.7264
500	0.3	1282.91	62.1639
550	0.1	1153.50	61.2404
550	0.2	1182.62	61.4569
550	0.3	1201.18	61.5922

Table 6.18 Response table for S/N ratios for yield strength

Level	Temperature (°C)	Strain rate (s^{-1})
1	50.93	49.86
2	50.37	50.36
3	49.72	50.79
Delta	1.21	0.93
Rank	1	2

Table 6.19 Response table for S/N ratios for hardness

Level	Temperature (°C)	Strain rate (s^{-1})
1	62.03	61.55
2	61.84	61.74
3	61.43	62.02
Delta	0.60	0.48
Rank	1	2

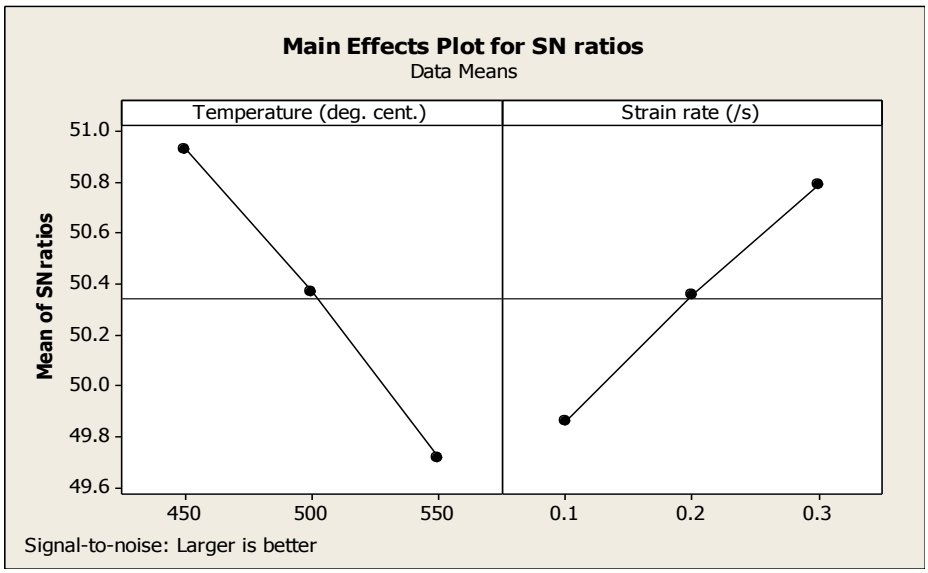

Fig. 6.99 Main effect plot for yield strength

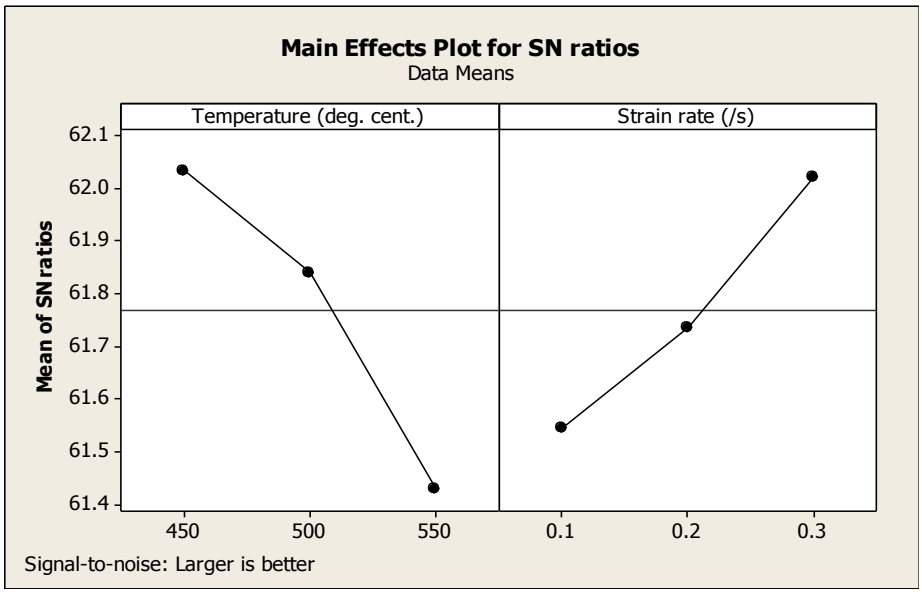

Fig. 6.100 Main effect plot for hardness

The interaction effects between process parameters for yield strength and hardness are shown in Fig. 6.101 and Fig. 6.102. Plots in Fig. 6.101 show the interaction between deformation temperature and strain rate for yield strength. All the three lines in Fig. 6.101 are parallel so, that the interaction effect between temperature and strain rate is absent for yield strength. Whereas, in the case of hardness, all three lines are non-parallel so there is interaction exist between the deformation temperature and strain rate.

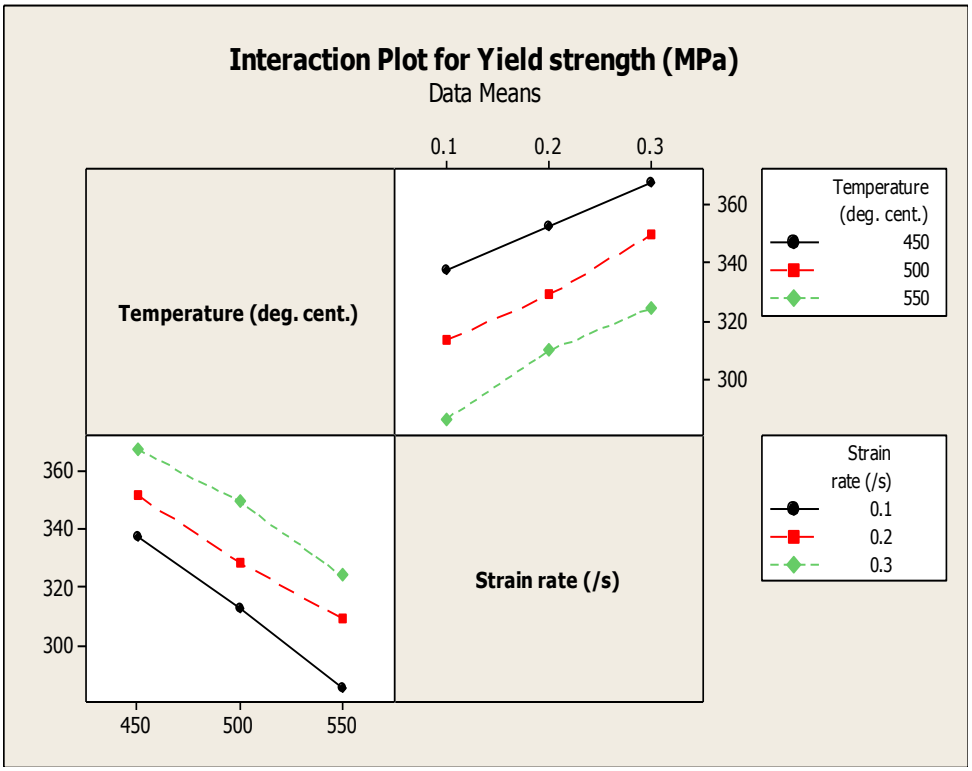

Fig. 6.101 Interaction effect plot for yield strength

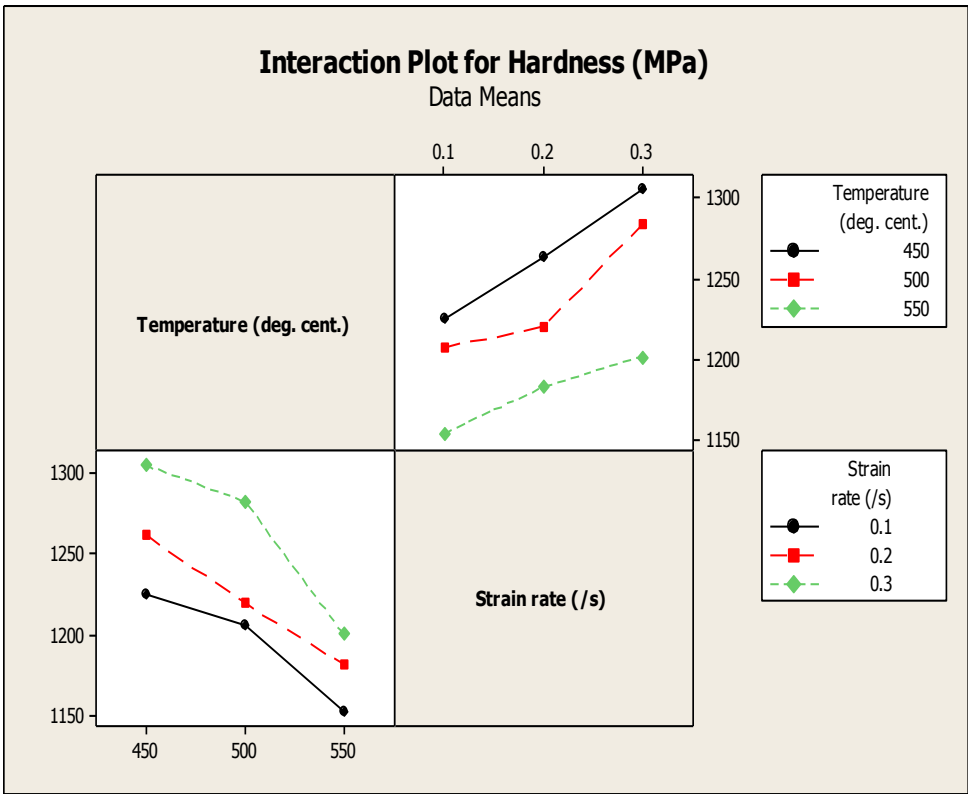

Fig. 6.102 Interaction effect plot for hardness

The influence of process parameters that contribute to enhanced mechanical properties of hot extruded P/M Al-alloys was investigated using ANOVA test and shown in Table 6.20 and 6.21. P-value is calculated based on 95% confidence interval so, that a P-value that is less than 0.05 would be more significant. From Table 6.20, it is observed that the deformation temperature is the major factor influencing the yield strength of hot extruded samples, followed by strain rate. The percentage contribution of deformation temperature was 62.58% and strain rate was 36.69% for yield strength. The influence of uncontrolled factors during deformation is shown as residual error in Table 6.20 and Table 6.21. The residual error shown in the case of yield strength was 0.71% which is negligible. The same phenomenon was observed in ANOVA results for hardness (Table 6.21). The percentage contribution of deformation temperature and strain rate was 60.39% and 36.61%, respectively. The coefficient of determination (R^2) for yield strength and hardness was observed to be 99.28% and 97.01%, respectively which is very close to 100%. This shows the adequacy of Taguchi analysis and accuracy of the experimental results.

Table 6.20 ANOVA for yield strength (MPa)

Source	DF	Seq SS	Adj MS	F	P	% contribution
Temperature	2	3122.0	1561.0	174.46	0.002	62.58
Strain rate	2	1830.4	915.2	102.28	0.024	36.69
Error	4	35.8	8.9			0.71
Total	8	4988.2				100

Table 6.21 ANOVA for hardness (MPa)

Source	DF	Seq SS	Adj MS	F	P	% contribution
Temperature	2	0.57144	0.28572	40.39	0.002	60.39
Strain rate	2	0.34644	0.17322	24.49	0.006	36.61
Error	4	0.02829	0.00707			2.98
Total	8	0.94617				100

CHAPTER 7

Conclusions

7.1 Summary of the research findings

The present investigations reported the deformation behavior of powder metallurgy (P/M) processed Al-Cu-Mg preforms using experimental and modeling under different deformation conditions during hot extrusion. The following major points are deduced from these studies.

The results of sintering behavior of Al-Cu-Mg P/M alloys revealed that the micro addition of Mg into Al-4%Cu led to higher sintering properties like higher density and hardness. The liquid fraction of Al-4%Cu matrix increased with increasing the addition of Mg content. This liquid phase was distributed in the gaps between particles and formed secondary phase particles such as Al_2Cu (θ) and Al_7Cu_2Fe (ω). The level of shrinkage increased following an increase in Mg content and it was observed to be maximum for a composition with 0.5% Mg i.e., Al-4%Cu-0.5%Mg. The formation of thicker grain boundaries and brittle grain boundary networks were observed in the compositions above 0.5% Mg due to excess liquid fraction. On the other hand, appreciable shrinkage was observed in the sample sintered at 600 °C temperature but it was identified as over sintering. Bulging of sample, coarsening of grains and reduction in formation of secondary strengthening phases (θ and ω) were observed in the samples sintered at 600 °C. The miximum sintered density of 2.63 g/cc or 95.38% of theoretical density (theoretical density: 2.76 g/cc) was observed in Al-4%Cu-0.5%Mg composition sintered at 550 °C. Similar trends were also observed in the case of microhardness as had been reflected in the sintered density. Thus, 550 °C and Al-4%Cu-0.5%Mg were optimized as sintering temperature and the desired composition for all future studies.

The optimized sintered samples (Al-4%Cu-0.5%Mg) were used as raw materials or initial preforms for the subsequent semi-solid and/or hot extrusion experimentation in order to enhance the microstructural and mechanical properties of Al-Cu-Mg P/M alloys. The working temperatures for semi-solid extrusion were chosen in between solidus (542.7 °C) and liquidus (662.8 °C) temperature ranges which were derived from TG/DTA analyses of sintered samples with different compositions. Uniform distribution of secondary strengthening phases (θ and ω)

was observed in the matrix and along the grain boundaries after deformation. The volume of Al_2Cu phase reduced with an increase in deformation temperatures as this phase is sensitive to elevated deformation temperatures. The pinning effect of secondary phase particles decreased, therefore the grain boundary migration increased with an increase in deformation temperature. The average grain size of semi-solid extrudates was increased with increasing deformation temperature and dies approach angle, and decreased with increasing extrusion ratio. The density and hardness of semi-solid extruded samples were increased with an increase in extrusion ratio, and decrease in dies approach angle and deformation temperature. In demarcated samples, grains in the front end were almost globular and this confirmed that the forming was taken in semi-solid state with α-Al grains gliding over one another due to high liquid fraction. On the other hand, the rear end of all the samples experienced higher deformation because of reduced liquid fraction and formed fine and elongated grains. Extrusion defects like hot shortness and cracks on the surface and edges were observed in semi-solid extrudates deformed above 550 °C deformation temperature because of higher liquid fraction which caused liquid segregation. Sample extruded at 550 °C and with extrusion ratio of 4 and die approach angle of 30° achieved good microstructural and mechanical properties without extrusion defects on surface and edges.

To reduce extrusion defects and increase the properties of extruded rods, the deformation temperature was reduced to below 550 °C and used an optimized die with extrusion ratio of 4 and approach angle of 30° for further studies of hot extrusion. Hot extrusion experiments were performed at temperatures of 450 °C, 500 °C and 550 °C, at strain rates of $0.1s^{-1}$, $0.2\ s^{-1}$ and $0.3\ s^{-1}$, and initial preform relative density (IPRD) of 70%, 80% and 90%, respectively. The true stress-true strain curves exhibited a peak flow stress (PFS) at a certain strain value and then held constant or decreased gradually till the stress reached at higher strain values. The materials undergo work hardening in the primary stage of deformation followed by dynamic softening attributed to the DRV and DRX. The PFS in the flow stress curves was decreased with increase in extrusion temperature and decreasing strain rate and IPRD. Arrhenius-type constitutive equation was developed to predict the flow stress of hot extruded products. Increase in IPRD was led to increase in the requirement of activation energy (Q) for deformation. Irrespective of IPRD, the activation energy was decreased with increase in deformation temperature and strain rate. The predicted PFS values showed an excellent agreement with the experimental PFS values which validates the accuracy of the developed model. The correlation coefficient (R^2) values

were observed to be 96.9%, 98.9% and, 99.1% for 70%, 80% and 90% IPRD samples, respectively and the maximum observed average absolute relative error (AARE) was 6.14% which are acceptable for deformation of Al-Cu-Mg sintered preforms. The constitutive equations formulated for hot extruded Al P/M alloys as a function of IPRD could precisely predict the flow stress for different deformation temperatures and strain rates. Microstructure evolution of hot extruded samples accompanying dynamic recover (DRV) and dynamic recrystallization (DRX) was studied. The average DRX grain size of hot extruded samples was increased with increase in deformation temperature and IPRD and decreasing strain rate. A mathematical model was developed between Z-H parameter and DRX grain size of hot extruded samples at various deformation temperatures, strain rates and IPRDs. The measured DRX grain size (d_m) was compared with mathematically calculated DRX grain size (d_c) to validate the accuracy of the developed model. It was observed that the measured DRX grain size agreed well with calculated DRX grain size thereby proving the precision and reliability of the developed mathematical model for various deformation conditions. Finite element analysis (FEA) based simulation studies were also performed to analyze the metal flow, stress behavior and the corresponding strain induced in the samples during hot extrusion. The effective stress and strain decreased with increasing deformation temperature and decreasing strain rate and IPRD.

A systematic study was carried out to establish a structure-property correlation of Al-Cu-Mg P/M alloys as a function of extrusion temperature and strain rate. Continuous dynamic recrystallization (CDRX) occurred by the accumulation of dislocations in subgrains, resulting in increasing misorientation angle. The average grain size of sintered sample was refined from 24.7 µm to 10.66 µm, 11.91 µm, and 12.67 µm in the samples extruded at 450 °C, 500 °C and 550 °C, respectively. The degree of refinement of microstructure was increased with increase in strain rate. A wide distribution of secondary phase particles (Al_2Cu and Al_7Cu_2Fe) was observed in SEM analyses which act as an effective barrier to the dislocation movement and consequently prevent the occurrence of discontinuous dynamic recrystallization (DDRX). The transformation of lower angle grain boundaries (LABs) into higher angle grain boundaries (HABs) was observed with increasing deformation temperature due to reduced pinning effect of secondary phase particles. The corresponding LABs were 72.5%, 56.7% and 45.3% in the samples extruded at 450 °C, 500 °C and 550 °C, respectively with 0.1 s^{-1} strain rate. The opposite phenomenon was observed with increase in strain rate. Hot extrusion process had a marked influence even on

the evolution of texture. Brass {110}<112>, Copper {112}<111> and S {123}<634> texture components were developed due to the deformation and Cube {100}<001> and Goss {110}<001> orientations were found to be strengthened due to the temperature effect. The yield strength (σ_y) and Young's modulus (E) were increased from 186 MPa and 61 GPa, respectively, in the sintered sample to a maximum of 367.24 MPa and 69.48 GPa in the sample extruded at 450 °C and 0.1 s^{-1} due to the formation of more number of dislocations, more uniform distribution of θ and ω phases and higher energy absorption. The dislocation density and residual stresses developed during the hot extrusion process were decreased with increase in deformation temperature and decrease in strain rate. It was found that the abrasion is the dominant wear mechanism in the samples extruded at 450 °C, whilst a combination of abrasion and delamination seemed to be the governing wear mechanisms at 550 °C for hot extruded samples. Wear rate and coefficient of friction (CoF) were higher for samples extruded at higher deformation temperatures and lower strain rate. The improvements observed in mechanical properties were attributed to work hardening, precipitate hardening, and dispersion strengthening effects associated with the extrusion process.

The experimental investigation on densification behavior of P/M Al-Cu-Mg preforms was carried out with a view to correlating the process parameters, namely deformation temperature, strain rate and IPRD with the final relative density of the preforms. A statistical methodology, Box-Behnken Design-Surface Response Methodology (RSM) was successfully modeled to predict the final relative density for varied input factors. ANOVA was used to validate model, which revealed that the experimental and predicted values were in good agreement (R^2 = 99.57%). The results also revealed that the effect of IPRD is having most imminent influence, followed by deformation temperature and strain rate on the final relative density. Model confirmation was performed and the maximum percentage of absolute relative error was observed as 0.29% which is reasonable. Taguchi analysis was used to predict the influence of process parameters on mechanical properties of hot extruded Al-Cu-Mg alloys. The percentage contribution of deformation temperature was 62.58% for yield strength and 60.39% for hardness, and the percentage contribution of strain rate was 36.69% for yield strength and 36.61% for hardness. These research findings can help researchers and industrialists for developing a robust, reliable and knowledge base processes for deformation of P/M materials,

and in early prediction of the final density and mechanical properties of P/M materials during deformation.

7.2 Scope for future work

The intensive research work on deformation behavior of P/M processed Al-Cu-Mg preforms using experimental and modeling under different deformation conditions during hot extrusion can be extended to various dimensions of the future research work as given as below:

1) Determination of formability limits of P/M Al-Cu-Mg preforms from establishing the forming limit diagrams during extrusion at elevated temperatures.
2) Investigation of aging behaviour of hot extruded Al-Cu-Mg preforms to improve microstructural and mechanical properties.
3) Addition of Si and rear earth elements to improve the wear resistance and yield strength of Al-4%Cu-0.5%Mg after hot extrusion.
4) Development of new functionally graded materials from Al-Cu-Mg preforms using hot extrusion.
5) Development of dislocation density evolution model, subgrain boundary area evolution model and recrystallization grain boundary are evolution model to gain many insights into the microstructures of hot extruded Al-Cu-Mg preforms.
6) Investigation of damage characterization or failure analysis of hot extruded Al-Cu-Mg P/M alloys.

References

[1] D. Ramakrishnan, "Automotive applications of powder metallurgy," *Adv. Powder Metall. Prop. Process. Appl.*, pp. 493–519, 2013.

[2] J. R. Pickens, "Aluminium powder metallurgy technology for high-strength applications," *J. Mater. Sci.*, vol. 16, no. 6, pp. 1437–1457, 1981.

[3] Y. Barbaux and G. Pons, "New rapidly solidified aluminum alloys for elevated temperature applications on aerospace structures," *J. Phys.*, vol. 3, no. 7 pt 1, pp. 191–196, 1993.

[4] C. C. Huang and J. H. Cheng, "An investigation into the forming limits of sintered porous materials under different operational conditions," *J. Mater. Process. Technol.*, vol. 148, no. 3, pp. 382–393, 2004.

[5] J. P. Maria Rosa Virdis, "Energy to 2050 Scenarios for a Sustainable Future," *International energy agency*, 2003. .

[6] G. Kelly, "Joining of Carbon Fibre Reinforced Plastics for Automotive Applications," Royal Institute of Technology, 2004.

[7] Y. Choi, H. T. Yeo, J. H. Park, G. H. Oh, and S. W. Park, "A study on press forming of automotive sub-frame parts using extruded aluminum profile," *J. Mater. Process. Technol.*, vol. 187–188, pp. 85–88, Jun. 2007.

[8] P. G. Sheasby and R. Pinner, "Introduction : Aluminium , Its Properties , Alloys and Finishes," *Met. Finish.*, pp. 435–450, 2001.

[9] E. J. Lavernia, J. D. Ayers, and T. S. Srivatsan, "Rapid solidification processing with specific application to aluminium alloys," *Int. Mater. Rev.*, vol. 37, no. 1, pp. 1–44, Jan. 1992.

[10] H M Flower, *High Performance Materials in Aerospace*. London: Chapman & Hall, 1995.

[11] X. Du, R. Liu, X. Xiong, and H. Liu, "Effects of sintering time on the microstructure and properties of an Al-Cu-Mg alloy," *Journal of Materials Research and Technology*, vol. 9, no. 5. pp. 9657–9666, 2020.

[12] C. Kammer, "Aluminum and aluminum alloys," *Springer Handbooks*, pp. 157–193, 2018.

[13] J. L. Murray, "The aluminium-copper system," *Int. Met. Rev.*, vol. 30, no. 1, pp. 211–233, Jan. 1985.

[14] X. J. Liu, C. P. Wang, I. Ohnuma, R. Kainuma, and K. Ishida, "Experimental investigation

and thermodynamic calculation of the phase equilibria in the Cu-Sn and Cu-Sn-Mn systems," *Metall. Mater. Trans. A Phys. Metall. Mater. Sci.*, vol. 35 A, no. 6, pp. 1641–1654, 2004.

[15] V. T. Witusiewicz, U. Hecht, S. G. Fries, and S. Rex, "The Ag-Al-Cu system part I: Reassessment of the constituent binaries on the basis of new experimental data," *J. Alloys Compd.*, vol. 385, no. 1–2, pp. 133–143, Dec. 2004.

[16] S. M. Liang and R. Schmid-Fetzer, "Thermodynamic assessment of the Al-Cu-Zn system, part II: Al-Cu binary system," *Calphad Comput. Coupling Phase Diagrams Thermochem.*, vol. 51, pp. 252–260, Dec. 2015.

[17] A. Gökçe, F. Findik, and A. O. Kurt, "Sintering and aging behaviours of Al4CuXMg PM alloy," *Can. Metall. Q.*, vol. 55, no. 4, pp. 391–401, 2016.

[18] D. R. H. J. Michael F. Ashby, *Engineering Materials 2: An Introduction to Microstructures, Processing and Design*, 3rd Editio. Cambridge, UK: Elsevier, 2013.

[19] L. W. Kempf, "Properties of Compressed and Heated Aluminum Alloy Powder Mixtures," pp. 314–316, 1942.

[20] S. J. Cho, S. J. L. Kang, and D. N. Yoon, "Effect of Entrapped Inert Gas on Pore Filling During Liquid Phase Sintering.," *Metall. Trans. A, Phys. Metall. Mater. Sci.*, vol. 17 A, no. 12, pp. 2175–2182, 1986.

[21] J.R. Pickens and M. M. Laboratories, "High-Strength Aluminum P/M Alloys," *ASM Handbook, Vol. 4 Heat Treat.*, vol. 4, p. p 841-879, 1990.

[22] C. D. Boland, R. L. Hexemer, I. W. Donaldson, and D. P. Bishop, "Industrial processing of a novel Al-Cu-Mg powder metallurgy alloy," *Mater. Sci. Eng. A*, vol. 559, pp. 902–908, 2013.

[23] A. Eksi, G. Veltl, F. Petzoldt, K. Lipp, and C. M. Sonsino, "Tensile and fatigue properties of cold and warm compacted Alumix 431 alloy," *Powder Metall.*, vol. 47, no. 1, pp. 60–64, 2004.

[24] G. N. Grayson, G. B. Schaffer, and J. R. Griffiths, "Fatigue crack propagation in a sintered 2xxx series aluminium alloy," *Mater. Sci. Eng. A*, vol. 434, no. 1–2, pp. 1–6, 2006.

[25] G. N. Grayson, G. B. Schaffer, and J. R. Griffiths, "Observations of oxide films on fatigue fracture surfaces of a sintered 2xxx series aluminium alloy," *Mater. Sci. Eng. A*, vol. 454–455, pp. 99–103, 2007.

[26] M. L. Delgado, E. M. Ruiz-Navas, E. Gordo, and J. M. Torralba, "Enhancement of liquid

phase sintering through Al-Si additions to Al-Cu systems," *J. Mater. Process. Technol.*, vol. 162–163, no. SPEC. ISS., pp. 280–285, 2005.

[27] M. Abdel-Rahman and M. N. El-Sheikh, "Workability in forging of powder metallurgy compacts," *J. Mater. Process. Tech.*, vol. 54, no. 1–4, pp. 97–102, 1995.

[28] R. Narayanasamy, V. Anandakrishnan, and K. S. Pandey, "Effect of geometric work-hardening and matrix work-hardening on workability and densification of aluminium-3.5% alumina composite during cold upsetting," *Mater. Des.*, vol. 29, no. 8, pp. 1582–1599, 2008.

[29] K. T. Kim, S. C. Lee, and H. S. Ryu, "Densification behavior of aluminum alloy powder mixed with zirconia powder inclusion under cold compaction," *Mater. Sci. Eng. A*, vol. 340, no. 1–2, pp. 41–48, 2003.

[30] S. Narayan and A. Rajeshkannan, "Densification behaviour in forming of sintered iron-0.35% carbon powder metallurgy preform during cold upsetting," *Mater. Des.*, vol. 32, no. 2, pp. 1006–1013, 2011.

[31] R. E. D. Mann, R. L. Hexemer, I. W. Donaldson, and D. P. Bishop, "Hot deformation of an Al-Cu-Mg powder metallurgy alloy," *Mater. Sci. Eng. A*, vol. 528, no. 16–17, pp. 5476–5483, 2011.

[32] E. S. P. B. V, P. Venugopal, S. Venkatraman, R. Vasudevan, and K. A. Padmanabhan, "Ring-compression tests on sintered iron preforms," vol. 16, pp. 51–64, 1988.

[33] P. Kapranos, P. J. Ward, H. V. Atkinson, and D. H. Kirkwood, "Near net shaping by semi-solid metal processing," *Mater. Des.*, vol. 21, no. 4, pp. 387–394, 2000.

[34] M. C. Flemings, "Behavior of metal alloys in the semisolid state," *Metall. Trans. A*, vol. 22, no. 5, pp. 957–981, 1991.

[35] E. Becker, R. Bigot, and L. Langlois, "Thermal exchange effects on steel thixoforming processes," *Int. J. Adv. Manuf. Technol.*, vol. 48, no. 9–12, pp. 913–924, 2010.

[36] Z. Fan, "Semisolid metal processing," *Int. Mater. Rev.*, vol. 47, no. 2, pp. 49–86, 2002.

[37] P. Kapranos, T. Haga, E. Bertoli, A. Pola, Z. Azpilgain, and I. Hurtado, "Thixo-extrusion of 5182 aluminium alloy," *Solid State Phenom.*, vol. 141–143, no. August 2016, pp. 115–120, 2008.

[38] C. G. Kang, C. K. Jin, and A. Bolouri, "Semisolid forming of thin plates with microscale features," *Procedia Eng.*, vol. 81, no. October, pp. 63–73, 2014.

[39] Y. Meng, S. Sugiyama, and J. Yanagimoto, "Microstructural evolution during RAP

process and deformation behavior of semi-solid SKD61 tool steel," *J. Mater. Process. Technol.*, vol. 212, no. 8, pp. 1731–1741, 2012.

[40] C. F. Wang, K. K. Wang, and Z. Luo, "Simulation on flexible thixo-extrusion of variable cross-section part based on deform-3d software," *Solid State Phenom.*, vol. 217–218, pp. 201–207, 2014.

[41] I. J. Polmear, "Light Alloys—Metallurgy of the Light Metals," *Am. Soc. Met.*, 1982.

[42] M. F. Wilson *et al.*, "Hot extrusion of a commercial aluminum powder metallurgy metal matrix composite material," *Mater. Perform. Charact.*, vol. 9, no. 4, 2020.

[43] G. Hirt, L. Khizhnyakova, R. Baadjou, F. Knauf, and R. Kopp, "Semi-Solid Forming of Aluminium and Steel -Introduction and Overview," *Thixoforming Semi-solid Met. Process.*, pp. 1–27, 2009.

[44] J. E. Hatch, *Aluminium : Properties and Physical Metallurgy*. Ohio: Aluminum Association Inc. and ASM International, 1984.

[45] X. Huang, H. Zhang, Y. Han, W. Wu, and J. Chen, "Hot deformation behavior of 2026 aluminum alloy during compression at elevated temperature," *Mater. Sci. Eng. A*, vol. 527, no. 3, pp. 485–490, 2010.

[46] Y. C. Lin, M. S. Chen, and J. Zhong, "Constitutive modeling for elevated temperature flow behavior of 42CrMo steel," *Comput. Mater. Sci.*, vol. 42, no. 3, pp. 470–477, 2008.

[47] Y. Yang, F. Li, Z. Yuan, and H. Qiao, "A modified constitutive equation for aluminum alloy reinforced by silicon carbide particles at elevated temperature," *J. Mater. Eng. Perform.*, vol. 22, no. 9, pp. 2641–2655, 2013.

[48] K. D. Amir Etaati, "A study on hot deformation behaviour of Ni-42.5Ti- 7.5Cu alloy," *Mater. Chem. Phys.*, vol. 140, p. 208e215, 2013.

[49] S. I. Oh, "Finite element analysis of metal forming processes with arbitrarily shaped dies," *Int. J. Mech. Sci.*, vol. 24, no. 8, pp. 479–493, Jan. 1982.

[50] D. C. Ko, B. M. Kim, and J. C. Choi, "Prediction of surface-fracture initiation in the axisymmetric extrusion and simple upsetting of an aluminum alloy," *J. Mater. Process. Technol.*, vol. 62, no. 1–3, pp. 166–174, Nov. 1996.

[51] W. R. D. Wilson, S. R. Schmid, and J. Liu, "Advanced simulations for hot forging: Heat transfer model for use with the finite element method," *J. Mater. Process. Technol.*, vol. 155–156, no. 1–3, pp. 1912–1917, Nov. 2004.

[52] S. Dowlatshahi, "An application of design of experiments for optimization of plastic

injection molding processes," *J. Manuf. Technol. Manag.*, vol. 15, no. 6, pp. 445–454, 2004.

[53] J.-H. KeunPark, "Design ofexperiment considering two- way interactions and its application to injection molding processes with numerical analysis," *J. Mater. Process. Technol.*, vol. 146, no. 2, pp. 221–227, 2004.

[54] R. S. Rao, C. G. Kumar, R. S. Prakasham, and P. J. Hobbs, "The Taguchi methodology as a statistical tool for biotechnological applications: A critical appraisal," *Biotechnol. J.*, vol. 3, no. 4, pp. 510–523, 2008.

[55] H. Singh and P. Kumar, "Optimizing cutting force for turned parts by Taguchi's parameter design approach," *Indian J. Eng. Mater. Sci.*, vol. 12, no. 2, pp. 97–103, 2005.

[56] S. Kamaruddin, Z. A. Khan, and S. H. Foong, "Application of Taguchi Method in the Optimization of Injection Moulding Parameters for Manufacturing Products from Plastic Blend," *Int. J. Eng. Technol.*, vol. 2, no. 6, pp. 574–580, 2010.

[57] Phillip J. Ross, *Taguchi technique for quality engineering*. McGraw Hill, 1996.

[58] H. J. Shim and J. K. Kim, "Cause of failure and optimization of a V-belt pulley considering fatigue life uncertainty in automotive applications," *Eng. Fail. Anal.*, vol. 16, no. 6, pp. 1955–1963, 2009.

[59] A. Mahfouz, S. A. Hassan, and A. Arisha, "Practical simulation application: Evaluation of process control parameters in Twisted-Pair Cables manufacturing system," *Simulation Modelling Practice and Theory*, vol. 18, no. 5. Elsevier, pp. 471–482, 01-May-2010.

[60] N. C. Fei, N. M. Mehat, and S. Kamaruddin, "Practical Applications of Taguchi Method for Optimization of Processing Parameters for Plastic Injection Moulding: A Retrospective Review," *ISRN Ind. Eng.*, vol. 2013, pp. 1–11, 2013.

[61] T. Senthilvelan, K. Raghukandan, and A. Venkatraman, "Modelling of process parameters on the working of P/M copper preforms," *J. Mater. Process. Technol.*, vol. 142, no. 3, pp. 767–772, 2003.

[62] R. P. Cherian, L. N. Smith, and P. S. Midha, "Neural network approach for selection of powder metallurgy materials and process parameters," *Artif. Intell. Eng.*, vol. 14, no. 1, pp. 39–44, Jan. 2000.

[63] S. B. Jurkovic Zoran, Jurkovic M, "Optimization of extrusion force prediction model using different techniques," *J. Achiev. Mater. Manuf. Eng.*, vol. 17, no. 1–2, pp. 353–356, 2006.

[64] S. Lakshmanan, P. Chinnakutti, M. K. Namballa, and M. a M. C. Engineering, "Optimization of Surface Roughness using Response Surface Methodology for EN31 Tool Steel EDM Machining," *Int. J. Recent Dev. Eng. Technol.*, vol. 1, no. 3, pp. 33–37, 2013.

[65] K. E. Alyamac, E. Ghafari, and R. Ince, "Development of eco-efficient self-compacting concrete with waste marble powder using the response surface method," *J. Clean. Prod.*, vol. 144, pp. 192–202, Feb. 2017.

[66] B. Şimşek, T. Uygunoğlu, H. Korucu, and M. M. Kocakerim, "Analysis of the effects of dioctyl terephthalate obtained from polyethylene terephthalate wastes on concrete mortar: A response surface methodology based desirability function approach application," *J. Clean. Prod.*, vol. 170, pp. 437–445, Jan. 2018.

[67] B. S. Mohammed, V. C. Khed, and M. F. Nuruddin, "Rubbercrete mixture optimization using response surface methodology," *J. Clean. Prod.*, vol. 171, pp. 1605–1621, Jan. 2018.

[68] M. Tyagi, A. Rana, S. Kumari, and S. Jagadevan, "Adsorptive removal of cyanide from coke oven wastewater onto zero-valent iron: Optimization through response surface methodology, isotherm and kinetic studies," *J. Clean. Prod.*, vol. 178, pp. 398–407, Mar. 2018.

[69] A. O. S. T. F. Awolusi, O. L. Oke, O. O. Akinkurolere, "Application of response surface methodology: Predicting and optimizing the properties of concrete containing steel fibre extracted from waste tires with," *Case Stud. Constr. Mater.*, vol. 10, pp. 1–21, 2019.

[70] P. Delarbre and M. Krehl, *Powder Metallurgy Aluminium and Light Alloys for Automotive Applications*. new Jersey: metal Powder industries Federation, 2000.

[71] W. H. Hunt, "New directions in aluminum-based P/M materials for automotive applications," in *SAE Transactions*, vol. 109, no. 5, 2000, pp. 90–97.

[72] W. B. James and H. Corporation, "Powder Metallurgy Methods and Applications," *Powder Metall.*, vol. 7, pp. 9–19, 2018.

[73] H. Carpenter and J. M. Robertson, "The metallography of some ancient Egyptian implements," *Nature*, vol. 125, no. 3162, pp. 859–862, 1930.

[74] R. J. Green, "A plasticity theory for porous solids," *Int. J. Mech. Sci.*, vol. 14, no. 4, pp. 215–224, Apr. 1972.

[75] G. S. Upadhyaya, *powder metallurgy technology*, 1st ed. Cambridge: cambridge international Science Publishing, 2002.

[76] S. S. M. Nor, M. M. Rahman, F. Tarlochan, B. Shahida, and A. K. Ariffin, "The effect of lubrication in reducing net friction in warm powder compaction process," *J. Mater. Process. Technol.*, vol. 207, no. 1–3, pp. 118–124, Oct. 2008.

[77] H. A. Al-Qureshi, M. R. F. Soares, D. Hotza, M. C. Alves, and A. N. Klein, "Analyses of the fundamental parameters of cold die compaction of powder metallurgy," *J. Mater. Process. Technol.*, vol. 199, no. 1, pp. 417–424, Apr. 2008.

[78] W. Li, S. J. Park, P. Suri, A. Antonyraj, and R. M. German, "Investigation on die wear behaviour during compaction of aluminium matrix composite powders," *Powder Metall.*, vol. 54, no. 3, pp. 202–208, Jul. 2011.

[79] O. S. G. Bockstiegel, "The influence of lubrication, die material and tool design upon die-wear in the compacting of iron powders, Modern Developments in Powder Metallurgy," in *Proceedings of the International Conference sponsored by MPIF & APMI,* 1971, vol. 4, pp. 87–125.

[80] J. Z. Wang, X. H. Qu, H. Q. Yin, M. J. Yi, and X. J. Yuan, "High velocity compaction of ferrous powder," *Powder Technol.*, vol. 192, no. 1, pp. 131–136, 2009.

[81] J. Robertson, J. T. Im, I. Karaman, K. T. Hartwig, and I. E. Anderson, "Consolidation of amorphous copper based powder by equal channel angular extrusion," *J. Non. Cryst. Solids*, vol. 317, no. 1–2, pp. 144–151, 2003.

[82] J. Duszczyk, D. Bialo, "The compaction of metal powders in rotary die pressing," *Powder Met. Int*, vol. 11, no. 3, pp. 103–105, 1979.

[83] A. Dudek and R. Włodarczyk, "Effect of sintering atmosphere on properties of porous stainless steel for biomedical applications," *Mater. Sci. Eng. C*, vol. 33, no. 1, pp. 434–439, 2013.

[84] M. A. Jabbari Taleghani, E. M. Ruiz Navas, and J. M. Torralba, "Microstructural and mechanical characterisation of 7075 aluminium alloy consolidated from a premixed powder by cold compaction and hot extrusion," *Mater. Des.*, vol. 55, pp. 674–682, 2014.

[85] A. Savitskii, "Liquid-Phase Sintering of the Systems With Interacting Components," pp. 19–28, 1999.

[86] Sercombe T B, "Non-Conventional Sintered Aluminum Powder Alloys," The University of Queensland, 1998.

[87] G. B. Schaffer, B. J. Hall, S. J. Bonner, S. H. Huo, and T. B. Sercombe, "The effect of the atmosphere and the role of pore filling on the sintering of aluminium," *Acta Mater.*, vol.

54, no. 1, pp. 131–138, Jan. 2006.

[88] and R. C. C.L Falticeanu, I.T.H Chang, J.S. Kim, “Sintering behaviour of Al-Cu-Mg-Si blends,” in *Powder Metallurgy, World COngress & Exhibition*, 2006, pp. 597–600.

[89] C. Padmavathi and A. Upadhyaya, “Sintering behaviour and mechanical properties of Al-Cu-Mg-Si-Sn aluminum alloy,” *Trans. Indian Inst. Met.*, vol. 64, no. 4–5, pp. 345–357, 2011.

[90] H. Rudianto, G. J. Jang, S. S. Yang, Y. J. Kim, and I. Dlouhy, “Evaluation of sintering behavior of premix al-Zn-mg-cu alloy powder,” *Adv. Mater. Sci. Eng.*, vol. 2015, 2015.

[91] D. N. F. Muche, M. A. T. Marple, S. Sen, and R. H. R. Castro, “Grain boundary energy, disordering energy and grain growth kinetics in nanocrystalline MgAl2O4 spinel,” *Acta Mater.*, vol. 149, pp. 302–311, 2018.

[92] R. N. Lumley, T. B. Sercombe, and G. B. Schaffer, “Surface oxide and the role of magnesium during the sintering of aluminum,” *Metall. Mater. Trans. A Phys. Metall. Mater. Sci.*, vol. 30, no. 2, pp. 457–463, 1999.

[93] A. D. McLeod and C. M. Gabryel, “Kinetics of the growth of spinel, MgAl2O4, on alumina particulate in aluminum alloys containing magnesium,” *Metall. Trans. A*, vol. 23, no. 4, pp. 1279–1283, Apr. 1992.

[94] D. P. Bishop, X. Y. Li, K. N. Tandon, and W. F. Caley, “Dry sliding wear behaviour of aluminum alloy 2014 microalloyed with Sn and Ag,” *Wear*, vol. 222, no. 2, pp. 84–92, Nov. 1998.

[95] C. D. Boland, R. L. Hexemer, I. W. Donaldson, and D. P. Bishop, “Industrial processing of a novel Al-Cu-Mg powder metallurgy alloy,” *Materials Science and Engineering A*, vol. 559. pp. 902–908, 2013.

[96] G. B. Schaffer, T. B. Sercombe, and R. N. Lumley, “Liquid phase sintering of aluminum alloys,” *Mater. Chem. Phys.*, vol. 67, no. 1–3, pp. 85–91, Jan. 2001.

[97] T. B. Sercombe and G. B. Schaffer, “On the use of trace additions of Sn to enhance sintered 2xxx series Al powder alloys,” *Mater. Sci. Eng. A*, vol. 268, no. 1–2, pp. 32–39, Aug. 1999.

[98] T. B. Sercombe and G. B. Schaffer, “The effect of trace elements on the sintering of Al - Cu alloys,” *Acta Mater.*, vol. 47, no. 2, pp. 689–697, Jan. 1999.

[99] K. F. and K. J. Pieczonka T., Gácsi Z., “Sintering behaviour of Al-SiC powder mixtures controlled by dilatometry,” in *Proc. PM2004*, 2004, pp. 95–100.

[100] J. H. Dudas and C. B. Thompson, “Improved Sintering Procedures for Aluminum P/M Parts,” *Mod. Dev. Powder Metall.*, pp. 19–36, 1971.

[101] H. B. J. Schaffer G.B., Sercombe T.B., Huo S.H. and and Sparklin J.A., “Atmosphere Effects in the Sintering of Aluminium,” in *Proc. PM2004*, 2004, pp. 11–16.

[102] R. G. Iacocca and R. M. German, “The experimental evaluation of die compaction lubricants using deterministic chaos theory,” *Powder Technol.*, vol. 102, no. 3, pp. 253–265, May 1999.

[103] L. F. Mondolfo:, *Aluminum alloys: structure and properties*. London: Butterworths, 1976.

[104] I. J. Polmear, *Light alloys: Metallurgy of the Light Metals*. Arnold, 1995.

[105] T. Pieczonka, T. Schubert, S. Baunack, and B. Kieback, “Sintering Behaviour of Aluminium in Different Atmospheres,” no. August 2016, pp. 5–8, 2005.

[106] J. M. Martín and F. Castro, “Liquid phase sintering of P/M aluminium alloys: Effect of processing conditions,” in *Journal of Materials Processing Technology*, 2003, vol. 143–144, no. 1, pp. 814–821.

[107] H. J. Rack and R. W. Krenzer, “Thermomechanical treatment of high purity 6061 aluminum,” *Metall. Trans. A*, vol. 8, no. 2, pp. 335–346, Feb. 1977.

[108] N. Park, “SEMI-SOLID METAL PROCESSING: CROSS REFERENCE TO RELATED APPLICATIONS,” US 6,311,759 B1, 2001.

[109] C. H. Shashikanth and M. J. Davidson, “Experimental and simulation studies on thixoforming of AA 2017 alloy,” *Mater. High Temp.*, vol. 32, no. 6, pp. 541–550, 2015.

[110] R. Song, Y. Kang, and A. Zhao, “Semi-solid rolling process of steel strips,” *J. Mater. Process. Technol.*, vol. 198, no. 1–3, pp. 291–299, 2008.

[111] C. H. Shashikanth and M. J. Davidson, “Simulation studies on deformation behaviour of AA2017 alloy in semi-solid state using FEA,” *Mater. High Temp.*, vol. 31, no. 3, pp. 274–281, 2014.

[112] M. M. Rovira, B. C. Lancini, and M. H. Robert, “Thixo-forming of Al-Cu alloys,” *J. Mater. Process. Technol.*, vol. 92–93, pp. 42–49, Aug. 1999.

[113] Y. Birol, E. A. Guven, and L. J. Capan, “Extrusion of en AW-2014 alloy in semisolid state,” *Mater. Sci. Technol.*, vol. 27, no. 12, pp. 1851–1857, 2011.

[114] M. S. Salleh, M. Z. Omar, J. Syarif, M. N. Mohammed, and K. S. Alhawari, “Thermodynamic simulation on thixoformability of aluminium alloys for semi-solid metal processing,” *Int. J. Math. Comput. Simul.*, vol. 7, no. 3, pp. 286–293, 2013.

[115] A. Neag, V. Favier, R. Bigot, and D. Frunză, “Study on thixo-extrusion of semi-solid aluminium,” *Solid State Phenom.*, vol. 141–143, pp. 659–664, 2008.

[116] D. Liu, H. V. Atkinson, P. Kapranos, W. Jirattiticharoean, and H. Jones, “Microstructural evolution and tensile mechanical properties of thixoformed high performance aluminium alloys,” *Mater. Sci. Eng. A*, vol. 361, no. 1–2, pp. 213–224, 2003.

[117] J. Dong, J. Z. Cui, Q. C. Le, and G. M. Lu, “Liquidus semi - continous casting, reheating and thixoforming of a wrought aluminum alloy 7075,” *Mater. Sci. Eng. A*, vol. 345, no. 1–2, pp. 234–242, 2003.

[118] S. Chayong, H. V. Atkinson, and P. Kapranos, “Thixoforming 7075 aluminium alloys,” *Mater. Sci. Eng. A*, vol. 390, no. 1–2, pp. 3–12, 2005.

[119] H. V. Atkinson, K. Burke, and G. Vaneetveld, “Recrystallisation in the semi-solid state in 7075 aluminium alloy,” *Mater. Sci. Eng. A*, vol. 490, no. 1–2, pp. 266–276, 2008.

[120] P. Li, T. Chen, S. Zhang, and R. Guan, “Research on semisolid microstructural evolution of 2024 aluminum alloy prepared by powder thixoforming,” *Metals (Basel).*, vol. 5, no. 2, pp. 547–564, 2015.

[121] I. Ozdemir, S. Muecklich, H. Podlesak, and B. Wielage, “Thixoforming of AA 2017 aluminum alloy composites,” *J. Mater. Process. Technol.*, vol. 211, no. 7, pp. 1260–1267, 2011.

[122] A. Onat, H. Akbulut, and F. Yilmaz, “Production and characterisation of silicon carbide particulate reinforced aluminium-copper alloy matrix composites by direct squeeze casting method,” *J. Alloys Compd.*, vol. 436, no. 1–2, pp. 375–382, 2007.

[123] R. S. Rachmat, H. Takano, N. Ikeya, S. Kamado, and Y. Kojima, “Application of semi-solid forming to 2024 and 7075 wrought aluminum billets fabricated by the EMC process,” *Mater. Sci. Forum*, vol. 329, pp. 487–492, 2000.

[124] W. G. Cho and C. G. Kang, “Mechanical properties and their microstructure evaluation in the thixoforming process of semi-solid aluminum alloys,” *J. Mater. Process. Technol.*, vol. 105, no. 3, pp. 269–277, Sep. 2000.

[125] K. Xia and G. Tausig, “Liquidus casting of a wrought aluminum alloy 2618 for thixoforming,” *Mater. Sci. Eng. A*, vol. 246, no. 1–2, pp. 1–10, May 1998.

[126] H. Kaufmann and P. J. Uggowitzer, “Fundamentals of the New Rheocasting process for magnesium alloys,” *Adv. Eng. Mater.*, vol. 3, no. 12, pp. 963–967, 2001.

[127] X. Zhang, T. Chen, H. Qin, and C. Wang, “A comparative study on permanent mold cast

and powder thixoforming 6061 aluminum alloy and Sicp/6061Al composite: Microstructures and mechanical properties," *Materials (Basel).*, vol. 9, no. 6, 2016.

[128] C. Tekmen, I. Ozdemir, U. Cocen, and K. Onel, "The mechanical response of Al-Si-Mg/SiCp composite: Influence of porosity," *Mater. Sci. Eng. A*, vol. 360, no. 1–2, pp. 365–371, Nov. 2003.

[129] D. G. Eskin, Suyitno, and L. Katgerman, "Mechanical properties in the semi-solid state and hot tearing of aluminium alloys," *Prog. Mater. Sci.*, vol. 49, no. 5, pp. 629–711, 2004.

[130] and T. A. L. Yufeng Wu, Gap-Yong Kim, Iver E. Anderson, "Fabrication of Al6061 composite with high SiC particle loading by semi-solid powder processing," *Acta Mater.*, vol. 58, pp. 4398–4405, 2010.

[131] A. Bolouri and C. G. Kang, "Thixoforging of wrought aluminum thin plates with microchannels," *Metall. Mater. Trans. A Phys. Metall. Mater. Sci.*, vol. 45, no. 5, pp. 2575–2589, 2014.

[132] S. and K. A. Kiuchi, M, Sugiyama, "Study of metal forming in the mushy state 2nd report: Extrusion of tube , bar and wire of alloys," in *Twentieth International Machine Tool Design and Research Conference*, 1980, pp. 79–80.

[133] Kiuchi, M, Sugiyana.S, and Arai.K, "Extrusion of Alloy in Mushy-State," *J. Jpn. Soc. Technol. Plast.*, vol. 20, no. 223, pp. 762–769, 1979.

[134] Kiuchi,M. and Sugiyama,S, "Mushy state Extrusion, Rolling and Forging," in *Proceedings of the 3rd International Conference on Semi-solid Processing of Alloys and Composites*, 1994, pp. 245–257.

[135] T. Möller, "Process development and determination of the thermal process window for thixostructure extrusion," RWTH Aachen University, 2004.

[136] S. Miwa, K. and Kawamura, "Semi-Solid extrusion forming process of Stainless steel," in *Proceedings of the 6th International Conference on Semi-solid Processing of Alloys and Composites*, 2000, pp. 279–281.

[137] A. Abdelfattah, S., Robelet, M., Rassili, A, Abdelfattah, S., Robelet, M., Rassili and M. Bobadilla, "Thixoforming of Steels Inductive Reheating and Basic Investigations," in *Proc. of the 6th Intl. Conference on Semi-Solid Processing of Alloys and Composites*, 2000, pp. 283–288.

[138] A. Neag, V. Favier, M. Pop, E. Becker, and R. Bigot, "Effect of experimental conditions on 7075 aluminium response during thixoextrusion," *Key Eng. Mater.*, vol. 504–506, pp.

345–350, 2012.

[139] G. Vaneetveld, A. Rassili, J. C. Pierret, and J. Lecomte-Beckers, “Extrusion tests of 7075 aluminium alloy at high solid fraction,” *Int. J. Mater. Form.*, vol. 1, no. SUPPL. 1, pp. 1019–1022, 2008.

[140] Z. Dazhi, L. Guimin, and C. Jianzhong, “Semi-solid extrusion of aluminum alloy ZL116,” *China Foundry*, vol. 5, no. 2, pp. 104–109, 2008.

[141] Y. Birol, “Response to T6 heat treatment of extruded and thixoformed EN AW 2014 alloys,” *Mater. Sci. Eng. A*, vol. 528, no. 16–17, pp. 5636–5641, 2011.

[142] M. Ketabchi, M. A. Shafaat, I. Shafaat, and M. Abbasi, “Effect of cooling rate on mechanical properties of 7075 aluminum rods extruded in semisolid state,” *J. Eng. Mater. Technol. Trans. ASME*, vol. 136, no. 2, pp. 1–8, 2014.

[143] A. Bolouri, Y. P. Jeon, and C. G. Kang, “The effect of billets extruded by a curved and flat-face die on the semisolid characteristics and tensile properties of thixoformed products,” *Int. J. Adv. Manuf. Technol.*, vol. 70, no. 9–12, pp. 2139–2149, 2014.

[144] C. J. Z. Dazhi, L. Guimin, “Semi–solid thixo-extrusion of AlSi7MgBe alloy,” *CHINESE J. Mater. Res.*, vol. 23, no. 2, pp. 127–132, 2009.

[145] C. Z. CHEN Yun-hai, “Application and development of plastic forming technique for double metal combined pipe,” *Process Equip. Pip.*, vol. 43, no. 5, p. 16−18, 2006.

[146] Henry S. Valberg, *Applied Metal Forming including FEM Analysis*. Cambridge: Cambridge University Press, 2010.

[147] M. Schikorra, L. Donati, L. Tomesani, and A. E. Tekkaya, “Microstructure analysis of aluminum extrusion: Grain size distribution in AA6060, AA6082 and AA7075 alloys,” *J. Mech. Sci. Technol.*, vol. 21, no. 10, pp. 1445–1451, 2007.

[148] R. N. Pearson, E. C., and Parkins, *The Extrusion of Metals*, 2nd ed. London, 1960.

[149] H. Valberg, “modified classification system for metal flow adapted to unlubricated hot extrusion of Al and Al-alloys,” in *Proceedings of the 6th Aluminum Extrusion Technology Seminar*, 1996, pp. 95–100.

[150] P. Venugopal, S. Venkatraman, R. Vasudevan, and K. A. Padmanabhan, “Some failure studies in the hooker extrusion of sintered iron powder metallurgical preforms,” *J. Mech. Work. Technol.*, vol. 16, pp. 165–174, 1988.

[151] W. Z. M. J. Zasadzinksi, W. Libura, J. Richert, “Modeling of Temperature-Speed Parameters In Aluminum Extrusion,” in *Proc. Fifth International Aluminum Extrusion*

Technology Seminar, 1992, pp. 385–387.

[152] S. O. Onuh, M. Ekoja, and M. B. Adeyemi, "Effects of die geometry and extrusion speed on the cold extrusion of aluminium and lead alloys," *J. Mater. Process. Technol.*, vol. 132, no. 1–3, pp. 274–285, Jan. 2003.

[153] J. S. Ajiboye and M. B. Adeyemi, "Effects of die land on the cold extrusion of lead alloy," *J. Mater. Process. Technol.*, vol. 171, no. 3, pp. 428–436, 2006.

[154] P. Tiernan and B. Draganescu, "Statistical modelling of surface hardness and roughness in cold extrusion of aluminium," *Int. J. Manuf. Res.*, vol. 3, no. 4, pp. 452–470, 2008.

[155] M. Shahzad and L. Wagner, "Influence of extrusion parameters on microstructure and texture developments, and their effects on mechanical properties of the magnesium alloy AZ80," *Mater. Sci. Eng. A*, vol. 506, no. 1–2, pp. 141–147, 2009.

[156] R. Das, U. S. Dixit, and S. Deb, "Effect of extrusion ratio, die land length and lubrication on hardness and surface roughness in multi-hole extrusion," *J. Manuf. Technol. Res.*, vol. 4, no. 1–2, pp. 35–47, 2012.

[157] G. Huang, X. Guo, Y. Han, L. Wang, W. Lu, and D. Zhang, "Effect of extrusion dies angle on the microstructure and properties of (TiB+TiC)/Ti6Al4V in situ titanium matrix composite," *Mater. Sci. Eng. A*, vol. 667, pp. 317–325, Jun. 2016.

[158] P. K. Saha, *Aluminum Extrusion Technology*. Materials Park, Ohio: ASM International, 2000.

[159] K. Laue and H. Stenger, *Extrusion*, 2nd ed. American Society for Metals, ASM International, 1981.

[160] K. Laue, *Isothermal Extrusion*. German, 1960.

[161] J. Kialka, "Isothermal Extrusion of Aluminum Alloys by Employing Force-Ram Speed Feedback," in *Proc. Sixth International Aluminum Extrusion Technology Seminar*, 1996.

[162] M. Pandit and K. Buchheit, "New Measurement and Control System for Isothermal Extrusion," in *Sixth International Aluminum Extrusion Technology Seminar*, 1996.

[163] I. S. I. Venas, J. Hergerg, "Isothermal Extrusion Principles and Effect on Extrusion Speed," in *Proc. Fifth International Aluminum Extrusion Technology Seminar*, 1992.

[164] M. M. Peres *et al.*, "Hot Extrusion of Nanostructured Al Alloy Powder: Extrusion Ratio and Temperature Effect on the Microstructure and Mechanical Properties," *Mater. Sci. Forum*, vol. 570, no. February, pp. 91–96, 2008.

[165] C. Zhang, G. Zhao, Z. Chen, H. Chen, and F. Kou, "Effect of extrusion stem speed on

extrusion process for a hollow aluminum profile," *Mater. Sci. Eng. B Solid-State Mater. Adv. Technol.*, vol. 177, no. 19, pp. 1691–1697, 2012.

[166] Z. Z. Chen, Z. L. Lou, and X. Y. Ruan, "Finite volume simulation and mould optimization of aluminum profile extrusion," *J. Mater. Process. Technol.*, vol. 190, no. 1–3, pp. 382–386, 2007.

[167] H. R. Ezatpour, M. Haddad Sabzevar, S. A. Sajjadi, and Y. Huang, "Investigation of work softening mechanisms and texture in a hot deformed 6061 aluminum alloy at high temperature," *Mater. Sci. Eng. A*, vol. 606, pp. 240–247, 2014.

[168] W. Sylwestrowicz and E. O. Hall, "The deformation and ageing of Mild steel," *Proc. Phys. Soc. Sect. B*, vol. 64, no. 6, pp. 495–502, 1951.

[169] N. J. Petch, "The cleavage strength of polycrystals," *J. Iron Steel InstInst*, vol. 174, no. 19, pp. 25–28, 1953.

[170] A. Elsayed, K. Kondoh, H. Imai, and J. Umeda, "Microstructure and mechanical properties of hot extruded Mg-Al-Mn-Ca alloy produced by rapid solidification powder metallurgy," *Mater. Des.*, vol. 31, no. 5, pp. 2444–2453, 2010.

[171] U. Mohammed Iqbal and V. Senthil Kumar, "Effect of process parameters on microstructure and mechanical properties on severe plastic deformation process of Aa7075-T6 aluminum alloy," *Adv. Mater. Res.*, vol. 622, pp. 705–709, 2013.

[172] B. S. and J. C. Kesheng Zuo, Haitao Zhang, Ke Qin, Xing Han, "Effects of Heat Treatment and Extrusion on Microstructure and Properties of A390 Alloy Hollow Billet Fabricated via DC Casting," *Mater. Trans.*, vol. 56, no. 9, pp. 1591–1598, 2015.

[173] C. Zhang, C. Wang, Q. Zhang, G. Zhao, and L. Chen, "Influence of extrusion parameters on microstructure, texture, and second-phase particles in an Al-Mg-Si alloy," *J. Mater. Process. Technol.*, vol. 270, no. March, pp. 323–334, 2019.

[174] Z. C. Sun, H. L. Wu, J. Cao, and Z. K. Yin, "Modeling of continuous dynamic recrystallization of Al-Zn-Cu-Mg alloy during hot deformation based on the internal-state-variable (ISV) method," *Int. J. Plast.*, vol. 106, no. November 2017, pp. 73–87, 2018.

[175] K. Sukumaran *et al.*, "Studies on squeeze casting of Al 2124 alloy and 2124-10% SiCp metal matrix composite," *Mater. Sci. Eng. A*, vol. 490, no. 1–2, pp. 235–241, 2008.

[176] P. Naga Raju, K. Srinivasa Rao, G. M. Reddy, M. Kamaraj, and K. Prasad Rao, "Microstructure and high temperature stability of age hardenable AA2219 aluminium alloy modified by Sc, Mg and Zr additions," *Mater. Sci. Eng. A*, vol. 464, no. 1–2, pp.

192–201, 2007.

[177] J. Wang, D. Yi, X. Su, and F. Yin, “Influence of deformation ageing treatment on microstructure and properties of aluminum alloy 2618,” *Mater. Charact.*, vol. 59, no. 7, pp. 965–968, 2008.

[178] K. Yu, W. Li, S. Li, and J. Zhao, “Mechanical properties and microstructure of aluminum alloy 2618 with Al3(Sc. Zr) phases,” *Mater. Sci. Eng. A*, vol. 368, no. 1–2, pp. 88–93, 2004.

[179] V. S. Krasnikov, A. E. Mayer, and V. V. Pogorelko, “Prediction of the shear strength of aluminum with θ phase inclusions based on precipitate statistics, dislocation and molecular dynamics,” *Int. J. Plast.*, vol. 128, no. January, 2020.

[180] A. E. Mayer, A. A. Ebel, and M. K. A. Al-Sandoqachi, “Plastic deformation at dynamic compaction of aluminum nanopowder: Molecular dynamics simulations and mechanical model,” *Int. J. Plast.*, vol. 124, pp. 22–41, Jan. 2020.

[181] L. Changgu, W. Xiaoding, Kysar Jeffrey W, and H. James, “Measurement of the elastic properties and intrinsic strength of monolayer graphene,” *Science (80-.).*, vol. 321, no. 5887, pp. 385–388, 2008.

[182] R. W. Cooke, R. L. Hexemer, I. W. Donaldson, and D. P. Bishop, “Dispersoid strengthening of Al-Cu-Mg P/M alloy utilising transition metal additions,” *Powder Metall.*, vol. 55, no. 3, pp. 191–199, 2012.

[183] R. A. Jeniski, B. Thanaboonsombut, and T. H. Sanders, “Effect of iron and manganese on the recrystallization behavior of hot-rolled and solution-heat-treated aluminum alloy 6013,” *Metall. Mater. Trans. A Phys. Metall. Mater. Sci.*, vol. 27 A, no. 1, pp. 19–27, 1996.

[184] S. Singh and D. B. Goel, “Influence of thermomechanical aging on fatigue behaviour of 2014 Al-alloy,” *Bull. Mater. Sci.*, vol. 28, no. 2, pp. 91–96, 2005.

[185] A. Gökçe, F. Findik, and A. O. Kurt, “Effects of Mg content on aging behavior of Al4CuXMg PM alloy,” *Mater. Des.*, vol. 46, pp. 524–531, 2013.

[186] C. Zhang, S. Yang, C. Wang, G. Zhao, A. Gao, and L. Wang, “Numerical and experimental investigation on thermo-mechanical behavior during transient extrusion process of high-strength 7 × × × aluminum alloy profile,” *Int. J. Adv. Manuf. Technol.*, vol. 85, no. 5–8, pp. 1915–1926, 2016.

[187] Z. Yan, Y. Yu, J. Qian, Y. Sang, and Y. Yao, “Hot deformation behavior and optimization

of processing parameters of a high-strength Mg-Gd-Nd-Zn-Sn-Zr alloy," *Trans. Indian Inst. Met.*, vol. 73, no. 10, pp. 2435–2445, 2020.

[188] D. X. Wen, Y. C. Lin, H. Bin Li, X. M. Chen, J. Deng, and L. T. Li, "Hot deformation behavior and processing map of a typical Ni-based superalloy," *Mater. Sci. Eng. A*, vol. 591, pp. 183–192, 2014.

[189] G. Liu *et al.*, "Hot deformation behavior and processing map of a superlight dual-phase Mg–Li alloy," *J. Alloys Compd.*, vol. 766, pp. 460–469, 2018.

[190] Y. B. Wang *et al.*, "Dislocation density evolution during high pressure torsion of a nanocrystalline Ni-Fe alloy," *Appl. Phys. Lett.*, vol. 94, no. 9, 2009.

[191] J. Lin, D. Balint, and M. Pietrzyk, *Microstructure evolution in metal forming processes*, 1st Editio. Cambridge, UK: Woodhead Publishing Limited, 2012.

[192] D. W. Wolla, M. J. Davidson, and A. K. Khanra, "Constitutive modeling of powder metallurgy processed Al-4%Cu preforms during compression at elevated temperature," *Mater. Des.*, vol. 65, pp. 83–93, 2015.

[193] S. Liu, J. You, X. Zhang, Y. Deng, and Y. Yuan, "Influence of cooling rate after homogenization on the flow behavior of aluminum alloy 7050 under hot compression," *Mater. Sci. Eng. A*, vol. 527, no. 4–5, pp. 1200–1205, 2010.

[194] H. R. R. Ashtiani and P. Shahsavari, "Strain-dependent constitutive equations to predict high temperature flow behavior of AA2030 aluminum alloy," *Mech. Mater.*, vol. 100, pp. 209–218, 2016.

[195] M. Zhou, Y. C. Lin, J. Deng, and Y. Q. Jiang, "Hot tensile deformation behaviors and constitutive model of an Al-Zn-Mg-Cu alloy," *Mater. Des.*, vol. 59, pp. 141–150, 2014.

[196] M. H. Wang, W. H. Wang, J. Zhou, X. G. Dong, and Y. J. Jia, "Strain effects on microstructure behavior of 7050-H112 aluminum alloy during hot compression," *J. Mater. Sci.*, vol. 47, no. 7, pp. 3131–3139, 2012.

[197] Q. Guo-Zheng, "Characterization for Dynamic Recrystallization Kinetics Based on Stress-Strain Curves," *Recent Dev. Study Recryst.*, 2013.

[198] S. Serajzadeh, "A mathematical model for evolution of flow stress during hot deformation," *Mater. Lett.*, vol. 59, no. 26, pp. 3319–3324, 2005.

[199] J. Wang, J. Chen, Z. Zhao, and X. Y. Ruan, "Hot deformation behavior and flow stress model of F40MnV steel," *J. Cent. South Univ. Technol.*, vol. 14, no. 1, pp. 19–23, 2007.

[200] Bert Verlinden Julian Driver Indradev Samajdar Roger Doherty, *Thermo-Mechanical*

Processing of Metallic Materials, 1st ed. New York: Elsevier Ltd., 2007.

[201] J. Kreyca and E. Kozeschnik, "Analysis of the Temperature and Strain-Rate Dependences of Strain Hardening," *Metall. Mater. Trans. A Phys. Metall. Mater. Sci.*, vol. 49, no. 1, pp. 18–21, 2018.

[202] S. Gourdet and F. Montheillet, "A model of continuous dynamic recrystallization," *Acta Mater.*, vol. 51, no. 9, pp. 2685–2699, 2003.

[203] Y. Li, B. Gu, S. Jiang, Y. Liu, Z. Shi, and J. Lin, "A CDRX-based material model for hot deformation of aluminium alloys," *International Journal of Plasticity*, vol. 134. 2020.

[204] J. Driver, "The limitations of continuous dynamic recrystallization (CDRX) of aluminium alloys," *Mater. Lett.*, vol. 222, pp. 135–137, 2018.

[205] Y. Wang, G. Zhao, X. Chen, X. Xu, L. Chen, and C. Zhang, "Effect of inter-annealing between two stages of extrusion on the microstructure and mechanical property for spray deposited Al-Cu-Li alloy 2195," *J. Mater. Res. Technol.*, vol. 8, no. 5, pp. 3891–3907, 2019.

[206] R. D. Doherty *et al.*, "Current issues in recrystallization: A review," *Mater. Today*, vol. 1, no. 2, pp. 14–15, 1998.

[207] S. J. Hales and R. A. Hafley, "Texture and anisotropy in Al-Li alloy 2195 plate and near-net-shape extrusions," *Mater. Sci. Eng. A*, vol. 257, no. 1, pp. 153–164, 1998.

[208] J. De Paula Martins, A. L. M. De Carvalho, and A. F. Padilha, "Texture analysis of cold rolled and annealed aluminum alloy produced by twin-roll casting," *Mater. Res.*, vol. 15, no. 1, pp. 97–102, 2012.

[209] S. Gourdet and F. Montheillet, "An experimental study of the recrystallization mechanism during hot deformation of aluminium," *Mater. Sci. Eng. A*, vol. 283, no. 1–2, pp. 274–288, 2000.

[210] H. E. Hu, L. Zhen, L. Yang, W. Z. Shao, and B. Y. Zhang, "Deformation behavior and microstructure evolution of 7050 aluminum alloy during high temperature deformation," *Mater. Sci. Eng. A*, vol. 488, no. 1–2, pp. 64–71, Aug. 2008.

[211] M. R. Rokni, A. Zarei-Hanzaki, A. A. Roostaei, and A. Abolhasani, "Constitutive base analysis of a 7075 aluminum alloy during hot compression testing," *Mater. Des.*, vol. 32, no. 10, pp. 4955–4960, 2011.

[212] Y. C. Lin, L. T. Li, Y. X. Fu, and Y. Q. Jiang, "Hot compressive deformation behavior of 7075 Al alloy under elevated temperature," *J. Mater. Sci.*, vol. 47, no. 3, pp. 1306–1318,

2012.

[213] Z. C. Sun, L. S. Zheng, and H. Yang, “Softening mechanism and microstructure evolution of as-extruded 7075 aluminum alloy during hot deformation,” *Mater. Charact.*, vol. 90, pp. 71–80, 2014.

[214] J. A. W. M. T. Lyttle, *Advances in Hot Deformation Textures and Microstructures*. Pittsburgh (PA): The Minerals, Metals and Materials Society, 1994.

[215] M. T. Lyttle and J. A. Wert, “Modelling of continuous recrystallization in aluminium alloys,” *J. Mater. Sci.*, vol. 29, no. 12, pp. 3342–3350, 1994.

[216] K. H. Min, S. P. Kang, B. H. Lee, J. K. Lee, and Y. Do Kim, “Liquid phase sintering of the commercial 2xxx series Al blended powder,” *J. Alloys Compd.*, vol. 419, no. 1–2, pp. 290–293, 2006.

[217] C. Zubizarreta, S. Giménez, J. M. Martín, and I. Iturriza, “Effect of the heat treatment prior to extrusion on the direct hot-extrusion of aluminium powder compacts,” *J. Alloys Compd.*, vol. 467, no. 1–2, pp. 191–201, 2009.

[218] M. Rashad, F. Pan, A. Tang, and M. Asif, “Effect of Graphene Nanoplatelets addition on mechanical properties of pure aluminum using a semi-powder method,” *Prog. Nat. Sci. Mater. Int.*, vol. 24, no. 2, pp. 101–108, 2014.

[219] S. J. Niteesh Kumar, R. Keshavamurthy, M. R. Haseebuddin, and P. G. Koppad, “Mechanical Properties of Aluminium-Graphene Composite Synthesized by Powder Metallurgy and Hot Extrusion,” *Trans. Indian Inst. Met.*, vol. 70, no. 3, pp. 605–613, 2017.

[220] R. J. Arsenault and N. Shi, “Dislocation generation due to differences between the coefficients of thermal expansion,” *Mater. Sci. Eng.*, vol. 81, no. C, pp. 175–187, 1986.

[221] K. T. Kashyap, C. Ramachandra, C. Dutta, and B. Chatterji, “Role of work hardening characteristics of matrix alloys in the strengthening of metal matrix composites,” *Bull. Mater. Sci.*, vol. 23, no. 1, pp. 47–49, 2000.

[222] L. F. Yi, N. Yoshida, T. Yamamoto, T. Onda, and Z. C. Chen, “Microstructure and thermal/mechanical properties of hot-extruded aluminum/graphite composites with Al–Si alloy addition,” *J. Mater. Sci.*, vol. 54, no. 13, pp. 9933–9944, 2019.

[223] I. Hisashi, K. Masashi, K. Katsuyoshi, and O. Isamu, “Characteristics of Hot Extruded P / M Aluminum Alloy when Using the Rapidly Solidified Powder SWAP Process †,” vol. 36, no. 2, pp. 33–38, 2007.

[224] D. Yu *et al.*, "Improving mechanical properties of ZM61 magnesium alloy by aging before extrusion," *J. Alloys Compd.*, vol. 690, pp. 553–560, 2017.

[225] Robson J, Henry D, and Davis b, "Particle effects on recrystallization in magnesium–manganese alloys: Particle-stimulated nucleation," *Acta Mater.*, no. 57, pp. 2739–2747, 2009.

[226] S. W. Xu, K. Oh-Ishi, S. Kamado, and T. Homma, "Twins, recrystallization and texture evolution of a Mg-5.99Zn-1.76Ca-0.35Mn (wt.%) alloy during indirect extrusion process," *Scr. Mater.*, vol. 65, no. 10, pp. 875–878, 2011.

[227] M. H. F.J. Humphreys, *Recrystallization and Related Annealing Phenomena*, 1st editio. Oxford: Pergramon Press, 1995.

[228] A. T. M. Mohammed Y. Abdellah, M. Mahmoud Moustafa, "Hot Extrusion of Reinforced Aluminum Powder Compacts," *Int. J. Mater. Lifetime*, vol. Vol. 1, no. 1, pp. 1–6, 2014.

[229] C. R. Shakespeare and D. A. Oliver, "The hot extrusion of metal powders," *Powder Metall.*, vol. 7, no. 14, pp. 202–212, 1964.

[230] P. J. M. Chare and T. Sheppard, "Powder extrusion as a primary fabricating process for al-fe alloys," *Powder Metall.*, vol. 16, no. 32, pp. 437–458, 1973.

[231] N. Hansen, "A note on the density of sintered aluminium products," *Powder Metall.*, vol. 7, no. 13, pp. 64–67, 1964.

[232] X. Wang *et al.*, "Characterization of hot extrusion and heat treatment on mechanical properties in a spray formed ultra-high strength Al-Zn-Mg-Cu alloy," *Mater. Charact.*, vol. 144, pp. 131–140, 2018.

[233] H. Che, X. Jiang, N. Qiao, and X. Liu, "Effects of Er/Sr/Cu additions on the microstructure and mechanical properties of Al-Mg alloy during hot extrusion," *J. Alloys Compd.*, vol. 708, pp. 662–670, 2017.

[234] G. A. W. Sweet, B. W. Williams, A. Taylor, R. L. Hexemer, I. W. Donaldson, and D. P. Bishop, "A microstructural and mechanical property investigation of a hot upset forged 2xxx series aluminum powder metallurgy alloy reinforced with AlN," *Journal of Materials Processing Technology*, vol. 284. 2020.

[235] B. D. Christensen, I. W. Donaldson, and D. P. Bishop, "Effects of process variables on the mechanical and physical properties of an Al–Cu–Mg powder metallurgy alloy," *SN Appl. Sci.*, vol. 1, no. 6, 2019.

[236] J. Wang, J. Chen, Z. Zhao, and X. Y. Ruan, "Hot deformation behavior and flow stress

model of F40MnV steel," *J. Cent. South Univ. Technol. (English Ed.*, vol. 14, no. 1, pp. 19–23, 2007.

[237] X. S. Li, L. Z. Wu, J. Chen, and H. B. Zhang, "New approach for modeling flow stress of aluminum alloy 6A10 considering temperature variation," *Trans. Nonferrous Met. Soc. China*, vol. 20, no. 8, pp. 1482–1487, 2010.

[238] Y. Deng, Z. Yin, and J. Huang, "Hot deformation behavior and microstructural evolution of homogenized 7050 aluminum alloy during compression at elevated temperature," *Mater. Sci. Eng. A*, vol. 528, no. 3, pp. 1780–1786, 2011.

[239] M. A. Jabbari Taleghani, E. M. Ruiz Navas, M. Salehi, and J. M. Torralba, "Hot deformation behaviour and flow stress prediction of 7075 aluminium alloy powder compacts during compression at elevated temperatures," *Mater. Sci. Eng. A*, vol. 534, pp. 624–631, 2012.

[240] S. Y. Chen, K. H. Chen, G. S. Peng, and L. Jia, "Effect of initial microstructure on hot workability of 7085 aluminum alloy," *Trans. Nonferrous Met. Soc. China*, vol. 23, no. 4, pp. 956–963, 2013.

[241] J. peng LI, J. SHEN, X. dong YAN, B. ping MAO, and L. ming YAN, "Microstructure evolution of 7050 aluminum alloy during hot deformation," *Trans. Nonferrous Met. Soc. China*, vol. 20, no. 2, pp. 189–194, 2010.

[242] Y. C. Lin and X. M. Chen, "A critical review of experimental results and constitutive descriptions for metals and alloys in hot working," *Mater. Des.*, vol. 32, no. 4, pp. 1733–1759, 2011.

[243] D. Samantaray, S. Mandal, and A. K. Bhaduri, "A comparative study on Johnson Cook, modified Zerilli-Armstrong and Arrhenius-type constitutive models to predict elevated temperature flow behaviour in modified 9Cr-1Mo steel," *Comput. Mater. Sci.*, vol. 47, no. 2, pp. 568–576, 2009.

[244] Y. C. Lin, Q. F. Li, Y. C. Xia, and L. T. Li, "A phenomenological constitutive model for high temperature flow stress prediction of Al-Cu-Mg alloy," *Mater. Sci. Eng. A*, vol. 534, pp. 654–662, 2012.

[245] Z. Wang, L. Qi, J. Zhou, J. Guan, and J. Liu, "A constitutive model for predicting flow stress of Al18B 4O33w/AZ91D composite during hot compression and its validation," *Comput. Mater. Sci.*, vol. 50, no. 8, pp. 2422–2426, 2011.

[246] J. Cai, F. Li, T. Liu, B. Chen, and M. He, "Constitutive equations for elevated temperature

flow stress of Ti-6Al-4V alloy considering the effect of strain," *Mater. Des.*, vol. 32, no. 3, pp. 1144–1151, 2011.

[247] C. M. Sellars and W. J. McTegart, "On the mechanism of hot deformation," *Acta Metall.*, vol. 14, no. 9, pp. 1136–1138, 1966.

[248] Y. C. Lin, M. S. Chen, and J. Zhang, "Modeling of flow stress of 42CrMo steel under hot compression," *Mater. Sci. Eng. A*, vol. 499, no. 1–2, pp. 88–92, 2009.

[249] J. Wu and R. Guo, "Constitutive behavior for quenching of Al-Cu-Mg alloy with consideration of precipitation," *J. Eng. Mater. Technol. Trans. ASME*, vol. 140, no. 4, 2018.

[250] S. F. Medina and C. A. Hernandez, "General expression of the Zener-Hollomon parameter as a function of the chemical composition of low alloy and microalloyed steels," *Acta Mater.*, vol. 44, no. 1, pp. 137–148, 1996.

[251] W. Liu, H. Zhao, D. Li, Z. Zhang, G. Huang, and Q. Liu, "Hot deformation behavior of AA7085 aluminum alloy during isothermal compression at elevated temperature," *Mater. Sci. Eng. A*, vol. 596, pp. 176–182, 2014.

[252] D. Feng, X. M. Zhang, S. D. Liu, and Y. L. Deng, "Constitutive equation and hot deformation behavior of homogenized Al-7.68Zn-2.12Mg-1.98Cu-0.12Zr alloy during compression at elevated temperature," *Mater. Sci. Eng. A*, vol. 608, pp. 63–72, 2014.

[253] S. He, C. S. Li, Z. Y. Huang, and J. J. Zheng, "A modified constitutive model based on Arrhenius-Type equation to predict the flow behavior of Fe-36%Ni Invar alloy," *J. Mater. Res.*, vol. 32, no. 20, pp. 3831–3841, 2017.

[254] J. Li, F. Li, J. Cai, R. Wang, Z. Yuan, and F. Xue, "Flow behavior modeling of the 7050 aluminum alloy at elevated temperatures considering the compensation of strain," *Mater. Des.*, vol. 42, pp. 369–377, 2012.

[255] N. Jin, H. Zhang, Y. Han, W. Wu, and J. Chen, "Hot deformation behavior of 7150 aluminum alloy during compression at elevated temperature," *Mater. Charact.*, vol. 60, no. 6, pp. 530–536, 2009.

[256] L. Saravanan and T. Senthilvelan, "Constitutive equation and microstructure evaluation of an extruded aluminum alloy," *J. Mater. Res. Technol.*, vol. 5, no. 1, pp. 21–28, 2016.

[257] D. W. Wolla, M. J. Davidson, and A. K. Khanra, "Studies on the formability of powder metallurgical aluminum-copper composite," *Mater. Des.*, vol. 59, pp. 151–159, 2014.

[258] T. Tabata and S. Masaki, "Determination of the coefficient of friction in forging of porous

metals from ring compression," *Int. J. Mech. Sci.*, vol. 20, no. 8, pp. 505–512, 1978.

[259] S. Serajzadeh and A. K. Taheri, "Prediction of flow stress at hot working condition," *Mech. Res. Commun.*, vol. 30, no. 1, pp. 87–93, 2003.

[260] H. Mirzadeh and A. Najafizadeh, "Flow stress prediction at hot working conditions," *Mater. Sci. Eng. A*, vol. 527, no. 4–5, pp. 1160–1164, 2010.

[261] H. Mirzadeh and A. Najafizadeh, "Prediction of the critical conditions for initiation of dynamic recrystallization," *Mater. Des.*, vol. 31, no. 3, pp. 1174–1179, 2010.

[262] M. Seyed Salehi and S. Serajzadeh, "A neural network model for prediction of static recrystallization kinetics under non-isothermal conditions," *Comput. Mater. Sci.*, vol. 49, no. 4, pp. 773–781, 2010.

[263] Y. C. Lin, M. S. Chen, and J. Zhong, "Microstructural evolution in 42CrMo steel during compression at elevated temperatures," *Mater. Lett.*, vol. 62, no. 14, pp. 2132–2135, 2008.

[264] H. Mirzadeh and A. Najafizadeh, "The rate of dynamic recrystallization in 17-4 PH stainless steel," *Mater. Des.*, vol. 31, no. 10, pp. 4577–4583, 2010.

[265] D. Li, Q. Guo, S. Guo, H. Peng, and Z. Wu, "The microstructure evolution and nucleation mechanisms of dynamic recrystallization in hot-deformed Inconel 625 superalloy," *Mater. Des.*, vol. 32, no. 2, pp. 696–705, 2011.

[266] M. Shaban and B. Eghbali, "Characterization of Austenite Dynamic Recrystallization under Different Z Parameters in a Microalloyed Steel," *J. Mater. Sci. Technol.*, vol. 27, no. 4, pp. 359–363, 2011.

[267] G. E. Kodzhaspirov and M. I. Terentyev, "Modeling the dynamically recrystallized grain size evolution of a superalloy," *Mater. Phys. Mech.*, vol. 13, no. 1, pp. 70–76, 2012.

[268] Q. Guo, D. Li, S. Guo, H. Peng, and J. Hu, "The effect of deformation temperature on the microstructure evolution of Inconel 625 superalloy," *J. Nucl. Mater.*, vol. 414, no. 3, pp. 440–450, 2011.

[269] Y. Huang, M. Li, Z. Xiao, H. Liu, and S. Wang, "A Dynamic Recrystallization (DRX) Constitutive Model for Elevated Temperature Flow Behavior of Cu-0.5Cr-0.1Zr Alloy," *Metallogr. Microstruct. Anal.*, vol. 8, no. 1, pp. 45–57, 2019.

[270] S. Wang, Y. Huang, Z. Xiao, Y. Liu, and H. Liu, "A modified Johnson-cook model for hot deformation behavior of 35CrMo steel," *Metals (Basel).*, vol. 7, no. 9, 2017.

[271] H. Zhang, L. Li, D. Yuan, and D. Peng, "Hot deformation behavior of the new Al-Mg-Si-Cu aluminum alloy during compression at elevated temperatures," *Mater. Charact.*, vol.

58, no. 2, pp. 168–173, 2007.

[272] E. I., G. Strang, and G. J. Fix, *An Analysis of the Finite Element Method*, vol. 28, no. 127. prentice-Hall, 1974.

[273] N. Bontcheva, G. Petzov, and L. Parashkevova, "Thermomechanical modelling of hot extrusion of Al-alloys, followed by cooling on the press," *Comput. Mater. Sci.*, vol. 38, no. 1, pp. 83–89, 2006.

[274] Y. S. Jang, D. C. Ko, and B. M. Kim, "Application of the finite element method to predict microstructure evolution in the hot forging of steel," *J. Mater. Process. Technol.*, vol. 101, no. 1, pp. 85–94, 2000.

[275] N. Bontcheva and G. Petzov, "Microstructure evolution during metal forming processes," *Comput. Mater. Sci.*, vol. 28, no. 3–4, pp. 563–573, 2003.

[276] R. Kuziak, M. Glowacki, and M. Pietrzyk, "Modelling of plastic flow, heat transfer and microstructural evolution during rolling of eutectoid steel rods," *J. Mater. Process. Technol.*, vol. 60, no. 1–4, pp. 589–596, 1996.

[277] G. P. N. Bontcheva, "FEM-Rationalized TEMPCOR-process in shape rolling of steel rods," in *International Congress Mechanical Engineering Technologies 04*, 2004, pp. 64–67.

[278] N. Bontcheva and G. Petzov, "Total simulation model of the thermo-mechanical process in shape rolling of steel rods," *Comput. Mater. Sci.*, vol. 34, no. 4, pp. 377–388, 2005.

[279] E. Nes and T. Furu, "Application of microstructurally based constitutive laws to hot deformation of aluminium alloys," *Scr. Metall. Mater.*, vol. 33, no. 1, pp. 87–92, 1995.

[280] E. D. Sweet, S. K. Caraher, N. V Danilova, X. Zhang, and C. A. Limited, "Effects of Extrusion Parameters on Coarse Grain Surface Layer in 6xxx Series Extrusions," in *Proc. of the 8th Alum. Ext. Sem. inum Extrusion Technology Seminar*, 2004, pp. 115–126.

[281] S. R. Claves, W. Z. Misiolek, and R. M. Kelly, "Effect of Die Design on Microstructure of Extruded Aluminum," in *Proc. of the 7th Aluminum Extrusion Technology Seminar*, 2000, pp. 225–231.

[282] S. Kobayashi, "Metal Forming and the Finite Element Method - Past and Future.," in *Proceedings of the International Machine Tool Design and Research Conference*, 1985, pp. 17–32.

[283] X. Duan, X. Velay, and T. Sheppard, "Application of finite element method in the hot extrusion of aluminium alloys," *Mater. Sci. Eng. A*, vol. 369, no. 1–2, pp. 66–75, Mar.

2004.

[284] T. Altan and M. Knoerr, “Application of the 2D finite element method to simulation of cold-forging processes,” *J. Mater. Process. Tech.*, vol. 35, no. 3–4, pp. 275–302, Oct. 1992.

[285] J. R. Cho, Y. S. Joo, and H. S. Jeong, “The Al-powder forging process: Its finite element analysis,” *J. Mater. Process. Technol.*, vol. 111, no. 1–3, pp. 204–209, Apr. 2001.

[286] J. B. Rao, S. Kamaluddin, J. A. Rao, M. M. M. Sarcar, and N. R. M. R. Bhargava, “Finite element analysis of deformation behavior of Aluminium-Copper alloys,” *Mater. Des.*, vol. 30, no. 4, pp. 1298–1309, Apr. 2009.

[287] Y. V. R. K. Prasad and K. P. Rao, “Materials modeling and finite element simulation of isothermal forging of electrolytic copper,” *Mater. Des.*, vol. 32, no. 4, pp. 1851–1858, Apr. 2011.

[288] Z. He, H. N. Wang, M. J. Wang, and G. Y. Li, “Simulation of extrusion process of complicated aluminium profile and die trial,” *Trans. Nonferrous Met. Soc. China*, vol. 22, no. 7, pp. 1732–1737, 2012.

[289] G. Liu, J. Zhou, and J. Duszczyk, “Process optimization diagram based on FEM simulation for extrusion of AZ31 profile,” *Trans. Nonferrous Met. Soc. China*, vol. 18, no. 1, pp. 1–5, 2008.

[290] M. M. Marín, A. M. Camacho, and J. A. Pérez, “Influence of the temperature on AA6061 aluminum alloy in a hot extrusion process,” *Procedia Manuf.*, vol. 13, pp. 327–334, 2017.

[291] X. Duan and T. Sheppard, “Simulation and control of microstructure evolution during hot extrusion of hard aluminium alloys,” *Mater. Sci. Eng. A*, vol. 351, no. 1–2, pp. 282–292, 2003.

[292] A. F. Bastani, T. Aukrust, and S. Brandal, “Study of isothermal extrusion of aluminum using finite element simulations,” *Int. J. Mater. Form.*, vol. 3, no. SUPPL. 1, pp. 367–370, 2010.

[293] T. Sheppard, “Prediction of structure during shaped extrusion and subsequent static recrystallisation during the solution soaking operation,” *J. Mater. Process. Technol.*, vol. 177, no. 1–3, pp. 26–35, 2006.

[294] X. Velay, “Prediction and control of subgrain size in the hot extrusion of aluminium alloys with feeder plates,” *J. Mater. Process. Technol.*, vol. 209, no. 7, pp. 3610–3620, 2009.

[295] F. Parvizian, T. Kayser, and B. Svendsen, “Modeling and simulation of microstructure

evolution in extruded aluminum profiles," *Key Eng. Mater.*, vol. 424, pp. 43–50, 2010.

[296] Q. Lin, W. Dong, Y. Li, H. Zhang, and Z. Wang, "Microstructure simulation of 2519 aluminum alloy in multi-pass hot compression process," *Procedia Eng.*, vol. 81, no. October, pp. 1259–1264, 2014.

[297] A. Foydl *et al.*, "Grain size evolution simulation in aluminium alloys AA 6082 and AA 7020 during hot forward extrusion process," *Mater. Sci. Technol. (United Kingdom)*, vol. 29, no. 1, pp. 100–110, 2013.

[298] D. Cardozo, "Three models of the 3D filling simulation for injection molding: A brief review," *J. Reinf. Plast. Compos.*, vol. 27, no. 18, pp. 1963–1974, 2008.

[299] M. K. A. Mohd Ariffin, M. I. Mohd Ali, S. M. Sapuan, and N. Ismail, "An optimise drilling process for an aircraft composite structure using design of experiments," *Sci. Res. Essays*, vol. 4, no. 10, pp. 1109–1116, 2009.

[300] N. S. Mohan, A. Ramachandra, and S. M. Kulkarni, "Influence of process parameters on cutting force and torque during drilling of glass-fiber polyester reinforced composites," *Compos. Struct.*, vol. 71, no. 3–4, pp. 407–413, 2005.

[301] S. J. Liu and J. H. Chang, "Application of the Taguchi method to optimize the surface quality of gas assist injection molded composites," *J. Reinf. Plast. Compos.*, vol. 19, no. 17, pp. 1352–1362, 2000.

[302] H. Li, Z. Guo, and D. Li, "Reducing the effects of weldlines on appearance of plastic products by Taguchi experimental method," *Int. J. Adv. Manuf. Technol.*, vol. 32, no. 9–10, pp. 927–931, 2007.

[303] Krishankant, J. Taneja, M. Bector, and R. Kumar, "Application of Taguchi Method for Optimizing Turning Process by the Effects of Machining Parameters," *Int. J. Eng. Adv. Technol.*, no. 2, p. 263, 2012.

[304] S. Athreya and Y. D. Venkatesh, "Application Of Taguchi Method For Optimization Of Process Parameters In Improving The Surface Roughness Of Lathe Facing Operation," *Int. Ref. J. Eng. Sci.*, vol. 1, no. 3, pp. 13–19, 2012.

[305] A. C. Mitra, M. Jawarkar, T. Soni, and G. R. Kiranchand, "Implementation of Taguchi Method for Robust Suspension Design," *Procedia Engineering*, vol. 144. pp. 77–84, 2016.

[306] Ö. Savaş and R. Kayikci, "Application of Taguchi's methods to investigate some factors affecting microporosity formation in A360 aluminium alloy casting," *Mater. Des.*, vol. 28, no. 7, pp. 2224–2228, 2007.

[307] N. Miloradović, B. Stojanović, S. Mitrović, and S. Veličković, "Application of Taguchi Method in the Optimization of Zinc Based Composite," *Proc. Eng. Sci.*, vol. 1, no. 1, pp. 104–109, 2019.

[308] T. Tamizharasan, N. Senthilkumar, V. Selvakumar, and S. Dinesh, "Taguchi's methodology of optimizing turning parameters over chip thickness ratio in machining P/M AMMC," *SN Appl. Sci.*, vol. 1, no. 2, 2019.

[309] S. J. Liu, C. H. Lin, and Y. C. Wu, "Minimizing the sinkmarks in injection-molded thermoplastics," *Adv. Polym. Technol.*, vol. 20, no. 3, pp. 202–215, 2001.

[310] M. Altan, "Reducing shrinkage in injection moldings via the Taguchi, ANOVA and neural network methods," *Mater. Des.*, vol. 31, no. 1, pp. 599–604, 2010.

[311] B. Ozcelik and T. Erzurumlu, "Comparison of the warpage optimization in the plastic injection molding using ANOVA, neural network model and genetic algorithm," *J. Mater. Process. Technol.*, vol. 171, no. 3, pp. 437–445, 2006.

[312] W. J. Hill and W. G. Hunter, "A Review of Response Surface Methodology: A Literature Survey," *Technometrics*, vol. 8, no. 4, p. 571, 1966.

[313] V. Muthuraman, R. Ramakrishnan, and L. Karthikeyan, "Modeling and analysis of MRR in WEDMed WC-CO composite by response surface methodology," *Indian J. Sci. Technol.*, vol. 5, no. 12, pp. 3736–3740, 2012.

[314] K. Velmanirajan, A. Syed Abu Thaheer, R. Narayanasamy, and C. Ahamed Basha, "Numerical modelling of aluminium sheets formability using response surface methodology," *Mater. Des.*, vol. 41, pp. 239–254, 2012.

[315] M. Y. Noordin, V. C. Venkatesh, S. Sharif, S. Elting, and A. Abdullah, "Application of response surface methodology in describing the performance of coated carbide tools when turning AISI 1045 steel," *J. Mater. Process. Technol.*, vol. 145, no. 1, pp. 46–58, Jan. 2004.

[316] P. Tiernan, B. Draganescu, and M. T. Hillery, "Modelling of extrusion force using the surface response method," *Int. J. Adv. Manuf. Technol.*, vol. 27, no. 1–2, pp. 48–52, Nov. 2005.

[317] C. S. K. P. R. M. Srinivasulu, M. Komaraiah, "Experimental investigations to predict mean diameter of AA6082 tube in flow forming process – A DOE approach," *IOSR J. Eng.*, vol. 02, no. 06, pp. 52–60, 2012.

[318] L. Wu, K. L. Yick, S. P. Ng, and J. Yip, "Application of the Box-Behnken design to the

optimization of process parameters in foam cup molding," *Expert Syst. Appl.*, vol. 39, no. 9, pp. 8059–8065, 2012.

[319] A. Gökçe, F. Findik, and A. O. Kurt, "Microstructural examination and properties of premixed Al-Cu-Mg powder metallurgy alloy," *Mater. Charact.*, vol. 62, no. 7, pp. 730–735, 2011.

[320] W. A. G. McPhee, G. B. Schaffer, and J. Drennan, "The effect of iron on liquid film migration and sintering of an Al-Cu-Mg alloy," *Acta Mater.*, vol. 51, no. 13, pp. 3701–3712, 2003.

[321] O. Toyran, A. Gökçe, and A. O. Kurt, "Effects of micro level Si addition on the properties of aluminium PM alloy," *6th Int. Powder Metall. Conf. Exhib.*, pp. 891–904, 2011.

[322] K. Kondoh, A. Kimura, and R. Watanabe, "Effect of Mg on sintering phenomenon of aluminium alloy powder particle," *Powder Metall.*, vol. 44, no. 2, pp. 161–164, 2001.

[323] R. Papirno, "Inelastic Buckling of Astm Standard E 9 Compression Specimens.," *J. Test. Eval.*, vol. 15, no. 3, pp. 133–135, 1987.

[324] M. F. Doerner and W. D. Nix, "A method for interpreting the data from depth-sensing indentation instruments," *J. Mater. Res.*, vol. 1, no. 4, pp. 601–609, 1986.

[325] J. Il Jang, "Estimation of residual stress by instrumented indentation: A review," *J. Ceram. Process. Res.*, vol. 10, no. 3, pp. 391–400, 2009.

[326] G. Venkateswarlu, M. Davidson, and G. Tagore, "Influence of process parameters on the cup drawing of aluminium 7075 sheet," *Int. J. Eng. Sci. Technol.*, vol. 2, no. 11, 2011.

[327] R. K. Roy, *A Primer on the Taguchi method*, 2nd editio. New York: Society of Manufacturing Engineers, 2010.

[328] D. Scott Mackenzie, *Analytical characterization of aluminum, steel and superalloys*, 1st Editio. London: CRC press, Taylor & Francis, 2006.

[329] D. W. Heard, I. W. Donaldson, and D. P. Bishop, "Metallurgical assessment of a hypereutectic aluminum-silicon P/M alloy," *J. Mater. Process. Technol.*, vol. 209, no. 18–19, pp. 5902–5911, 2009.

[330] D. P. Bishop, J. R. Cahoon, M. C. Chaturvedi, G. J. Kipouros, and W. F. Caley, "Diffusion-based microalloying of aluminium alloys by powder metallurgy and reaction sintering," *J. Mater. Sci.*, vol. 33, no. 15, pp. 3927–3934, 1998.

[331] Y. Birol, E. A. Guven, and L. J. Capan, "Extrusion of EN AW-2014 alloy in semisolid state," *Mater. Sci. Technol.*, vol. 27, no. 12, pp. 1851–1857, 2011.

[332] S. Yuan, F. Li, and Z. He, “Effects of guiding angle on plastic metal flow and defects in extrusion of aluminum alloy,” *J. Mater. Sci. Technol.*, vol. 24, no. 2, pp. 256–260, 2008.

[333] Y. R. S. Akbar Ahmed A, “Study of the Direct Extrusion Behavior of Aluminum and Aluminum Alloy-2014 Using Conical Dies,” vol. 30, pp. 950–958.

[334] O. P. Gbenebor, O. S. I. Fayomi, A. P. I. Popoola, A. O. Inegbenebor, and F. Oyawale, “Extrusion die geometry effects on the energy absorbing properties and deformation response of 6063-type Al-Mg-Si aluminum alloy,” *Results Phys.*, vol. 3, pp. 1–6, 2013.

[335] K. Bharath, A. K. Khanra, and M. J. Davidson, “Structural Properties Evaluation of Semisolid Extruded Al–Cu–Mg Powder Metallurgy Alloys,” *Trans. Indian Inst. Met.*, vol. 72, no. 4, pp. 1063–1074, 2019.

[336] E. Cerri, E. Evangelista, A. Forcellese, and H. J. McQueen, “Comparative hot workability of 7012 and 7075 alloys after different pretreatments,” *Mater. Sci. Eng. A*, vol. 197, no. 2, pp. 181–198, 1995.

[337] G. Z. Quan, Y. P. Mao, C. T. Yu, W. Q. Lv, and J. Zhou, “The flow behavior modeling of as-extruded 3Cr20Ni10W2 austenitic heat-resistant alloy at elevated temperatures considering the effect of strain,” *Mater. Res.*, vol. 17, no. 2, pp. 451–460, 2014.

[338] H. Hollomon and C. Zener, “Effect of Strain Rate Upon Plastic Flow of Steel,” *J. Appl. Phys.*, vol. 15, pp. 22–32, 1944.

[339] P. wei LI, H. zhong LI, L. HUANG, X. peng LIANG, and Z. xiao ZHU, “Characterization of hot deformation behavior of AA2014 forging aluminum alloy using processing map,” *Trans. Nonferrous Met. Soc. China (English Ed.*, vol. 27, no. 8, pp. 1677–1688, 2017.

[340] L. Chen, G. Zhao, J. Yu, and W. Zhang, “Constitutive analysis of homogenized 7005 aluminum alloy at evaluated temperature for extrusion process,” *Mater. Des.*, vol. 66, no. PA, pp. 129–136, 2015.

[341] H. E. Hu, L. Zhen, L. Yang, W. Z. Shao, and B. Y. Zhang, “Deformation behavior and microstructure evolution of 7050 aluminum alloy during high temperature deformation,” *Mater. Sci. Eng. A*, vol. 488, no. 1–2, pp. 64–71, 2008.

[342] W. Wang, Q. Pan, Y. Sun, X. Wang, A. Li, and W. Song, “Study on hot compressive deformation behaviors and corresponding industrial extrusion of as-homogenized Al–7.82Zn–1.96Mg–2.35Cu–0.11Zr alloy,” *J. Mater. Sci.*, vol. 53, no. 16, pp. 11728–11748, 2018.

[343] H. Zhang, K. Zhang, H. Zhou, Z. Lu, C. Zhao, and X. Yang, “Effect of strain rate on

microstructure evolution of a nickel-based superalloy during hot deformation," *Mater. Des.*, vol. 80, pp. 51–62, 2015.

[344] Q. M. Guo, D. F. Li, and S. L. Guo, "Microstructural models of dynamic recrystallization in hot-deformed inconel 625 superalloy," *Mater. Manuf. Process.*, vol. 27, no. 9, pp. 990–995, 2012.

[345] F. Chen, Z. Cui, and S. Chen, "Recrystallization of 30Cr2Ni4MoV ultra-super-critical rotor steel during hot deformation. Part I: Dynamic recrystallization," *Mater. Sci. Eng. A*, vol. 528, no. 15, pp. 5073–5080, 2011.

[346] F. Bedir, "Modeling approach and plastic deformation analysis of 6063 aluminum alloy during compression at elevated temperatures," *Mater. Des.*, vol. 49, pp. 953–956, 2013.

[347] A. Deschamps and Y. Bréchet, "Influence of quench and heating rates on the ageing response of an Al-Zn-Mg-(Zr) alloy," *Mater. Sci. Eng. A*, vol. 251, no. 1–2, pp. 200–207, 1998.

[348] Z. Mingjie, L. Fuguo, W. Shuyun, and L. Chenyi, "Characterization of hot deformation behavior of a P/M nickel-base superalloy using processing map and activation energy," *Mater. Sci. Eng. A*, vol. 527, no. 24–25, pp. 6771–6779, 2010.

[349] J. Cai, F. Li, T. Liu, B. Chen, and M. He, "Constitutive equations for elevated temperature flow stress of Ti-6Al-4V alloy considering the effect of strain," *Mater. Des.*, vol. 32, no. 3, pp. 1144–1151, Mar. 2011.

[350] S. W. T. Matsui, H. Takizawa, H. Kikuchi, "The Microstructure prediction of alloy 720LI for turbine disk applications," *Superalloys*, pp. 127–133, 2000.

[351] R. Seetharam, S. Kanmani Subbu, and M. J. Davidson, "Microstructure Modeling of Dynamically Recrystallized Grain Size of Sintered Al-4 wt % B4C Composite during Hot Upsetting," *J. Eng. Mater. Technol. Trans. ASME*, vol. 140, no. 2, pp. 1–18, 2018.

[352] P. Wouters, B. Verlinden, H. J. McQueen, E. Aernoudt, L. Delaey, and S. Cauwenberg, "Effect of homogenization and precipitation treatments on the hot workability of an aluminium alloy AA2024," *Mater. Sci. Eng. A*, vol. 123, no. 2, pp. 239–245, 1990.

[353] X. Li, A. Ramazani, U. Prahl, and W. Bleck, "Quantification of complex-phase steel microstructure by using combined EBSD and EPMA measurements," *Mater. Charact.*, vol. 142, pp. 179–186, 2018.

[354] J. Northwood, D.; Rang, T.; De Hosson, *Materials and Contact Characterisation VIII*. Southamptom, Boston, UK: WIT press, 2017.

[355] J. M. Martín and F. Castro, “Sintering response & microstructural evolution of an Al-Cu-Mg-Si premix,” *Int. J. Powder Metall. (Princeton, New Jersey)*, vol. 43, no. 6, pp. 59–69, 2007.

[356] M. R. Rokni, A. Zarei-Hanzaki, A. A. Roostaei, and H. R. Abedi, “An investigation into the hot deformation characteristics of 7075 aluminum alloy,” *Mater. Des.*, vol. 32, no. 4, pp. 2339–2344, 2011.

[357] W.D. Callister, *Fundamentals of materials science and engineering*, 2nd Editio. New York: John Wiley & Sons, 2008.

[358] Y. Yang, Z. Zhang, X. Li, Q. Wang, and Y. Zhang, “The effects of grain size on the hot deformation and processing map for 7075 aluminum alloy,” *Mater. Des.*, vol. 51, pp. 592–597, 2013.

[359] J. B. Pethica, *Ion Implantation into Metals*. Oxford: Pergamon Press, 1982.

[360] A. Mandal *et al.*, “Cold-bending of linepipe steel plate to pipe, detrimental or beneficial?,” *Mater. Sci. Eng. A*, vol. 746, pp. 58–72, 2019.

[361] Z. H. Xu and J. Ågren, “An analysis of piling-up or sinking-in behaviour of elastic-plastic materials under a sharp indentation,” *Philos. Mag.*, vol. 84, no. 23, pp. 2367–2380, 2004.

[362] W. D. Nix and H. Gao, “Indentation size effects in crystalline materials: A law for strain gradient plasticity,” *J. Mech. Phys. Solids*, vol. 46, no. 3, pp. 411–425, 1998.

[363] A. Barnoush, “Correlation between dislocation density and nanomechanical response during nanoindentation,” *Acta Mater.*, vol. 60, no. 3, pp. 1268–1277, 2012.

[364] K. Durst, B. Backes, and M. Göken, “Indentation size effect in metallic materials: Correcting for the size of the plastic zone,” *Scr. Mater.*, vol. 52, no. 11, pp. 1093–1097, 2005.

[365] S. Suresh and A. E. Giannakopoulos, “A new method for estimating residual stresses by instrumented sharp indentation,” *Acta Mater.*, vol. 46, no. 16, pp. 5755–5767, 1998.

[366] S. Yang *et al.*, “Effect of zirconium on the mechanical properties of a super-high strength aluminum alloy,” *Cailiao Yanjiu Xuebao/Chinese J. Mater. Res.*, vol. 16, no. 4, pp. 406–412, 2002.

[367] A. Morozova, Y. Olkhovikova, E. Tkachev, A. Belyakov, and R. Kaibyshev, “Effect of deformation temperature on microstructure and mechanical properties of low-alloyed copper alloy,” *Mater. Sci. Forum*, vol. 941 MSF, pp. 982–987, 2018.

[368] M. Joseph Davidson, K. Balasubramanian, and G. R. N. Tagore, “Surface roughness

prediction of flow-formed AA6061 alloy by design of experiments," *J. Mater. Process. Technol.*, vol. 202, no. 1–3, pp. 41–46, 2008.

[369] Madhav S Phadke, *Quality Engineering Using Robust Design*. Englewood Cliffs, 1989.

List of Publications

1. **Katti Bharath**, Asit Kumar Khanra, M.J. Davidson: "Structural Properties Evaluation of Semi-solid Extruded Al-Cu-Mg Powder Metallurgy Alloys", **Transaction of Indian Institute of Metals,** 72 (4) (2019) 1063-1074 (**SCI**)

2. **Katti Bharath**, Arka Mandal, Anish Karmakar, Asit Kumar Khanra and M.J. Davidson, "Understanding the effect of hot extrusion on the evolution of microstructure and associated mechanical properties in sintered Al-Cu-Mg alloys", **Materials Characterization** 170 (2020) 110715**. (SCI)**

3. **Katti Bharath**, Asit Kumar Khanra, M.J. Davidson: "Hot Deformation behavior and Dynamic Recrystallization Constitutive Modeling of Al-Cu-Mg Powder Compacts processed by Extrusion at Elevated Temperatures", **Journal of Materials: Design and Applications**, (2020) 1-16. (**SCI**)

4. **Katti Bharath**, Asit Kumar Khanra, M.J. Davidson: "Microstructural analysis and Simulation studies of Semi-solid Extruded Al-Cu-Mg Powder Metallurgy Alloys", **Advances in Materials and Metallurgy (LNME),** (2019) 101-114 (**Scopus**)

5. **Katti Bharath**, Asit Kumar Khanra, M.J. Davidson: "Microstructural Evolution of Al-Cu-Mg Sintered Alloys Processed by semi-solid extrusion process", **Materials Science and Technology (MS&T),** (2018) 1440-1446 (**Scopus/proceeding**)

National/International Conferences:

1. **Katti Bharath**, Asit Kumar Khanra, M.J. Davidson: "Effect of Temperature and Densification behavior of Semi-solid Extruded Al-Cu-Mg Powder Metallurgy Alloys", **NMD-ATM 2017, Goa, India.**

2. **Katti Bharath**, Asit Kumar Khanra, M.J. Davidson: "Effect of Temperature and Densification behavior of Semi-solid Extruded Al-Cu-Mg Powder Metallurgy Alloys", **NMD-ATM 2017, Goa, India.**
3. **Katti Bharath**, Asit Kumar Khanra, M.J. Davidson: "Grain size distribution and Simulation studies of Semi-solid Extruded Al-Cu-Mg Powder Metallurgy Alloys", **ICEMMM-2018, Chennai, India. (Best Paper Award)**

4. **Katti Bharath**, Asit Kumar Khanra, M.J. Davidson: "Microstructural Modeling and Dynamic Recrystallization of sintered Al-4%Cu-0.5%Mg alloy during Hot Extrusion Process", **ICAM5-2019, Warangal, India.**

Appendix I Material constants obtained for various processing conditions for hot extruded Al-Cu-Mg P/M preforms with IPRD of 70%

IPRD (%)	Temp (K)	έ (/s)	σ	β	n	α	n'	m	Q	Z	ln(Z)	lnsinh(ασ)	lnA
70	723	0.1	192.34	0.183	35.53	0.0052	16.42	1.64	223.88	1.487E+15	34.936	0.2607	29.7
		0.2	195.46				16.42	1.62	221.15	1.889E+15	35.175	0.2826	29.7
		0.3	198.34				16.42	1.6	218.42	1.799E+15	35.126	0.3028	29.7
	773	0.1	179.78	0.193	34.65	0.0056	16.17	1.64	220.47	7.873E+13	31.997	0.1703	29.7
		0.2	182.11				16.17	1.62	217.78	1.036E+14	32.272	0.1873	29.7
		0.3	185.32				16.17	1.6	215.09	1.023E+14	32.259	0.2106	29.7
	823	0.1	153.03	0.201	33.61	0.006	15.93	1.64	217.20	6.077E+12	29.435	-0.035	29.7
		0.2	154.9				15.93	1.62	214.55	8.253E+12	29.742	-0.02	29.7
		0.3	158.39				15.93	1.6	211.90	8.406E+12	29.76	0.0079	29.7

Appendix II Material property relations of hot extruded Al-Cu-Mg P/M preforms with IPRD of 70%

Temperature (k)	ε (/s)	σ (MPa)	ln(σ) (MPa)	ln(ε) (/S)	1/T*1000	lnsinh (ασ)
723	0.1	192.34	5.25926	-2.30258509	1.38312586	0.260664
	0.2	195.46	5.27536	-1.60943791	1.38312586	0.282632
	0.3	198.34	5.28998	-1.2039728	1.38312586	0.302756
773	0.1	179.78	5.19173	-2.30258509	1.29366106	0.170309
	0.2	182.11	5.20461	-1.60943791	1.29366106	0.187319
	0.3	185.32	5.22208	-1.2039728	1.29366106	0.210561
823	0.1	153.03	5.03063	-2.30258509	1.21506683	-0.03482
	0.2	154.9	5.04278	-1.60943791	1.21506683	-0.0198
	0.3	158.39	5.06506	-1.2039728	1.21506683	0.007919

Appendix III Material constants obtained for various processing conditions for hot extruded Al-Cu-Mg P/M preforms with IPRD of 80%

IPRD (%)	Temp (K)	ε̇ (/s)	σ	β	n	α	n'	m	Q	Z	ln(Z)	lnsinh(ασ)	lnA
80	723	0.1	208.78	0.189	40.35	0.004684	19.58	1.473	239.787	2.094E+16	37.58	0.2451	31.82
		0.2	212.94					1.44	234.415	1.714E+16	37.38	0.2719	31.82
		0.3	214.39					1.41	229.531	1.141E+16	36.973	0.2811	31.82
	773	0.1	188.11	0.2	39.89	0.005014	19.35	1.473	236.97	1.024E+15	34.563	0.1075	31.82
		0.2	191.17					1.44	231.661	8.971E+14	34.43	0.1283	31.82
		0.3	193.63					1.41	226.835	6.351E+14	34.085	0.145	31.82
	823	0.1	168.55	0.215	39.42	0.005454	18.97	1.473	232.317	5.529E+13	31.644	-0.031	31.82
		0.2	171.06					1.44	227.112	5.169E+13	31.576	-0.013	31.82
		0.3	173.65					1.41	222.38	3.884E+13	31.29	0.006	31.82

Appendix IV Material property relations of hot extruded Al-Cu-Mg P/M preforms with IPRD of 80%

Temperature (k)	ε̇ /s	σ (MPa)	ln(σ) (MPa)	ln(ε̇) (/S)	1/T*1000	lnsinh (ασ)
723	0.1	208.78	5.34128	-2.30258509	1.38283897	0.245058
	0.2	212.94	5.36101	-1.60943791	1.38283897	0.271864
	0.3	214.39	5.3678	-1.2039728	1.38283897	0.281145
773	0.1	188.11	5.23703	-2.30258509	1.29341008	0.107459
	0.2	191.17	5.25316	-1.60943791	1.29341008	0.128338
	0.3	193.63	5.26595	-1.2039728	1.29341008	0.144986
823	0.1	168.55	5.12723	-2.30258509	1.21484541	-0.03103
	0.2	171.06	5.14201	-1.60943791	1.21484541	-0.01272
	0.3	173.65	5.15704	-1.2039728	1.21484541	0.005989

Appendix V Material constants obtained for various processing conditions for hot extruded Al-Cu-Mg P/M preforms with IPRD of 90%

	Temp (K)	ε (/s)	σ	β	n	α	n'	m	Q	Z	ln(Z)	lnsinh(ασ)	lnA
90 % IPRD	723	0.1	219.38	0.195	43.759	0.0045	23.15	1.28	246.36	6.248E+16	38.674	0.2019	33.02
		0.2	222.41					1.25	240.586	4.783E+16	38.406	0.2202	33.02
		0.3	224.22					1.21	232.888	1.994E+16	37.531	0.2311	33.02
	773	0.1	198.08	0.2	43.46	0.0046	22.9	1.28	243.7	2.919E+15	35.61	0.069	33.02
		0.2	201.05					1.25	237.988	2.4E+15	35.414	0.088	33.02
		0.3	202.71					1.21	230.373	1.101E+15	34.635	0.0985	33.02
	823	0.1	185.24	0.215	42.26	0.0051	22.84	1.28	243.061	2.658E+14	33.214	-0.015	33.02
		0.2	187.64					1.25	237.365	2.312E+14	33.074	0.0008	33.02
		0.3	189.62					1.21	229.769	1.143E+14	32.37	0.0139	33.02

Appendix VI Material property relations of hot extruded Al-Cu-Mg P/M preforms with IPRD of 90%

Temperature (k)	έ (/s)	σ (MPa)	ln(σ) (MPa)	ln(έ) (/S)	1/T*1000	lnsinh (ασ)
723	0.1	219.38	5.39081	-2.30258509	1.38312586	0.201916
	0.2	222.41	5.40452	-1.60943791	1.38312586	0.22024
	0.3	224.22	5.41263	-1.2039728	1.38312586	0.231124
773	0.1	198.08	5.28867	-2.30258509	1.29366106	0.068973
	0.2	201.05	5.30355	-1.60943791	1.29366106	0.087984
	0.3	202.71	5.31178	-1.2039728	1.29366106	0.098538
823	0.1	185.24	5.22165	-2.30258509	1.21506683	-0.01525
	0.2	187.64	5.23453	-1.60943791	1.21506683	0.000756
	0.3	189.62	5.24502	-1.2039728	1.21506683	0.013868